

TECHNICAL UNIVERSITY OF DENMARK

DOCTORAL THESIS

**Phase Equilibrium Modeling for Shale
Production Simulation**

Author:

Diego Sandoval

Supervisors:

Assoc. Prof. Wei Yan

Prof. Michael L. Michelsen

Prof. Erling H. Stenby



*A thesis submitted in partial fulfillment of the requirements
for the degree of Ph.D.*

DTU - Kemi
Kongens Lyngby, Denmark
June 30, 2017

Abstract

Production of oil and gas from shale reservoirs has gained more attention in the past few decades due to its increasing economic feasibility and the size of potential sources around the world. Shale reservoirs are characterized by a more tight nature in comparison with conventional reservoirs, having pore size distributions ranging in the nanometer scale. Such a confined nature introduces new challenges in the fluid phase behavior. High capillary forces can be experienced between the liquid and vapor, and selective adsorption of components onto the rock becomes relevant. The impact of these effects is of great importance to understanding the storage of hydrocarbons inside and to forecasting its production.

In this thesis, a study focused on the effects of capillary pressure and adsorption on phase behavior, and their impact on oil production is provided. An efficient algorithm for phase envelope calculations in the presence of the capillary pressure is presented, and it is used to analyze the main changes on the phase boundary for several fluids of interest. The results show changes in the saturation pressure and temperature along the phase envelope, except at the critical point. A linear analysis is presented to explain such changes, as a result, useful mathematical relationships that estimate the magnitude of these changes were obtained. Moreover, a flash algorithm that accounts for capillarity was developed. The algorithm was implemented into a fully implicit compositional reservoir simulator, which was then used to assess the impact of the capillary pressure on phase behavior in oil and gas production from tight reservoirs.

Since capillary pressure and adsorption occur simultaneously in shale, its combined effect was studied. A model comparison for high-pressure adsorption in shale is presented. The adsorption data in shale is generally scarce, therefore, additional capabilities besides the accuracy were considered in the comparison. The multicomponent potential theory of adsorption yields the best results. Moreover, it shows to be useful to extrapolate adsorption data for hydrocarbons that are not available in the literature. An algorithm for phase split calculations considering both capillary pressure and adsorption was developed. The results show that adsorption and capillary pressure can significantly change the phase behavior. In general, a much shrunk phase envelope with a shifted critical point is obtained for hydrocarbon mixtures. Such behavior is mainly caused by compositional changes in the bulk phase due to selective adsorption of the heavier components onto the rock, while the change in bubble point pressure is mainly due to capillary pressure.

This study has developed several robust calculation tools for phase equilibrium in porous media with capillary pressure and adsorption effects. Analysis using these tools have shown that capillary pressure and adsorption have non-negligible effects on phase equilibrium in shale. As general tools, they can be used to calculate phase equilibrium in other porous media as well. The compositional simulator with added capillary pressure effects on phase equilibrium can be used for evaluating the effects in dynamic and more complex scenarios.

Resumé på Dansk

Produktion af olie og gas fra skifergas reservoirer har fået mere opmærksomhed i de seneste årtier på grund af øget økonomisk incitament og mængden af potentielle kilder i hele verden. Skifergas reservoirer er karakteriseret ved tættere struktur i forhold til traditionelle reservoirer, med en distribution af pore størrelser i nanometer skala. En sådan tæt struktur medfører nye udfordringer i fluid fasernes opførsel. Kraftige kapillærer kræfter kan forventes mellem væske og gas og selektiv adsorption på stenen bliver relevant. Virkningen af disse effekter har stor vigtighed for forståelsen af oplagret carbonhydrider og for forudsigelsen af produktionen.

I denne afhandling er der udført et studie med fokus på effekten af kapillærtryk og adsorption på fase opførelse og deres virkning på olie produktionen. En effektiv algoritme for fasekonvolut beregninger under indflydelse af kapillærtryk er præsenteret, og den er brugt til at analysere de væsentligste ændringer af fasevægt for en række fluider af interesse. Resultaterne viser ændringer i mætningstryk og temperatur langs fasekonvolutten, med undtagelse af det kritiske punkt. En lineær analyse er præsenteret for at forklare sådanne ændringer, og som et resultat af dette blev fundet brugbare matematiske forbindelser, der estimerer størrelsen af disse ændringer. Derudover er der udviklet en flash algoritme der tager højde for kapillaritet. Denne algoritme blev implementeret i en fuldt implicit kompositorisk reservoir simulator, der da er brugt til at beregne virkningen af kapillærtrykket på fase opførelsen ved olie og gas produktion fra tætte reservoirer.

Da kapillærtryk og adsorption sker simultant i skifer er den kombineret effekt undersøgt. En model sammenligning for høj tryk adsorption i skifer er præsenteret. Adsorptions data i skifer er generelt få, og derfor, er andre egenskaber ud og præcision taget i betragtning i denne sammenligning. Modellen multicomponent potential theory of adsorption giver de bedste resultater. Det viser sig derudover at den er brugbar til ekstrapolering af adsorptions data for carbonhydrider der ikke er tilgængelige i litteraturen. En algoritme for fase split beregninger med både kapillærtryk og adsorption taget i betragtning er udviklet. Resultaterne viser at adsorption og kapillærtryk kan ændre fase opførelsen signifikant. Generelt er set en meget skumpet fasekonvolut med et forskudt kritisk punkt for carbonhydrider. Denne opførsel er primært forskyldt af sammensætnings ændringer i den primære, frie, fase, på grund af selektiv adsorption af de tungere komponenter til stenen, mens ændringen i boblepunktstryk er primært forskyldt af kapillærtrykket.

Dette studie har udviklet flere robuste beregnings værktøjer for fase ligevægt i porøse medier under indflydelse af kapillærtryk og adsorption. Analyser lavet ved brug af disse værktøjer viser at kapillærtryk og adsorption har en ikke ubetydelig effekt på fase ligevægt i skifer. Som generelle værktøjer kan de også bruges til at beregne fasevægt i andre porøse materialer. Den kompositoriske simulator hvor kapillærtryks effekt på fasevægt var tilføjet kan bruges til evaluering af effekter i dynamiske og mere komplekse scenarier.

*Dedicated to my family for showing me the meaning of union
in the distance*

*Dedicado a mi familia por enseñarme el significado de unión
en la distancia*

Acknowledgements

I am deeply grateful to my supervisors Dr. Wei Yan, Prof. Michael Michelsen, and Prof. Erling Stenby who guided me and cared so much about my work during the entire process. Without their support and encouragement, this work would not have been possible. I am also thankful to Prof. Kristian Jessen for his valuable input and suggestions in reservoir simulation. A very special gratitude goes to ConocoPhillips and ExxonMobil for helping and providing the funding for the work.

I would like to thank my office friends and colleagues, Farhad, Teresa, Duncan, and Christos, for making of the workplace an enjoyable and productive environment. I am particularly grateful for the assistance given by Anders Schlaikjer with the translation to danish.

Last but not least, I would like to thank my parents, Mynor and Nora; and my siblings, Pedro, Andrea, and Mynor, for their unconditional support and love sent from back home. To my friends, and second family: Luisa, André, Isis, Ale, Pepe, Azahar, Álvaro and Ana, thanks for your friendship and believing in me from the beginning.

Contents

1. Introduction	1
2. Phase Equilibrium Involving Capillary Pressure	7
2.1. The Phase Envelope in the Presence of Capillary Pressure	9
2.1.1. The System of Equations	9
2.1.2. Solution Approach	11
2.1.3. Analysis of the Phase Envelope Shift	14
Saturation Pressure	14
Saturation Temperature	17
Relationship with the Multicomponent Clapeyron Equation . .	18
2.1.4. Results and Discussion	19
Effect of the Feed Composition	24
Capillary Radius	29
Quality Lines	29
Sensitivity on Scaling Exponent (E) and Parachors (χ)	31
2.2. Two-phase Flash Involving Capillary Pressure	33
2.2.1. Successive Substitution	36
2.2.2. Gibbs Energy Minimization	37
2.2.3. Flash Strategy	38
2.2.4. Stability Analysis	39
2.2.5. P_l and P_g Flash Specifications	41
2.3. Conclusions	45
3. Multicomponent Adsorption in Shale	47
3.1. Adsorption Models	48
3.1.1. Multicomponent Langmuir (ML)	48
3.1.2. Ideal Adsorbed Solution Theory (IAST)	50
3.1.3. Multicomponent Potential Adsorption Theory (MPTA)	54
3.2. Experimental data	55
3.3. Results	57

3.4. Conclusions	66
4. Phase Equilibrium Involving Both Capillary Pressure and Adsorption	67
4.1. Phase Envelope Including Capillary Pressure and Adsorption Film . .	68
4.2. Artificial Adsorption Data from MPTA	70
4.3. Flash Calculations Involving Both Capillary Pressure and Adsorption	76
4.3.1. Methodology	78
Direct Substitution	79
Quadratic Update on Vapor Flows	81
4.4. Results	84
4.4.1. Binary System	85
4.4.2. Ternary System	90
4.4.3. Low-GOR and High-GOR Systems	93
4.4.4. Discussion on Perceived Phase Envelope Changes	97
4.5. Conclusions	101
5. Compositional Reservoir Simulation with Capillary Pressure	103
5.1. Compositional Reservoir Simulator (COSI)	105
5.1.1. Mathematical Model	105
Constraints	106
5.1.2. Numerical Model	107
5.1.3. Choice of Variables	110
Cell Average Variables	111
Cell Boundary Variables	111
5.2. Integration of Capillary Pressure Effect on Phase Behavior in COSI .	112
5.2.1. Change of Variables in Thermodynamic Subroutines	112
5.2.2. The Capillary Pressure Model	113
5.3. Case of Study	116
5.3.1. Fixed Pore Size	119
5.3.2. Variable Pore Size	119
5.4. Results	122
5.5. Conclusions	124
6. Conclusions	133
A. Artificial Adsorption Data of Alkanes on Shale Using MPTA	137
Bibliography	159

List of Figures

2.1.	Convergence behavior for the first point in the construction of the phase envelope of System I, described in table 2.1	20
2.2.	Phase Envelope in the presence of capillary pressure of System (I) using a capillary radius of 10 nm. Highlighted circles show the main differences and similarities with respect the normal phase envelope.	21
2.3.	Phase envelope of C ₁ -C ₄ mixtures at different feed compositions. The solid lines (—) represent the normal phase envelopes; Dashed lines (- - -) represent the modified phase envelopes due to a capillary pressure difference using $r_c = 10\text{nm}$	25
2.4.	Phase envelope of reservoir fluid mixtures described in Table 2.7 with GOR ranging from 500 to 4000 scf/STB. The solid lines (—) represent the normal phase envelopes; Dashed lines (- - -) represent the modified phase envelopes due to a capillary pressure difference using $r_c = 10\text{nm}$	27
2.5.	Phase envelope of reservoir fluid mixtures described in Table 2.7 with GOR ranging from 6667 to 33333 scf/STB. The solid lines (—) represent the normal phase envelopes; Dashed lines (- - -) represent the modified phase envelopes due to a capillary pressure difference using $r_c = 10\text{nm}$	27
2.6.	Saturation pressure variation respect GOR at (400 K) for mixtures shown in Table 2.7	28
2.7.	Saturation pressure variation respect OGR at (400 K) for mixtures shown in Table 2.7	28
2.8.	Bubble point change at different capillary radius (r_c) for a 70-30 mol% C ₁ -C ₄ mixture.	30
2.9.	Bubble point change at different temperatures as a function of ($\frac{1}{r_c}$) for a 70-30 mol% C ₁ -C ₄ mixture. Dashed lines (- - -) show the approximation given by (Eq. 2.54).	30

2.10. Dew point change at different temperatures as a function of $(\frac{1}{r_c})$ for a 70-30 mol% C ₁ -C ₄ mixture. Dashed lines (- - -) show the approximation given by (Eq. 2.54).	31
2.11. Quality lines at different vapor fractions (β) for a 70-30 mol% C ₁ -C ₄ system. (—) Normal quality lines; (\cdots) P_l ; and (- - -) P_g due to capillary pressure difference. $r_c=10nm$	32
2.12. Pressure profiles as a function of the vapor fraction. $T = 250 K$	32
2.13. Sensitivity analysis on scaling exponent E for System I	34
2.14. Sensitivity analysis on the parachor of the lightest hydrocarbon for System I.	34
2.15. Sensitivity analysis on the parachor of the heaviest hydrocarbon for System I.	35
2.16. P_l flash specification. 70% – 30% C ₁ -C ₄ mixture inside a capillary tube of $r_c = 10nm$. Dashed lines (- - -) represent the gas pressure at the saturation point.	43
2.17. P_g flash specification. 70% – 30% C ₁ -C ₄ mixture inside a capillary tube of $r_c = 10nm$. Dashed lines (- - -) represent the liquid pressure at the saturation point.	43
2.18. P_l flash specification. Bakken oil inside a capillary tube of $r_c = 10nm$. Dashed lines (- - -) represent the gas pressure at the saturation point.	44
2.19. P_g flash specification. Bakken oil inside a capillary tube of $r_c = 10nm$. Dashed lines (- - -) represent the liquid pressure at the saturation point.	44
3.1. Common supercritical isotherm for C ₁ in shale at 323 K. Data generated with MPTA	49
3.2. Experimental adsorption measurements of CO ₂ at 65°C for a Namurian shale sample performed by different laboratories. Figure taken from Gasparik et al. [23]	56
3.3. Methane adsorption data fitting example for the three models. Experimental data taken from [23], sample "Namurian: Lab 5" T=338 K	58
3.4. Ethane adsorption data fitting example for the three models. Experimental data taken from [64]. T=313 K	59
3.5. CO ₂ adsorption data fitting example for the three models. Experimental data taken from [23], sample "Namurian: Lab 5" T=338 K	59
3.6. Fitting of pure component data used to predict the binary system in Figure 3.11 and Figure 3.8	62

3.7. Prediction of adsorbed amounts for a C_1 - C_2 mixture with a molar composition of 70%-30% [24]	63
3.8. Selectivity of C_2 with respect to C_1 for a C_1 - C_2 mixture with a molar composition of 70%-30% [24]	63
3.9. Fitting of pure component data used to predict the binary system in Figure 3.7 and Figure 3.10	64
3.10. Absolute adsorbed amount prediction for C_1 - CO_2 mixture with a molar composition of 80%-20%. Experimental data taken from (#3 Shale [65]).	64
3.11. CO_2 adsorbed amount prediction for C_1 - CO_2 mixture with a molar composition of 80%-20%. Experimental data taken from (#3 Shale [65]).	65
4.1. Phase envelope of two C_1 - C_4 mixtures at different compositions. The solid line (—) represents the normal phase envelope; the dashed line (- - -) considering P_c with effective capillary radius $r_c = 3 \text{ nm}$; and the dotted line (···) considering P_c +Adsorption with a total radius of $r = 3 \text{ nm}$ and variable effective capillary radius $r_c = r - t_a$. The surface area considered was $A = 28 \text{ m}^2/\text{g}$	71
4.2. Adsorption data from Wang et al. [64] fitted with MPTA.	72
4.3. Energy term as a function of the carbon number in alkanes (Monsalvo and Shapiro [57]). Adsorbents: Activated Carbon (AC) and Molecular Sieves (MS)	73
4.4. Blue spheres correspond to the bulk phases (gas and liquid), and green spheres correspond to the excess adsorbed phase. The first blue/green layer next to the wall corresponds to the absolute adsorbed layer. Figure taken from Mason et al. [71]	76
4.5. Convergence for C_1 - C_2 binary system in the single phase region at (240 K, 70 bar). Acceleration of z_b after each 4 steps. Tolerance limit (- - -); Vanishing of the gas phase (···).	86
4.6. Convergence for C_1 - C_2 binary system near to the bubble point, ($T=240 \text{ K}$, P_l 53.9 bar). Acceleration of z_b after each 4 steps. Tolerance limit (- - -); Vanishing/appearance of the gas phase (···).	86
4.7. C_1 - C_2 binary system. [Left] Normal phase envelope in red; with capillary pressure and adsorption in yellow. [Right] Phase envelope with relative vapor fractions. Dashed line (- - -) represent the pressure in the gas phase.	88

4.8.	C ₁ -C ₂ binary system. [<i>Left</i>] Change of the C ₂ molar fraction in bulk phase \mathbf{z}_b . [<i>Right</i>] C ₂ molar fraction in the absolute adsorbed phase \mathbf{x}^{abs}	89
4.9.	Excess adsorbed phase fraction (θ) for C ₁ -C ₂ binary system. Continuous line (—) represents the feed phase pressure, dashed line (- - -) represent the incipient phase pressure.	89
4.10.	Ternary system. [<i>Left</i>] Normal phase envelope in red; with capillary pressure and adsorption in yellow. [<i>Right</i>] Excess adsorbed phase fraction (θ) plotted against the liquid phase pressure. Dashed line (- - -) represents the gas phase pressure.	91
4.11.	Ternary system. [<i>Left</i>] Change of the C ₁₀ molar fraction in the bulk phase \mathbf{z}_b . [<i>Right</i>] C ₁₀ molar fraction in the absolute adsorbed phase \mathbf{x}^{abs}	91
4.12.	Composition profile of the bulk phase (\mathbf{z}_b) as a function of the pressure (P_l) at $T = 400\text{ K}$ and $T = 450\text{ K}$ respectively.	92
4.13.	Adsorption selectivity with respect to C ₁ as a function of the pressure (P_l) at $T = 400\text{ K}$ and $T = 450\text{ K}$ respectively.	92
4.14.	Normal phase envelope in red; with capillary pressure and adsorption in yellow. [<i>Left</i>] Low-GOR. [<i>Right</i>] High-GOR.	94
4.15.	Excess adsorbed phase fraction (θ) plotted against the liquid phase pressure. Dashed line (- - -) represents the gas phase pressure. [<i>Left</i>] Low-GOR. [<i>Right</i>] High-GOR.	94
4.16.	C ₁₆ molar fraction change in bulk phase \mathbf{z}_b . [<i>Left</i>] Low-GOR, reference feed ($z_{C_{16}} = 0.501$). [<i>Right</i>] High-GOR, reference feed ($z_{C_{16}} = 0.0174$).	95
4.17.	C ₁₆ molar fraction in the absolute adsorbed phase \mathbf{x}^{abs} . [<i>Left</i>] Low-GOR. [<i>Right</i>] High-GOR.	95
4.18.	Composition profile of the bulk phase (\mathbf{z}_b) as a function of the pressure (P_l). [<i>Left</i>] Low-GOR at $T = 400\text{ K}$. [<i>Right</i>] High-GOR at $T = 350\text{ K}$	96
4.19.	Adsorption selectivity with respect to C ₁ as a function of the pressure (P_l). [<i>Left</i>] Low-GOR at $T = 400\text{ K}$. [<i>Right</i>] High-GOR at $T = 300\text{ K}$	96
4.20.	Phase envelope comparison for the low-GOR system with and without the in-situ correction. Phase envelope using z^b without capillary and adsorption effects in red.	99

4.21. Phase envelope comparison for the high-GOR system with and without the in-situ correction. Phase envelope using z^b without capillary and adsorption effects in red.	99
4.22. Composition profile of the bulk phase (\mathbf{z}_b) as a function of the pressure (P_l). [Left] Low-GOR at $T = 450$ K. [Right] High-GOR at $T = 400$ K.	100
5.1. Top view of the two-dimensional reservoir with 10 planar fractures. x-length = 914.4m (3000 ft), y-length = 182.9m (600 ft), z-thickness = 76.2 m (250 ft).	117
5.2. Relative permeability curves for the oil and gas phases. Data obtained from Yu et al. [83]	117
5.3. [Left] J-function (taken from Brooks and Corey [86]). [Right] Effective capillary radius based on J-function at different rock permeability. . .	120
5.4. Cumulative oil production. Rock permeability $K = 1\mu D$	125
5.5. Cumulative gas production. Rock permeability $K = 1\mu D$. Cases A_1 to F_1	126
5.6. Oil saturation map at $yr = 30$ for case A_1 . Solid lines (—) indicate the tip of the fractures	126
5.7. Oil saturation map at $yr = 30$ for case C_1 . Solid lines (—) indicate the tip of the fractures	126
5.8. Bubble point of the Bakken fluid for cases A_1 and C_1	127
5.9. Solution Gas-Oil ratio (R_s) as function of the average pressure of the reservoir. Cases A_1 to F_1	127
5.10. Producing Gas-Oil ratio over time. Cases A_1 to F_1	128
5.11. C_1 molar composition at production. Rock permeability $K = 1\mu D$. Cases A_1 to F_1	128
5.12. Average pressure profile of the reservoir. Rock permeability $K = 1\mu D$. Cases A_1 to F_1	129
5.13. Pressure map at $yr = 30$ for case A_1 . Solid lines (—) indicate the tip of the fractures	129
5.14. Pressure map at $yr = 30$ for case C_1 . Solid lines (—) indicate the tip of the fractures	129
5.15. Cumulative oil production. Rock permeability $K = 100$ nD. Cases A_2 to F_2	130
5.16. Producing Gas-Oil ratio over time. Cases A_2 to F_2	130

5.17. Solution Gas-Oil ratio (R_s) as function of the average reservoir pressure. Cases A_2 to F_2 131

5.18. Average pressure profile of the reservoir. Cases A_2 to F_2 131

List of Tables

- 2.1. System I. Natural gas mixture, description of basic model parameters including non zero binary interaction parameters (k_{ij}) 20
- 2.2. Values corresponding to highlighted points in Figure 2.2. 21
- 2.3. Direction of change of the saturation pressure in the bubble point region due to a capillary pressure difference in the system. 22
- 2.4. Direction of change of the saturation pressure in the dew point region due to a capillary pressure difference in the system. 23
- 2.5. Direction of change of the saturation temperature in the dew point region due to a capillary pressure difference in the system. 23
- 2.6. Binary system. Description of basic model parameters ($k_{ij} = 0$) 24
- 2.7. Reservoir fluid systems general description. Taken from Whitson and Sunjerga [44] 26
- 2.8. Maximum saturation pressure change for GOR systems in the temperature range of 300 K to 500 K. From Figure 2.5 and 2.4 26
- 2.9. Capillary pressure and interfacial tension values for the bubble point branch of the 500 GOR reservoir fluid. 26
- 2.10. Compositional data for Bakken oil 42

- 3.1. Experimental data for adsorption of pure components in shale. 57
- 3.2. Experimental data for adsorption of multicomponent mixtures in shale. 57
- 3.3. Comparison of the three models for pure component adsorption. Fitting of data summarized in Table 3.1 58
- 3.4. Description of the type and quantity of regressed parameters for each model. 60
- 3.5. Comparison of three models tested for the prediction of the multicomponent adsorption data summarized in Table 3.2 61

- 4.1. Thickness of the adsorption film (t_a), interfacial tension (σ), and capillary pressure (P_c) for C₁-C₄ 70%-30% mixture shown in Figure 4.1. AF:Adsorption Film. 70

4.2. Thickness of the adsorption film (t_a), interfacial tension (σ), and capillary pressure (P_c) for C ₁ -C ₄ 30%-70% mixture shown in Figure 4.1. AF:Adsorption Film.	71
4.3. MPTA fitting parameters corresponding to data in Figure 4.2	72
4.4. Extrapolated energy parameters for different alkanes	73
4.5. Summary of Langmuir fittings for the artificial data.	75
4.6. Summary of the fitting for the Langmuir temperature dependent parameters.	75
4.7. Molar composition of the systems.	84
4.8. EoS component parameters and parachor constants.	84
4.9. Correlation constants for temperature dependent Langmuir parameters.	84
4.10. Molar composition with and without in-situ correction.	98
5.1. Gridding along the Y-axis (along the fracture). See Figure 5.1 for reference.	118
5.2. Periodic gridding along the X-axis (along the well). See Figure 5.1 for reference.	118
5.3. Compositional data for Bakken oil	119
5.4. Simulation scenarios. Labeling given by letter and subscript.	122
A.1. Summary of Langmuir fittings for the artificial data.	138
A.2. Artificial MPTA data (n^{exp}), and Langmuir fit (n^L) for C ₁ at 223 K.	139
A.3. Artificial MPTA data (n^{exp}), and Langmuir fit (n^L) for C ₁ at 323 K.	139
A.4. Artificial MPTA data (n^{exp}), and Langmuir fit (n^L) for C ₁ at 373 K.	140
A.5. Artificial MPTA data (n^{exp}), and Langmuir fit (n^L) for C ₁ at 423 K.	140
A.6. Artificial MPTA data (n^{exp}), and Langmuir fit (n^L) for C ₁ at 473 K.	141
A.7. Artificial MPTA data (n^{exp}), and Langmuir fit (n^L) for C ₁ at 573 K.	141
A.8. Artificial MPTA data (n^{exp}), and Langmuir fit (n^L) for C ₂ at 223 K.	142
A.9. Artificial MPTA data (n^{exp}), and Langmuir fit (n^L) for C ₂ at 323 K.	142
A.10. Artificial MPTA data (n^{exp}), and Langmuir fit (n^L) for C ₂ at 373 K.	143
A.11. Artificial MPTA data (n^{exp}), and Langmuir fit (n^L) for C ₂ at 423 K.	143
A.12. Artificial MPTA data (n^{exp}), and Langmuir fit (n^L) for C ₂ at 473 K.	144
A.13. Artificial MPTA data (n^{exp}), and Langmuir fit (n^L) for C ₂ at 573 K.	144
A.14. Artificial MPTA data (n^{exp}), and Langmuir fit (n^L) for C ₄ at 323 K.	145
A.15. Artificial MPTA data (n^{exp}), and Langmuir fit (n^L) for C ₄ at 373 K.	145
A.16. Artificial MPTA data (n^{exp}), and Langmuir fit (n^L) for C ₄ at 423 K.	146
A.17. Artificial MPTA data (n^{exp}), and Langmuir fit (n^L) for C ₄ at 473 K.	146
A.18. Artificial MPTA data (n^{exp}), and Langmuir fit (n^L) for C ₄ at 573 K.	147

A.19. Artificial MPTA data (n^{exp}), and Langmuir fit (n^L) for C ₈ at 323 K .	147
A.20. Artificial MPTA data (n^{exp}), and Langmuir fit (n^L) for C ₈ at 373 K .	148
A.21. Artificial MPTA data (n^{exp}), and Langmuir fit (n^L) for C ₈ at 423 K .	148
A.22. Artificial MPTA data (n^{exp}), and Langmuir fit (n^L) for C ₈ at 473 K .	149
A.23. Artificial MPTA data (n^{exp}), and Langmuir fit (n^L) for C ₈ at 573 K .	149
A.24. Artificial MPTA data (n^{exp}), and Langmuir fit (n^L) for C ₁₀ at 323 K .	150
A.25. Artificial MPTA data (n^{exp}), and Langmuir fit (n^L) for C ₁₀ at 373 K .	150
A.26. Artificial MPTA data (n^{exp}), and Langmuir fit (n^L) for C ₁₀ at 423 K .	151
A.27. Artificial MPTA data (n^{exp}), and Langmuir fit (n^L) for C ₁₀ at 473 K .	151
A.28. Artificial MPTA data (n^{exp}), and Langmuir fit (n^L) for C ₁₀ at 573 K .	152
A.29. Artificial MPTA data (n^{exp}), and Langmuir fit (n^L) for C ₁₂ at 323 K .	152
A.30. Artificial MPTA data (n^{exp}), and Langmuir fit (n^L) for C ₁₂ at 373 K .	153
A.31. Artificial MPTA data (n^{exp}), and Langmuir fit (n^L) for C ₁₂ at 423 K .	153
A.32. Artificial MPTA data (n^{exp}), and Langmuir fit (n^L) for C ₁₂ at 473 K .	154
A.33. Artificial MPTA data (n^{exp}), and Langmuir fit (n^L) for C ₁₂ at 573 K .	154
A.34. Artificial MPTA data (n^{exp}), and Langmuir fit (n^L) for C ₁₆ at 323 K .	155
A.35. Artificial MPTA data (n^{exp}), and Langmuir fit (n^L) for C ₁₆ at 373 K .	155
A.36. Artificial MPTA data (n^{exp}), and Langmuir fit (n^L) for C ₁₆ at 423 K .	156
A.37. Artificial MPTA data (n^{exp}), and Langmuir fit (n^L) for C ₁₆ at 473 K .	156
A.38. Artificial MPTA data (n^{exp}), and Langmuir fit (n^L) for C ₁₆ at 573 K .	157

List of Abbreviations

AAD	A bsolute A verage D eviation
DFT	D ensity F unctional T heory
DRA	D ubinin R adushkevich A stakhov
EOR	R ecovery O il R ecovery
EoS	E quation of S tate
FIM	F ully I mplicit M ethod
GOR	G as O il R atio
IAST	I deal A dsorbed S olution T heory
IFD	I ntegral F inite D ifference
IMPEC	I mplicit P ressure E xplicit C omposition
ML	M ulticomponent L angmuir
MPTA	M ulticomponent P otential T heory of A dsorption
PR	P eng R obinson
PVT	P ressure V olume T emperature
SRK	S oave R edlich K wong
STO	S tack T ank O il

List of Symbols

Latin Symbols

b	Langmuir equilibrium constant
f	Fugacity
k_{ij}	Binary interaction parameter
k	Permeability
l	Liquid flows
m^i	Mass flows
n	Molar amounts
r_c	Capillary radius
t_a	Thickness of adsorbed phase
u	Flow velocity vector
v_i	Vapor Flows
w_i	Molar fraction excess adsorbed phase
x_i	Molar fraction liquid phase
x_i^a	Molar fraction absolute adsorbed phase
y_i	Molar fraction gas phase
z_i	Molar fraction feed phase
z_i^b	Molar fraction bulk phase
z_0	Adsorption capacity
A	Surface Area
C^i	Mass fraction
D	Diffusion tensor
E	Scaling exponent
E_h	Enthalpy of adsorption
G	Gibbs energy
G_f	Geometric factor
H	Hessian
J	Jacobian
K_i	Equilibrium factor
N_c	Number of components
P	Pressure
P_c	Capillary pressure
P_{crit}	Critical pressure
R	Gas constant Curvature
R_c	Solution gas-oil ratio
S	Entropy, Saturation
$S_{i,j}$	Selectivity of i wrt j

T	Temperature
T_{crit}	Critical Temperature
U	Internal energy
V	Volume
V_m	Molar volume
Z	Compressibility factor

Greek Letters

β	Vapor fraction, Scaling exponent
ϵ	Solid-fluid interaction energy parameter
ϕ	Porosity
φ	Fugacity coefficient
μ	Chemical potential, Viscosity
π	Spreading pressure
θ	Contact angle, Phase fractions
ρ	Density
σ	Interfacial tension
ω	Accentric factor
Φ	Fugacity derivative wrt molar amounts
Γ	Surface excess

CHAPTER 1

Introduction

Global demand for energy and fuels increases every day as the world's population grows and new large economies emerge. The continuous seek for new technologies and feasible energy resources is needed to meet that energy demand. On one hand, production of oil and gas from conventional resources decreases every year due to the depletion of reserves around the world. On the other hand, new technologies such as wind and solar power, are still not sufficiently mature and economically viable to cover the gap between the energy demand and supply. As a result, exploitation towards unconventional energy resources has grown in the past few decades. New technologies such as horizontal drilling and multistage hydraulic fracturing have been crucial to economically produce oil and gas from shale reservoirs, which once were considered to be of no technical viability. The Barnett Shale in central Texas is recognized to be the shale play that led the so-called Shale Gas Boom, being the first economically viable to produce [1]. Since then, production from shale has been the fastest growing energy sector in the United States, being able to partly substitute electricity production from coal-fired power plants [2]. The same trend is expected in other parts of the world. However, current recovery factors of producing fields are very low in comparison to conventional reservoirs. The recovery factor for shale gas ranges from 20% to 30%, and for shale oil from 3% to 7% [3]. A better understanding of the processes involved in the subsurface and throughout their production can lead to improve existing techniques and develop new ones that can achieve higher recovery factors.

Around 60% of the earth's sedimentary crusts consists of shale, which serves as

a the source rock for conventional reservoirs. It possesses ultra-low permeability of several orders of magnitude lower than that of conventional reservoirs. It is not unlikely to find a shale reservoir with porosities from 0.1 to 0.25 and a rock permeability in the nano-Darcy scale [4–6]. The poor flowability of the contained fluids is one of the reasons of its low recovery factor. Moreover, shale consists of a heterogeneous mixture of organic and inorganic matter resulting in a wide variety of surface chemistry and pore shapes/sizes [7]. The combination of both ultra-tight nature and surface heterogeneity introduces many challenges at different stages from its storage to its final production. A better understanding of phase behavior in confined systems is of great importance to address many of these challenges. It would allow us to better estimate the physical and thermodynamic properties that determine its storage and flow in the subsurface. Moreover, knowledge of phase equilibrium in shale could serve to develop models and algorithms, that in the long run could be used in reservoir simulation to study the oil and gas production at the field scale.

Phase equilibrium in confined spaces differs from that in bulk. High capillary forces and wall effects become relevant in pores ranging in the nanometer scale. The effect of the capillary pressure in phase equilibrium has been studied both theoretically and experimentally. A key finding was obtained by Fisher and Israelachvili [8–10] when they confirmed the validity of the Kelvin equation down to a few nanometers ($\sim 4\text{nm}$ or eight times the molecular diameter) for pure cyclohexane by measuring liquid bridges between crossed mica cylinders. In relation to Fisher and Israelachvili's work, Christenson [11] demonstrated the validity of the Laplace equation between water and oil to radii of two nanometers suggesting the validity of continuously curved interfaces at nanometer scale for liquid-liquid systems. The picture is more complicated for mixtures. Adsorption of components to the solid, and to the liquid-vapor interface, are difficult to control within standard experimental setups. Nevertheless, attempts have been made using differential scanning calorimetry for fluids inside controlled pore glasses with pore sizes in the nanometer scale [12]. Deviations from the bulk phase behavior are observed, however, due to the complex interplay of the adsorption effects and capillarity in the experiment, it is difficult to draw strong conclusions. From a theoretical point of view, the Kelvin equation has been extended to mixtures by Shapiro and Stenby [13]. In their subsequent work [14], they provided a solid analysis establishing the boundaries on the intensive variables in which phase equilibrium under capillary pressure can exist. In addition, Sherafati et al. [15] presented an algorithm for stability analysis including capillarity based

on the minimization of the modified tangent plane distance proposed by Michelsen [16]. Furthermore, the impact of the capillary pressure on phase behavior in oil production has been studied using reservoir simulations by several authors obtaining common findings [17–20]. In general, the cumulative oil production increases and changes in the producing GOR are encountered compared to the case where no capillarity is accounted in the phase equilibrium. These changes become negligible at pore sizes above 50-100 nm.

Adsorption effects become more relevant as the pore sizes decrease and the surface-volume ratio of the system increases. Adsorption is considered the principal effect occurring in micro-pores and small mesopores of natural reserves [21]. The storage of gas in shale mostly occurs within the organic micropores and mesopores. Moreover, the density of the adsorbed phase can be 1.8–2.5 times larger than that of bulk [22]. Experimental measurements of adsorption at reservoir conditions are challenging. A complete study on the reproducibility of high-pressure adsorption measurements in shale was recently presented by Gasparik et al. in an inter-laboratory comparison [23]. Shale samples were distributed among research groups to measure adsorption isotherms of methane, ethane and carbon dioxide at high pressures. Results show significant deviations among the reported adsorption isotherms by the involved groups. Thus, establishing guidelines for standardized procedures is necessary to obtain reproducibility of results at high-pressure in shale. Furthermore, experimental data for binary systems and mixtures are scarce and just limited to few hydrocarbon gases and CO₂. However, molecular simulations can be utilized to mimic controlled experimental setups that can help us improve the knowledge of the adsorption processes occurring inside shale organic matter [24, 25].

Capillary pressure and adsorption effects occur simultaneously in confined spaces. Capillary condensation and pore filling are some examples of the combined effect of capillary forces and adsorption. For instance, for a pure component at sub-critical temperatures, its adsorption isotherm inside a capillary tube will describe the thickening of the adsorbed phase next to the wall as a function of the pressure. As the wall thickens, capillary forces will be enhanced due to the reduction of the effective capillary radius. The combined effect will result in a capillary condensation at a lower dew point pressure than that of bulk. Moreover, for a heterogeneous porous media, the subcritical adsorption isotherm will describe both thickening of the adsorbed phase onto the wall and the pore filling process. Due to the heterogeneous nature of the system, the condensation will start at the smallest micro-pores. As the pressure increases, phase transition will occur in an increasing order from small

to large pores, describing a pore filling process. For multicomponent mixtures, the picture is more complex. Selective adsorption of components can modify the composition of the bulk phase (middle of the pore), and therefore, the properties that determine the capillary forces also change. To describe such processes, advanced models and tools are required. The Multicomponent Potential Theory of Adsorption (MPTA) is an example that can handle both, adsorption and phase changes of multicomponent mixtures inside porous materials. It was developed by Shapiro and Stenby [26] as an extension of the potential concept originally suggested by Polanyi [27]. Moreover, Li et al. [28] applied the Density Functional Theory (DFT) to describe phase behavior of confined multicomponent mixtures. Similar to MPTA, it is able to handle adsorption and phase behavior simultaneously. Both MPTA and DFT are predictive tools that can give an insight of the phase behavior in confined spaces. However, they still remain as computationally expensive models in the context of reservoir simulation. Therefore, relatively simple models that can capture the essential effects of adsorption in phase behavior are required. Incorporation of wall effects into EoS based models has been presented by Travalloni et al. [29, 30] showing promising results. Dong et al. [31] presented a framework for phase equilibrium calculations considering the adsorption film. An enhancement in the capillary pressure is observed due to a reduction of the effective capillary radius, however, no compositional changes due to selective adsorption were considered. In general, describing simultaneously capillary and adsorption effects is not trivial. Furthermore, development of tools that capture such effects is fundamental to understand and improve current technologies in shale production.

The scope of this research is the study of phase equilibrium inside shale reservoirs. Throughout the research process several algorithms were developed. They served as a tool to study the effect of capillary pressure and adsorption on phase behavior for various fluids of interest. Several findings were obtained and are presented in this thesis. A brief description of the main content for each chapter is given below.

Chapter 2: An efficient algorithm for phase envelope calculations involving capillary pressure is presented. It served to study the effect on the phase envelope of various fluids inside a capillary tube using different capillary radii. Moreover, a mathematical analysis based on the linearization close to the phase boundary is provided. Useful linear relationships that can show the direction of the changes in the phase envelope were obtained. Additionally, a flash algorithm that accounts for capillary effects on phase behavior was developed. It uses a stability analysis procedure

based on a modified tangent plane distance condition involving capillary pressure.

- Chapter 3: A comparison of different models for high-pressure adsorption data in shale found in recent literature and molecular simulations is presented. Three different models were tested for the fitting of pure component isotherms: the Langmuir, Toth-Langmuir, and MPTA using the Dubinin-Radushkevich-Astakhov (DRA) potential. For multicomponent mixtures, three methods are compared: the Multicomponent Langmuir (ML), Ideal Adsorbed Solution Theory and MPTA-DRA.
- Chapter 4: Capillary pressure and adsorption effects are studied simultaneously. In order to study various fluids, MPTA is used as a tool to generate adsorption data of various hydrocarbons of which experimental data is currently not available. An analysis on the effect of the thickness of the adsorption film on the phase envelope of a mixture is given. It is based on the phase envelope construction considering capillary pressure inside a tube with a variable capillary radius modified by the adsorption film thickness. Additionally, a new algorithm for flash calculations inside shale reservoirs, involving both capillary pressure and selective adsorption is proposed. The algorithm is used to analyze how the phase equilibrium changes at different regions of the phase envelope.
- Chapter 5: The implementation of a flash algorithm accounting for the capillary pressure effect on phase behavior into a compositional reservoir simulator is described. It allowed us to test a natural depletion case of a tight reservoir at various conditions with different capillary pressure models. The case of study consists of a two-dimensional reservoir with ten planar fractures using local grid refinement to capture the fracture-matrix flow exchange. Capillary pressure models using fixed and variable pore sizes were used to study the effect in the production.

CHAPTER 2

Phase Equilibrium Involving Capillary Pressure

Phase equilibrium in confined spaces is present in many natural systems and industrial applications. One important example is phase equilibrium in shale reservoirs, which has recently received a lot of attention due to the shale gas boom. Oil and gas production from shale reportedly show different trends from conventional reservoirs. It is speculated by many that the shift of the phase equilibrium in the nanoscale pores of shale is one of the major reasons for the abnormal field observations. However, there is no consensus on how phase equilibrium changes in the small pores. It is worthwhile to investigate phase equilibrium in confined spaces more carefully in order to better estimate the initial reserves in shale and better forecast its production.

Three important effects in confined space are the high capillary pressure between the oil and the gas phases, selective component adsorption, and molecular confinement effects. The present chapter focuses on the effect of the capillary pressure inside pore radii sizes above 5 nm and the other two effects are neglected here. The effect of capillary pressure on the phase equilibrium has been investigated theoretically and experimentally by numerous authors. Fisher and Israelachvili [9] confirmed the validity of the Kelvin equation down to a few nanometers ($\approx 4\text{nm}$ or eight times the molecular diameter) for pure cyclohexane by measuring liquid bridges between crossed mica cylinders. However, they found it difficult to validate the Kelvin equation when the pressure of the cyclohexane was controlled by adding *n*-dodecane as

a nonvolatile solute. This difference may be attributed to the accumulation of *n*-dodecane in the interface and binary interactions with the cyclohexane in the liquid phase. These problems were addressed by Shapiro and Stenby [13, 14, 21] in the formulation of the multicomponent Kelvin equation and its corresponding thermodynamic analysis of multicomponent mixtures under a capillary pressure difference. In relation to Fisher and Israelachvili's work, Christenson [11] demonstrated the validity of the Laplace equation between water and oil to radii of two nanometers suggesting the validity of continuously curved interfaces at nanometer scale for liquid-liquid systems.

Calculations of saturation pressure and phase envelope for multicomponent mixtures under a capillary pressure difference have been presented by several authors. Shapiro and Stenby[21] provided a first-order approximation of the exact solution for the capillary condensation using the Kelvin equation for multicomponent mixtures. They also presented algorithms to solve the flash problem by means of direct substitution utilizing the Rachford-Rice equation and modified equilibrium factors. Nojabaei et al.[32] and Pang et al.[33] calculated the phase envelope in the presence of capillary pressure by solving the fugacity equations coupled with the capillary pressure equation. Both studies show that the phase envelope changes everywhere except at the critical point and at the cricondentherm. They also showed that the change in the saturation pressure is negligible unless the pore radius is in the order of tens of nanometers.

From a computation viewpoint, both phase envelope and flash calculations involving capillary pressure are of great importance for several processes inside tight porous materials. In this chapter, an algorithm for the phase envelope and isothermal flash involving capillary pressure is presented. The phase envelope section shows a study of the effect of capillary pressure on the phase envelope at different compositions, capillary radii, and vapor fractions. Furthermore, a mathematical analysis that leads to the approximate equations for the shift in saturation conditions is provided. The equations indicate exactly the same directions of the changes as those from the phase envelope algorithm and explain theoretically why the change happens in various directions. The flash section provides a framework for isothermal flash calculations at a specified gas or liquid pressure. It also uses a stability analysis procedure based on a modified tangent plane distance condition involving capillary pressure [15]. Comparative plots of liquid and gas pressure specification flash procedures are presented.

2.1. The Phase Envelope in the Presence of Capillary Pressure

The phase envelope calculation algorithm described by Michelsen [34] was employed as the basis for the extension to the calculation with capillary pressure. Michelsen's algorithm traces and constructs the whole phase boundary instead of calculating individual saturation points. The calculation is initialized at low pressures, using Wilson approximation for the equilibrium factors as initial estimates. The convergence can easily be reached with successive substitution followed by Newton's method. After the first point is converged, the subsequent points on the phase envelope are traced sequentially using initial estimates based on polynomial extrapolation of the previous converged points. The algorithm works for any vapor fraction between 0 and 1, with 0 and 1 corresponding to the special cases of bubble point and dew point respectively.

Several modifications are needed to calculate the phase envelope with capillary pressure. An obvious modification is to include the capillary pressure equation in the system of equations consisting of equality of fugacity and mass balance. This results in a computational problem since one of the phase pressures can become negative. Hence, P instead of $\ln P$ is used as the independent variable. The fugacity coefficients at negative pressure are also negative. As a result, it is recommended to use the product of the pressure and its corresponding fugacity coefficient (F_i^α) to avoid indefinite values of the its logarithmic values. It is worthwhile mentioning that this requires some modifications in the traditional fugacity coefficient based routines in order to get the desired values and derivatives.

2.1.1. The System of Equations

The system consists of $N_c + 3$ equations, where N_c is the number of components in the mixture. It has the following form:

$$\left\{ \begin{array}{l} \ln K_i + \ln F_i^g(T, P_g, \mathbf{y}) - \ln F_i^l(T, P_l, \mathbf{x}) = 0; \quad i = 1, \dots, N_c \\ \sum_{i=1}^{N_c} (y_i - x_i) = 0 \\ P_l - P_g + P_c(T, P_g, P_l, \mathbf{x}, \mathbf{y}) = 0 \end{array} \right. \quad (2.1)$$

where:

$$K_i = \frac{y_i}{x_i}, \quad F_i^\alpha = P^\alpha \varphi_i^\alpha$$

The set of $N_c + 3$ unknown variables are $X = \{\ln K_1, \dots, \ln K_{N_c}, \ln T, P_l, P_g\}$, where K_i is the equilibrium constant for component i ; T is the temperature; P_l is the pressure in the liquid phase; P_g is the pressure in the gas phase; and P_c is the capillary pressure.

The mole fractions x_i, y_i are expressed as a function of the equilibrium constant K_i and feed compositions z_i :

$$x_i = \frac{z_i}{1 - \beta + \beta K_i}, \quad y_i = \frac{K_i z_i}{1 - \beta + \beta K_i} \quad (2.2)$$

To complete the set of equations an equation where the desired variable X_s can be specified (i.e. $\ln K_i, \ln T, P_g, P_l$) is introduced.

$$X_s - S = 0 \quad (2.3)$$

where s is the index for the variable to be specified, and S is the desired value of this variable. The system is now completed and has the form of:

$$\mathbf{f}(\mathbf{X}) = \begin{cases} \ln K_i + \ln F_i^g(T, P_g, \mathbf{y}) - \ln F_i^l(T, P_l, \mathbf{x}), & i = 1, \dots, N_c \\ \sum_{i=1}^{N_c} (y_i - x_i) \\ P_l - P_g + P_c(T, P_g, P_l, \mathbf{x}, \mathbf{y}) \\ X_s - S \end{cases} = \mathbf{0} \quad (2.4)$$

The capillary pressure model adopted for the calculations is the Young-Laplace equation:

$$P_c = P_g - P_l = \sigma \left(\frac{1}{R_1} + \frac{1}{R_2} \right) \quad (2.5)$$

where R_1 and R_2 are the main curvature radii of the curved interface, and σ is the interfacial tension (IFT). Moreover, a capillary tube is chosen to represent the geometry of a single pore, and the liquid is considered the wetting phase. Thus, the equation (Eq. 2.5) can be simplified to

$$P_c = P_g - P_l = \frac{2\sigma \cos \theta}{r_c} \quad (2.6)$$

where θ is the contact angle between the wetting phase and the wall of the tube, and r_c is the capillary radius. In all the cases complete wetting is also assumed (i.e. $\theta = 0$). From a computational point of view, in (Eq. 2.6) the most important variable is σ since it is a function of all the variables in the system (i.e. $T, P_l, P_g, \mathbf{x}, \mathbf{y}$).

There exist several models to compute the IFT for mixtures, and the one considered in this chapter is an extension of the McLeod and Sugden equation:

$$\sigma^{1/E} = \chi(\rho^l - \rho^g) \quad (2.7)$$

where E is the critical scaling exponent, χ is the parachor for each component and ρ^l and ρ^g are the densities of each phase. The modified equation for multicomponent mixtures was presented by Weingaug and Katz[35]:

$$\sigma^{1/E} = \sum_{i=1}^{Nc} \chi_i (x_i \rho^l - y_i \rho^g) \quad (2.8)$$

Several models that differ in the choice of scaling exponents and parachor values can be found in the literature [35–39]. In this chapter, a critical scaling exponent of $E = 4$ is unless it is specified otherwise. The parachor values were taken from Schechter and Guo (Table 2 of Ref. [39]).

2.1.2. Solution Approach

The initialization of the phase envelope is made at low gas pressures without taking into account a capillary pressure difference (i.e. $P_l = P_g$) using the algorithm proposed by Michelsen [34]. After the first point is converged, the pressure in the liquid is updated using the capillary pressure of the system evaluated by (Eq. 2.6). At this stage it is possible to switch to the complete system in (Eq. 2.4) and start tracing the phase envelope in a sequential way. For each individual point Newton's method was used:

$$\mathbf{X}_{n+1} = \mathbf{X}_n - \mathbf{J}^{-1} \mathbf{f}(\mathbf{X}) \quad (2.9)$$

where \mathbf{J} is the Jacobian matrix and has the following form:

$$\mathbf{J} = \begin{pmatrix} \frac{\partial f_1}{\partial \ln K_1} & \cdots & \frac{\partial f_1}{\partial P_g} \\ \vdots & \ddots & \vdots \\ \frac{\partial f_{Nc+3}}{\partial \ln K_1} & \cdots & \frac{\partial f_{Nc+3}}{\partial P_g} \end{pmatrix} \quad (2.10)$$

where

$$\frac{\partial f_i}{\partial \ln K_j} = \delta_{ij} + \frac{\beta x_j y_j}{z_j} \frac{\partial \ln F_i^l}{\partial x_j} + (1 - \beta) \frac{x_j y_j}{z_j} \frac{\partial \ln F_i^g}{\partial y_j}, \quad i = 1, \dots, N_c, \quad j = 1, \dots, N_c \quad (2.11)$$

$$\frac{\partial f_i}{\partial \ln T} = T \left(\frac{\partial \ln F_i^g}{\partial T} - \frac{\partial \ln F_i^l}{\partial T} \right), \quad i = 1, \dots, N_c \quad (2.12)$$

$$\frac{\partial f_i}{\partial P_l} = -\frac{\partial \ln F_i^l}{\partial P_l}, \quad i = 1, \dots, N_c \quad (2.13)$$

$$\frac{\partial f_i}{\partial P_g} = \frac{\partial \ln F_i^g}{\partial P_g}, \quad i = 1, \dots, N_c \quad (2.14)$$

$$\frac{\partial f_{N_c+1}}{\partial \ln K_j} = \frac{x_j y_j}{z_j}, \quad j = 1, \dots, N_c \quad (2.15)$$

$$\frac{\partial f_{N_c+1}}{\partial \ln T} = 0; \quad \frac{\partial f_{N_c+1}}{\partial \ln P_l} = 0; \quad \frac{\partial f_{N_c+1}}{\partial \ln P_g} = 0 \quad (2.16)$$

$$\frac{\partial f_{N_c+2}}{\partial \ln K_j} = -\beta \frac{x_j y_j}{z_j} \frac{\partial P_c}{\partial x_j} + (1 - \beta) \frac{x_j y_j}{z_j} \frac{\partial P_c}{\partial y_j}, \quad j = 1, \dots, N_c \quad (2.17)$$

$$\frac{\partial f_{N_c+2}}{\partial \ln T} = T \frac{\partial P_c}{\partial T} \quad (2.18)$$

$$\frac{\partial f_{N_c+2}}{\partial P_l} = 1 + \frac{\partial P_c}{\partial P_l} \quad (2.19)$$

$$\frac{\partial f_{N_c+1}}{\partial P_g} = -1 + \frac{\partial P_c}{\partial P_g} \quad (2.20)$$

$$\frac{\partial f_{N_c+3}}{\partial X_k} = \delta_{ks}, \quad k = 1, \dots, N_c + 3 \quad (2.21)$$

And the necessary P_c derivatives are:

$$\frac{\partial P_c}{\partial T} = \frac{2 \cos \theta}{r_c} E \sigma^{\frac{E-1}{E}} \sum_{i=1}^{N_c} \chi_i \left[-\frac{x_i}{V_l^2} \frac{\partial V_l}{\partial T} + \frac{y_i}{V_g^2} \frac{\partial V_g}{\partial T} \right] \quad (2.22)$$

$$\frac{\partial P_c}{\partial P_l} = -\frac{2 \cos \theta}{r_c} E \sigma^{\frac{E-1}{E}} \sum_{i=1}^{N_c} \chi_i \left[\frac{x_i}{V_l^2} \frac{\partial V_l}{\partial P_l} \right] \quad (2.23)$$

$$\frac{\partial P_c}{\partial P_g} = \frac{2 \cos \theta}{r_c} E \sigma^{\frac{E-1}{E}} \sum_{i=1}^{N_c} \chi_i \left[\frac{y_i}{V_g^2} \frac{\partial V_g}{\partial P_g} \right] \quad (2.24)$$

$$\frac{\partial P_c}{\partial x_j} = -\frac{2 \cos \theta}{r_c} E \sigma^{\frac{E-1}{E}} \left[\frac{\chi_j}{V_l} + \frac{V_l - V_{lj}}{V_l^2} \sum_i^{N_c} \chi_i x_i \right] \quad (2.25)$$

$$\frac{\partial P_c}{\partial y_j} = \frac{2 \cos \theta}{r_c} E \sigma^{\frac{E-1}{E}} \left[\frac{\chi_j}{V_g} + \frac{V_g - V_{gj}}{V_g^2} \sum_i^{N_c} \chi_i y_i \right] \quad (2.26)$$

After obtaining the first point of the phase envelope, sensitivity analysis is recommended to select the right variable (S) in (Eq. 2.4) for the subsequent steps. To get the rate of change of the independent variables with respect to one specified, it is necessary to differentiate (Eq. 2.4) with respect to S and solve the corresponding system:

$$\frac{\partial \mathbf{f}}{\partial \mathbf{X}} \frac{\partial \mathbf{X}}{\partial S} + \frac{\partial \mathbf{f}}{\partial S} = 0 \quad (2.27)$$

From the expression above $\frac{\partial \mathbf{f}}{\partial \mathbf{X}}$ is the Jacobian (\mathbf{J}) and the vector $\frac{\partial \mathbf{f}}{\partial S}$ is simply $(0, 0, \dots, 0, -1)^T$ assuming that we start with S as the $N_c + 3$ indexed variable, which for this case is the pressure of the gas phase P_g .

After solving (Eq. 2.27) the vector $\frac{\partial \mathbf{X}}{\partial S}$ with the sensitivities is obtained. The variable that changes the fastest must be chosen as the specified variable X_s to solve the system in the next step. In the present formulation, the pressures in both phases (P_g, P_l) are the only variables that are not in a logarithmic scale. Therefore, for a proper comparison of the sensitivities, the derivatives must be converted to an

approximated logarithmic sensitivity:

$$\frac{\partial \ln P}{\partial S} = \frac{\partial \ln P}{\partial P} \frac{\partial P}{\partial S} = \frac{1}{|P|} \frac{\partial P}{\partial S} \quad (2.28)$$

To avoid singularities at $P = 0$ the scaling is changed to:

$$\frac{\partial \ln P}{\partial S} \approx \left(\frac{1}{1 + |P|} \right) \frac{\partial P}{\partial S} \quad (2.29)$$

This scaled sensitivity is more suitable to make a fair comparison within the rest of variables that are logarithmically scaled. The vector of sensitivities is also helpful in the stepping process of the phase envelope tracing. After obtaining more than one point with its respective sensitivity (local derivatives), linear or higher order polynomial can be used to extrapolate the next points which will be used as initial guesses in the subsequent calculations.

2.1.3. Analysis of the Phase Envelope Shift

Any multicomponent mixture at equilibrium in the presence of a capillary pressure difference will satisfy the system of equations in (Eq. 2.1). Thus, it also applies to all the saturation points. The aim of the analysis presented in this section is to check the direction (and to some extent also the magnitude) of the change in the saturation pressure and temperature along the phase envelope prior to solving the system in (Eq. 2.1). This analysis is somewhat inspired by Shapiro and Stenby's[13] work on the multicomponent Kelvin equation.

Saturation Pressure

Calculations of the decrease of the *bubble point* pressure in a multicomponent mixture due to a capillary pressure difference has been presented by many authors [32, 33, 40]. A detailed mathematical analysis is given here. Let us consider any point in the bubble point curve without any capillary pressure difference. At a fixed temperature, the point will satisfy the following equality:

$$\ln f_i^l(P_b, \mathbf{z}) = \ln f_i^g(P_b, \mathbf{y}_b), \quad (i = 1, \dots, N_c) \quad (2.30)$$

where P_b is the normal bubble point pressure, \mathbf{z} is the molar feed composition and \mathbf{y}_b is the molar composition in the incipient gas phase. If we place the same mixture inside a pore with an infinitesimal capillary pressure difference ($\delta P_c = P_g - P_l$), the bubble point pressure will change accordingly ($\epsilon_p = P_l - P_b$), as well as the molar composition in the gas phase ($\epsilon_y = \mathbf{y} - \mathbf{y}_b$). Thus the new equilibrium point satisfying the capillary pressure difference (δP_c) is:

$$\ln f_i^l(P_l, \mathbf{z}) = \ln f_i^g(P_g, \mathbf{y}) \quad (2.31)$$

where P_l and P_g can be again written as a function of the normal bubble point pressure (P_b) and composition (\mathbf{y}_b):

$$\ln f_i^l(P_b + \epsilon_p, \mathbf{z}) = \ln f_i^g(P_b + [\epsilon_p + \delta P_c], \mathbf{y}_b + \epsilon_y) \quad (2.32)$$

Approximating each term with a linear expansion we get:

$$\begin{aligned} \ln f_i^l(P_b + \epsilon_p, \mathbf{z}) &\approx \ln f_i^l(P_b, \mathbf{z}) + \frac{\partial \ln f_i^l(P_b, \mathbf{z})}{\partial P} \epsilon_p \\ &\approx \ln f_i^l(P_b, \mathbf{z}) + \frac{\bar{V}_i^l}{RT} \epsilon_p \end{aligned} \quad (2.33)$$

$$\begin{aligned} \ln f_i^g(P_b + [\epsilon_p + \delta P_c], \mathbf{y}_b + \epsilon_y) &\approx \ln f_i^g(P_b, \mathbf{y}_b) + \frac{\partial \ln f_i^g(P_b, \mathbf{y}_b)}{\partial P} (\epsilon_p + \delta P_c) \\ &\quad + \sum_{j=1}^{N_c} \frac{\partial \ln f_i^g(P_b, \mathbf{y}_b)}{\partial y_j} \epsilon_{y_j} \\ &\approx \ln f_i^g(P_b, \mathbf{y}_b) + \frac{\bar{V}_i^g}{RT} (\epsilon_p + \delta P_c) + \sum_{j=1}^{N_c} \frac{\partial \ln f_i^g(P_b, \mathbf{y}_b)}{\partial y_j} \epsilon_{y_j} \end{aligned} \quad (2.34)$$

Replacing (Eq. 2.33-2.34) in (Eq. 2.32) and using (Eq. 2.30) we obtain:

$$\frac{\bar{V}_i^l}{RT} \epsilon_p \approx \frac{\bar{V}_i^g}{RT} (\epsilon_p + \delta P_c) + \sum_{j=1}^{N_c} \frac{\partial \ln f_i^g(P_b, \mathbf{y}_b)}{\partial y_j} \epsilon_{y_j} \quad (2.35)$$

Multiplying (Eq. 2.35) by the individual molar fraction (y_{b_i}) and summing over all the components i from 1 to N_c we get:

$$\epsilon_p \sum_{i=1}^{N_c} y_{b_i} \bar{V}_i^l \approx V^g (\epsilon_p + \delta P_c) + RT \sum_{i=1}^{N_c} \sum_{j=1}^{N_c} y_{b_i} \frac{\partial \ln f_i^g(P_b, \mathbf{y}_b)}{\partial y_j} \epsilon_{y_j} \quad (2.36)$$

At constant pressure (P) and temperature (T) we can substitute the last term of the right hand side with:

$$RT \sum_{i=1}^{N_c} \sum_{j=1}^{N_c} y_{b_i} \frac{\partial \ln f_i^g(P_b, \mathbf{y}_b)}{\partial y_j} \epsilon_{y_j} = \sum_{j=1}^{N_c} \sum_{i=1}^{N_c} y_{b_i} \frac{\partial \mu_i^g(P_b, \mathbf{y}_b)}{\partial y_j} \epsilon_{y_j} \quad (2.37)$$

This term vanishes due to the Gibbs-Duhem equation:

$$\sum_i^{N_c} y_i d\mu_i = 0 \quad (2.38)$$

Hence our approximation takes the form of:

$$\epsilon_p \sum_{i=1}^{N_c} y_{b_i} \bar{V}_i^l \approx V^g (\epsilon_p + \delta P_c) \quad (2.39)$$

Replacing the left hand side by the so-called mixed volume [13] :

$$\sum_{i=1}^{N_c} y_{b_i} \bar{V}_i^l = V^{lg} \quad (2.40)$$

Consequently, we arrive at our final expression:

$$\epsilon_p \approx \delta P_c \left[\frac{V^g}{V^{lg} - V^g} \right] \quad (2.41)$$

Considering our definition of capillary pressure ($P_c = P_g - P_l$) and assuming that our system is a liquid wet capillary tube, the capillary pressure is positive ($\delta P_c > 0$). Hence the direction of the change in the bubble point is indicated by the sign of the dimensionless term $\left[\frac{V^g}{V^{lg} - V^g} \right]$. A positive value of this term suggests an increase in the bubble point pressure while a negative value suggests a decrease of it.

The *dew point* analysis can be treated similarly to the bubble point analysis. At a dew point without capillary pressure, the condition of equilibrium is as follows:

$$\ln f_i^l(P_d, \mathbf{x}_d) = \ln f_i^g(P_d, \mathbf{z}) \quad (2.42)$$

Again an infinitesimal capillary pressure difference is considered ($\delta P = P_g - P_l$), and the equilibrium condition becomes:

$$\ln f_i^l(P_d + [\epsilon_p - \delta P_c], \mathbf{x}_d + \boldsymbol{\epsilon}_x) = \ln f_i^g(P_d + \epsilon_p, \mathbf{z}) \quad (2.43)$$

Each term is linearly expanded, and following the same procedure as in the bubble point region one arrives at:

$$\epsilon_p \approx \delta P_c \left[\frac{V^l}{V^l - \sum_{i=1}^{N_c} x_{d_i} \bar{V}_i^g} \right] = \delta P_c \left[\frac{V^l}{V^l - V^{gl}} \right] \quad (2.44)$$

An equivalent form of this equation was presented by Shapiro and Stenby [14]¹. Similar to the bubble point criterion, the direction of the change in the dew point is indicated by the sign of the term $\left[\frac{V^l}{V^l - V^{gl}} \right]$. The above analysis can be generalized to any type of saturation point. The analysis would be done using feed phase and incipient phase instead. The general criterion would be:

$$\epsilon_p \approx -(P^{incp} - P^{feed}) \left[\frac{V^{incp}}{\sum_{i=1}^{N_c} w_i (\bar{V}_i^{incp} - \bar{V}_i^{feed})} \right] \quad (2.45)$$

where (*incp*) refers to the incipient phase, and w_i is the molar composition of component i in the incipient phase.

Saturation Temperature

A similar analysis can be performed for the saturation temperature change. This analysis is particularly useful to explain the shift of the cricondentherm. Instead of fixing the temperature, the pressure in the feed phase is held constant. This means that the pressure of the gas phase remains the same as the dew point pressure ($P_d = P_g$), the pressure in the liquid phase is calculated by the capillary pressure difference ($P_l = P_g - \delta P_c$), and the dew point temperature changes due to the capillary pressure disturbance in the system ($T = T_d + \epsilon_t$). The new saturation point of the mixture will satisfy the following equation.

$$\ln f_i^l(P_d - \delta P_c, T + \epsilon_t, \mathbf{x}_d + \boldsymbol{\epsilon}_x) = \ln f_i^g(P_d, T + \epsilon_t, \mathbf{z}) \quad (2.46)$$

¹Refer to Eq. 11 in the cited article. $P_c = P_d \left(\frac{V_{gl}}{V^l} - 1 \right) P_d (\chi - 1)$ with $\chi = P_g / P_d$

Following the same procedure as for the saturation pressure, by expanding linearly each term and summing over the liquid individual compositions x_{d_i} , one arrives at:

$$\epsilon_t = \frac{V^l \delta P_c}{RT \sum_{i=1}^{N_c} x_{d_i} \left(\frac{\partial \ln f_i^l(Pd, T, \mathbf{x}_d)}{\partial T} - \frac{\partial \ln f_i^g(Pd, T, \mathbf{z})}{\partial T} \right)} = - \frac{V^l \delta P_c}{\sum_{i=1}^{N_c} x_{d_i} (\bar{S}_i^l - \bar{S}_i^g)} \quad (2.47)$$

where \bar{S}_i is the partial molar entropy. Using an analogous term for the partial molar entropies as in the mixed volume. We arrive at to the final expression of:

$$\epsilon_t = \left[\frac{V^l}{S^{gl} - S^l} \right] \delta P_c \quad (2.48)$$

Once more, the sign of the term $\left[\frac{V^l}{S^{gl} - S^l} \right]$ determines the direction of the temperature shift. A similar analysis can be done in the bubble point. Moreover, this analysis can also be generalized for any saturation temperature as it was done for the saturation pressure in (Eq. 2.45). The general criterion would be:

$$\epsilon_t \approx (P^{incip} - P^{feed}) \left[\frac{V^{incip}}{\sum_{i=1}^{N_c} w_i (\bar{S}_i^{incip} - \bar{S}_i^{feed})} \right] \quad (2.49)$$

where w_i is the molar composition of component i in the incipient phase.

Relationship with the Multicomponent Clapeyron Equation

It is worth noting that the multicomponent Clapeyron equation [41, 42] can be used to interpret the phase envelope shift due to capillary pressure at cricondentherm and cricondenbar. The multicomponent Clapeyron equation is less known in comparison to the pure component Clapeyron equation. However, it also depicts how the saturation pressure changes with the temperature, but in this case, for a multicomponent system along the phase boundary. Michelsen [41] presented the multicomponent Clapeyron equation in the following form:

$$\frac{dP}{dT} = - \frac{\sum_{i=1}^{N_c} w_i \left(\frac{\partial \ln \varphi_i(\mathbf{w})}{\partial T} - \frac{\partial \ln \varphi_i(\mathbf{z})}{\partial T} \right)}{\sum_{i=1}^{N_c} w_i \left(\frac{\partial \ln \varphi_i(\mathbf{w})}{\partial P} - \frac{\partial \ln \varphi_i(\mathbf{z})}{\partial P} \right)} = \frac{\Delta S}{\Delta V} \quad (2.50)$$

where the superscript (*incip*) refers to the incipient phase, and \mathbf{w} is its molar composition. The form of the above equation is similar to the pure component Clapeyron equation but the entropy change and the volume change have a slightly different meaning here. The two terms are given by:

$$\Delta S = \sum_{i=1}^{N_c} w_i (\bar{S}_i^{incip} - \bar{S}_i^{feed}); \quad \Delta V = \sum_{i=1}^{N_c} w_i (\bar{V}_i^{incip} - \bar{V}_i^{feed}) \quad (2.51)$$

ΔV and ΔS are the changes in the system volume and the system entropy, respectively, when an infinitesimal amount of feed phase is moved to the new incipient phase. From (Eq. 2.45) and (Eq. 2.49) it is possible to notice that the direction of the change in the saturation pressure is related to ΔV and the direction of the change in the saturation temperature is related to ΔS . At the cricondentherm, from the multicomponent Clapeyron equation, we obtain:

$$\frac{dT}{dP} = 0 \Rightarrow \sum_{i=1}^{N_c} w_i (\bar{V}_i^{incip} - \bar{V}_i^{feed}) = 0 \quad (2.52)$$

which suggests a change of sign in the volume difference of the system. Therefore, it implies a change of sign in (Eq. 2.44) which leads to a change in the direction of the saturation pressure shift around the cricondentherm. The same analysis can be done for change in the saturation temperature around the cricondenbar. At the cricondenbar, from the multicomponent Clapeyron equation we obtain:

$$\frac{dP}{dT} = 0 \Rightarrow \sum_{i=1}^{N_c} w_i (\bar{S}_i^{incip} - \bar{S}_i^{feed}) = 0 \quad (2.53)$$

which suggests a change of sign in the entropy difference of the system. Therefore, it implies a change of sign in (Eq. 2.48) which also leads to a change in the direction of the saturation temperature shift around the cricondenbar. These changes can be confirmed numerically.

2.1.4. Results and Discussion

The Soave-Redlich-Kwong Equation of State (SRK EoS) has been used in all the calculations but the calculation can be coupled with any EoS [43]. The proposed algorithm was able to handle all the tested systems at all the specified conditions. The systems tested are: a binary C₁-C₄ system at different concentrations; a 7-component natural gas system; and a set of reservoir fluids with different Gas Oil

Ratios (GOR). The algorithm, as well as being robust, is fast and quadratically convergent. Figure 2.1 shows an example of the convergence of a point using Newton's method. Typically, between 2 and 3 iterations are expected per point, and between 20 and 30 points to trace the entire phase envelope.

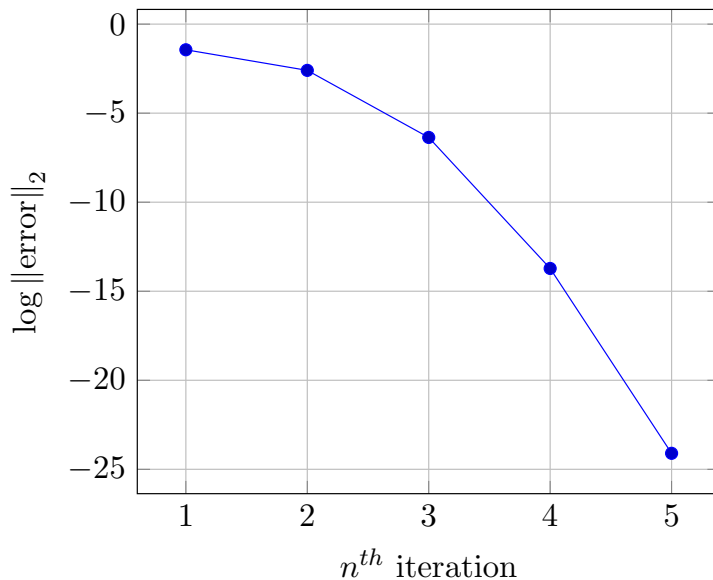


FIGURE 2.1.: Convergence behavior for the first point in the construction of the phase envelope of System I, described in table 2.1

Before a more detailed analysis, it is helpful to highlight some general features of the change of the phase envelopes encountered in every system. The specific example of System (I) described in Table 2.1 is used to illustrate these differences. Figure 2.2 shows the phase envelope, and Table 2.2 shows the numerical values of each highlighted point in the corresponding figure.

TABLE 2.1.: System I. Natural gas mixture, description of basic model parameters including non zero binary interaction parameters (k_{ij})

Component	mol %	parachor (χ)	P_c (bar)	T_c (K)	ω	k_{N_2j}	k_{CH_4j}
N ₂	1.40	61.12	126.20	34.00	0.0377	0	0.0278
CH ₄	94.30	74.05	190.56	45.99	0.0115	0.0278	0
C ₂ H ₆	2.70	112.91	305.32	48.72	0.0995	0.4070	-0.0078
C ₃ H ₈	0.74	154.03	369.83	42.48	0.1523	0.0763	0.0090
nC ₄	0.49	193.90	425.12	37.96	0.2002	0.0700	0.0056
nC ₅	0.27	236.00	469.70	33.70	0.2515	0.0787	0.0190
nC ₆	0.10	276.71	507.60	30.25	0.3013	0.1496	0.0374

In the bubble point branch of the phase envelope, the saturation pressure is suppressed until the critical point is reached. The suppression increases with the distance from the critical point. For this part of the phase envelope, the reference

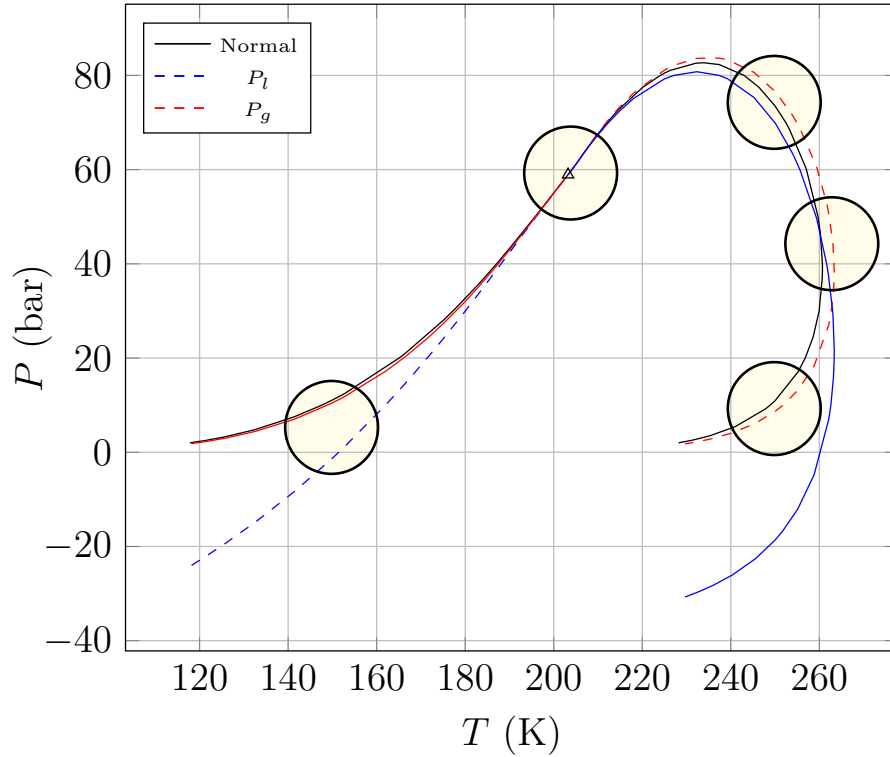


FIGURE 2.2.: Phase Envelope in the presence of capillary pressure of System (I) using a capillary radius of 10 nm. Highlighted circles show the main differences and similarities with respect the normal phase envelope.

TABLE 2.2.: Values corresponding to highlighted points in Figure 2.2.

Observation	T (K)	P (bar)	P_l (bar)	P_g (bar)	ΔP_{sat}	ΔP_c	$\sigma \left(\frac{mN}{m} \right)$
BP ^a	150.00	11.09	-1.26	10.48	-12.35	11.74	5.87
CP ^b	203.24	58.94	58.94	58.94	0.00	0.00	0.00
DP ^c upper	250.00	73.52	69.92	76.59	3.07	6.67	3.34
CT ^d normal	260.71	38.94	-	-	-	-	-
CT ^d with ΔP_c	263.37	-	21.61	38.94	-	17.33	8.67
DP ^c lower	250.00	10.94	-18.64	8.66	-2.28	27.3	13.65

^a Bubble Point; ^b Critical Point; ^c Dew Point; ^d Cricondentherm.

pressure is the liquid pressure (P_l) since the liquid phase is the feed phase; Graphically, the difference in the saturation pressure is the distance between the black line and the blue dashed line in Figure 2.2. The decreasing behavior can be compared with (Eq. 2.41). If we compute $\left[\frac{V^g}{V^{lg}-V^g} \right]$ for the saturation points belonging to the bubble point curve we can notice that all the values are negative (see Table 2.3), which confirms numerically the correctness of the analysis done in the previous section for the bubble point.

The critical point does not show any change because the properties of both phases

TABLE 2.3.: Direction of change of the saturation pressure in the bubble point region due to a capillary pressure difference in the system.

T (K)	P (bar)	$\left[\frac{V^g}{V^l_g - V^g} \right]$
120.74	2.41	-1.01
139.03	6.69	-1.02
166.43	21.09	-1.06
186.52	39.50	-1.26
193.05	46.82	-1.53
202.63	58.20	-16.32

are indistinguishable and no apparent interface is formed, corresponding to a zero capillary pressure value.

The dew point branch of the phase envelope shows different behaviors depending on which part of it we refer to. For the dew point branch, the reference pressure is the gas phase pressure (P_g). Graphically, this means that the difference in the saturation pressure is the distance between the black line and the red dashed line in Figure 2.2. Firstly, from the critical point to the cricondentherm (upper dew point) the saturation pressure increases; around the cricondentherm, the phase envelope shows a shift to a higher temperatures; and finally, from the cricondentherm onwards (lower dew point) the saturation pressure decreases. The difference in the dew point seems to decrease gradually while lowering the gas pressure and the difference becomes apparently zero at very low pressures.

Again, this behavior can be compared using (Eq. 2.44). Table 2.4 shows the direction of the pressure change along the dew point region. The sign of these values also confirms an increase of the dew point pressure in the upper branch and a decrease in the lower branch given by (Eq. 2.44). Moreover, at very low pressures this value is close to zero due to big changes in the volume of the incipient phase in comparison with the volume in the feed. It is worthwhile to notice that in Table 2.4 a change from negative infinity to positive infinity occurs at the cricondentherm. For this reason, to have a clear picture of the behavior around the cricondentherm, the saturation temperature must be analyzed instead of the saturation pressure. The direction of the change in the saturation temperature can be obtained from (Eq. 2.48) Table 2.5 shows the direction in the change of the saturation temperature along the dew point curve. The sign of these values confirms numerically the validity of analysis done in the previous section for the temperature shift around the cricondentherm.

The changes of sign in the cricondenthem and cricondenbar for the shift in saturation pressure and saturation temperature shown in Table 2.4 and Table 2.5 respectively, are a direct consequence of the multicomponent Clapeyron equation. From (Eq. 2.52) and (Eq. 2.53) we can notice that a change of sign is guaranteed. As a result, ϵ_p and ϵ_t in (Eq. 2.44) and (Eq. 2.48) respectively, change from positive infinity to negative infinity or vice versa.

TABLE 2.4.: Direction of change of the saturation pressure in the dew point region due to a capillary pressure difference in the system.

T (K)	P (bar)	$\left[\frac{V^l}{V^l - V^{gl}}\right]$
226.51	1.74	-0.01
239.08	4.66	-0.02
247.36	8.76	-0.04
260.55	33.17	-0.26
257.16	60.46	1.98
236.71	82.39	0.39
229.37	82.03	0.35
214.80	72.92	0.32
203.71	59.50	11.95

TABLE 2.5.: Direction of change of the saturation temperature in the dew point region due to a capillary pressure difference in the system.

P (bar)	T (K)	$\left[\frac{V^l}{S^{gl} - S^l}\right]$
1.74	226.51	0.088
8.76	247.36	0.107
18.33	256.26	0.124
33.17	260.55	0.148
58.10	258.56	0.213
60.46	257.16	0.226
82.39	236.71	2.002
82.03	229.37	-1.308
78.52	221.71	-0.494
72.92	214.80	-0.347
67.61	209.75	-0.358
60.40	204.45	-9.403

The above general features remain the same as long as the liquid phase is assumed to be the wetting phase. Moreover, these features are consistent with the results of previous authors with an important difference in the shift of the cricondenthem [32, 33]. This difference was probably caused by a numerical artifact in these previous

studies due to the absence or poor initial estimates. This may have caused difficulties finding solutions in regions that are not present in the normal phase envelope problem. It also shows the necessity of having a robust and efficient algorithm to automatically trace the whole phase envelope in the presence of capillary pressure.

The following subsections present a more detailed discussion regarding the influence of the feed composition composition and capillary radius; the quality lines in the phase envelope; and sensitivity analysis in the scaling factor and parachor values for the interfacial tension model.

Effect of the Feed Composition

In this subsection, several systems with different feed composition and its changes on the phase envelope are evaluated. Figure 2.3 shows the phase envelope of a binary mixture described in Table 2.6. It can be noticed that the bubble point region is affected greatly when increasing the feed of the heavy component. The dew point region is also affected when increasing the light component in the feed. However, in contrast with the bubble point region, the dew point region is less affected.

TABLE 2.6.: Binary system. Description of basic model parameters ($k_{ij} = 0$)

Component	parachor (χ)	P_c (bar)	T_c (K)	ω
CH ₄	74.05	190.56	45.99	0.0115
nC ₄	193.9	425.12	37.96	0.2002

A set of reservoir fluids with different Gas Oil Ratio (GOR) described in Table 2.7 were also tested. These fluids were taken from Whitson and Sunjerga [44]. They represent an example of a real set of confined hydrocarbon mixtures. Figure 2.4 and Figure 2.5 show the phase envelope of these systems and show the same trend as in the binary mixtures. While the heavier mixtures (low GOR) present a bigger change in the bubble point region, the lighter mixtures (high GOR) present it in the dew point region. Also, the change in the bubble point region is more pronounced in comparison to the one in the dew point region.

These behaviors are intimately related to the density difference between the feed phase and the new incipient phase formed. A bigger difference in the density creates a higher interfacial tension which contributes to a higher capillary pressure difference as it can be seen in (Eq. 2.8) and (Eq. 2.6). For the heavier systems, the gas phase formed in bubble point transition is very light in comparison to the liquid phase, consequently the capillary pressure is high. For the dew point transition, the gas

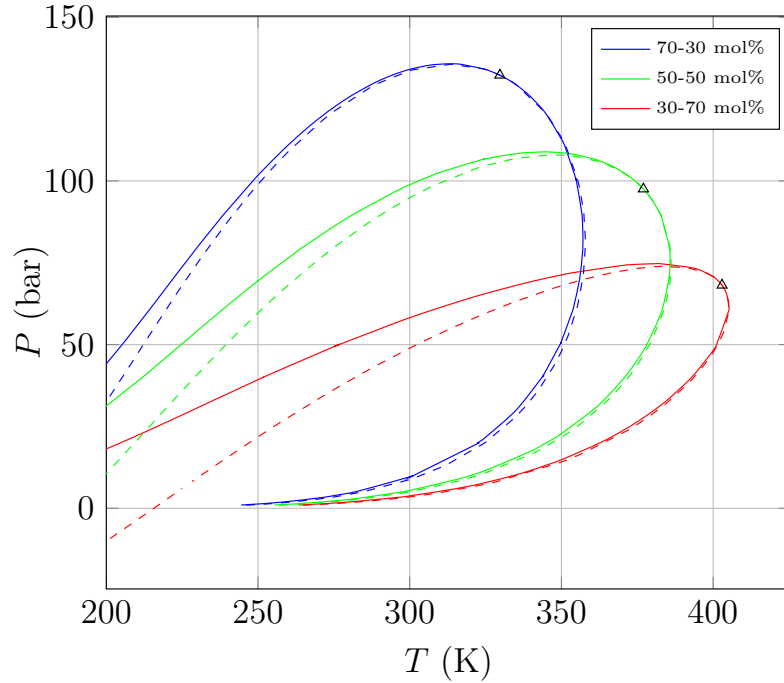


FIGURE 2.3.: Phase envelope of C_1 - C_4 mixtures at different feed compositions. The solid lines (—) represent the normal phase envelopes; Dashed lines (- -) represent the modified phase envelopes due to a capillary pressure difference using $r_c = 10\text{nm}$.

phase contains heavy components and when the liquid phase is formed, the difference in the densities is not that high. The opposite analysis can be done for the lighter systems.

To have an idea of the magnitude of change in the saturation pressure, Figure 2.6 and Figure 2.7 show the changes in the saturation pressure of the different GOR/OGR reservoir fluids at the constant temperature of 400 K, and Table 2.9 shows values of the capillary pressure and interfacial tension of the 500 GOR mixture along the bubble point branch. It can be noticed that at this temperature the bubble point systems are affected the most. The heavier the system, the higher the change in the saturation pressure. However, this only shows one fixed temperature. In order to have a better picture of what can be expected in reservoirs at different temperatures containing different reservoir fluids, it is necessary to compare changes in a range of temperatures rather than in a fixed temperature. Table 2.8 shows the maximum change in the saturation pressure for the different GOR systems in the temperature range of 300 K to 500 K. It can be noticed that the heavy fluids have big negative changes in the bubble point pressure and the lightest have positive changes in the dew point pressure. The fluids that lay in the middle have small changes since at those temperatures the fluids are placed into the critical region.

TABLE 2.7.: Reservoir fluid systems general description. Taken from Whitson and Sunjerga [44]

GOR (scf/STB)	OGR (STB/MMscf)	STO API	C_7^+ MW (mol/g)	C_7^+ (mol%)
33333	30	51.4	123	3.47
20000	50	49.8	132	4.51
10000	75	47.5	145	7.08
6667	150	46.2	153	9.48
4000	250	44.5	164	13.78
2857	350	43.4	171	17.59
2000	500	42.3	178	22.59
1000	1000	40.0	195	34.88
500	2000	37.7	216	49.49

TABLE 2.8.: Maximum saturation pressure change for GOR systems in the temperature range of 300 K to 500 K. From Figure 2.5 and 2.4

GOR (scf/STB)	Bubble point (bar)	Dew point (bar)
33333	-	7.38
20000	-	3.53
13333	-0.04	2.76
10000	-0.06	1.37
6667	-0.34	0.52
4000	-1.06	0.01
2857	-2.24	-
2000	-3.79	-
1000	-7.85	-
500	-11.86	-

TABLE 2.9.: Capillary pressure and interfacial tension values for the bubble point branch of the 500 GOR reservoir fluid.

T (K)	P (bar)	P_g (bar)	P_l (bar)	ΔP_c (bar)	σ (mN/m)
200	24.66	22.96	2.85	20.10	10.05
250	61.96	58.98	46.45	12.52	6.26
300	102.53	99.07	90.68	8.39	4.20
350	135.11	131.50	125.18	6.32	3.16
400	157.33	153.72	148.78	4.94	2.47
450	170.01	166.53	162.76	3.76	1.88
500	174.54	171.33	168.65	2.68	1.34
550	174.54	169.39	167.70	1.69	0.85
600	172.15	161.59	160.71	0.88	0.44
650	163.71	148.19	147.88	0.31	0.16
700	128.93	128.40	128.35	0.04	0.02
752.9	98.02	96.31	96.31	0.00	0.00

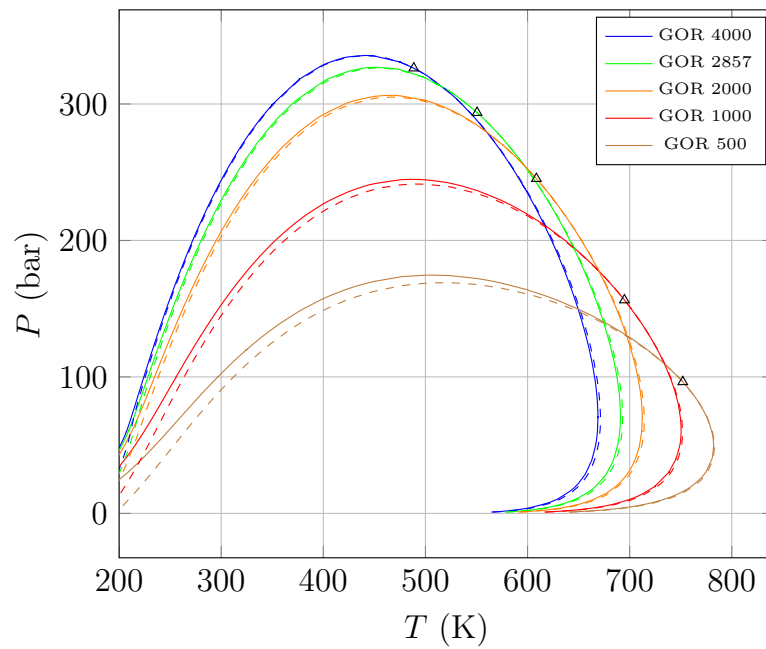


FIGURE 2.4.: Phase envelope of reservoir fluid mixtures described in Table 2.7 with GOR ranging from 500 to 4000 scf/STB. The solid lines (—) represent the normal phase envelopes; Dashed lines (- - -) represent the modified phase envelopes due to a capillary pressure difference using $r_c = 10\text{nm}$.

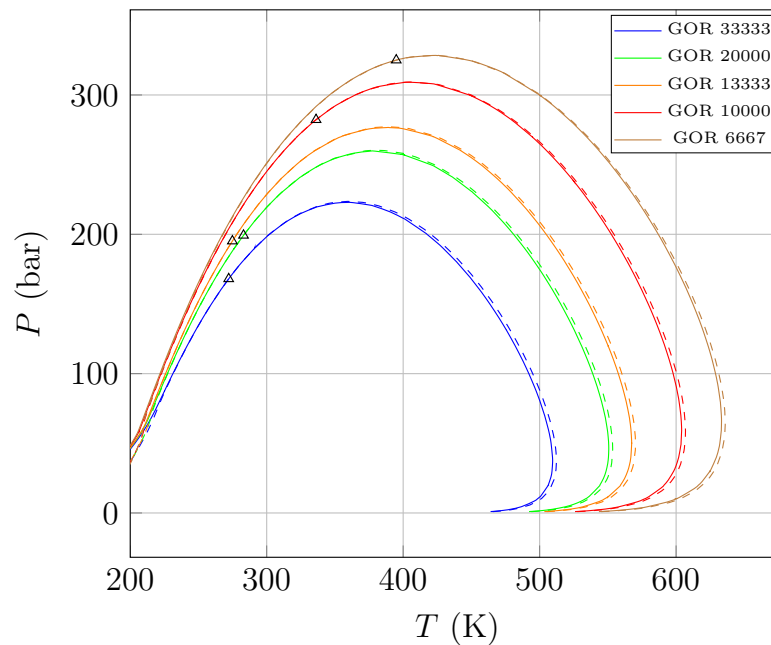


FIGURE 2.5.: Phase envelope of reservoir fluid mixtures described in Table 2.7 with GOR ranging from 6667 to 33333 scf/STB. The solid lines (—) represent the normal phase envelopes; Dashed lines (- - -) represent the modified phase envelopes due to a capillary pressure difference using $r_c = 10\text{nm}$.

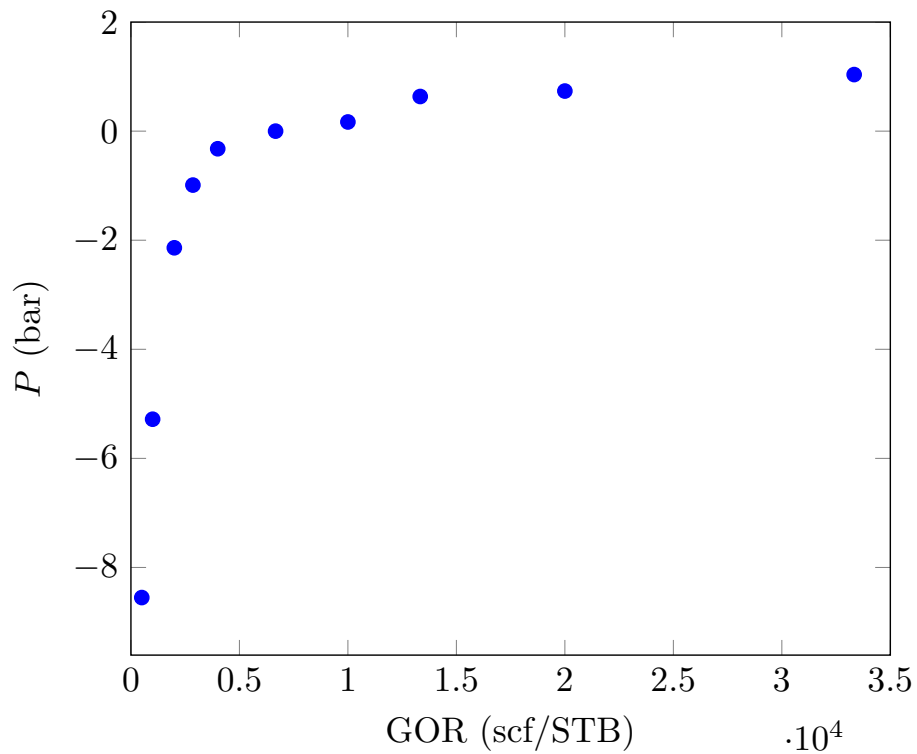


FIGURE 2.6.: Saturation pressure variation respect GOR at (400 K) for mixtures shown in Table 2.7

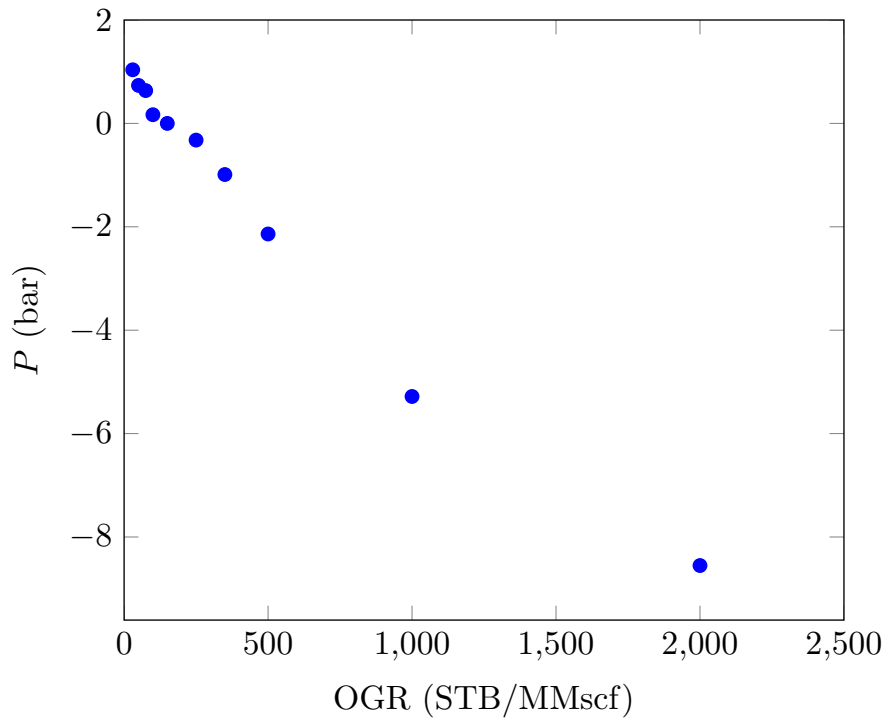


FIGURE 2.7.: Saturation pressure variation respect OGR at (400 K) for mixtures shown in Table 2.7

Capillary Radius

The effect of the capillary radius on the phase envelope is quite intuitive. At smaller capillary radii the change in the saturation pressure will be increased due to a bigger capillary pressure difference. Figure 2.8 shows the changes of the saturation pressure at different capillary radii for a binary system. Additionally, it is possible to show that the change of the saturation pressure is approximately linear to the inverse of the capillary radii, making use of the relationships derived in the mathematical analysis section. If we replace (ΔP_c) with $(2\sigma/r_c)$ in (Eq. 2.41) and (Eq. 2.44) we obtain that the shift in the saturation pressure can be approximated as a function of the capillary radius.

$$\epsilon_p^{bubble} \approx \frac{2\sigma}{r_c} \left[\frac{V^g}{V^{lg} - V^g} \right] \quad ; \quad \epsilon_p^{dew} \approx \frac{2\sigma}{r_c} \left[\frac{V^l}{V^l - V^{gi}} \right] \quad (2.54)$$

If we plot the real change in the saturation pressure at a constant temperature against the inverse of the capillary radius and compare with the expressions in (Eq. 2.54) we get very close plots as shown in Figure 2.9 and Figure 2.10. Taking into account that this is only a linear approximation, we can say that the effect of the inverse of the capillary radius on the change of the saturation change is almost linear. Therefore, we can approximate the change of phase envelope at different capillary radii using the linear expansions obtained in the previous sections. In other words, by having the normal saturation point and the capillary radius, we can approximate of the shift in the saturation pressure with a simple linear relationship. This means that the mathematical analysis based on linear expansions is not only useful in showing the direction of the shift in the phase envelope, but also to estimate the magnitude. In many cases, this approximation is sufficiently accurate, specially for the bubble point branch.

Quality Lines

An important feature of the algorithm presented here is the ability of constructing the quality lines of any vapor fraction ($0 \leq \beta \leq 1$) in addition to the bubble point curve ($\beta = 0$) and the dew point curve ($\beta = 1$). These calculations are remarkably absent in the literature in spite of its usefulness for understanding the behavior of multicomponent mixtures in the two phase region.

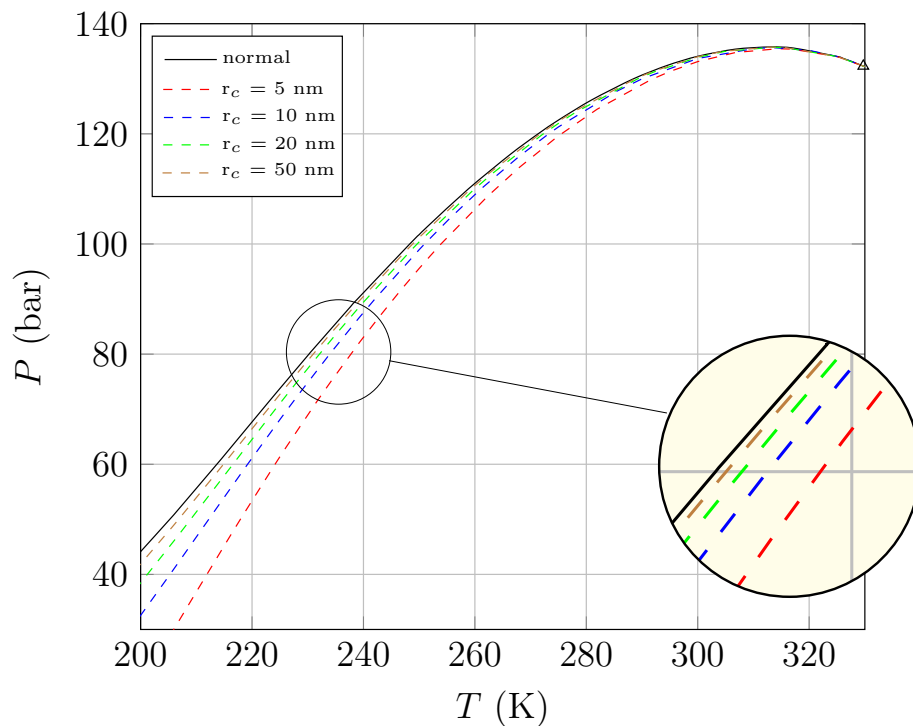


FIGURE 2.8.: Bubble point change at different capillary radius (r_c) for a 70-30 mol% C₁-C₄ mixture.

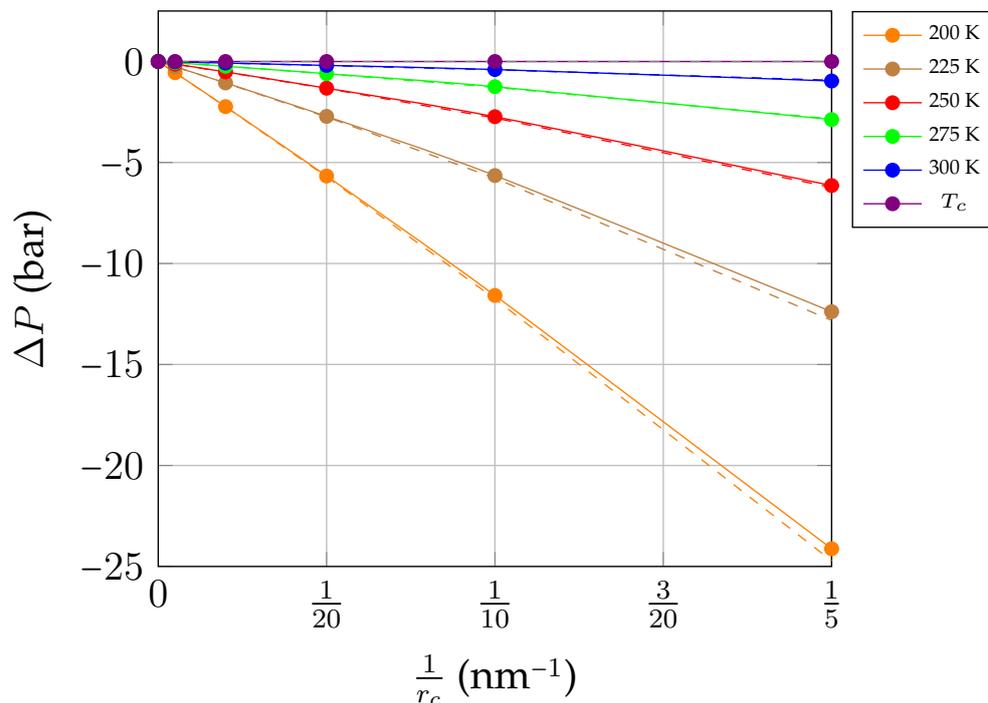


FIGURE 2.9.: Bubble point change at different temperatures as a function of $(\frac{1}{r_c})$ for a 70-30 mol% C₁-C₄ mixture. Dashed lines (- -) show the approximation given by (Eq. 2.54).

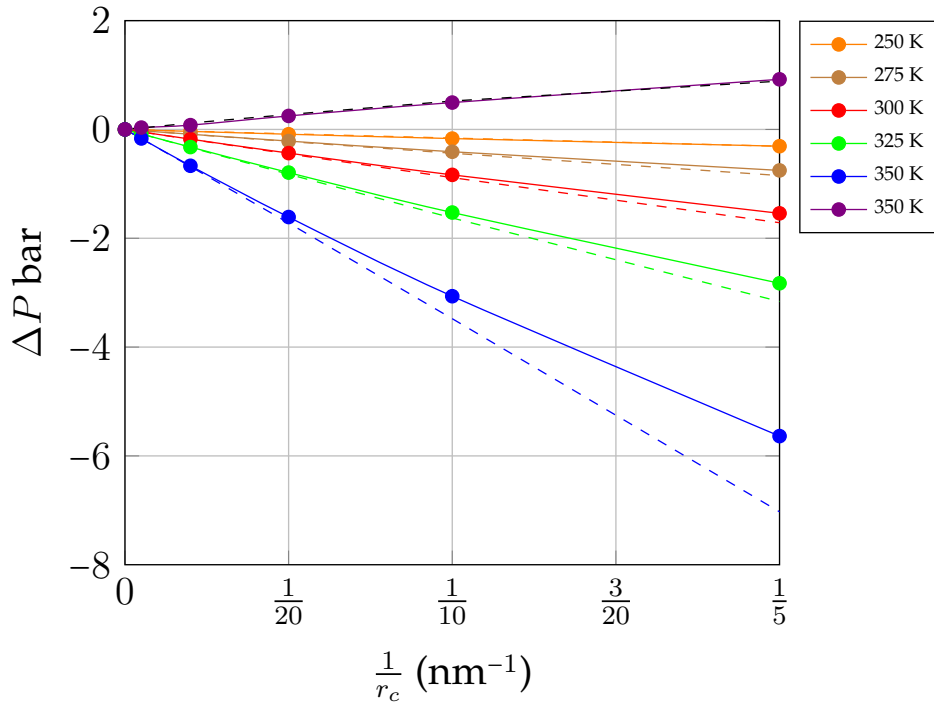


FIGURE 2.10.: Dew point change at different temperatures as a function of $(\frac{1}{r_c})$ for a 70-30 mol% C_1 - C_4 mixture. Dashed lines (- -) show the approximation given by (Eq. 2.54).

Figure 2.11 shows an example of a phase envelope with its quality lines. This figure gives an insight to the phase split of a mixture in the presence of capillary pressure in comparison to a normal bulk phase split. Moreover, if we select a decreasing pressure path at constant temperature it gives us an idea of the constant mass expansion experiment using a capillary tube.

Sensitivity on Scaling Exponent (E) and Parachors (χ)

A common concern on the calculation results, is the accuracy of the interfacial tension and consequently the capillary pressure. Schechter and Guo [39] presented a comparison of different methods to estimate the interfacial tension of hydrocarbon mixtures using different values for the parachors and scaling exponent. They concluded that if these values are properly selected it is possible to estimate the interfacial tension within a 10% of accuracy. Another common concern is the accuracy of the interfacial tension at high pressures using (Eq. 2.8). It is well known that a more theoretical approach as gradient theory can be employed to have better estimates at such conditions. However, the simplicity and usefulness of the parachor model makes it a very popular choice for engineering purposes. The purpose

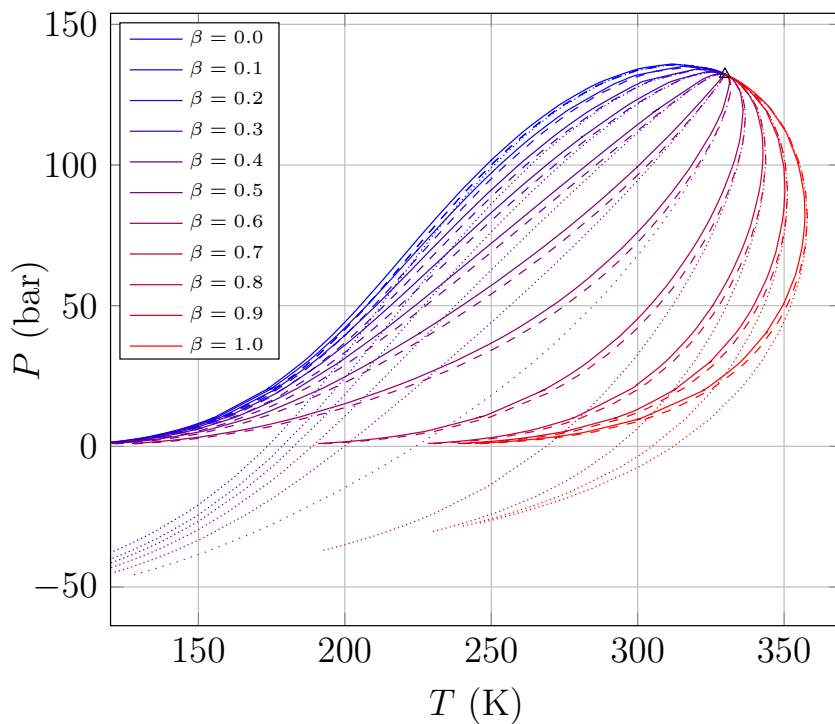


FIGURE 2.11.: Quality lines at different vapor fractions (β) for a 70-30 mol% C_1 - C_4 system. (—) Normal quality lines; (\cdots) P_l ; and (- - -) P_g due to capillary pressure difference. $r_c=10\text{nm}$

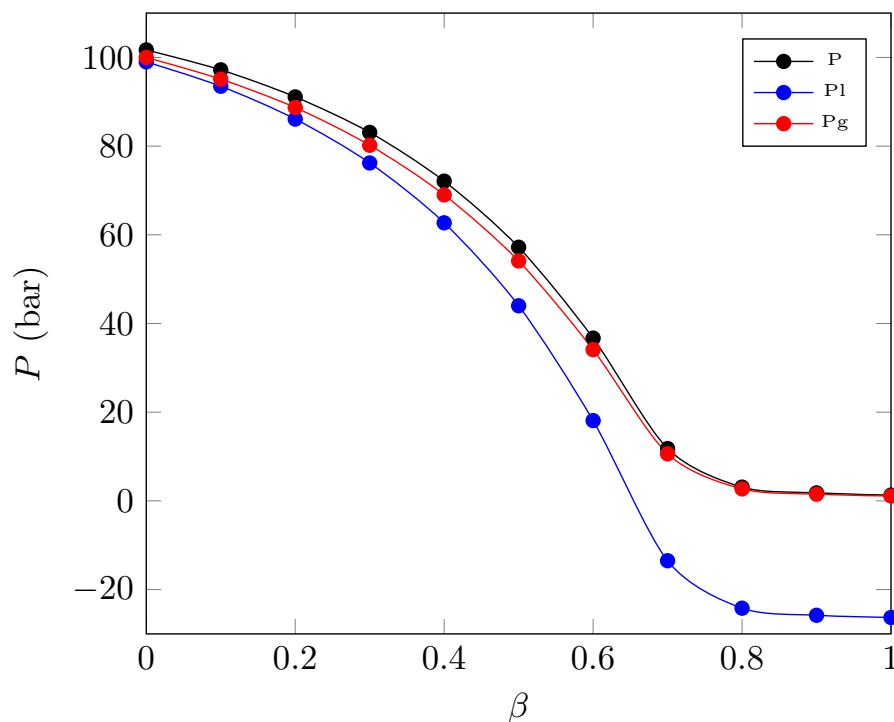


FIGURE 2.12.: Pressure profiles as a function of the vapor fraction. $T = 250\text{ K}$

of this section is to identify the sensitivity of the phase envelope with respect to the parachor model parameters.

A common value for the scaling exponent in (Eq. 2.8) is ($E = 4$) but it can vary around that value depending on the author. A reasonable range of the scaling factor was selected and different phase envelopes were plotted for System (I). Figure 2.13 shows the sensitivity at the scaling exponent. It can be noticed that the scaling exponent it is only sensitive to very low temperatures and pressures in the bubble point region. On the other hand, at high pressures and temperatures it is not very sensitive, especially close to the critical point.

The parachor value is an intrinsic property, and theoretically it does not vary with respect to the temperature or pressure. Therefore, the sets of parachor values found in literature, either theoretically calculated or experimentally measured, should not vary much. A range of $\pm 10\%$ in the parachor values is reasonable for a sensitivity analysis. Figure 2.14 and Figure 2.15 show the changes in the phase envelope by modifying the parachor values of the lightest and heaviest component. For the case of the lightest component, which for this case is also the most abundant in the mixture, it is possible to observe a bigger effect in the bubble curve. For the case of the heaviest component, the effect is more pronounced in the the dew point curve. However, it is not as important as the impact of the lightest component for this mixture, but it would be increased if a heavier mixture is tested.

We can conclude that the sensitivity of the phase envelope with respect to the parachor values, especially that of the lightest component, seems more important than the selection of the scaling exponent. Moreover, the bubble point region is more affected than the dew point region. However, the change is not substantial at the tested conditions, and the qualitative behavior is unchanged.

2.2. Two-phase Flash Involving Capillary Pressure

Same as for the phase envelope calculations, the isothermal flash problem involving capillary pressure is of great importance in oil and gas production from tight reservoirs. The inclusion of capillary pressure poses additional challenges and should be addressed in order to have a robust flash that can be used in the reservoir simulation context. The isothermal flash problem including capillarity consists in determining the global minimum of the Gibbs energy for a mixture of overall feed composition \mathbf{z} , at a specified phase pressure (P_l or P_g) and temperature (T), holding a capillary

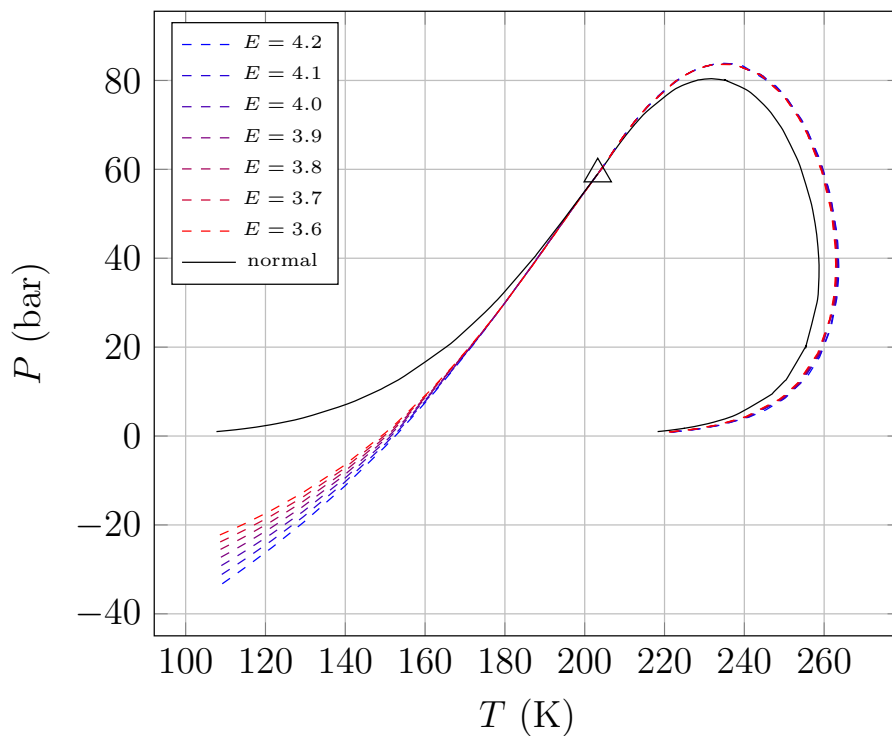
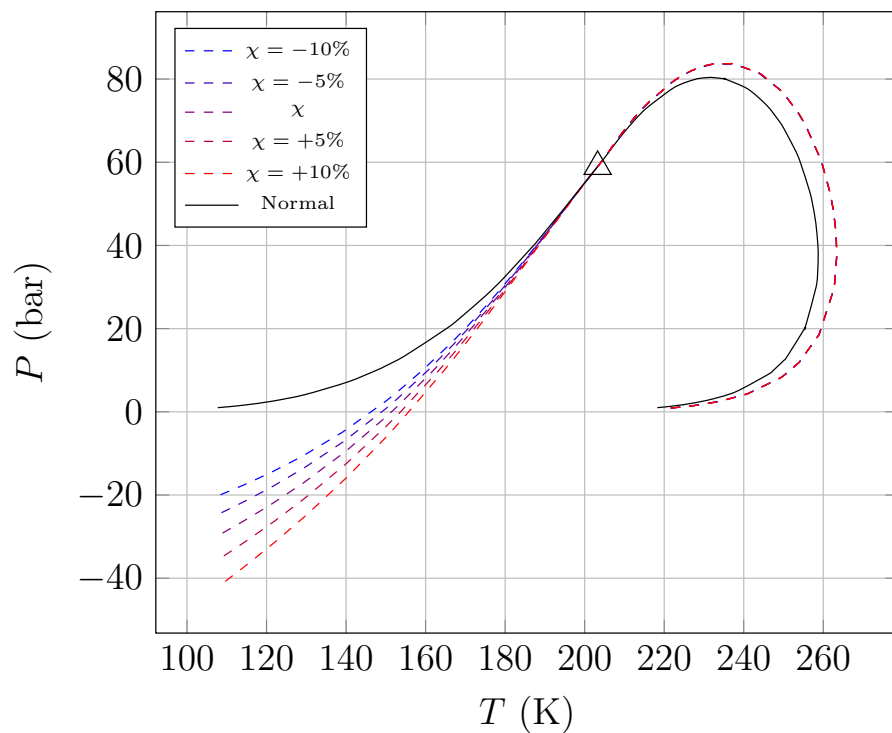
FIGURE 2.13.: Sensitivity analysis on scaling exponent E for System I

FIGURE 2.14.: Sensitivity analysis on the parachor of the lightest hydrocarbon for System I.

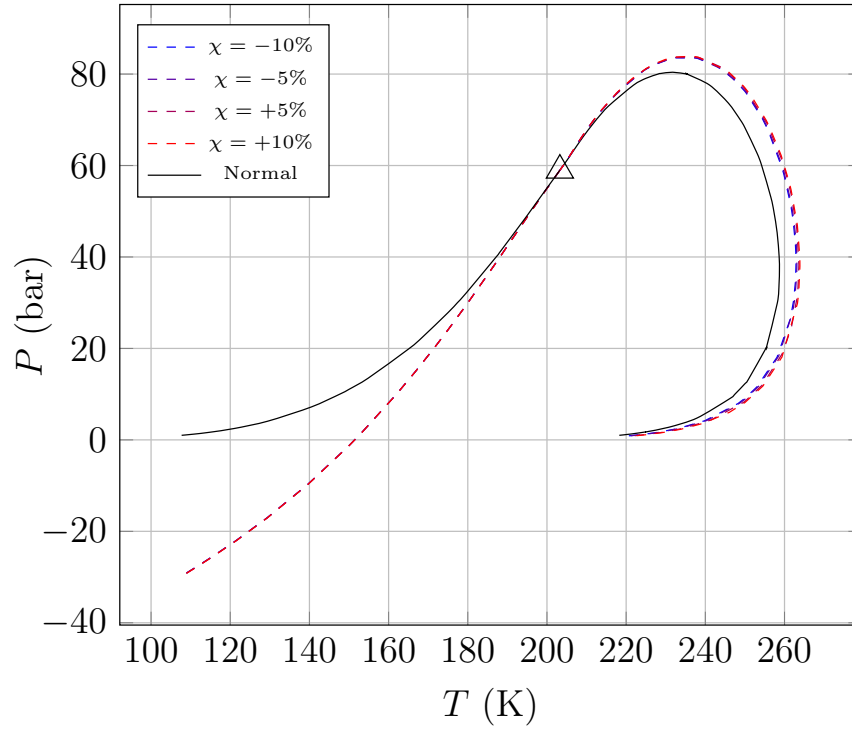


FIGURE 2.15.: Sensitivity analysis on the parachor of the heaviest hydrocarbon for System I.

pressure constraint. At the minimum, the stationary condition of equal fugacities in both phases must hold.

$$\ln f_i^l(P_l, \mathbf{x}) = \ln f_i^g(P_g, \mathbf{y}), \quad i = 1, \dots, N_c \quad (2.55)$$

Additionally, the selected capillary pressure model and the mass balance must be satisfied

$$P_c(P_g, P_l, \mathbf{x}, \mathbf{y}) = P_g - P_l \quad (2.56)$$

$$z_i = v_i + l_i \quad i = 1, \dots, N_c \quad (2.57)$$

where v_i and l_i are the vapor and liquid molar flows respectively. Similar to phase envelope calculations, when introducing a capillary pressure difference it is possible to encounter negative pressures in the liquid phase. Therefore, it is recommended to use the product of the pressure and fugacity coefficient ($F_i = P\varphi_i$) in the intermediate calculations instead of the fugacity coefficient alone.

In order to solve the two-phase flash problem, a procedure similar to that given in Michelsen and Mollerup [41] is followed. The details are presented in the next

sections.

2.2.1. Successive Substitution

An iterative procedure of solving the Rachford-Rice equation while updating the equilibrium factors accounting for capillary pressure in an outer loop is employed in the early steps before switching to a Gibbs energy minimization procedure. The Rachford-Rice equation finds the vapor fraction (β) that meets the mass balance constraints of the system at a specified equilibrium factor

$$g(\beta) = \sum_i z_i^b \frac{K_i - 1}{1 - \beta + \beta K_i} = 0 \quad (2.58)$$

The equation can be solved by Newton's equation quite safely since (Eq. 2.58) is monotonically decreasing. If $g(0) > 0$ and $g(1) < 0$, a solution in the interval (0,1) is guaranteed. If the solution of β is found outside the (0,1) interval, the solution will correspond to a sub-cooled liquid ($\beta < 0$) or superheated vapor ($\beta > 1$), which corresponds to a single phase solution. To initialize the successive substitution procedure Wilson's approximation is recommended. After solving the Rachford-Rice equation the new compositions, capillary pressure and equilibrium factors are updated by direct substitution. For the phase compositions we get:

$$x_i = \frac{z_i}{1 - \beta + \beta K_i}, \quad y_i = \frac{K_i z_i}{1 - \beta + \beta K_i} \quad (2.59)$$

and for the capillary pressure and equilibrium factors:

$$P_c(P_g, P_l, \mathbf{x}, \mathbf{y}) = P_g - P_l, \quad K_i = \frac{P_l \varphi_i^l(P_l, \mathbf{x})}{P_g \varphi_i^g(P_g, \mathbf{y})} \quad (2.60)$$

Notice that the update in the equilibrium factors differs slightly from the conventional

$$K_i = \frac{\varphi_i^l(P, \mathbf{x})}{\varphi_i^g(P, \mathbf{y})} \quad (2.61)$$

This is due to the difference of pressures from capillary effect. Furthermore, the update in the phase pressures is made according to the specified phase pressure. For instance, if P_g is specified the update ($P_l = P_g - P_c$) is used, and if P_l is specified the update ($P_g = P_l + P_c$) is used. It is often the case that the capillary pressure P_c depends on the final pressures P_l and P_g . Therefore, an implicit function is obtained when updating the new phase pressures. Nevertheless, the exact capillary pressure

must hold only at the final solution and a direct substitution procedure is therefore convenient for early iterations.

2.2.2. Gibbs Energy Minimization

The successive substitution procedure can be intolerably slow close to the critical point where the eigenvalues of the Jacobian matrix are close to unity. In this situation, second order methods are performed for faster convergence of the solution. The flash problem without capillary pressure can be posed as an unconstrained minimization using the vapor molar amounts as independent variables and eliminating the liquid molar amounts by means of the overall mass balance

$$\min G(\mathbf{v}, \mathbf{l}(\mathbf{v})), \quad \text{with } \mathbf{l} = \mathbf{z} - \mathbf{v} \quad (2.62)$$

where G is the Gibbs energy of the system. The stationary point of the solution corresponds to the phase equilibrium condition

$$\frac{\partial}{\partial v_i} \left(\frac{G}{RT} \right) = g_i = \ln f_i^g - \ln f_i^l = 0 \quad (2.63)$$

where \mathbf{g} is the gradient vector. Finally the Hessian matrix of (Eq. 2.63) can be written as follows:

$$H_{ij} = \frac{\partial g_i}{\partial v_j} = \frac{1}{\beta(1-\beta)} \left(\frac{z_i^b}{x_i y_i} \delta_{ij} - 1 + (1-\beta)\Phi_{ij}^g + \beta\Phi_{ij}^l \right) \quad (2.64)$$

where

$$\Phi_{ij} = n_T \left(\frac{\partial \ln \varphi_i}{\partial n_j} \right)_{T,P}, \quad n_T = \sum_k n_k \quad (2.65)$$

For details in the derivation the reader is referred to Michelsen and Mollerup [41]. The update in the vapor flows can be obtained by solving the following system

$$\mathbf{H}\Delta\mathbf{v} + \mathbf{g} = \mathbf{0} \quad (2.66)$$

The system is commonly solved by using Hebden's algorithm [45], which is very convenient in cases near to the critical point where the determinant of the Hessian is close to zero. Hebden's method secure the step sizes where the Newton method overshoots to undesired points. It is important to use the second order method with good quality initial estimates in order to have local convergence. Therefore, it is

recommended to perform several cycles of successive substitution before changing to second order methods.

When a capillary pressure difference is considered between the two phases, an additional degree of freedom is introduced and the unknown vector of independent variables is increased by one (\mathbf{v}, P_l or P_g) depending on the specified phase pressure. In order to satisfy the capillary pressure constraint it is necessary to modify the gradient by introducing an additional term

$$g_{Nc+1} = P_c - P_g + P_l \quad (2.67)$$

and the modified matrix will correspond to the Jacobian of the entire system.

$$\mathbf{J} = \begin{pmatrix} \mathbf{H} & \left(\frac{\partial \ln \mathbf{F}}{\partial P_g} \right) \\ \left(\frac{\partial P_c}{\partial \mathbf{v}} \right)^T & \frac{\partial P_c}{\partial P_g} - 1 \end{pmatrix} \quad (2.68)$$

This new matrix is less attractive to solve in comparison with the one in (Eq. 2.66) and safe methods such as Hebden's method cannot be used. Instead it is recommended to solve (Eq. 2.66) while updating the capillary pressure in an outer loop. Moreover, to ensure steps in the right direction the capillary pressure update must be exact, i.e. the implicit function ($P_c - P_g + P_l = 0$) must be solved at each step. A Newton iterative method is suggested to converge the capillary pressure at each step of the vapor flows:

$$P_g^{k+1} = P_g^k - \frac{g_{Nc+1}}{\frac{\partial P_c}{\partial P_g} - 1} \quad (2.69)$$

This ensures the stationary condition of the capillary pressure at each step. The procedure is also applicable for P_l updates if it is the case of the P_g flash specification.

2.2.3. Flash Strategy

Similar to standard flash calculations, it is assumed prior to any calculation that the two phases will be present at equilibrium. Wilson equilibrium factors are used as a starting point and successive substitution is performed until obtaining a desired tolerance or a set number of iterations is reached. The disappearance of a phase during early steps is taken as a single phase solution, but it is confirmed by means of stability analysis involving capillary pressure to ensure safety. Second order methods are used to speed up the convergence in situations where successive substitution is

slow and the specified tolerance cannot be reached in a small number of iterations. In summary, the procedure can be described with the following steps:

- i Initialize with Wilson's equilibrium factors.
- ii Perform 5-10 cycles of successive substitution.
- iii Continue with second order methods, while updating the capillary pressure in an outer loop.
- iv If one of the bulk phases disappear at any point during steps ii) or iii) perform stability analysis of the current system. If stable, terminate; otherwise return to step ii) with the new approximation given by the stability analysis test.

2.2.4. Stability Analysis

The flash problem is often complemented with stability analysis. The idea behind evaluating the stability of the feed phase is to check if we are at the global minimum of the Gibbs energy. For instance, if we are at the minimum, the formation of an infinitesimal amount of a new phase with a composition (\mathbf{w}) must result in an increase of the Gibbs energy.

$$\delta G = \delta \epsilon \sum_i RT w_i (\ln f_i(\mathbf{w}, P_w) - \ln f_i(\mathbf{z}, P)) \geq 0 \quad (2.70)$$

Moreover, the condition must hold for any value of $\delta \epsilon$.

$$\sum_i w_i (\ln f_i(\mathbf{w}, P_w) - \ln f_i(\mathbf{z}, P)) \geq 0 \quad (2.71)$$

This is the Gibbs tangent plane condition. Notice that when including capillarity, each composition (\mathbf{w}) introduces a constraint in the pressure of the new phase (i.e. $P_w = P \pm P_c$) which sometimes does not have a solution depending on the capillary pressure model considered. In many situations, it is an indication of a single phase solution. This happens when the mixture exceeds the capillary pressure boundary where two-phase equilibrium is no longer possible [14].

A detailed procedure to implement stability analysis including capillarity, based on finding the stationary points of the modified tangent plane distance, is given by Sherafati et al. [15] and it is the procedure used to confirm solutions of the flash algorithm described in this chapter. As in Michelsen [16], the procedure uses a variable transformation from molar fractions to molar amounts to solve the problem

as an unconstrained minimization. The transformation of variables is as follows

$$\ln W_i = \ln w_i - k \quad (2.72)$$

where k is the reduced TPD at the stationary point of (Eq. ??), and the reduced TPD is

$$tm(\mathbf{W}) = 1 + \sum_i W_i (\ln W_i + \ln F_i^w - d_i - 1) \quad (2.73)$$

with

$$d_i = \ln z_i + \ln F_i^z, \quad \text{and} \quad P^w - P^z = \pm P_c \quad (2.74)$$

where $F_i = \varphi_i P$ to avoid undefined $\ln \varphi_i$ at negative pressures. The (\pm) sign in the capillary pressure constraint depends on the feed phase we are testing. For instance, if we assume our feed as the wetting phase, the sign is negative. If our feed phase is stable, the stationary points of (Eq. 2.73) must be greater than zero, and negative otherwise. If negative, the composition of the stationary point can be used as an initial estimate for phase splitting calculations.

The recommended solution procedure by Sherafati et al. [15] to find the stationary points of (Eq. 2.73) is based on an accelerated direct substitution procedure, and second order methods when needed.

$$\ln W_i + \ln F_i^w(\mathbf{w}, P^w) - d_i = 0 \quad (2.75)$$

where P^w is initialized as the feed phase, and it is updated using (Eq. 2.74). Accelerated substitution based on the dominant eigenvalue method is suggested to obtain a more rapid convergence. Close to the critical point it is convenient to switch to second order methods on the molar amounts while updating in an outer loop the capillary pressure. The optimal scaling for the Hessian of 2.73 comes with the choice of $\{\mathbf{v} = [2\sqrt{W_1}, 2\sqrt{W_2}, \dots, 2\sqrt{W_{N_c}}]\}$ as independent variables

$$H_{ij} = \frac{\partial^2 tm}{\partial v_i \partial v_j} = \delta_{ij} + \sqrt{W_i W_j} \frac{\partial \varphi_j^w}{\partial W_j} + \frac{1}{2} \frac{g_i}{v_i} \delta_{ij} \quad (2.76)$$

where g_i is the gradient

$$g_i = \frac{\partial tm}{\partial v_i} = \sqrt{W_i} (\ln W_i + \ln F_i^w - d_i) \quad (2.77)$$

the quadratic step on \mathbf{v} , using restricted step algorithms is given by:

$$(\mathbf{H} + \beta\mathbf{I}) \Delta\mathbf{v} + g = 0 \quad (2.78)$$

where β is the diagonal correction factor. It was found that updating P^w is as efficient as using an update based on the full Jacobian of (Eq. 2.73) with $\{\mathbf{v}, P^w\}$ as the independent variables. In addition to the presented procedure, we found useful to make exact updates in the capillary pressure when the pressure model depends on the composition and the final pressure:

$$P^w - P^z = \pm P_c(P^z, P^w, \mathbf{z}, \mathbf{w}) \quad (2.79)$$

This is useful since each introduced composition \mathbf{w} will satisfy the capillary pressure constraint. In some cases, (Eq. 2.79) do not have a solution at the specified \mathbf{w} , therefore smaller steps on \mathbf{w} must be taken. If the step-size cannot longer be reduced, it is taken as an indication of stability.

2.2.5. P_l and P_g Flash Specifications

The described algorithm in the previous sections can be applied to two different scenarios: P_l and P_g specifications. Both tools are of great importance depending on the nature of process or system. For instance the P_l flash specification is convenient in simulations of tight reservoirs that are initialized in the liquid region, where the pressure of oil phase is known. On the other hand, processes such as compression of a gas mixtures in which capillary condensation can occur, the P_g flash specification is more convenient. The main difference on its design will be on how the capillary pressure is updated. For the P_l flash specification, the pressure in the gas phase is the one updated; and for the P_g flash specification, the pressure in the liquid phase is the one updated.

Both procedures have its own particular difficulties. For instance, the P_l flash procedure (where P_g is updated) can be more unstable since the capillary pressure model is often a function of the densities (IFT) or phase saturation (J-function), which are highly sensitive to the gas pressure update. This is not a problem when P_g is specified (where P_l is updated) since the liquid density is a weak function of pressure. On the other hand, when P_g is specified P_l can reach negative values and modifications

on the standard thermodynamic libraries to obtain $F_i = \varphi_i P$ instead of φ_i alone are necessary.

The P_l and P_g specification flash, following the recommended procedure in the previous sections, were tested in a fine grid (500×500) over a wide PT range using a C_1 - C_4 binary mixture and an oil mixture from the Bakken field [32]. The binary system is described in Table 2.6 and the oil mixture is described in Table 2.10. The algorithm shows to be robust and converges in all the tested points as shown from Figure 2.16 to Figure 2.19. The average relative cost to a standard flash without considering capillary pressure is of 1.42 for the binary mixture and 1.38 for the Bakken fluid.

At a simple glance, the plots appear very different from each other. This seems to be counter intuitive if we think that the P_l flash and the P_g flash can correspond to each other. For example, supposing that the flash at P_l and T give the results $(P_g, \beta, \mathbf{y}, \mathbf{x})$, apparently the flash at P_g and T will give the results of $(P_l, \beta, \mathbf{y}, \mathbf{x})$. This seems to suggest that Figure 2.16 can be converted to Figure 2.17 and vice versa, and the same is true to Figure 2.18 and Figure 2.19. However, since the difference between P_g and P_l is not a constant, and actually dependent on the location in the phase diagram (it can be easily seen at the saturation boundary), the conversion is not simple vertical translation of the plot. Therefore, although the figures using two specifications essentially reflect the same reality and are convertible, they do not have the exactly same appearance.

Moreover, the plotted figures confirm the same changes that the phase envelope calculations have shown. Specifically, Figure 2.17 and Figure 2.16 show the same results as Figure 2.11. This means that the points shown in the previous sections correspond to the global minimum of the Gibbs energy, thus confirming its correctness.

TABLE 2.10.: Compositional data for Bakken oil

Component	Composition	P_{crit} (bar)	T_{crit} (K)	ω	Parachor
C_1	0.36736	45.162	186.297	0.0102	74.8
C_2	0.14885	49.779	305.538	0.1028	107.7
C_3	0.09334	42.455	369.983	0.1520	151.9
C_4	0.05751	37.677	421.782	0.1894	189.6
C_5 - C_6	0.06406	31.804	486.377	0.2684	250.2
C_7 - C_{12}	0.15854	25.051	585.138	0.4291	350.2
C_{13} - C_{21}	0.0733	17.210	740.052	0.7203	590.0
C_{22} - C_{80}	0.03704	13.108	1024.717	1.0159	1216.8

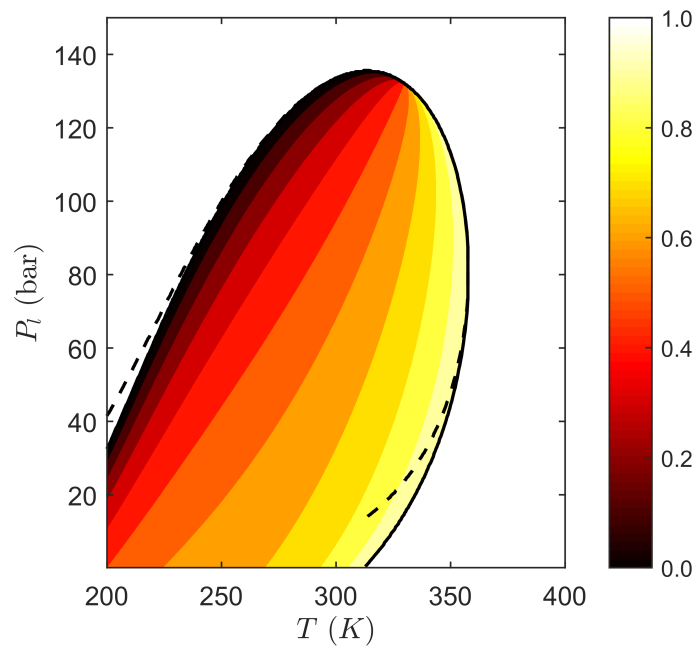


FIGURE 2.16.: P_l flash specification. 70% – 30% C_1 - C_4 mixture inside a capillary tube of $r_c = 10nm$. Dashed lines (- - -) represent the gas pressure at the saturation point.

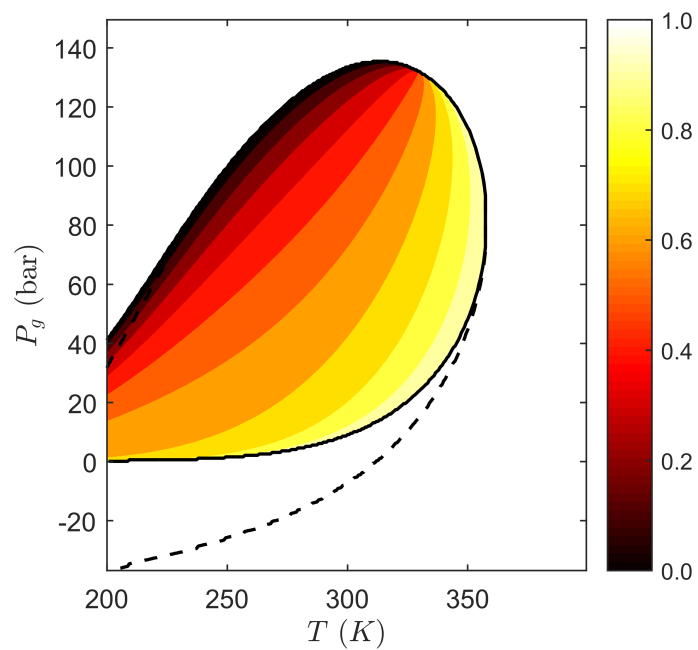


FIGURE 2.17.: P_g flash specification. 70% – 30% C_1 - C_4 mixture inside a capillary tube of $r_c = 10nm$. Dashed lines (- - -) represent the liquid pressure at the saturation point.

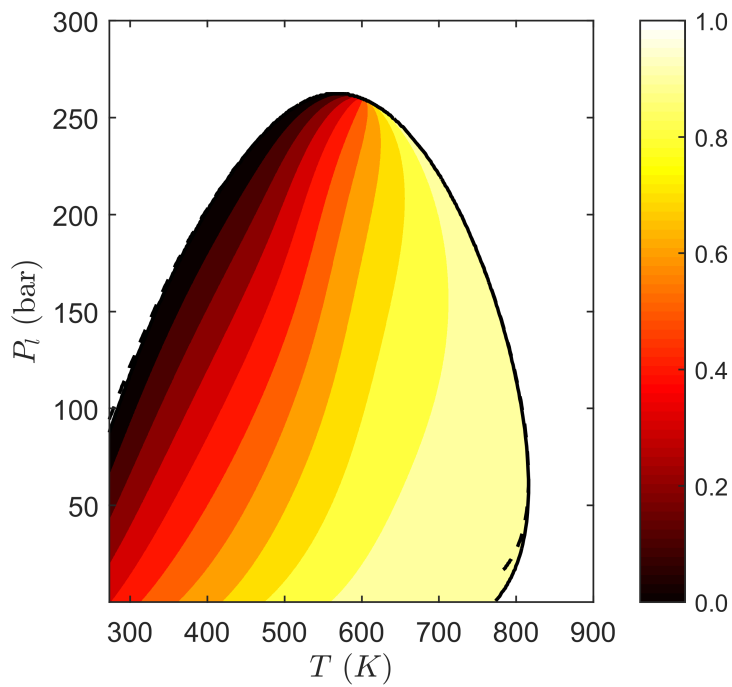


FIGURE 2.18.: P_l flash specification. Bakken oil inside a capillary tube of $r_c = 10\text{nm}$. Dashed lines (- -) represent the gas pressure at the saturation point.

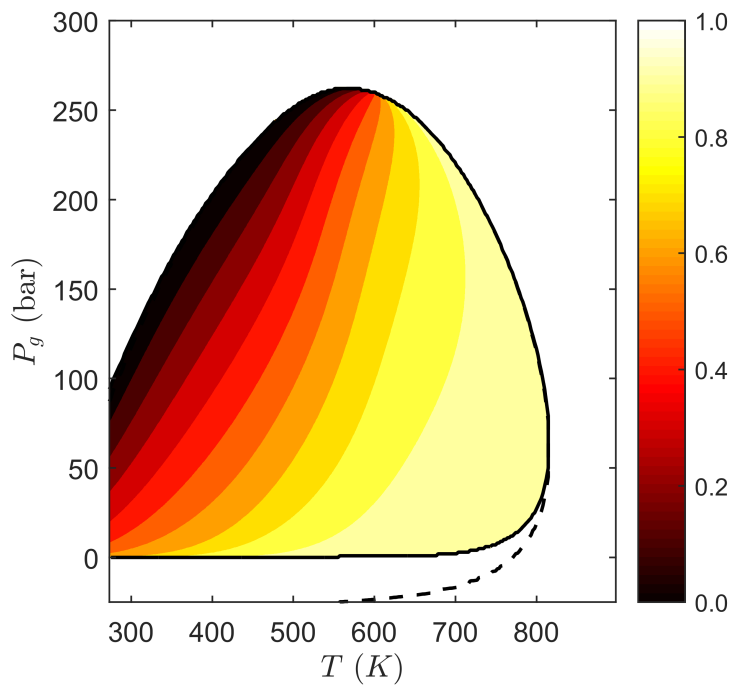


FIGURE 2.19.: P_g flash specification. Bakken oil inside a capillary tube of $r_c = 10\text{nm}$. Dashed lines (- -) represent the liquid pressure at the saturation point.

2.3. Conclusions

Two different algorithms for phase envelope and flash calculations for systems in the presence of a capillary pressure difference were presented. The phase envelope algorithm shows to be efficient and robust. It serves as a useful tool for studying the effects of capillary pressure on phase envelope at different feed compositions, capillary radii and vapor phase fractions. Furthermore, the P_l and P_g flash algorithms show to be robust and able to handle different systems in a wide range of pressure and temperature without any evident problems.

Both, phase envelope and flash algorithms, were used to test various systems from simple binary mixtures to multicomponent natural gas and reservoir fluids. The results show that capillary pressure shifts the phase boundary in all the places except at the critical point: the bubble point pressure decreases and the pressure suppression increases as the condition is further away from the critical point; the dew point part of the phase envelope is expanded with an increase of the dew point pressure in the upper branch, a shift of the cricondenterm to a higher temperature, and a decrease of the dew point pressure in the lower branch. The results provided by the phase envelope calculations generally agree with the recent studies[32, 33] based on individual saturation point calculation except that the cricondenterm is shown to be shifted in the results presented in this chapter. The correctness of the results was confirmed by flash calculations using the proposed P_g and P_l flash algorithm. Therefore, the unchanged cricondenterm reported in the previous studies is likely a trivial solution caused by the absence or poor quality of initial estimates at the cricondenterm.

The flash algorithms, both P_g and P_l specifications, showed to converge in all the temperature and pressure range tested. The increase of the computational cost associated to capillary pressure effect in flash calculations is around 40% for the systems tested. Moreover, a stability analysis, based in a modified tangent plane distance considering capillary pressure, is used to check the correctness of the results obtained by the flash algorithm.

In addition to the presented algorithms, a mathematical analysis through linear approximation at the saturation point was presented. The linear approximations provide a way to judge the direction of the shift and to estimate its magnitude based only on the saturation point without capillary pressure. In other words, no saturation point calculation with capillary pressure is needed to use the equations.

The results show that the equations predict the same directions of change as those from the phase envelope calculation. Moreover, these equations relate the saturation point shift to the change in volume or entropy if an infinitesimal amount of the incipient phase is formed, thus providing a physical interpretation for the effect of capillary pressure. In particular, multicomponent Clayperon equation indicates that the volume change is zero at the cricondentherm and the entropy change is zero at the cricondenbar. As a result, the saturation pressure shift and the saturation temperature shift change the direction at these two points, respectively. These linear approximation equations can be used as initial estimates for saturation points, and in many cases may be sufficiently accurate for bubble point calculation with capillary pressure.

The magnitude of saturation pressure change was found to be case dependent. However, for the range of capillary radii studied here (larger than 5 nm), the change seems to be moderate. In practice, the picture will be more complicated, not only due to pore size heterogeneity of real porous materials, but also due to dynamic effects like selective adsorption and confinement effects. Therefore, additional considerations should also be taken into account for a more complete analysis.

CHAPTER 3

Multicomponent Adsorption in Shale

Natural gas inside shale is stored in three different forms: as free gas inside the macro- and meso-pores; as adsorbed gas inside organic and inorganic micro-pores; and as dissolved gas in oil and water [46]. The high content of micro-pores inside the shale matrix can make the adsorbed hydrocarbons be up to 50% of the total oil and gas in place. Not only can the adsorbed amount inside the reservoir be considerably high, but also can the adsorption process plays an important role in the phase equilibrium close to the saturation point as demonstrated by [26] and [31]. Thus, fundamental understanding of adsorption at reservoir and production conditions is of great importance.

Shale is a heterogeneous mixture of organic and inorganic matter which results in a wide variation of surface chemistry and pore shapes/sizes. In some shales the micro-pores responsible for adsorption are associated with mineral grains [47], however, for the great majority of shales the small size micro-pores are located in organic patches, representing the main source of adsorbed gas. This suggests that the organic content in shale might determine the adsorption capacity [46]. The heterogeneity of shale as an adsorbent makes adsorption very hard to study. In addition, its experimental measurements at high pressures (up to 250 bar) and temperatures (up to 338 K) restricted by low uptakes have shown to be very challenging as presented in an inter-laboratory comparison by Gasparik et al. [23]. The inter-laboratory comparison reported significant discrepancies of the measurements and reproducibility between different laboratories. Several adsorption data inside shale for pure components such as methane, ethane, and CO₂ can be found in literature [48–50]. However,

experimental data for binary and multicomponent systems are very limited. In order to study multicomponent adsorption inside shale additional experimental data and reliable predictive adsorption models at high pressures and temperatures are required.

Many adsorption theories can be applied to study high pressure adsorption. For instance, the Multicomponent Langmuir (ML), Ideal Adsorbed Solution Theory (IAST), and the Multicomponent Potential Theory of Adsorption (MPTA). Moreover, several validations and comparisons of models can be found in the literature for different adsorbents [51–53]. However, to the best of our knowledge, there is no such comparison for adsorption in shale. The main objective of this chapter is to provide a comparison of different models for high pressure adsorption data in shale found in recent literature and molecular simulations. Three different models were tested for the fitting of pure component isotherms: the Langmuir, Toth-Langmuir and MPTA using the Dubinin-Radushkevich-Astakhov (DRA) potential. For multicomponent mixtures three methods were compared: the Extended or Multicomponent Langmuir (ML), IAST and MPTA-DRA.

3.1. Adsorption Models

In this section, we briefly describe the adsorption models used in the chapter. This includes models for pure component fitting and multicomponent adsorption prediction in shale.

3.1.1. Multicomponent Langmuir (ML)

The Langmuir model is a single layer adsorption model [54]. It assumes that the adsorbent has a limited number of active sites to adsorb molecules, and the site can be either empty or occupied. The occupation of an active site by a molecule is associated to an equilibrium constant dependent on the heat of adsorption. Eq. 3.1 shows the Langmuir model for a pure component at high pressures:

$$n^{abs} = n^{max}(T) \frac{b(T)f}{1 + b(T)f} \quad (3.1)$$

where n^{abs} is the absolute adsorbed amount, $n^{max}(T)$ is the maximum adsorption capacity, $b(T)$ is the adsorption equilibrium constant, and f is the fugacity of the

fluid in contact with the adsorbed phase. The Langmuir model has been developed to calculate the absolute adsorbed amount or the actual number of molecules attached to the surface of the rock. Although, from an experimental point of view, it is impossible to measure the absolute amount without making a series of assumptions on the density of the adsorbed phase and the occupied volume. Only tools like molecular simulations can give the absolute adsorbed amount in well defined geometries. The raw experimental measurements obtained by gravimetric or volumetric methods reported in literature correspond exclusively to excess amounts [55]. The excess adsorption refers to the number of molecules in the nanopores in excess of the amount that would be present in the pore volume at the equilibrium density of the bulk gas. Figure 3.1 depicts the difference between excess adsorption and absolute adsorption (Δn). This term is negligible at low pressures and therefore, the Langmuir model can be applied without any problems. Nonetheless, the difference between the absolute and excess adsorption at high pressure is too large to ignore. In such cases, the following modification to (Eq. 3.1) is needed:

$$n^{exc} = n^{max}(T) \frac{b(T)f}{1 + b(T)f} - \rho^b V_{ads} \quad (3.2)$$

where ρ^b is the molar density of the bulk phase and V_{ads} is the volume occupied by the adsorbed phase. The second term on the right-hand side is the correction for the amount occupied by the bulk phase inside the adsorbed volume, it is also the link between absolute and excess amounts.

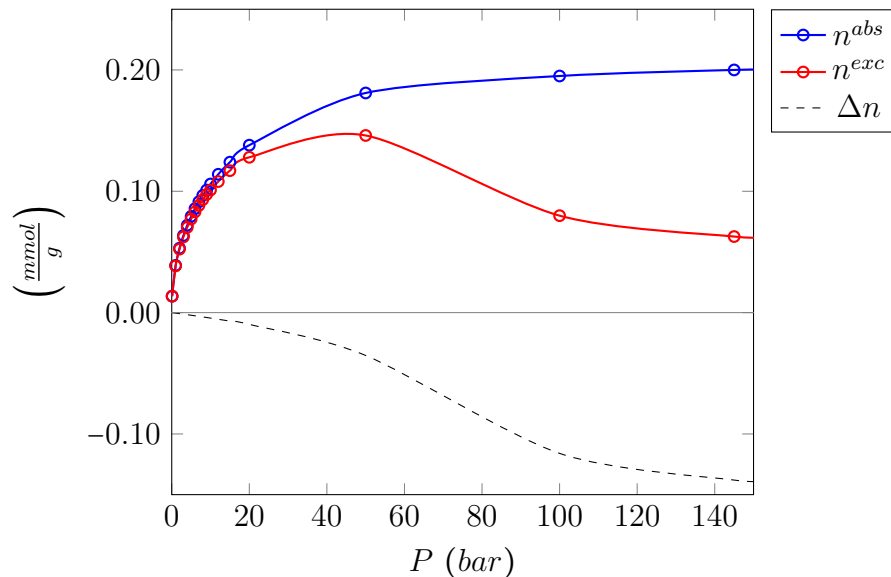


FIGURE 3.1.: Common supercritical isotherm for C_1 in shale at 323 K. Data generated with MPTA

In many cases, the adsorbed volume can be approximated by the micro-pore volume. However, if no information is given regarding the pore structure, V_{ads} should be treated as a separate fitting parameter of the adsorbent. This implies that the fitting of pure components belonging to the same rock sample should be done simultaneously.

The fitting of pure components is very crucial in adsorption thermodynamics. Calculation of the thermodynamic properties of the adsorbed phase and the prediction of multicomponent adsorption relies only on the pure component adsorption isotherms. The simplicity of the Langmuir model makes its extension to the multicomponent case quite straightforward. The Multicomponent Langmuir (ML) has the following form:

$$n_i^{abs} = n_i^{max}(T) \frac{b_i(T)f_i}{1 + \sum_{j=1}^{N_c} b_j(T)f_j} \quad (3.3)$$

where N_c is the number of components in the mixture, and the subscript (i) refers to component i in the mixture. Notice that the ML model is again exclusively for absolute adsorbed amounts. Therefore, in order to express the excess amounts, the same correction as before has to be applied

$$n_i^{exc} = n_i^{max}(T) \frac{b_i(T)f_i}{1 + \sum_{j=1}^{N_c} b_j(T)f_j} - y_i \rho^b V_{ads} \quad (3.4)$$

where y_i is the molar fraction of the gas phase, and ρ^b the density of the gas mixture in contact with the adsorbed phase. The presented model (ML), from the computational point of view, is the simplest among the three multicomponent models tested here. Its implementation is straightforward since no numerical procedures are required for evaluating the properties of the adsorbed phase for the pure or for the multicomponent case.

3.1.2. Ideal Adsorbed Solution Theory (IAST)

IAST was introduced by Myers and Prausnitz [56] and is based on the concept of an ideal adsorbed solution using classical surface thermodynamics. It is a framework that only needs the experimental adsorption data for the pure components in order to predict adsorption of the mixture. The principal idea on which IAST is based, is the definition of an ideal adsorbed solution in a similar form to that used for

liquid solutions. A concept of partial pressures for the adsorbed components is used to calculate equilibrium between the adsorbed molecules and the fluid. The thermodynamic equations describing the adsorbed phase are analogous to those of real fluids and are based on three fundamental assumptions:

1. The adsorbent is thermodynamically stable, meaning that any isothermal change in the system (fluid + adsorbed phase) will not affect the internal energy of the adsorbent.
2. The area of the adsorbent is invariant for changes in the temperature and pressure of the system. Moreover, the area is the same for all the adsorbates.
3. The zero dividing Gibbs surface definition applies for the adsorbed phase. Thus, measurements procedures based on the excess adsorbed amount apply without any modifications for the calculation of the properties.

The two main differences of the thermodynamic equations for the adsorbed phase with respect to those of real fluids, are the replacement of the pressure P for the spreading pressure π , and the replacement of the volume V for the surface area A . Therefore, same as for real fluids, the change of internal energy U and Gibbs energy G as function of the extensive (S, A, n) and intensive variables (T, π, μ) of the system.

$$dU = TdS - \pi dA + \sum_i \mu_i dn_i \quad (3.5)$$

$$dG = -SdT - Ad\pi + \sum_i n_i d\mu_i \quad (3.6)$$

Following a procedure similar to that in solution thermodynamics, we can arrive at the equilibrium condition based on equal fugacities of the adsorbed phase and the bulk phase in contact,

$$\begin{cases} Py_i\varphi_i = f_i^0(\pi_i)x_i \\ \pi_i = \pi_j \\ \sum_i y_i = \sum_i x_i = 1 \end{cases} \quad i, j = 1, \dots, N_c \quad (3.7)$$

where for the bulk phase: P is the pressure, φ_i is the fugacity coefficient, z_i^b is the molar composition; for the adsorbed phase: f_i^0 is the fugacity of the pure component i alone at a spreading pressure π , x_i^a is the molar composition, and γ_i is the activity coefficient, which for the IAST framework is equal to one ($\gamma = 1$). For a detailed derivation the reader is referred to [56].

The fugacity dependence on the spreading pressure $f_i(\pi)$ is crucial to solve the system of equations in (Eq. 3.7). It is obtained by means of the Gibbs adsorption isotherm of the pure components:

$$-Ad\pi + nd\mu = 0 \quad (3.8)$$

The integration of this equation and its following inversion gives us the relationship for the spreading pressure.

$$\pi(f^0) = \frac{RT}{A} \int_0^{f^0} n(t) d \ln t \quad \rightarrow \quad f^0 = f^0(\pi) \quad (3.9)$$

At low pressures, it is possible to substitute P^0 for f_0 , but formally the fugacity term is the one defined. In the IAST framework, in order to obtain the thermodynamic properties of the adsorbed phase, the surface excess amounts are used [57–59].

At low pressures, where the absolute adsorbed amount coincides with the excess amount, the adsorption data can be fitted with Langmuir isotherms and (Eq. 3.9) can be integrated analytically.

$$\pi(f^0) = \frac{RT}{A} n^{max} \ln(1 + bf_0) \quad (3.10)$$

This relationship can be inverted to get the fugacity as an explicit function of the spreading pressure.

$$f^0(\pi) = \frac{1}{b} \exp \left[\frac{1}{n^{max}} \frac{A\pi}{RT} \right] - \frac{1}{b} \quad (3.11)$$

It is worth noticing that b and n^{max} are temperature dependent, therefore experimental data at different temperatures are necessary when calculations for a variety of temperatures are required. On the other hand, at high pressures the normal Langmuir fitting is no longer satisfactory and models such as (Eq. 3.2) should be used to get the spreading pressure in (Eq. 3.9),

$$\pi(f^0, T) = \frac{RT}{A} \int_0^{f^0} \left[n^{max} \frac{bt}{1+bt} - \rho^b(t) V_{ads} \right] d \ln t \quad (3.12)$$

Unfortunately, this equation cannot be integrated analytically due to its bulk density dependent term ρ^b . Therefore, numerical methods are necessary. The standard procedure to solve the system of equations on (Eq. 3.7), is to sum up the molar

fractions in the adsorbed phase and solve for the spreading pressure of the system:

$$F(\pi) = \sum_i \frac{P\varphi_i z_i^b}{f_i^0(\pi)} - 1 = 0 \quad (3.13)$$

The initial estimate of the spreading pressure can be obtained with (Eq. 3.12) by assuming pure component adsorbed phase of the most abundant component in the bulk phase. Newton's method is then used to reach the solution.

$$\pi^{k+1} = \pi^k - \frac{F(\pi)}{F'(\pi)} \quad (3.14)$$

After solving for π , the adsorbed phase molar compositions x_i are readily obtained by substituting the spreading pressure into (Eq. 3.7), and the excess adsorbed amount can be obtained by applying ideal mixing properties

$$\sum_i \frac{x_i}{n_i^0(\pi)} = \frac{1}{n} \quad (3.15)$$

where n_i^0 is the adsorbed amount of component i at spreading pressure π in the absence of the other components in the mixture.

To summarize the procedure: First, the pure component experimental data are regressed to an adsorption model. Then, the integral in Eq. 3.9 is evaluated and inverted for each component to yield the relation between the fugacity (f^0) and the spreading pressure (π). Finally the system of equations in Eq. 3.7 is solved with respect to the spreading pressure (π), which can be subsequently use to compute the excess amounts and molar fractions.

The IAST framework was applied using two different isotherm models fitted to the experimental data for the multicomponent adsorption comparison described in the following sections. One of them is the modified Langmuir in (Eq. 3.2), and the other is the Toth equation, which is an empirical modification of the Langmuir model to yield improved fitting results.

$$n^{exc} = n^{max}(T) \frac{b(T)f}{[1 + (b(T)f)^c]^{\frac{1}{c}}} - \rho^b V_{ads} \quad (3.16)$$

where c is a correction exponent parameter. In principle, it is also possible to use the raw experimental data and perform a discrete numerical integration. However, unless the experimental data have low noise and are sufficiently smooth, it is recommended to use analytical fittings for IAST framework engine.

3.1.3. Multicomponent Potential Adsorption Theory (MPTA)

The MPTA theory was developed by Shapiro and Stenby [26] on the basis of the potential concept originally suggested by Polanyi [27]. MPTA describes the adsorbate as a distributed fluid inside an external potential field emitted by the adsorbent. The properties in the adsorbed phase not only differ from those in the bulk, but also depend on the position with respect to the wall. In comparison with ML and IAST, MPTA is a very descriptive model, which can be used to compute other properties besides the adsorbed amounts, such as density, pressure, and composition profiles inside the adsorbed phase. It can also be used to predict the condensation of mixtures close to the wall where the pressure increases notably and can form liquid layers on the wall.

MPTA considers that each component i , at any position z from the wall, is at chemical equilibrium with the bulk phase. For a pure component at a constant temperature, the equilibrium between the bulk phase and any point in the adsorbate is given by:

$$\mu(P(z)) - \epsilon(z) = \mu(P_b) \quad (3.17)$$

where μ is the chemical potential, $P(z)$ is the pressure at a distance z from the wall, $\epsilon(z)$ is the potential contribution emitted by the wall, and the subscript (b) refers to the bulk phase. For multicomponent mixtures, Eq. 3.17 can be extended to:

$$\mu_i(\mathbf{x}(z), P(z)) - \epsilon_i(z) = \mu_i(\mathbf{x}_b, P_b) \quad (3.18)$$

where \mathbf{x} is the vector of molar fractions (x_1, \dots, x_{N_c}). The solution of Eq. 3.18 depends on the choice of the EoS to describe fluid properties, and the choice of the wall potential function ϵ . In this work, the Peng-Robinson (PR) EoS was used [60]. The PR EoS is easy to implement and gives satisfactory results for density of hydrocarbon mixtures, which is an important property used to calculate the adsorbed amount. For the wall, the Dubinin-Radushkevich-Astakhov (DRA) potential was chosen. The DRA potential is an empirical potential introduced by Dubinin [61] to describe the adsorption of gases on active carbon, although it has been successfully applied to different adsorbents and fluids ([57, 62, 63]). It was also applied at high pressures by Monsalvo [52] obtaining low deviations. The DRA potential has the following form:

$$z(\epsilon) = z_0 \exp \left[- \left(\frac{\epsilon}{\epsilon_0} \right)_i^\beta \right] \leftrightarrow \epsilon(z) = \epsilon_0 \left(\ln \frac{z_0}{z} \right)^{1/\beta_i} \quad (3.19)$$

where z_0 is common adsorption capacity for all components, $\epsilon_{0,i}$ is the characteristic energy for the solid-fluid interaction, and β_i the scaling exponent. All three parameters are fitted from pure component experimental data and in principle, are temperature independent. It is worth noting that in the context of DRA, z is treated as the volume of a given pore, and $\epsilon(z)$ as the energy associated to that pore.

In order to solve Eq. 3.18, only the bulk pressure and composition needs to be specified. This is sufficient to determine the properties of the adsorbate at every position or pore volume z . This allows us to compute the excess adsorbed amount by integrating the density along z as follows:

$$\Gamma_i = \int_0^{z_0} (\rho_i(z)x_i(z) - \rho_b x_{b,i}) dz, \quad \Gamma_i = \frac{n_i}{A} \quad (3.20)$$

where Γ is the surface excess and A the surface area of the adsorbent. Immediately, the average composition of the adsorbed amount can be computed as follows:

$$x_i = \frac{\Gamma_i}{\sum_{i=1}^{N_c} \Gamma_i} \quad (3.21)$$

The general strategy for solving Eq. 3.18 is to discretize z (i.e. $z \rightarrow \mathbf{z} = \{z^1, \dots, z^k, \dots, \approx 0.1\text{\AA}\}$) and solve the system point-wise. It is recommended to start far away from the wall ($z^1 \approx z_0$), where the adsorbate behaves similarly to the bulk phase. Moreover, the bulk phase properties can be used as initial guess. When the first point is converged, i.e. $P(z^1)$ and $\mathbf{x}(z^1)$ are determined at position ($z \approx z_0$), a small step is taken towards the wall using the previous point as the initial guess. This procedure is repeated until z reaches an established limit to the wall. Same procedure can be used to discretize $\epsilon(z)$ instead of z . This approach avoids coarse intervals in z , especially close to the wall, where good resolution is needed for an accurate numerical integration of (Eq. 3.20).

3.2. Experimental data

Experimental measurements in shale are quite challenging to conduct due to low adsorption capacities, as well as the range of temperature and pressure the experiments are performed under. For instance, adsorption capacity in activated carbon can approximately 100 times higher than in shale. As a result, the relative accuracy for shale measurement becomes lower even without accounting for the challenging

temperature and and pressure conditions where the measurements are of interest. Gasparik et al. [23] pointed out these challenges in an inter-laboratory comparison for methane, ethane, and carbon dioxide adsorption measurements at high pressures and temperatures. Although, similar standard procedures were used by different laboratories on a shale sample from the same rock, a wide range of results were obtained as shown in Figure 3.2. Difficulties in the reproducibility of the measurements are observed especially at high pressures, which are the ones of greatest interest for shale reservoir conditions. To obtain more consistent adsorption data in shale at high pressures, standardized methods are needed to have a quality data bank. Despite big efforts are being made to obtain experimental data at high pressures in shale, the data available in literature are still limited, especially for binary systems. Nevertheless, a model comparison is useful to study their capabilities and limitations in the fitting of the pure component isotherms, and the prediction of multicomponent systems. The tested pure component data contain a total of 55

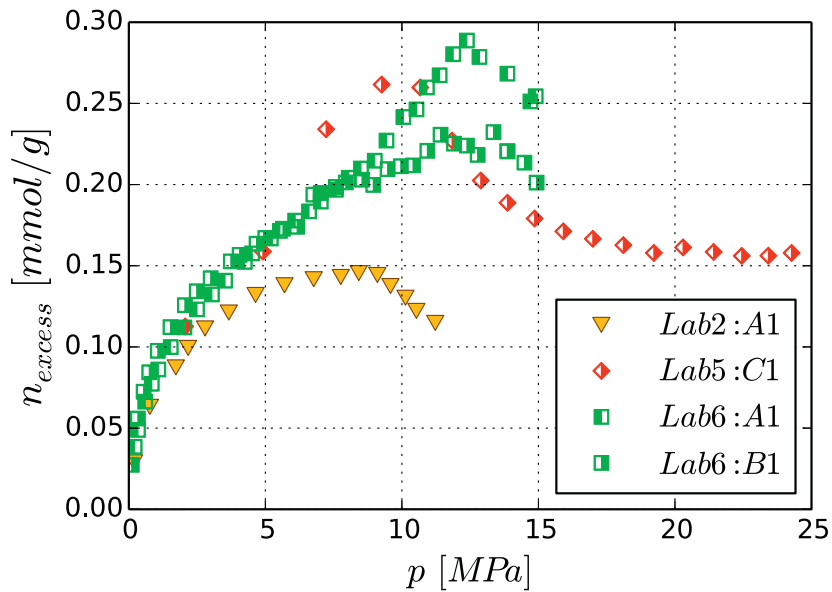


FIGURE 3.2.: Experimental adsorption measurements of CO_2 at 65°C for a N-murrian shale sample performed by different laboratories. Figure taken from Gasparik et al. [23]

isotherms for methane, ethane and CO_2 . Even though adsorption data of longer hydrocarbons are of great interest in shale, experimental data at high pressures, to the best of our knowledge, is not available in literature.

Experimental data for adsorption of mixtures in shale available in the literature is very limited. Only a limited data for binary mixtures can be found. Therefore, we

TABLE 3.1.: Experimental data for adsorption of pure components in shale.

Component	P (bar)	T (K)	Isotherms	Source
C ₁	0-250	300-473	36	[23][49][50][24, 64, 65]
C ₂	0-200	308-368	10	[23][24]*
CO ₂	0-250	308-358	9	[23][65]

* Molecular simulation

also include the molecular simulation data from [24] as experimental data. In the present work three systems were tested and are summarized in table 3.2.

TABLE 3.2.: Experimental data for adsorption of multicomponent mixtures in shale.

System	Pressure (bar)	Temperature (K)	Source
C ₁ -C ₂	0-125	313-333	[64]
C ₁ -C ₂	0-200	308-368	[24]*
C ₁ -CO ₂	0-100	308-358	[65]

* Molecular simulation

In summary the data considered are in the range of (0-200 bar) and (308-368 K). Such conditions are relevant for the study of the adsorption process at reservoir conditions.

3.3. Results

This section summarizes the capability of the three adsorption isotherm models (Langmuir, Toth-Langmuir and MPTA-DRA) to match the pure component experimental data. Moreover, the predictability of the three multicomponent adsorption models (ML, IAST, and MPTA) to represent the multicomponent experimental data are compared and discussed.

For the pure component experimental data, Figure 3.3, Figure 3.4, and Figure 3.5 show fitting examples of the C₁, C₂ and CO₂ isotherms, respectively. For the case of C₁, Figure 3.3 shows that the MPTA+DRA matches the data slightly better than the other two models. Figure 3.4 shows that for the C₂ case, both MPTA+DRA and Toth match the data quite accurately. Finally, for the CO₂ data, Figure 3.5 shows that Langmuir and Toth match the data better. It is worth mentioning that for components measured in the same shale sample the fitting must be done simultaneously since some parameters, such as the adsorbed volume (V_{ads} and z_0), belong to the adsorbent. This might introduce difficulties for pairs of components

such as C_1 and CO_2 , since the adsorption of CO_2 can be considerably greater than C_1 as shown in the three figures.

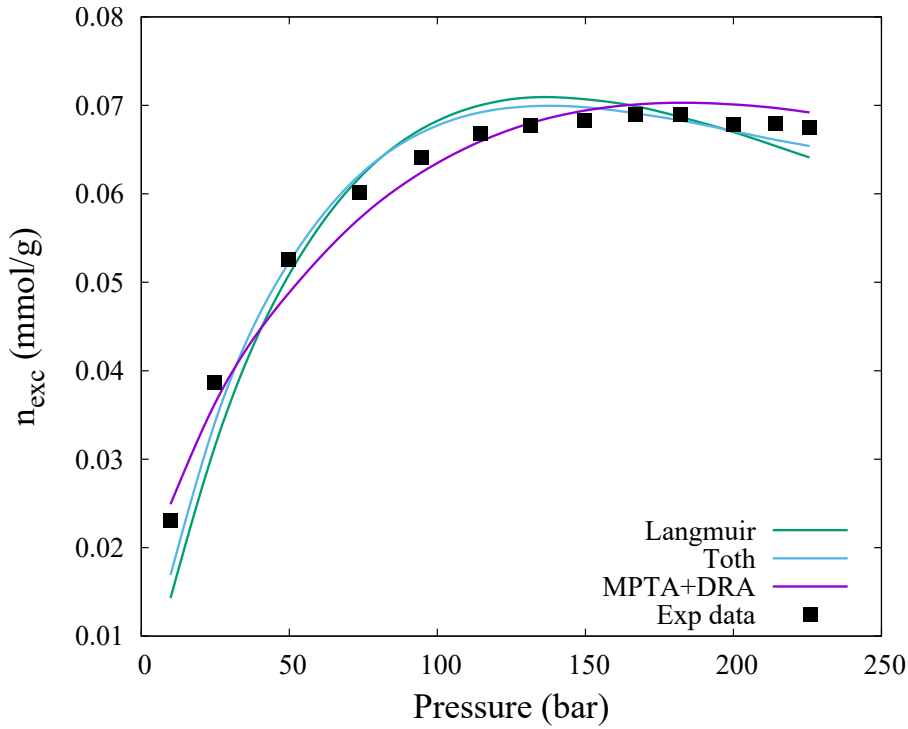


FIGURE 3.3.: Methane adsorption data fitting example for the three models. Experimental data taken from [23], sample "Namurian: Lab 5" T=338 K

The presented figures are just examples, and obviously each set of adsorption data will have different results. The summarized results for the three models are presented in Table 3.3, where the Absolute Average Deviation (AAD) is defined as follows:

$$AAD \% = \left| \frac{n - n_{exp}}{n_{exp}} \right| \times 100\% \quad (3.22)$$

TABLE 3.3.: Comparison of the three models for pure component adsorption. Fitting of data summarized in Table 3.1

Model	AAD %	No. parameters	Temperature
Langmuir	7.78	3	dependent
Toth-Langmuir	5.70	4	dependent
MPTA + DRA	9.12	3	independent

The lowest deviation is given by the Toth-Langmuir model (Eq. 3.16). Nevertheless, the difference among the three models is small and the evaluation of the models

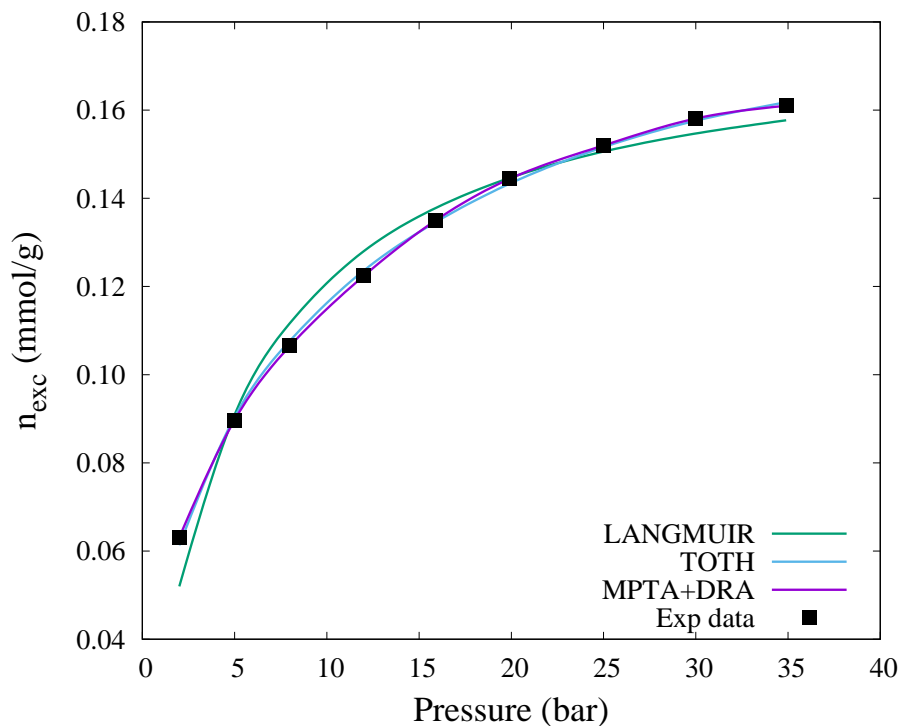


FIGURE 3.4.: Ethane adsorption data fitting example for the three models. Experimental data taken from [64]. $T=313$ K

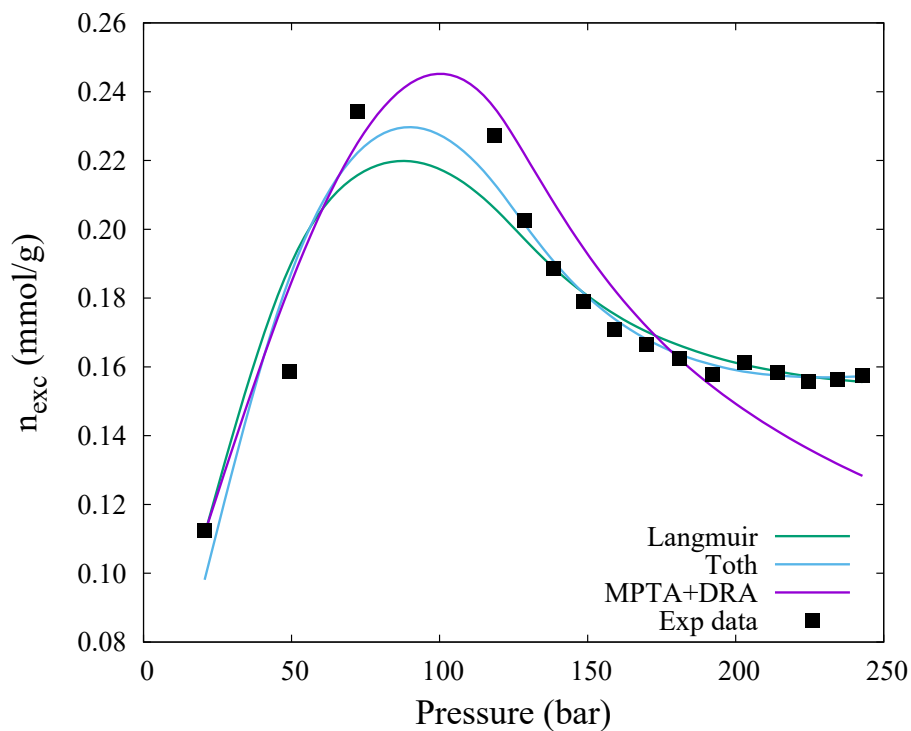


FIGURE 3.5.: CO_2 adsorption data fitting example for the three models. Experimental data taken from [23], sample "Namurian: Lab 5" $T=338$ K

should take into account other aspects of modeling. MPTA-DRA shows the advantage that the regressed parameters are temperature independent. This considerably reduces the amount of parameters when working with different components at different temperatures. Table 3.4 shows the type of parameters for each model and the total number of parameters fitted for the comparison. In summary MPTA+DRA has (N_c+2) parameters for each set of isotherms performed in the same sample. This are considerably fewer parameters in comparison with Langmuir and Toth-Langmuir that have $(2N_cN_T+1)$ and $(3N_cN_T+1)$, respectively. With N_c being the number of components and N_T the number of measured temperatures.

TABLE 3.4.: Description of the type and quantity of regressed parameters for each model.

Model	Parameter type		Total regressed parameters
	component	rock	
Langmuir	2^T	1	119
Toth-Langmuir	3^T	1	174
MPTA + DRA	1	2	65

^T Temperature dependent parameter

In principle, the temperature dependent parameters from Langmuir or Toth, can be fitted either to empirical correlations or temperature dependent thermodynamic relationships. For instance, the b equilibrium parameter is connected to the enthalpy of adsorption[66] by the following relationship:

$$b = \frac{1}{P^o} \exp\left(\frac{E_s}{R}\right) \exp\left(-\frac{E_h}{RT}\right) \quad (3.23)$$

where E_h is the enthalpy of adsorption and the temperature independent factor $\left\{\frac{1}{P^o} \exp\left(\frac{E_s}{R}\right)\right\}$ is called the entropic factor. In both cases, for empirical correlations or thermodynamic relationships, we still need to consider additional correlation parameters for the temperature dependence that will introduce an additional error.

For the mixtures, the AAD in the adsorbed amounts is presented in Table 3.5. As mentioned in the previous section, for the IAST framework, the Langmuir and the Toth models were tested for the description of the pure component isotherms. This will allow us to examine if the selection on how to model the isotherms has a big impact on the final results. It is shown that MPTA-DRA has the lowest deviation among the different models, followed by ML and IAST+Langmuir. IAST-Toth gives the highest deviation in spite of the good fitting capabilities for pure component isotherm.

TABLE 3.5.: Comparison of three models tested for the prediction of the multicomponent adsorption data summarized in Table 3.2

Model	AAD %
MPTA + DRA	17.9
IAST + Langmuir	27.0
IAST + Toth	31.7
M-Langmuir	26.1

Figure 3.7 and Figure 3.8 show the comparison of the models for a C₁-C₂ system. The comparison was made for the adsorbed amounts and also for the selectivity. The selectivity refers to the preference of the adsorbent towards a component with respect to other. It is defined as:

$$S_{i,j} = \frac{x_i/y_i}{x_j/y_j} \quad (3.24)$$

where x_i is the molar fraction in the adsorbed phase and y_i is the molar fraction in the gas phase. In Figure 3.7, the adsorbed amounts are equally well represented by all the methods, with a minor deviation for ML at high pressures. One of the reasons of the good prediction for all the models is the ability to fit the underlying pure component isotherms. Figure 3.6a and Figure 3.6b show the fitting of the pure component isotherms that were used for the binary prediction. Moreover, differences between the C₁ and C₂ isotherms, in terms of shape and magnitude of adsorption, are minor. Therefore, one could expect that the behavior of a binary mixture will not be too far from that of the pure components. On the other hand, prediction of the selectivity is not represented as satisfactory as the adsorbed amounts. IAST gives better results for the selectivity towards C₂ in the whole pressure range as shown in Figure 3.8, while ML shows low deviation at high pressures, and MPTA at low pressures.

In comparison with the magnitude of adsorption amounts presented in Figure 3.3 and Figure 3.4, the ones presented in Figure 3.7 are notably higher. This is due to the fact that the molecular simulation data taken from Collell et al. [24] is for adsorption in pure kerogen, which is considered the organic matter responsible for the adsorption in shale. Nevertheless, the shape of the adsorption isotherms of shale and pure kerogen are very similar and can be fitted quite accurately in both cases. Although, figures of the results are not shown here, the prediction of the C₁-C₂ binary mixtures in Wang et al. [64], shows to be very accurate for the three models tested.

Adsorption prediction for binary mixtures containing CO_2 does not give results as satisfactory as for the C_1 - C_2 binary system. Figure 3.10 and Figure 3.11 are examples for the predictions of a C_1 - CO_2 mixture. Visibly MPTA gives the best prediction among the tested models for the absolute adsorbed amount and also for the individual CO_2 adsorbed amount. However, in comparison with the C_1 - C_2 system, all the methods give higher deviations and none of them are accurate enough. This may be partly attributed to the difficulties found in the simultaneous pure component fitting of C_1 and CO_2 presented in Figure 3.9a and Figure 3.9b. In contrast to the C_1 - C_2 predictions, mixtures containing CO_2 are considerably more difficult. This might be attributed to different reasons. One reason might be that hydrocarbon components are similar to each other, hence the interaction with the shale or kerogen molecules is also similar. Furthermore, its pure adsorption isotherms can be fitted accurately with all the described models, increasing the confidence of a good binary prediction. Another reason, is the pressure range of the experiments. For instance, CO_2 shows a distinctive behavior after the critical pressures, yielding difficult isotherms for fitting. Therefore, different models must be evaluated in the future for the fitting of pure CO_2 data.

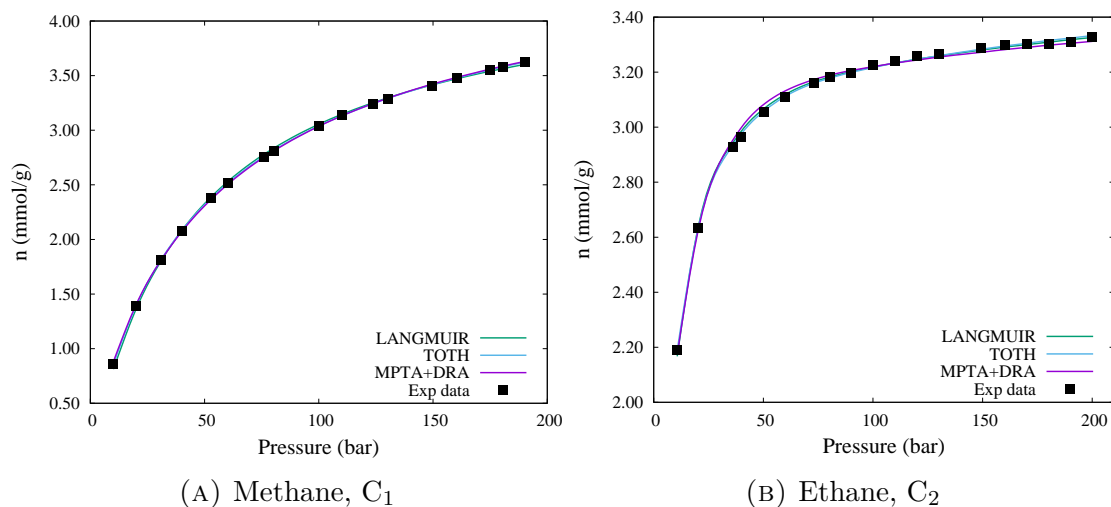


FIGURE 3.6.: Fitting of pure component data used to predict the binary system in Figure 3.11 and Figure 3.8

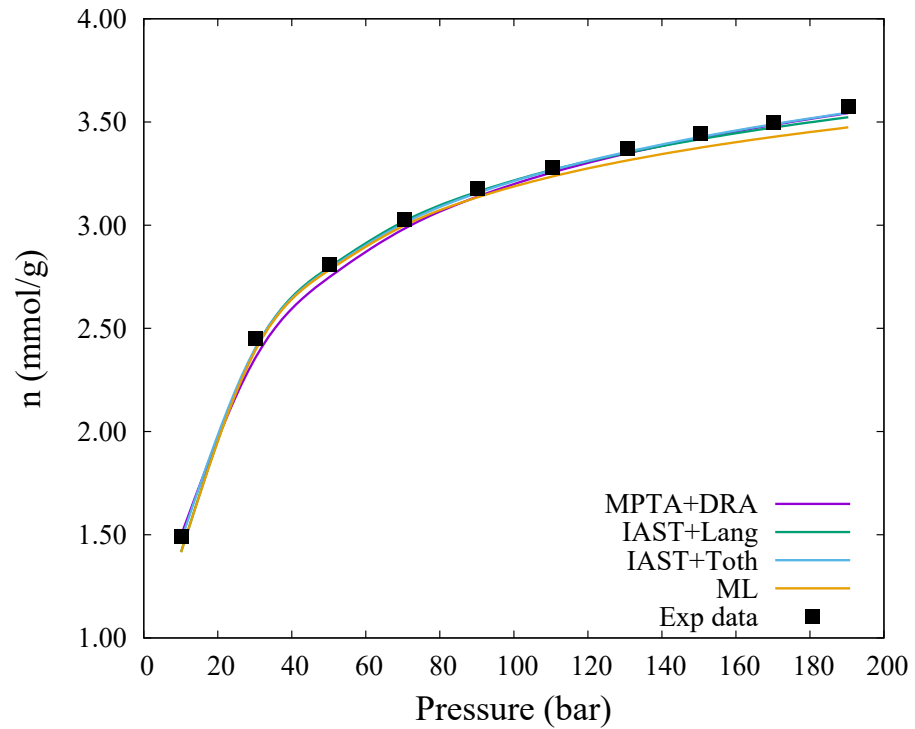


FIGURE 3.7.: Prediction of adsorbed amounts for a C_1 - C_2 mixture with a molar composition of 70%-30% [24]

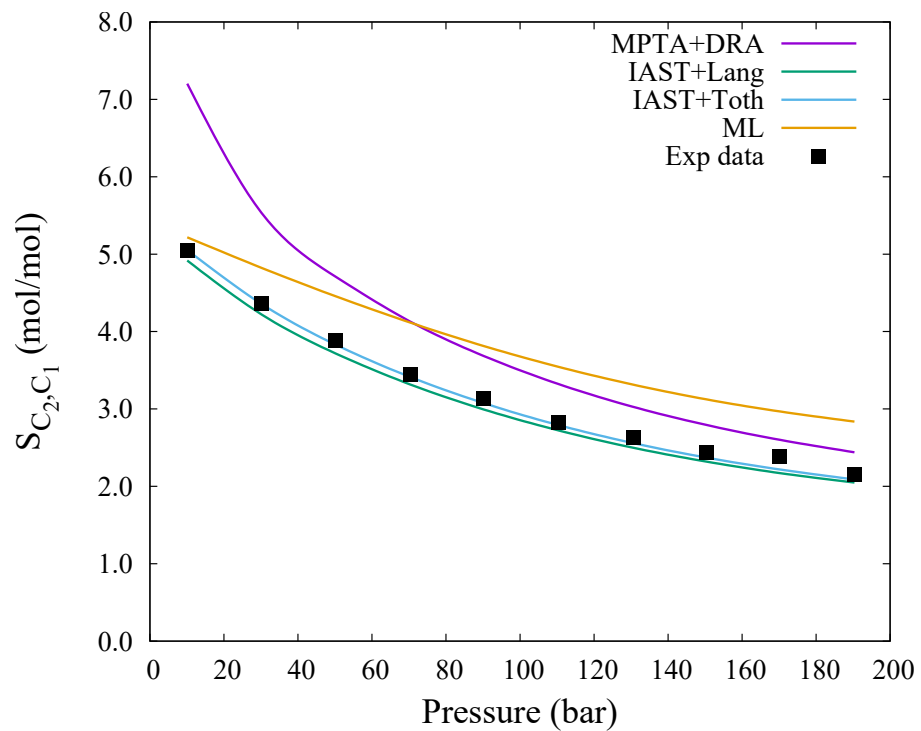


FIGURE 3.8.: Selectivity of C_2 with respect to C_1 for a C_1 - C_2 mixture with a molar composition of 70%-30% [24]

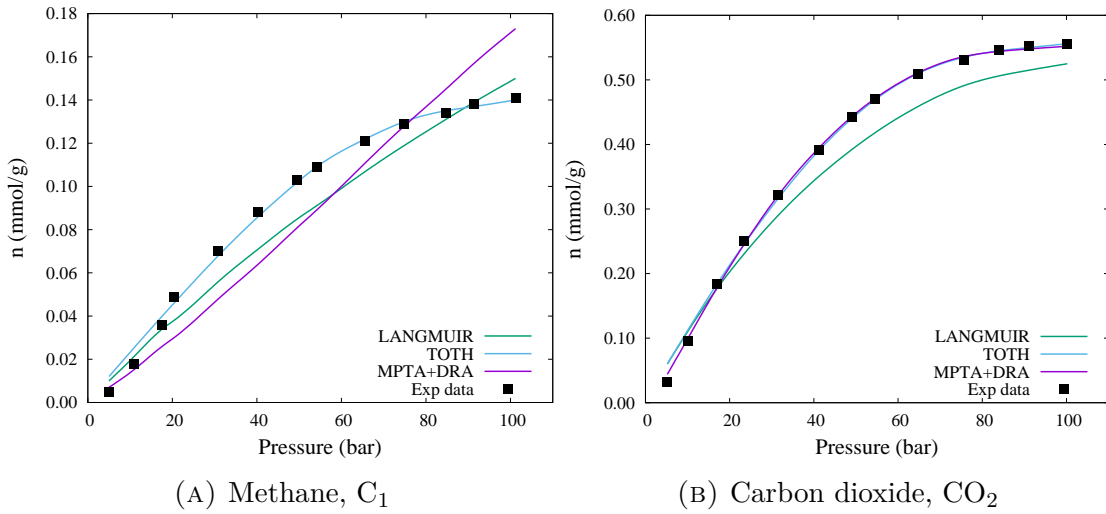


FIGURE 3.9.: Fitting of pure component data used to predict the binary system in Figure 3.7 and Figure 3.10

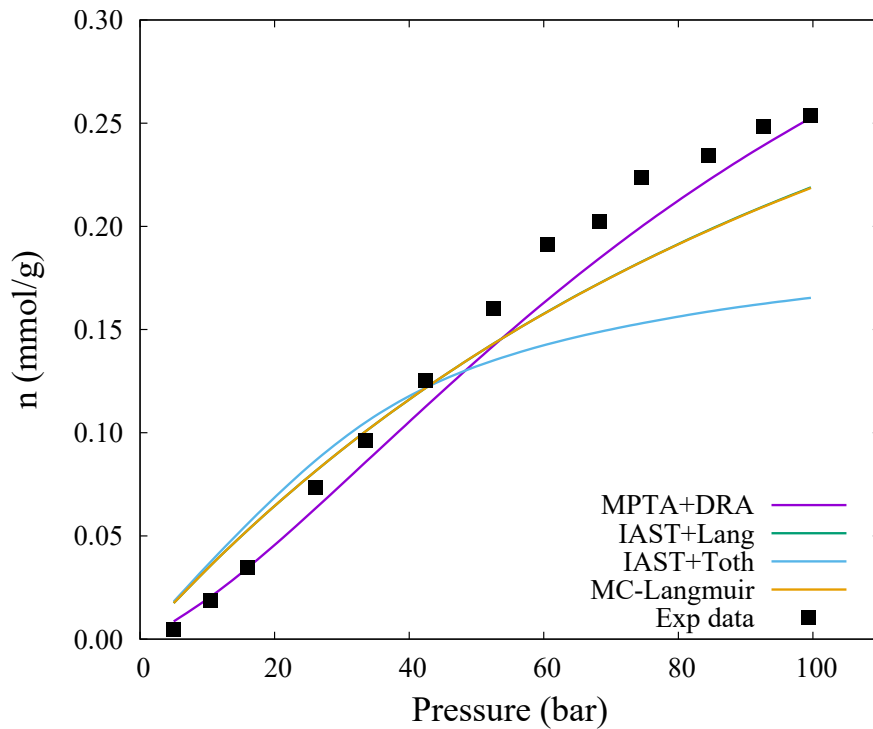


FIGURE 3.10.: Absolute adsorbed amount prediction for C_1 - CO_2 mixture with a molar composition of 80%-20%. Experimental data taken from (#3 Shale [65]).

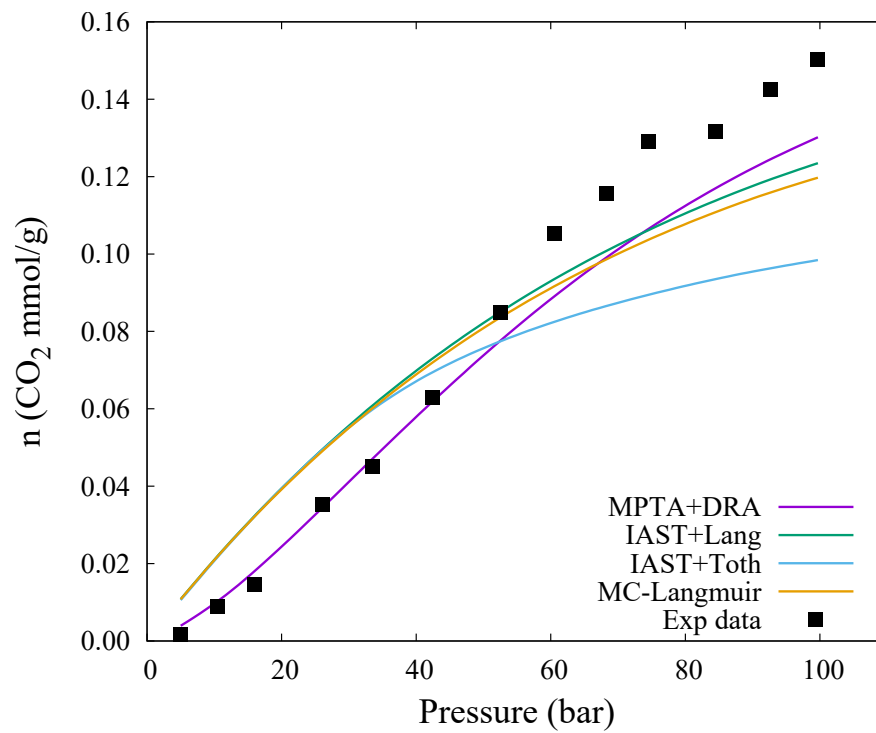


FIGURE 3.11.: CO₂ adsorbed amount prediction for C₁-CO₂ mixture with a molar composition of 80%-20%. Experimental data taken from (#3 Shale [65]).

3.4. Conclusions

A model comparison for adsorption of pure components and multicomponent mixtures in shale was presented in this chapter. Although there are limited experimental data in literature, the comparison still sheds light on how the tested models perform for shale. Their performance should also be discussed in connection with the number of parameters used, their temperature dependence and the computational cost of these models. It was found that for pure components the Langmuir, Toth, and MPTA-DRA models show comparable results with AADs lower than 10%. In spite of the computational effort required to fit the pure component adsorption isotherms, MPTA+DRA has much fewer fitting parameters in comparison with Langmuir and Toth models, for a system with different components and isotherms at different temperatures. The reason behind is the temperature dependence of the parameters in the Langmuir and Toth models, making them less predictive when applying to a wide temperature range where experimental data are not available. This advantage makes MPTA+DRA a more attractive method for describing multiple adsorption isotherms at different temperatures with a total of N_c+2 parameters.

For multicomponent systems, MPTA+DRA shows the best prediction for the adsorbed amount with an AAD of 17.9% followed by ML and IAST+Langmuir with 26.1% and 27.0%, respectively. While IAST+Langmuir shows a slightly better prediction for the composition in the adsorbed phase. Furthermore, the binary system C_1 - CO_2 shows to be considerably more challenging than the C_1 - C_2 system where all the models were able to describe adsorbed amounts and sensitivities quite satisfactorily. CO_2 data at supercritical conditions are difficult to fit with the proposed models. Moreover, the simultaneous fitting of CO_2 with a component with considerably lower adsorption capacity such as C_1 , makes the fitting process even more challenging. Additional modifications in the models, such as component independent adsorption capacities should be considered in future work to improve the results for the C_1 - CO_2 system. In summary, for the multicomponent case, MPTA+DRA is also preferred due to its better prediction capabilities. However the ML, in spite of its simplicity, gives reasonable results and should be considered into account when simple and fast simulation is required.

CHAPTER 4

Phase Equilibrium Involving Both Capillary Pressure and Adsorption

Since capillary pressure and adsorption effects exist simultaneously in porous media, it is better to include both effects in the study of phase equilibrium. For instance, an adsorption isotherm at subcritical temperatures is strongly connected to capillary condensation. The adsorption isotherm represents the saturation of small pores until a liquid film appears (phase transition) and the pore filling starts to take place. The combination of the thickening of adsorption film and the enhancement of the capillary pressure can shift the saturation pressure of the fluid in the pores.

Changes due to capillary pressure alone were presented in Chapter 2 where it was shown that the phase envelope experiences changes everywhere except in the critical point. Moreover, smaller capillary radii magnify these changes, suggesting that the contribution of the adsorption film should be evaluated. Dong et al. have recently shown that the thickness of adsorption film modifies the effective capillary radius and enhances the capillary effect[31]. Additionally, efforts in considering wall effects and adsorption into equations of state have been presented, showing deviations from conventional phase equilibrium [29, 30]. Selective adsorption may occur, modifying the composition in the bulk space of the pore causing changes in the phase behavior of the overall system. Such changes might have a big impact when preferred adsorption of specific components happens. One example is the selectivity towards heavier hydrocarbons in gas mixtures as presented in Chapter 3.

Without considering capillary pressure and compositional changes due to adsorption together, incorrect predictions on fluid properties might be obtained. In order to generate useful predictive tools, it would be ideal to have experimental adsorption data of different hydrocarbons at a wide range of temperatures and pressures. However, there is virtually no adsorption data for longer hydrocarbons in shale. Therefore, it is necessary to develop a method to estimate adsorption of heavier components in liquid rich shale reservoirs.

In this chapter, we study the effect of the capillary pressure, adsorption film, and selective adsorption in phase behavior of shale reservoirs. An analysis on the effect of the thickness of the adsorption film on the phase envelope of a mixture is presented. It is based on the phase envelope construction considering capillary pressure presented in Chapter 2. But the capillary radius is considered variable depending on the magnitude of the adsorption film thickness. MPTA is used as a tool to generate adsorption data of various hydrocarbons of which experimental data is currently not available. Additionally, a new algorithm for flash calculations inside shale reservoirs, involving both capillary pressure and selective adsorption is presented. The algorithm is used to analyze how the phase equilibrium changes at different regions of the phase envelope.

4.1. Phase Envelope Including Capillary Pressure and Adsorption Film

For a system under a capillary pressure difference, the phase equilibrium changes everywhere except at the critical point (Chapter 2). If we consider an adsorbed phase in the system, its film thickness will reduce the effective capillary radius increasing the pressure difference between the phases as shown by [31]. In order to evaluate the effect of the adsorption film on the phase envelope the following system of equations is solved:

$$\left\{ \begin{array}{l} \ln K_i + \ln F_i^g(T, P_g, \mathbf{y}) - \ln F_i^l(T, P_l, \mathbf{x}) = 0; \quad i = 1, \dots, N_c \\ \sum_{i=1}^{N_c} (y_i - x_i) = 0 \\ P_l - P_g + \frac{2\sigma \cos \theta}{r_c} = 0 \end{array} \right. \quad (4.1)$$

coupled with:

$$r_c = r - t_a \quad (4.2)$$

where K_i is the equilibrium constant for component i , T is the temperature, P_l is the pressure in the liquid phase, P_g is the pressure in the gas phase, σ is the interfacial tension, r is the pore radius, r_c is the effective capillary radius, and t_a is the thickness of the adsorption film. The system in (Eq. 4.1) can be solved for each point of the phase envelope at a given r_c by the method presented in Chapter 2. After (Eq. 4.1) is converged for each r_c , the thickness t_a is then updated in an outer loop. The solution is finally reached by means of successive substitution. The thickness of the adsorption film is calculated using the following relationship:

$$t_a = \frac{n^{abs}}{\rho_{ads}A} \quad (4.3)$$

where n^{abs} is the absolute adsorbed amount, ρ_{ads} the density in the adsorbed phase, and A is the surface area of the adsorbent. At the saturation point, the density of the adsorbed phase is close to the density of the liquid phase ρ_l . Therefore, ρ_{ads} can be approximated in by ρ_l in (Eq. 4.3). The adsorbed amount n , is calculated by using the ML model in (Eq. 3.3) yielding:

$$t_a = \frac{1}{\rho_l A} \left[\sum_{i=1}^{N_c} n_i^{max}(T) \frac{b_i(T) f_i}{1 + \sum_{j=1}^{N_c} b_j(T) f_j} \right] \quad (4.4)$$

The ML is easy to implement and the computational cost is low but has the drawback that the equilibrium parameters b_i and n_i^{max} must be known in advance at different temperatures. As presented in Chapter 3, the experimental data in shale are very limited, making it difficult to apply to the whole range of temperature of the phase envelope. In contrast, MPTA is computationally expensive, but the adjustable parameters are temperature independent. Therefore, it can in principle be applied to the whole range of temperature of the phase envelope.

An alternative solution to get the computational benefit of ML and the flexibility of MPTA is proposed in this work. MPTA is employed to generate artificial adsorption isotherms at different temperatures, and the generated data are then used to fit the Langmuir parameters in ML. In this way, it is possible to get the temperature dependent ML parameters for each pure component. Allowing an interpolation of the temperature dependent parameters at the desired temperature. The detailed procedure is presented in the following section 4.2.

A C₁-C₄ system was tested at two molar concentrations: 70%-30% and 30%-70%. Figure 4.1 shows the results. It can be seen that the adsorption film enhances the effect of the capillary pressure in the phase envelope, especially in the bubble point branch. Table 4.1 and Table 4.2 show the calculated adsorption thickness for both systems at different temperatures along the bubble point. The adsorption film is more relevant in regions farther away from the critical point where the surface tension is higher, and even a small difference in the effective capillary radius can be of importance. Close to the critical point, the effect of the adsorption film is very small. Near the critical point, the interfacial tension is close to zero corresponding to a very small capillary pressure difference. Therefore, changes in the saturation pressure/temperature will be negligible. Moreover, it is important to notice that a very small radius of $r_c = 3 \text{ nm}$ is intentionally selected to test the effect of the adsorption in film in limiting cases. This means that for bigger radii of interest, the effect would be even smaller, thus, negligible. On the other hand, Dong et al. [31] showed a similar calculation considering the effect of the adsorption film in phase equilibrium, showing considerable changes close to the critical point. They assumed that the pure component critical properties used in the thermodynamic models should be changed by the confinement. With this artificial change of model parameters, the obtained phase envelopes are significantly smaller and the critical points are also shifted. However, there is not enough ground for the artificial adjustment of the critical properties in our opinion. Therefore, for purposes of this work, the critical properties for the bulk phases are kept unchanged.

TABLE 4.1.: Thickness of the adsorption film (t_a), interfacial tension (σ), and capillary pressure (P_c) for C₁-C₄ 70%-30% mixture shown in Figure 4.1. AF:Adsorption Film.

T	t_a (nm)	σ (mN/m)		P_c (bar)	
		$(r_c = 3 \text{ nm})$	$(r_c = 3 \text{ nm}) + \text{AF}$	$(r_c = 3 \text{ nm})$	$(r_c = 3 \text{ nm}) + \text{AF}$
200	0.467	2.549	2.573	16.993	20.33
250	0.453	0.191	0.217	1.270	1.705
300	0.526	0.004	0.004	0.023	0.034

4.2. Artificial Adsorption Data from MPTA

Adsorption literature data in shale are only available, to the best of our knowledge, for methane, ethane, and CO₂. Therefore, we must seek for alternatives to generate reasonable adsorption isotherms for higher hydrocarbons at different temperatures

TABLE 4.2.: Thickness of the adsorption film (t_a), interfacial tension (σ), and capillary pressure (P_c) for C₁-C₄ 30%-70% mixture shown in Figure 4.1. AF:Adsorption Film.

T	t_a (nm)	σ (mN/m)		P_c (bar)	
		($r_c = 3 \text{ nm}$)	($r_c = 3 \text{ nm}$) + AF	($r_c = 3 \text{ nm}$)	($r_c = 3 \text{ nm}$) + AF
200	0.466	3.398	3.418	22.650	26.99
250	0.451	1.818	1.810	12.120	14.18
300	0.474	0.795	0.780	5.329	6.13
350	0.538	0.185	0.187	1.236	1.50

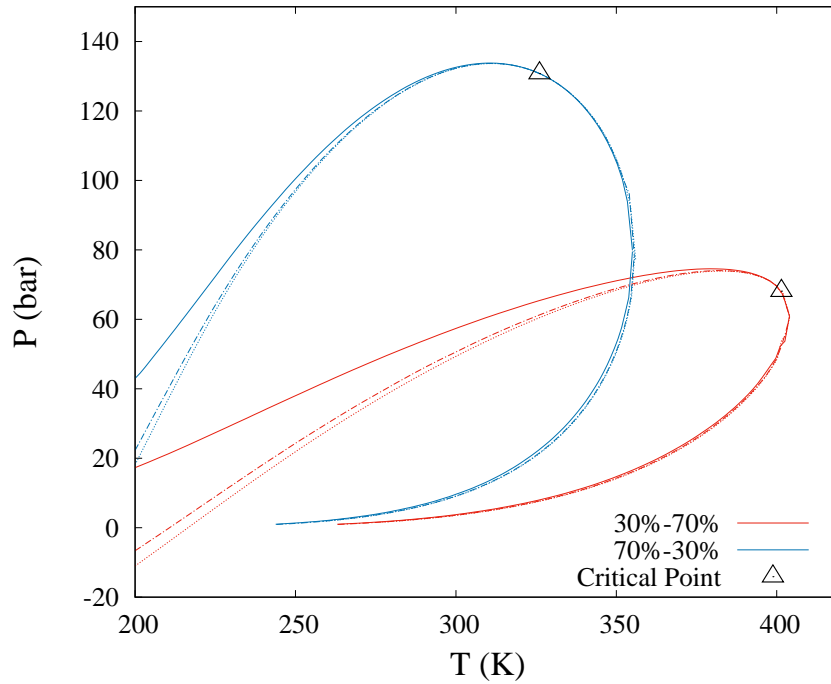


FIGURE 4.1.: Phase envelope of two C₁-C₄ mixtures at different compositions. The solid line (—) represents the normal phase envelope; the dashed line (— · —) considering P_c with effective capillary radius $r_c = 3 \text{ nm}$; and the dotted line (···) considering P_c +Adsorption with a total radius of $r = 3 \text{ nm}$ and variable effective capillary radius $r_c = r - t_a$. The surface area considered was $A = 28 \text{ m}^2/\text{g}$

in order to study reservoir fluid mixtures containing these hydrocarbons. An alternative approach to obtain such data is presented in this section. It is based on MPTA predictions of alkane adsorption using extrapolated data from methane and ethane.

The adsorption data from Wang et al. [64] are used as a starting point in order to obtain necessary parameters of a shale sample, such as adsorption volume z_0 , scaling exponent β and rock-fluid interactions parameters ϵ_{0i} for methane and ethane. All the parameters were fitted simultaneously, and are summarized in Table 4.3. Figure

4.2 shows the fitting of MPTA for the methane and ethane adsorption data. The absolute average deviation obtained is of 5.82%, which is quite satisfactory considering that all the parameters are temperature independent.

MPTA parameter	Value
$z_0 \left(\frac{\text{mm}^3}{\text{g}} \right)$	11.23
β	1.02
$C_1, \epsilon_{0_i}/R \text{ (K)}$	506.6
$C_2, \epsilon_{0_i}/R \text{ (K)}$	724.8

TABLE 4.3.: MPTA fitting parameters corresponding to data in Figure 4.2

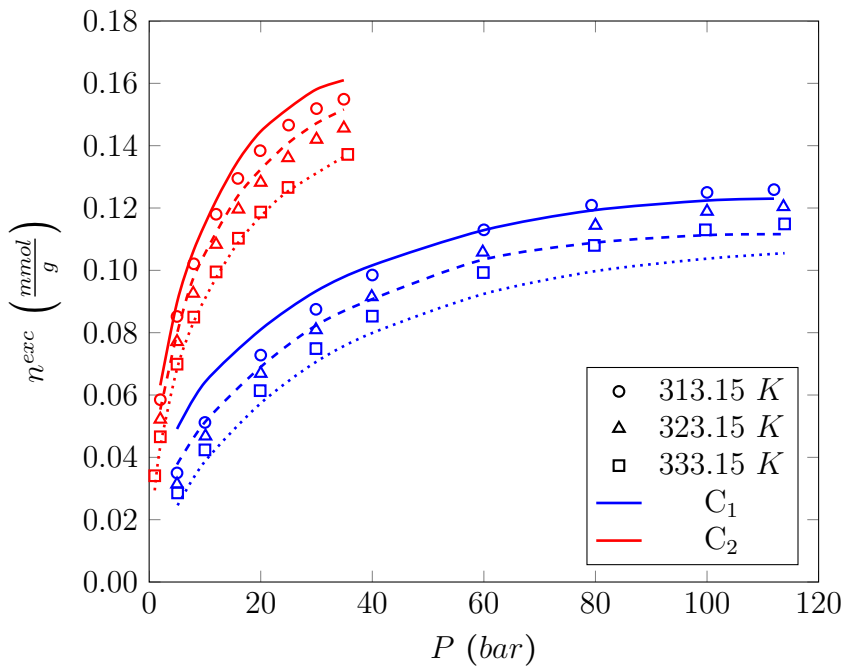


FIGURE 4.2.: Adsorption data from Wang et al. [64] fitted with MPTA.

The only parameter that is dependent on the fluid is adsorption energy term ϵ_{0_i} , the other parameters (z_0, β) correspond to the rock itself. This means that if one can estimate the energy terms for different hydrocarbons, it is possible to generate adsorption predictions since the rock parameters are not going to change. Previous studies have shown that for alkanes, the energy term increases as the carbon number increases [57]. This can be seen in Figure 4.3.

Since there are no adsorption data for alkanes longer than ethane, we have to extrapolate the energy parameters based on the methane and ethane parameters. We are aware of the inaccuracy associated with the extrapolation. Nonetheless, it should

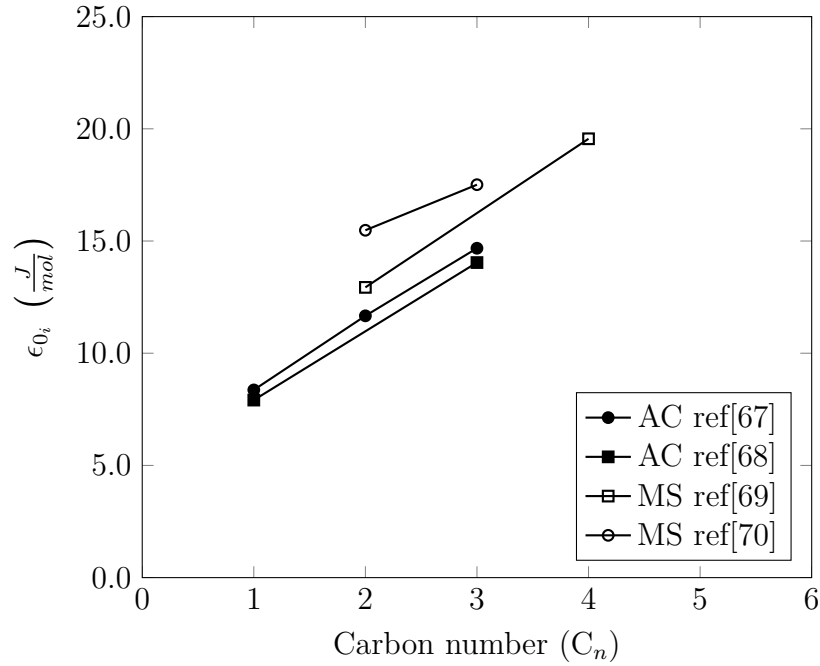


FIGURE 4.3.: Energy term as a function of the carbon number in alkanes (Monsalvo and Shapiro [57]). Adsorbents: Activated Carbon (AC) and Molecular Sieves (MS)

capture the increasing fluid-wall interaction energy term with the chain length. Table 4.4 shows a linear extrapolation of the energy parameter for alkanes used in this study.

Alkane	ϵ_{0_i}/R (K)
C ₁	506.6
C ₂	724.8
C ₄	1161.2
C ₈	2034.0
C ₁₀	2470.3
C ₁₂	2906.7
C ₁₆	3779.5

TABLE 4.4.: Extrapolated energy parameters for different alkanes

Artificial adsorption data, using MPTA and the energy parameters in Table 4.4, are presented in Table A.3 to Table A.38 in Appendix A. These data were subsequently fitted using Langmuir isotherms as functions of the fugacity.

$$n^{abs} = n^{max} \frac{bf}{1 + bf} \quad (4.5)$$

The fitting parameters are summarized in Table 4.5. With the parameters fitted at different temperatures, it is possible to interpolate these values to the desired temperature. However, it is even better to find some regular trends for the temperature dependent parameters rather than to use a simple linear interpolation. The maximum uptake (n^{max}) shows a linear trend with the temperature, and the equilibrium constants (b) follow an exponential relationship:

$$n_i^{max}(T) = m_i T + c_i, \quad \ln b_i(T) = \ln A_i - \frac{E_{h_i}}{R} \left(\frac{1}{T} \right) \quad (4.6)$$

where E_h is the enthalpy of adsorption and the temperature independent factor $\ln A$ is called the entropic factor $\left\{ A = \frac{1}{P^o} \exp\left(\frac{E_s}{R}\right) \right\}$. Table 4.6 shows that excellent fittings can be obtained for the different alkanes using (Eq. 4.6).

In summary, we obtained four parameters ($a_i, b_i, \ln A_i, E_{h_i}/R$) for each component that describe the Langmuir isotherms in a wide range of temperatures (223K – 573K). This result is easy and fast to implement with the ML, thus, gaining computational advantages over a direct incorporation of MPTA while still describing a similar adsorption behavior over the whole temperature and pressure range.

TABLE 4.5.: Summary of Langmuir fittings for the artificial data.

Alkane	T (K)	n^{max}	b (bar ⁻¹)	RMS ($\frac{mmol}{g}$)	AAD
C ₁	223.15	3.37·10 ⁻¹	8.16·10 ⁻²	1.24·10 ⁻²	9.4%
	323.15	2.85·10 ⁻¹	1.93·10 ⁻²	7.14·10 ⁻³	15.5%
	373.15	2.71·10 ⁻¹	1.15·10 ⁻²	5.21·10 ⁻³	17.5%
	423.15	2.61·10 ⁻¹	7.60·10 ⁻³	3.66·10 ⁻³	17.8%
	473.15	2.53·10 ⁻¹	5.49·10 ⁻³	2.53·10 ⁻³	16.8%
C ₂	573.15	2.16·10 ⁻¹	4.15·10 ⁻³	1.83·10 ⁻³	9.0%
	223.15	2.46·10 ⁻¹	2.05·10 ⁰	1.37·10 ⁻²	7.0%
	323.15	2.34·10 ⁻¹	9.86·10 ⁻²	7.81·10 ⁻³	7.8%
	373.15	2.19·10 ⁻¹	5.07·10 ⁻²	6.32·10 ⁻³	10.5%
	423.15	2.06·10 ⁻¹	3.01·10 ⁻²	5.25·10 ⁻³	12.6%
C ₄	473.15	1.95·10 ⁻¹	1.93·10 ⁻²	4.38·10 ⁻³	14.5%
	573.15	1.81·10 ⁻¹	9.58·10 ⁻³	2.83·10 ⁻³	17.0%
	323.15	1.40·10 ⁻¹	2.26·10 ⁰	5.82·10 ⁻³	2.5%
	373.15	1.37·10 ⁻¹	5.07·10 ⁻¹	5.65·10 ⁻³	3.3%
	423.15	1.32·10 ⁻¹	2.16·10 ⁻¹	5.45·10 ⁻³	6.0%
C ₈	473.15	1.26·10 ⁻¹	1.19·10 ⁻¹	4.99·10 ⁻³	8.2%
	573.15	1.13·10 ⁻¹	5.31·10 ⁻²	3.87·10 ⁻³	11.4%
	323.15	7.09·10 ⁻²	3.97·10 ²	4.58·10 ⁻³	4.0%
	373.15	6.95·10 ⁻²	6.61·10 ¹	8.66·10 ⁻³	16.8%
	423.15	6.79·10 ⁻²	1.88·10 ¹	8.18·10 ⁻³	25.3%
C ₁₀	473.15	6.64·10 ⁻²	6.72·10 ⁰	6.75·10 ⁻³	21.9%
	573.15	6.26·10 ⁻²	1.86·10 ⁰	6.01·10 ⁻³	38.7%
	323.15	5.69·10 ⁻²	2.26·10 ³	1.03·10 ⁻³	1.7%
	373.15	5.49·10 ⁻²	4.66·10 ²	3.80·10 ⁻³	5.1%
	423.15	5.41·10 ⁻²	1.09·10 ²	6.78·10 ⁻³	16.1%
C ₁₂	473.15	5.31·10 ⁻²	2.09·10 ¹	5.45·10 ⁻³	14.6%
	573.15	5.10·10 ⁻²	6.50·10 ⁰	5.60·10 ⁻³	22.9%
	323.15	4.60·10 ⁻²	2.20·10 ⁴	9.60·10 ⁻⁴	1.6%
	373.15	4.53·10 ⁻²	3.69·10 ³	4.37·10 ⁻³	8.4%
	423.15	4.48·10 ⁻²	3.41·10 ²	4.02·10 ⁻³	7.8%
C ₁₆	473.15	4.43·10 ⁻²	4.86·10 ¹	4.81·10 ⁻³	10.9%
	573.15	4.31·10 ⁻²	1.22·10 ¹	4.92·10 ⁻³	20.2%
	323.15	3.23·10 ⁻²	1.44·10 ⁶	1.20·10 ⁻³	1.5%
	373.15	3.22·10 ⁻²	2.96·10 ⁴	4.10·10 ⁻³	7.5%
	423.15	3.19·10 ⁻²	4.63·10 ³	6.18·10 ⁻³	21.5%
C ₁₆	473.15	3.16·10 ⁻²	1.41·10 ³	5.87·10 ⁻³	31.6%
	573.15	3.10·10 ⁻²	2.98·10 ²	4.83·10 ⁻³	48.1%

TABLE 4.6.: Summary of the fitting for the Langmuir temperature dependent parameters.

Alkane	$\frac{E_b}{R}$ (K)	$\ln A$	R^2	m ($\frac{mmol}{g \cdot K}$)	c ($\frac{mmol}{g}$)	R^2
C ₁	-1115.9	-7.48	0.997	-2.66·10 ⁻⁴	0.3985	0.963
C ₂	-1947.9	-8.13	0.996	-2.13·10 ⁻⁴	0.2931	0.981
C ₄	-2758.5	-7.91	0.987	-1.09·10 ⁻⁴	0.1769	0.985
C ₈	-3989.1	-6.44	0.998	-3.32·10 ⁻⁵	0.0818	0.996
C ₁₀	-4502.1	-6.11	0.990	-2.24·10 ⁻⁵	0.0637	0.978
C ₁₂	-5871.2	-8.00	0.984	-1.14·10 ⁻⁵	0.0496	0.997
C ₁₆	-6189.2	-5.68	0.965	-5.41·10 ⁻⁶	0.0341	0.983

4.3. Flash Calculations Involving Both Capillary Pressure and Adsorption

Isothermal flash calculations are perhaps the most important phase equilibrium calculations in practical applications. They are at the core of compositional reservoir simulations and many process engineering tools to determine the equilibrium phase composition and properties at specified pressure and temperature. Incorporation of the adsorption effects and capillary pressure in isothermal flash is essential to the analysis of phase equilibrium inside shale reservoirs, and inside confined systems in general.

The system to be dealt with in this section is depicted by Figure 4.4. It shows a fluid inside a pore with specific surface area A and void volume V . Although a cylindrical geometry is shown, the method we propose can be applied to any system with a known void volume and specific surface area. A total of three phases are present in the system: a liquid phase, a gas phase, and an excess adsorbed phase. A capillary pressure difference P_c is accounted for across the interface of the liquid and gas phases. The goal is to determine the phase fractions and compositions of the adsorbed phase, liquid phase and gas phase in the system at a specified pressure P , temperature T , and overall composition \mathbf{z}^f .

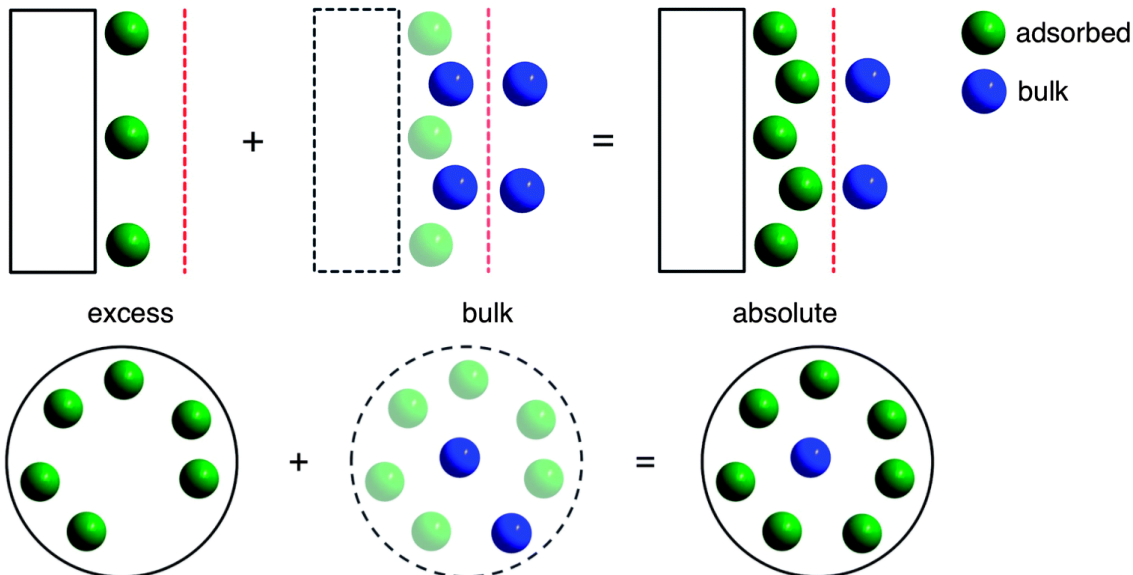


FIGURE 4.4.: Blue spheres correspond to the bulk phases (gas and liquid), and green spheres correspond to the excess adsorbed phase. The first blue/green layer next to the wall corresponds to the absolute adsorbed layer. Figure taken from Mason et al. [71]

Phase equilibrium in the system is assumed. Therefore, we can write that the fugacity (and chemical potential) of each component in the liquid, gas and adsorbed phase is the same.

$$f_i^g = f_i^l = f_i^a \quad (4.7)$$

where f_i^α is the fugacity of component i in phase α . Throughout the entire chapter the superscripts g , l and a would be used for the gas, liquid and adsorbed phases respectively. The system is subject to mass balance constraints:

$$z_i^f = \theta^g y_i + \theta^l x_i + \theta^a w_i \quad (4.8)$$

where z_i^f is the normalized feed composition, y_i and θ^g are the molar compositions and molar phase fraction in the vapor phase respectively; x_i and θ^l in the liquid phase; and w_i and θ^a in the excess adsorbed phase. The summation of the phase fractions must sum to unity

$$\theta^l + \theta^g + \theta^a = 1 \quad (4.9)$$

and the molar compositions in each phase must also sum to unity.

$$\sum_i y_i = \sum_i x_i = \sum_i w_i = 1 \quad (4.10)$$

For the mass balance, it is advantageous to use the excess adsorbed phase fraction instead of the absolute one. By referring to Figure 4.4 we can notice that the space inside the cylinder is filled by the bulk phases in the middle and the absolute adsorbed phase attached to the wall. Furthermore, to delimit the space that corresponds to the adsorbed phase and the bulk phases, it is necessary to introduce an assumption on the thickness of the adsorbed layer. However, this issue can be avoided by utilizing the excess adsorbed phase fraction (green spheres in Figure 4.4), instead of the absolute adsorbed phase fraction (first layer next to the wall). In this way, there is no need to introduce a reference, since the excess adsorbed phase will occupy empty spaces that the bulk phase would not occupy in the absence of an adsorbed phase. This is clearly shown in the left-hand side of Figure 4.4.

Another constraint arises from the mechanical equilibrium between the oil and gas phases. In this section, the thickness of the adsorption film was neglected in the contribution of the capillary pressure. Hence, the pore radius and effective capillary radius are the same $r = r_c$. Furthermore, the Young-Laplace equation in a tube is

employed to describe the capillary pressure difference

$$P_c = P^g - P^l = \frac{2\sigma}{r_c} \quad (4.11)$$

where P_c is the capillary pressure, P^g the pressure in the gas phase, P^l the pressure in the liquid phase (wetting phase), and σ is the interfacial tension, which for this work was calculated using the Sugden and Macleod model, commonly known as the parachor method.

$$\sigma = \left[\sum_i \chi_i (x_i \rho^l - y_i \rho^g) \right]^4 \quad (4.12)$$

where χ_i are the parachor constants, ρ^l and ρ^g are the molar densities in (mol/cm^3), and σ is the interfacial tension in ($dyne/cm^3$).

The adsorbed phase is always present in the system regardless of the number of bulk phases (i.e. liquid and gas). Physically, this phase is dependent on the other phases. For the scope of this study, the adsorbed phase exists as long as there is a bulk phase present. Consequently, the adsorbed amount is modeled as a function of the fugacity of one of the phases of the bulk phase (f^b). We can therefore write:

$$\Gamma_{exc} = \Psi(f^b) \quad (4.13)$$

where Γ_{exc} is the surface excess (n_{exc}/A) and it represents the amount in excess to the bulk, and Ψ represents the model used for the adsorbed phase. For this work it refers to ML. The input fugacity in Γ_{exc} can be either the gas or liquid fugacity if both phases are present in the system.

4.3.1. Methodology

In principle, the system can be solved with a nested robust isothermal flash updating the adsorbed amounts in an outer loop. However, we found that it is more convenient and efficient to couple adsorption calculations with the bulk equilibrium calculations. The developed algorithm follows the methodology used for the two-phase flash algorithm by Michelsen [41] with various adjustments to account for the capillary pressure difference and the composition changes in the bulk phase due to adsorption. The bulk phases were modeled with the Peng-Robinson (PR) equation of state, and the adsorbed phase was modeled using the Multicomponent-Langmuir (ML).

Direct Substitution

The Wilson equilibrium factors were employed as a starting point with the gas or liquid pressure as the desired input.

$$\ln K_i = \ln \frac{P_{c_i}}{P} + 5.737(1 + w_i) \left(1 - \frac{T_{c_i}}{T}\right) \quad (4.14)$$

where T_{c_i} , P_{c_i} and w_i are the critical temperature, critical pressure and acentric factor for component i . The calculation is followed by solving the Rachford-Rice equation iteratively with the corresponding update of the fugacity coefficients, capillary pressure and total bulk composition changes at each step. The Rachford-Rice can be written as follows:

$$g(\beta) = \sum_i z_i^b \frac{K_i - 1}{1 - \beta + \beta K_i} = 0 \quad (4.15)$$

where β is the relative vapor fraction in the bulk phase, \mathbf{z}^b is the total composition of the bulk phase, and K_i are the equilibrium factors. The relative vapor fraction β is not the equivalent to the absolute fraction θ^g , both are related through the following equation:

$$\beta = \frac{\theta^g}{\theta^g + \theta^l} \quad (4.16)$$

Updates of capillary pressure P_c , bulk composition \mathbf{z}_b and equilibrium factors K_i at each solution of (Eq. 4.15) are required. The capillary pressure is computed using (Eq. 4.11) and the update of the phase pressures is done.

$$P^g = P^l + P_c \quad \text{or} \quad P^l = P^g - P_c \quad (4.17)$$

where P^g is updated if the pressure of the liquid is the input pressure, and P^l if the pressure of the gas is the input. It can be noted that at high values of P_c and small values of P_g the update in the liquid pressure can be negative. Therefore, throughout the calculation, it is always recommended to use the product of the pressure and fugacity coefficient (i.e. $F_i^\alpha = P^\alpha \varphi_i^\alpha$), instead of the fugacity coefficients φ_i^α alone. After the capillary pressure update, the K_i values are updated as follows:

$$K_i = \frac{F_i^l(T, P^l, \mathbf{x})}{F_i^g(T, P^g, \mathbf{y})} \quad (4.18)$$

The last variable to be updated is the total bulk composition. The total composition in the bulk phase will change at each step since some components will be adsorbed to

the surface. By subtracting the components of the adsorbed phase from the overall feed composition we get:

$$z_i^b = \frac{z_i^f - \theta^a w_i}{1 - \theta^a} \quad (4.19)$$

where \mathbf{z}_b is the overall bulk composition (i.e. the liquid and gas phase together). The composition of the adsorbed phase is obtained from (Eq. 4.13) using the liquid fugacity, gas fugacity, or an average of both. This is allowed during intermediate calculations since at the solution both the liquid and gas phases will have the same fugacity. The absolute molar fractions \mathbf{x}^{abs} can be obtained straightforward with the ML model

$$n_i^{abs} = n_i^{max}(T) \frac{b_i(T) f_i}{1 + \sum_{j=1}^{Nc} b_j(T) f_j} \quad \rightarrow \quad x_i^{abs} = \frac{n_i^{abs}}{\sum_j n_j^{abs}} \quad (4.20)$$

However, to obtain the composition \mathbf{w} in the excess adsorbed phase we have to make the correction for the excess amounts.

$$n_i^{exc} = n_i^{abs} - z_i^b \rho^b V^{ads} \quad \rightarrow \quad w_i = \frac{n_i^{exc}}{\sum_j n_j^{exc}} \quad (4.21)$$

where V^{ads} is obtained by fitting the excess adsorption data of pure components with MPTA ($z_0 = V^{ads}$) or (Eq. 3.2) in Chapter 4, and ρ^b is the overall density in the bulk phase

$$\rho^b = \frac{1}{\beta V_m^g + (1 - \beta) V_m^l} \quad (4.22)$$

where V_m^l and V_m^g are the molar volumes of the liquid and gas phase respectively.

The molar fraction of the excess adsorption phase θ^a in (Eq. 4.19) is not determined yet. As will be shown below, it can be expressed using relationships between the phase molar densities or volumes, and the geometry of the system. Since our calculation is done at constant pressure, the volume is allowed to change, but the ratio of the surface area to the void volume is assumed to remain constant. We can make use of the geometrical properties of the system to rewrite the surface area, and the volume of the system as follows:

$$A = \frac{n^{exc}}{\Gamma^{exc}} \quad , \quad V = n^b \bar{V}_m \quad (4.23)$$

where Γ^{exc} is the surface excess (excess adsorbed moles per unit area) ; \bar{V}_m is the molar volume of the bulk, n^b are the moles in the bulk phase, and n^{exc} the moles in

the excess phase ($n^T = n^{exc} + n^b$). The molar volume of bulk refers to the average molar volume of the liquid and gas phases

$$\bar{V}_m = \beta V_m^g + (1 - \beta) V_m^l \quad (4.24)$$

where β is the relative vapor fraction in (Eq. 4.16). Moreover, (Eq. 4.23) and (Eq. 4.24) can be used to express the geometric factor of the porous system $G_f = A/V$ as follows:

$$G_f = \frac{n^{exc}/\Gamma^{exc}}{n^b \bar{V}_m} = \frac{\theta^a}{(1 - \theta^a) \Gamma^{exc} \bar{V}_m} \quad (4.25)$$

The geometric factor is constant for a specific porous system. For a cylinder is $\frac{2}{r_c}$. Solving for the excess adsorbed fraction we obtain

$$\theta^a = \frac{G_f \bar{V}_m \Gamma^{exc}}{1 + G_f \bar{V}_m \Gamma^{exc}} \quad (4.26)$$

With (Eq. 4.26), the update in (Eq. 4.19) is completed. It is worthwhile to notice that the surface amount of component i in the excess adsorbed phase Γ_i^{exc} can be negative in cases where there is a higher concentration of one component in the bulk phase than in the excess adsorbed phase

$$n_i^{exc} = n_i^{ads} - z_i^b \rho^b V^{ads} < 0 \quad (4.27)$$

This shows that the excess adsorbed phase is merely an hypothetical concept instead of a separate physical entity. The mole fractions in this hypothetical phase fulfill the mass balance equations and are not directly used to calculate other thermodynamic properties. Therefore it is not a problem for them to be negative.

In summary, an iterative procedure solving the Rachford-Rice equation using direct substitution in the equilibrium factors K_i (Eq. 4.18), capillary pressure P_c (Eq. 4.17), and bulk concentration \mathbf{z}_b (Eq. 4.19) can be performed until reaching a desired tolerance or number of iterations.

Quadratic Update on Vapor Flows

The procedure can be accelerated using a second order method in the phase split of the bulk phases while updating P_c and \mathbf{z}_b in an outer loop. This procedure is especially useful when we are close to the critical point. The equilibrium equations

of the gas and liquid phases can be written as a function of the vapor flows

$$g_i(\mathbf{v}) = \ln f_i^g - \ln f_i^l = 0 \quad (4.28)$$

By using the mass balance for the bulk phase we can write the liquid flows as a function of the overall bulk phase and vapor flows, $l_i = z_i^b - v_i$. The vapor flows are selected as independent variables, and we can thus write the Jacobian matrix for the system in (Eq. ??) as follows

$$J_{ij} = \frac{1}{\theta(1-\theta)} \left(\frac{z_i^b}{x_i y_i} \delta_{ij} - 1 + (1-\theta)\Phi_{ij}^g + \theta\Phi_{ij}^l \right) \quad (4.29)$$

where

$$\Phi_{ij}^\alpha = n_T \left(\frac{\partial \ln \varphi_i}{\partial n_j} \right)_{T, P^\alpha}, \quad n_T = \sum_k n_k \quad (4.30)$$

For details in the derivation, the reader is referred to Michelsen and Mollerup[41]. The update in the vapor flows can be obtained by solving the following system

$$\mathbf{J}\Delta\mathbf{v} + \mathbf{g} = \mathbf{0} \quad (4.31)$$

The system was solved using Hebden's algorithm[45], which is very convenient in cases near the critical point where the determinant of the Jacobian is close to zero. This method secures the step sizes where the Newton method overshoots to undesired points. Even though the bulk composition \mathbf{z}_b changes at each step, this update looks for a decrease of the Gibbs energy of the bulk phase. It is important to use the second order method with high-quality initial estimates in order to have local convergence. The linear convergence on \mathbf{z}_b can be accelerated by using the dominant eigenvalue method every 4-5 steps. It is recommended to perform some cycles of successive substitution before switching to the quadratic update in the vapor flows.

If at some point during the calculation, the vapor phase converges to zero, stability analysis including capillary pressure, suggested by Sherafati et al. [15], is performed to confirm the solution.

In summary, the solution procedure is as follows:

- i Initialize with Wilson's equilibrium constants for the bulk phases. (Eq. 4.14)

-
- ii Perform 5 cycles of accelerated successive substitution. (Eq. 4.15), (Eq. 4.17), (Eq. 4.18), and (Eq. 4.19). Confirm that step on \mathbf{z}_b is sufficiently small to ensure mass balance before switching to second order update.
 - iii Continue with the second order method for the bulk phase vapor flows while updating by means of successive substitution the capillary pressure and bulk compositions in the outer loop. (Eq. 4.31)
 - iv If one of the bulk phases disappears at any point during steps ii) or iii) continue with the phase split of single bulk phase and adsorbed phase. Check the final solution with stability analysis. If stable terminate, otherwise return to step ii.

4.4. Results

The suggested procedure given Section 4.3.1 is able to handle the tested systems described in Table 4.7. The component EoS parameters and parachor constants are presented in Table 4.8, and the adsorption parameters in Table 4.9.

Alkane	Binary	Ternary	Low GOR	High GOR
C ₁	0.50	0.42	0.7000	0.8997
C ₂	0.50	-	-	-
C ₄	-	0.33	0.1200	0.0300
C ₈	-	-	0.0700	0.0297
C ₁₀	-	0.25	-	-
C ₁₂	-	-	0.0599	0.0232
C ₁₆	-	-	0.0501	0.0174

TABLE 4.7.: Molar composition of the systems.

Alkane	T_{crit}	P_{crit}	ω	Parachor	$k_{ij}(c_1/c_n)$
C ₁	190.6	45.99	0.0115	74.05	-
C ₂	305.3	48.72	0.0995	112.91	-0.0026
C ₄	425.1	37.96	0.2002	193.90	0.0168
C ₈	568.7	24.90	0.3996	359.33	0.0451
C ₁₀	617.7	21.10	0.4923	440.69	0.0422
C ₁₂	658.0	18.20	0.5764	522.26	0.0500
C ₁₆	723.0	14.00	0.7174	688.50	0.0561

TABLE 4.8.: EoS component parameters and parachor constants.

TABLE 4.9.: Correlation constants for temperature dependent Langmuir parameters.

Alkane	$\frac{E_a}{R} (K)$	$\ln A$ *	$m \left(\frac{mmol}{g \cdot K} \right)$	$c \left(\frac{mmol}{g} \right)$ **
C ₁	-1115.9	-7.48	$-2.66 \cdot 10^{-4}$	0.3985
C ₂	-1947.9	-8.13	$-2.13 \cdot 10^{-4}$	0.2931
C ₄	-2758.5	-7.91	$-1.09 \cdot 10^{-4}$	0.1769
C ₈	-3989.1	-6.44	$-3.32 \cdot 10^{-5}$	0.0818
C ₁₀	-4502.1	-6.11	$-2.24 \cdot 10^{-5}$	0.0637
C ₁₂	-5871.2	-8.00	$-1.14 \cdot 10^{-5}$	0.0496
C ₁₆	-6189.2	-5.68	$-5.41 \cdot 10^{-6}$	0.0341

* $\ln b_i = \ln A_i - \left(\frac{E_{a_i}}{R} \right) \frac{1}{T}$, ** $n_i^{max} = m_i T + c_i$

The Peng-Robinson EoS was used to model the bulk phase, but the calculations can be performed with any other EoS. It is worthwhile to mention that the Langmuir

isotherm fitting for pure components was performed also using Peng-Robinson EoS in order to have consistency when evaluating the fugacity term. A cylinder geometry with a capillary radius (r_c) of 10 nm was assumed for all the calculations. Nevertheless, the considered framework can be applied to any geometry. For instance, for a shale rock sample, the specific surface area and porosity are required. For such case, the capillary pressure model is suggested to be a function of the saturation because the complicated pore geometry and pore distribution cannot be expressed by the Young-Laplace equation with an average pore radius.

The algorithm was tested in a fine grid of 500×500 for each system and the plots are shown from Figure 4.7 to Figure 4.17. The average combined iterations of successive substitution and Newton steps to reach convergence are from 9 to 15 depending on the system. The algorithm shows to be robust, and most of the time linearly convergent. The limitations on fast convergence are the linear updates in P_c and \mathbf{z}_b , especially the latter. The convergence was improved by using the dominant eigenvalue method for acceleration on \mathbf{z}_b .

Figure 4.5 shows the convergence of a point in the liquid zone; after two iterations the gas phase disappears and then every four steps an acceleration on the composition is performed. On the other hand, Figure 4.6 shows a more difficult case of convergence behavior close to the bubble point; after four iterations the gas phase disappears and convergence is reached in the ninth iteration. Subsequently, stability analysis[15] considering capillary pressure is performed, where the gas phase is again introduced and iteration is continued by (Eq. 4.31) and accelerated linear updates in the \mathbf{z}_b and P_c . Finally, convergence is reached around the 14th iteration.

4.4.1. Binary System

The first system tested was an equimolar binary mixture of methane and ethane. The mixture of these two components is usually of great importance in shale gas reservoirs. However, the temperatures of two-phase coexistence are extremely low in comparison with the real reservoir conditions. Nevertheless, an example of a binary mixture provides a simple and useful analysis of the main characteristics of the bulk-adsorbed phase split. The results from Figure 4.7 to Figure 4.9. Figure 4.7 shows the main differences of the phase envelope with and without capillary pressure and adsorption. The phase envelope shows to be considerably smaller and shifted. As shown in previous studies, the capillary pressure has an effect on the whole phase envelope except in the critical point. The bubble point pressures and lower dew

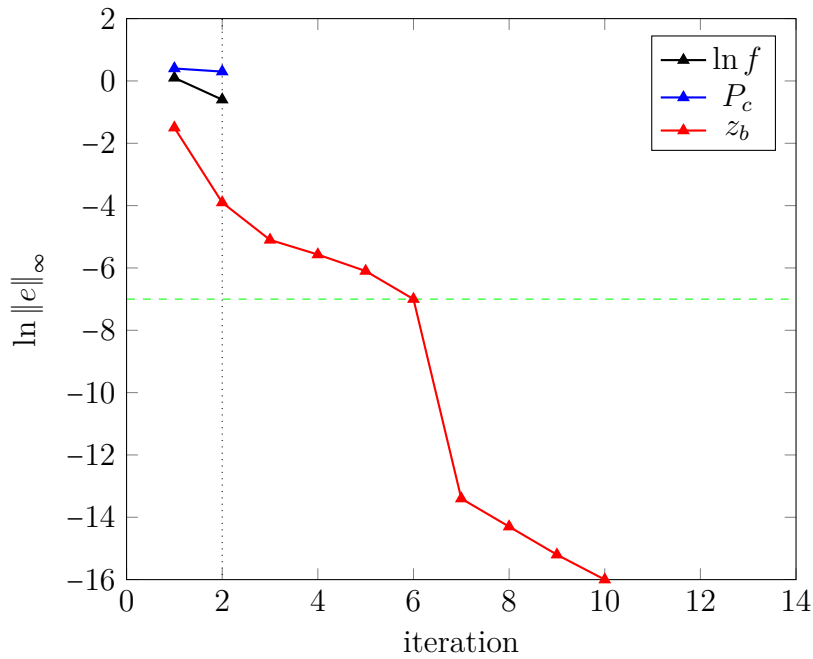


FIGURE 4.5.: Convergence for C_1 - C_2 binary system in the single phase region at (240 K, 70 bar). Acceleration of z_b after each 4 steps. Tolerance limit (- -); Vanishing of the gas phase (···).

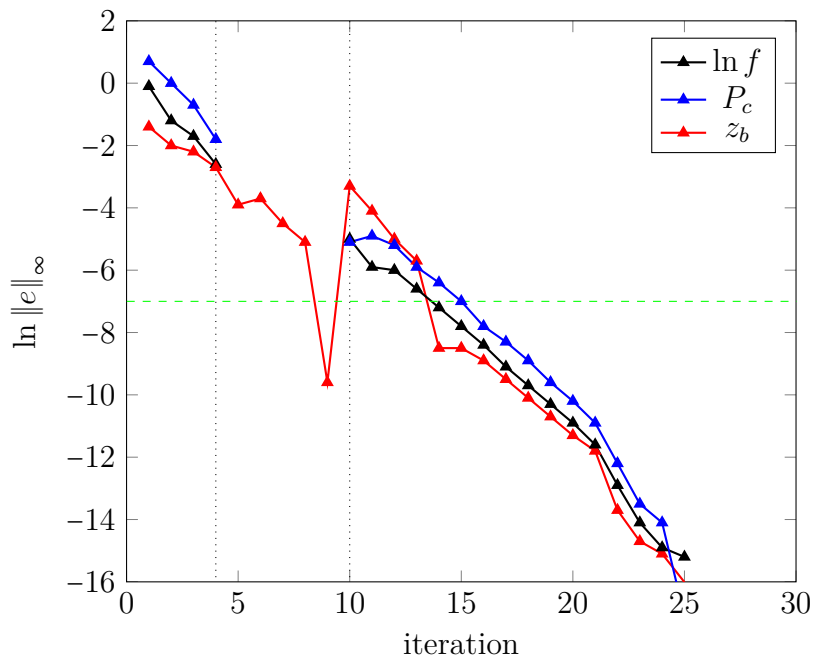


FIGURE 4.6.: Convergence for C_1 - C_2 binary system near to the bubble point, ($T=240$ K, P_l 53.9 bar). Acceleration of z_b after each 4 steps. Tolerance limit (- -); Vanishing/appearance of the gas phase (···).

point pressures are decreased, and the upper dew point pressures increased. On the other hand, the effect of the adsorbed phase is less obvious. The differences in the

phase envelope are due to compositional changes in the bulk phase. In other words, each point in the phase diagram has the same overall feed composition \mathbf{z}_f , but the bulk composition \mathbf{z}_b is different (see Eq.4.8).

Figure 4.8 shows the change of C_2 molar composition in the bulk phase with respect to the feed phase. It is possible to observe that in the liquid region at low temperatures, the composition of the bulk phase changes very little and the change in the phase envelope in this region is mainly caused by capillary effects. In contrast, at very low pressures of the gas region, one can expect excess adsorbed phase fractions up to 0.8 (Figure 4.7), due to big differences between the bulk phase and adsorbed phase molar densities. Furthermore, the composition change is more dramatic and C_1 molar fraction in the bulk phase can get as high as 90% creating a significantly lighter bulk phase.

Figure 4.9 shows the adsorbed phase fraction of the system plotted against the pressure of the liquid phase (P_l), and the pressure of the gas phase (P_g). The aim of this is to show the bubble point and the dew point boundaries plotted against the respective feed pressures. P_l for the bubble point branch, and P_g for the dew point branch. Notice that both graphs are not identical, the plotting against P_g in Figure 4.9a is smoother in the dew point branch than Figure 4.9b. This is because the feed phase pressure does not have a discontinuity when the incipient pressure appears, unlike the P_l plot at the dew point.

Moreover, for the bubble point boundary at low temperatures, the excess adsorbed phase fraction and the change in the bulk composition is close to zero, meaning that the bulk phase and the absolute adsorbed phase are almost identical. If we decrease the pressure at a constant temperature, when the bubble point pressure is crossed, rapid changes in the composition and phase fractions occur as shown in Figure 4.8 and 4.9. As soon as the gas phase appears, C_1 is released from the adsorbed phase to the bulk phase more rapidly than C_2 creating a lighter phase in the bulk space. Therefore, the two-phase region shrinks and the dew point is encountered at higher pressures as seen in Figure 4.7.

Another interesting region is close to the critical point. We considered that, the critical point still has the same definition, i.e. no difference between the coexisting gas and liquid phases. Moreover, we assume here that adsorption will hold close to the critical point and its thermodynamic properties will solely rely on the calculated isotherms as functions of the bulk fugacities. If we increase the temperature along the bubble point boundary towards the critical point, we can observe that the excess

adsorbed phase fraction increases and so does the composition of C_1 in the bulk phase. Due to the selective adsorption and resulting change in the bulk phase composition, the critical point of the bulk phase has shifted.

In summary, we observe changes in all the PT phase envelope due to adsorption, and additional changes in the two-phase region and vicinity of the phase boundary due to a capillary pressure difference. In general, adsorption selectivity towards C_2 is observed everywhere. It is moderate at high pressures and low temperatures, but increases as the pressure is lowered and temperature increased. Excess amounts in the liquid region are small, close to zero, however in the gas region at low pressures can be as large as 80%.

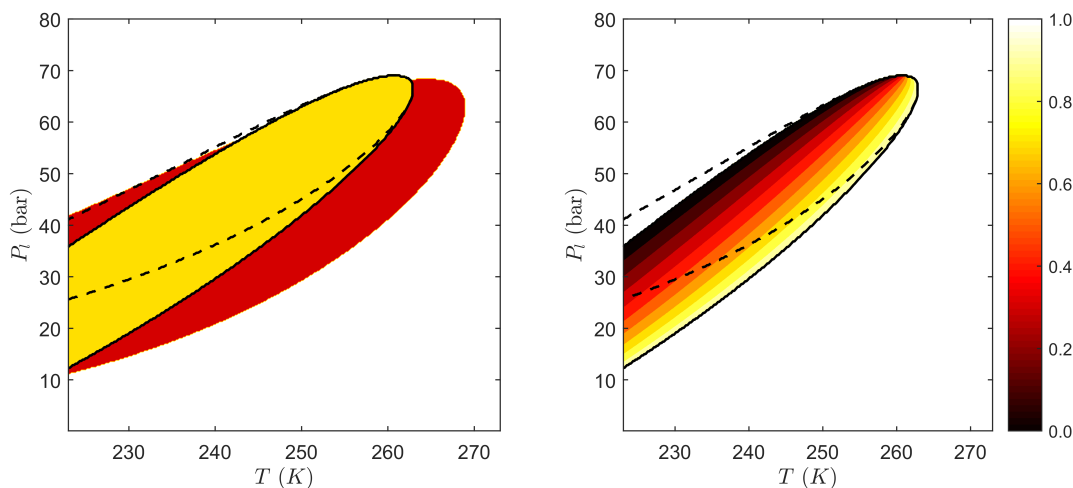


FIGURE 4.7.: C_1 - C_2 binary system. [Left] Normal phase envelope in red; with capillary pressure and adsorption in yellow. [Right] Phase envelope with relative vapor fractions. Dashed line (- - -) represent the pressure in the gas phase.

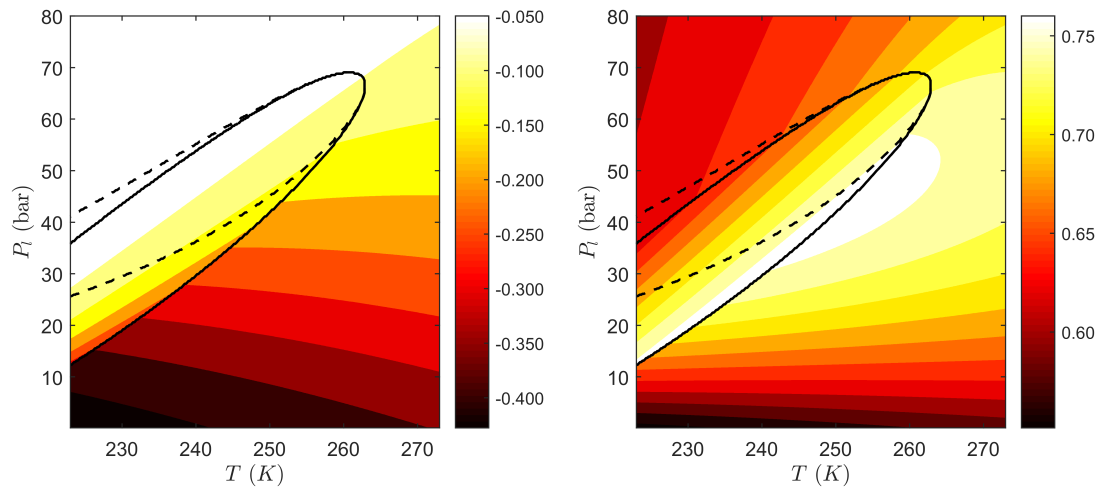
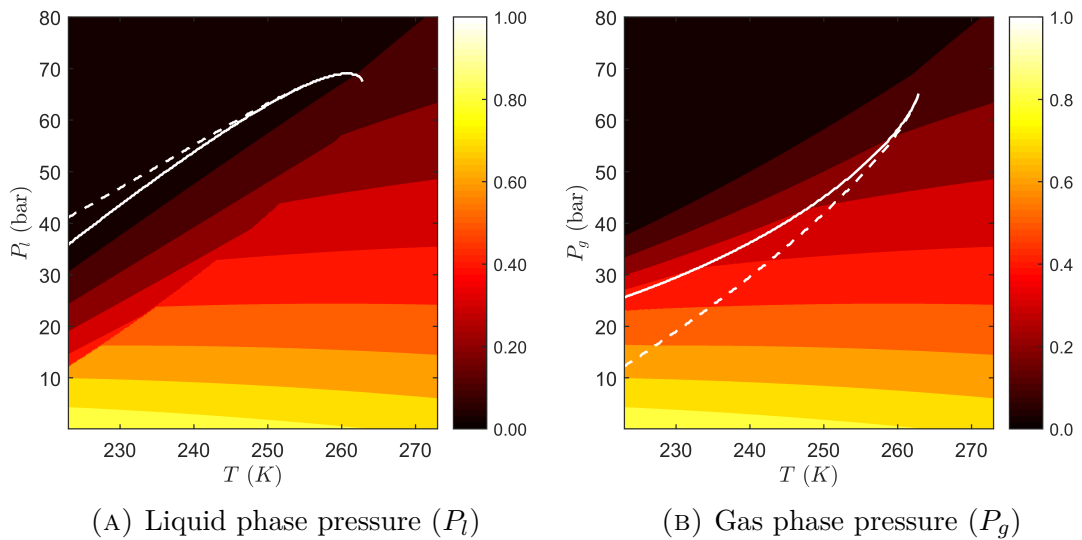


FIGURE 4.8.: C_1 - C_2 binary system. [Left] Change of the C_2 molar fraction in bulk phase \mathbf{z}_b . [Right] C_2 molar fraction in the absolute adsorbed phase \mathbf{x}^{abs} .



(A) Liquid phase pressure (P_l)

(B) Gas phase pressure (P_g)

FIGURE 4.9.: Excess adsorbed phase fraction (θ) for C_1 - C_2 binary system. Continuous line (—) represents the feed phase pressure, dashed line (---) represent the incipient phase pressure.

4.4.2. Ternary System

The algorithm was also tested with a ternary mixture (C₁-C₄-C₁₀) presented on Table 4.7. The mixture was constructed in a way to represent a light, intermediate and heavy fraction of an oil mixture while keeping a moderate simplicity to analyze the changes of each fraction. Similar to the binary system, the algorithm shows to be convergent and no particular difficulties were encountered. Figure 4.10 shows the change of the phase envelope and excess adsorbed phase fraction at different T and P. Figure 4.11 shows the change in composition of C₁₀ in the bulk phase and the absolute composition in the adsorbed phase.

A shrink of the phase envelope due to capillary pressure and compositional changes is observed. This behavior is consistent with the phase envelope shrink in the binary system presented before. The excess adsorbed phase fraction in the liquid region is close to zero, and appears to be less sensitive to changes in the pressure and the temperature as shown in Figure 4.10. Nevertheless, the composition of decane in the adsorbed phase shows to be sensitive to pressure and temperature changes in the liquid region. Therefore, in spite of the apparent zero value of the excess fraction in the liquid region, the individual contributions n_i^{exc} are the ones responsible of the compositional changes in the bulk phase. Thus, affecting the shape of the phase envelope at higher temperatures.

If we considered a constant temperature and start decreasing the pressure, as soon as the mixture enters the two-phase zone compositional changes become more sensitive to changes as can be seen in Figure 4.11. In order to illustrate this changes, a fixed reservoir temperature of 400K was selected and the bulk phase compositions and adsorption selectivities $\left(S_{i,j} = \frac{x_i^{ads}/z_{b_i}}{x_{ads_j}/z_{b_j}}\right)$ were plotted against the pressure and are shown in Figure 4.12 and Figure 4.13 respectively. It can be seen that liquid phase gets enriched with lighter components due to higher adsorption selectivity towards decane. As the pressure is decreased, the adsorption selectivity towards heavier components is enhanced, reaching several thousand at very low pressures. Furthermore, the composition profile of the bulk phase shows important changes when the two-phase zone is entered, and the change becomes larger as the pressure is decreased. The bulk phase gets richer in lighter components as the pressure is decreased, reaching compositions of C₁ greater than 0.9 at very low pressures. This suggests that, in a depletion production scenario, the heavier components become harder to recover as the pressure of the reservoir decreases. Staying in the adsorbed phase, making it practically impossible to recover them at low pressures.

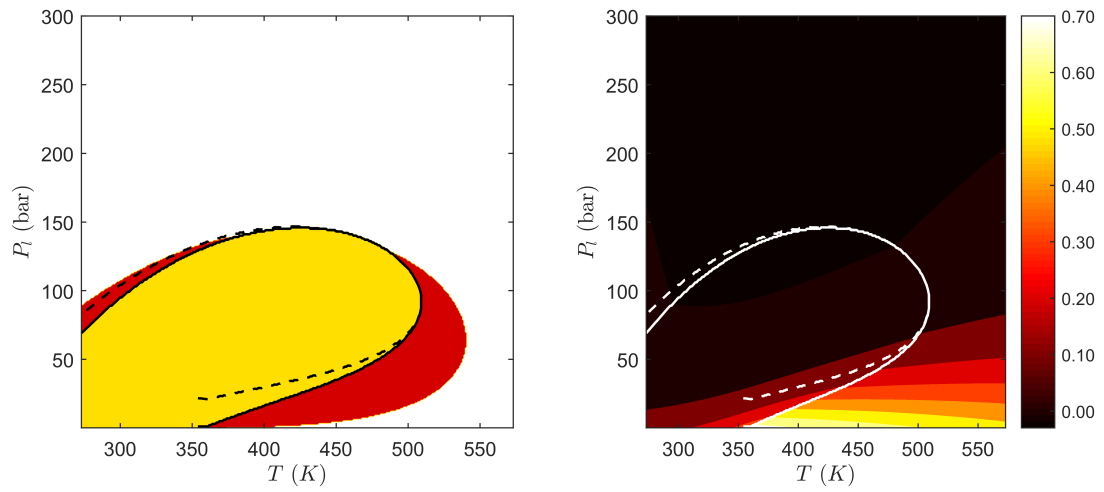


FIGURE 4.10.: Ternary system. [Left] Normal phase envelope in red; with capillary pressure and adsorption in yellow. [Right] Excess adsorbed phase fraction (θ) plotted against the liquid phase pressure. Dashed line (- -) represents the gas phase pressure.

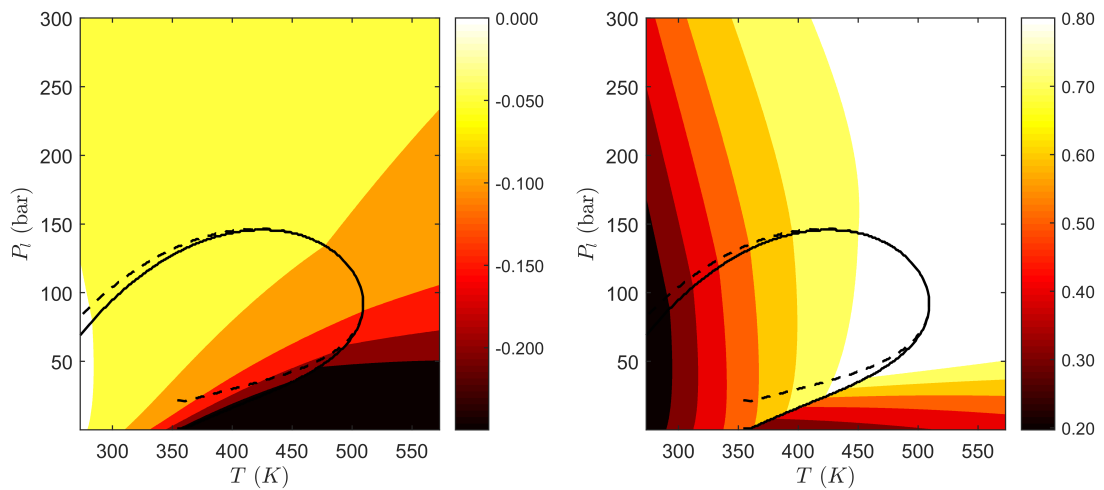


FIGURE 4.11.: Ternary system. [Left] Change of the C_{10} molar fraction in the bulk phase z_b . [Right] C_{10} molar fraction in the absolute adsorbed phase x^{abs} .

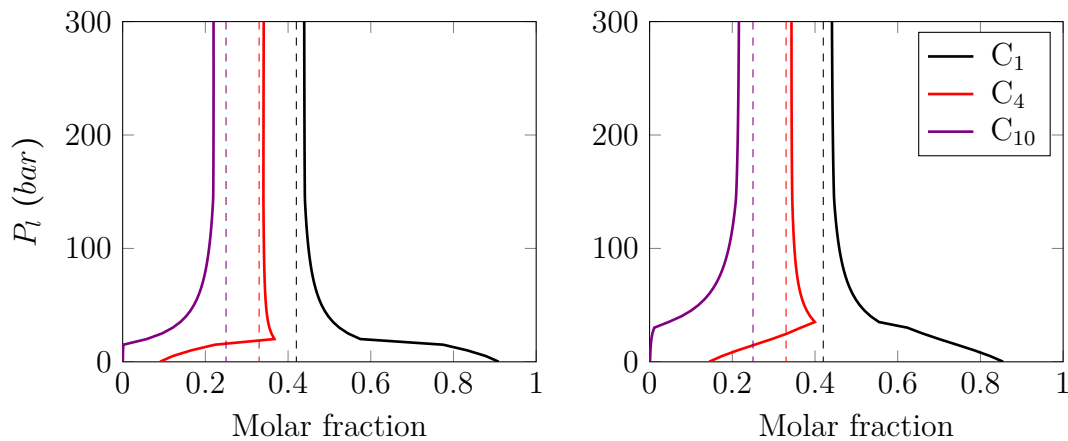


FIGURE 4.12.: Composition profile of the bulk phase (\mathbf{z}_b) as a function of the pressure (P_l) at $T = 400\text{ K}$ and $T = 450\text{ K}$ respectively.

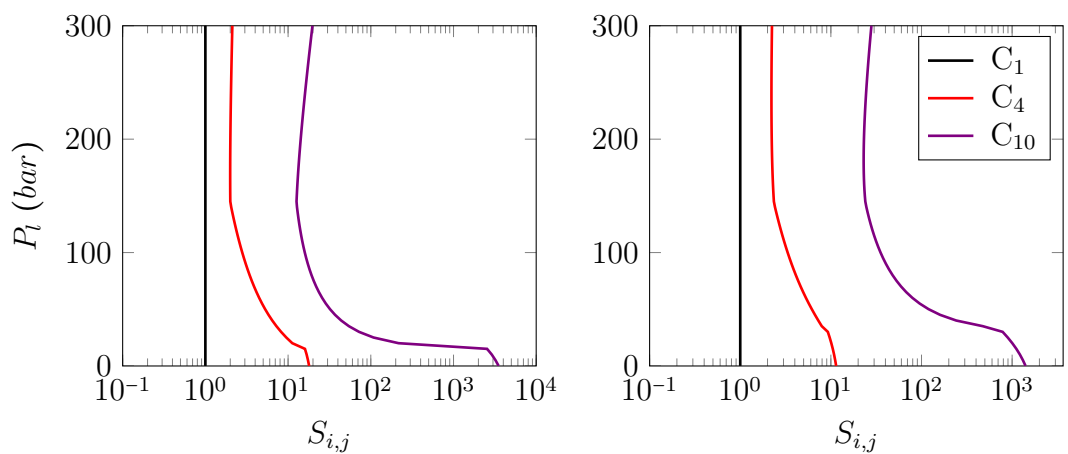


FIGURE 4.13.: Adsorption selectivity with respect to C_1 as a function of the pressure (P_l) at $T = 400\text{ K}$ and $T = 450\text{ K}$ respectively.

4.4.3. Low-GOR and High-GOR Systems

Two more complex systems that mimic real reservoir fluids are tested. The low-GOR system (lower methane content) represents a heavy oil system and the high-GOR system represents a gas condensate system ($T_c = 318.5\text{ K}$). The critical temperature of the high-GOR system is $T_c = 515.0\text{ K}$, and for the low-GOR system is $T_c = 318.5\text{ K}$. The comparison of both are shown in Figure 4.14 to Figure 4.17. Once again it can be seen that the two-phase zone shrinks and shifts in the same way as the binary and ternary system. However, some differences are observed in the high-GOR system. The shift in the upper dew point region is more pronounced in comparison to the other systems. For instance, if we set a reservoir temperature of 350 K , unlike the other systems the two-phase zone will be reached several bars later than expected. This shows the importance of the compositional changes caused by the adsorbed components. In general, it can be seen that the two-phase zone shrinks when adsorption is considered. However, it is not completely clear whether the saturation point will increase or decrease as it is known with the capillary pressure effect alone. With the considered EoS and adsorption models we can observe that adsorption of heavier alkanes is strongly preferred in the gas phase. On the other hand, moderate preference is observed in the liquid region. Hence, having regions in which the composition of the liquid and adsorbed phase are very close to each other as shown in Figure 4.18 and Figure 4.19. This means that there are temperature regions in which the adsorbed phase will not have an obvious effect until the two-phase region is reached. However, this assumption could be dangerous outside this region, where the changes in bulk composition due to adsorption are enhanced as seen in Figure 4.17 for the low-GOR system. In general, it should be noted that the role of the adsorbed phase will become more relevant when it changes from the liquid phase zone to a two-phase zone due to the appearance of a gas phase. Therefore, it is recommended not to disregard its effect when the phase equilibrium of a confined system is being evaluated.

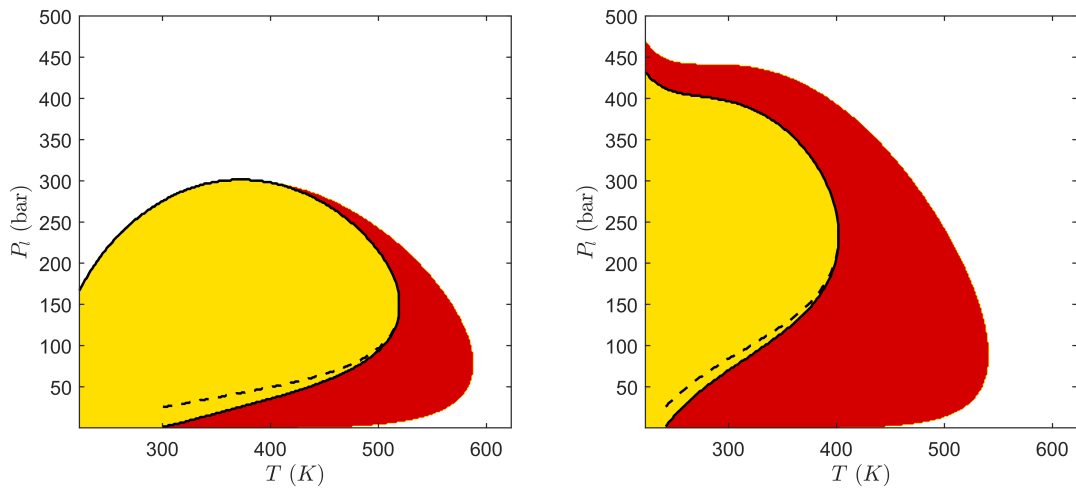


FIGURE 4.14.: Normal phase envelope in red; with capillary pressure and adsorption in yellow. [Left] Low-GOR. [Right] High-GOR.

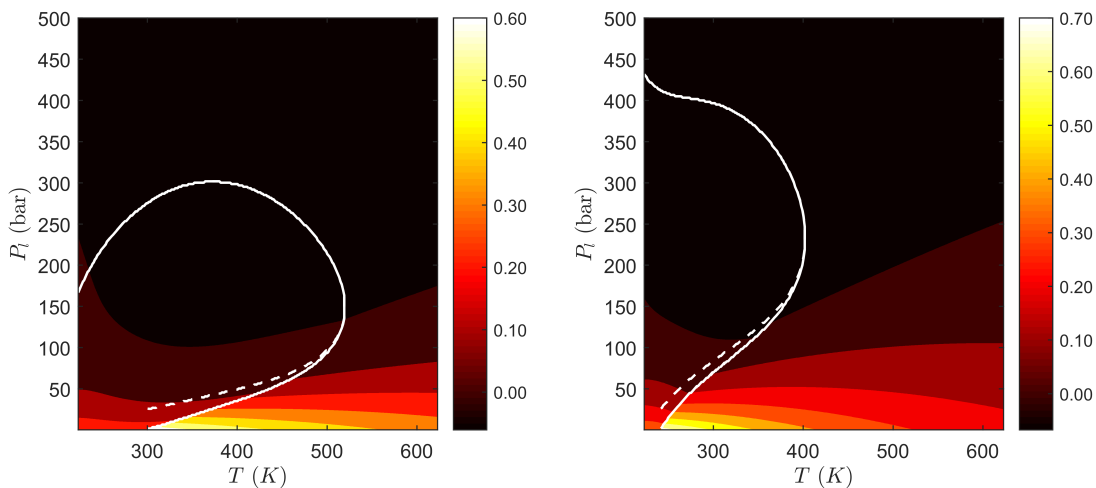


FIGURE 4.15.: Excess adsorbed phase fraction (θ) plotted against the liquid phase pressure. Dashed line (- - -) represents the gas phase pressure. [Left] Low-GOR. [Right] High-GOR.

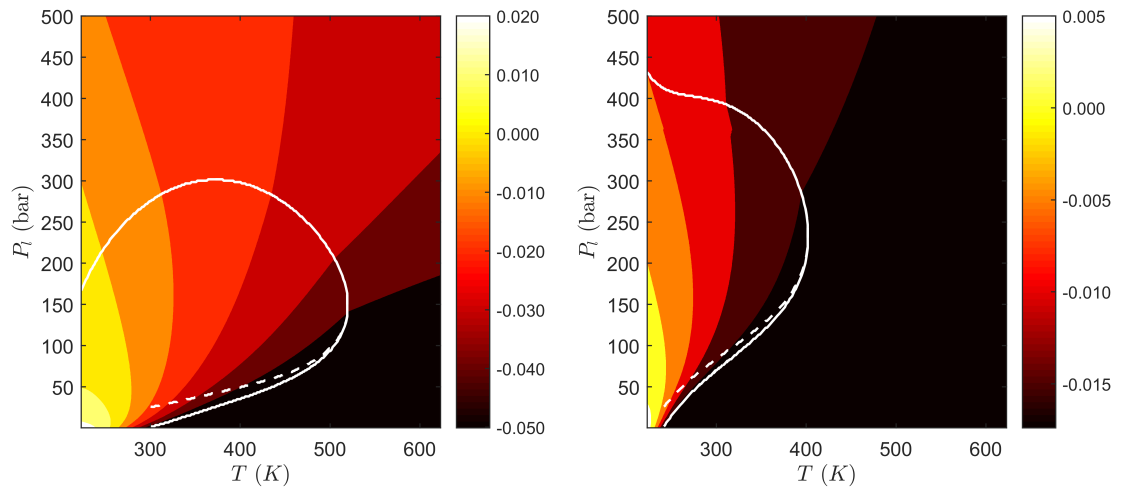


FIGURE 4.16.: C_{16} molar fraction change in bulk phase \mathbf{z}_b . [Left] Low-GOR, reference feed ($z_{C_{16}} = 0.501$). [Right] High-GOR, reference feed ($z_{C_{16}} = 0.0174$).

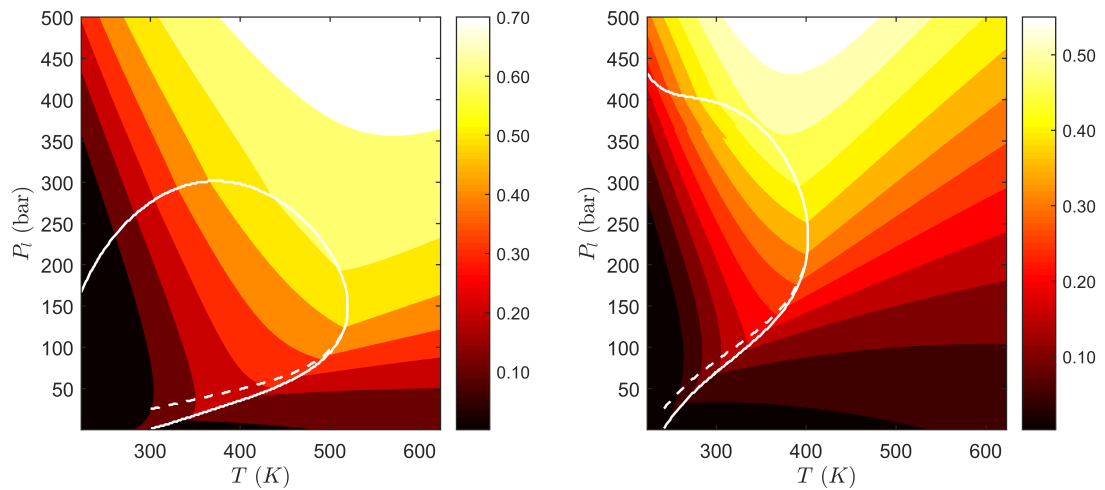


FIGURE 4.17.: C_{16} molar fraction in the absolute adsorbed phase \mathbf{x}^{abs} . [Left] Low-GOR. [Right] High-GOR.

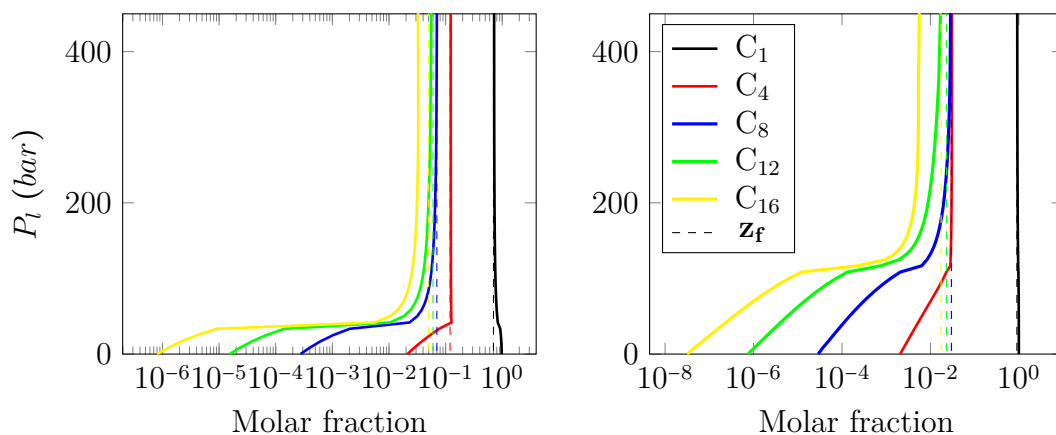


FIGURE 4.18.: Composition profile of the bulk phase (\mathbf{z}_b) as a function of the pressure (P_l). [Left] Low-GOR at $T = 400$ K. [Right] High-GOR at $T = 350$ K.

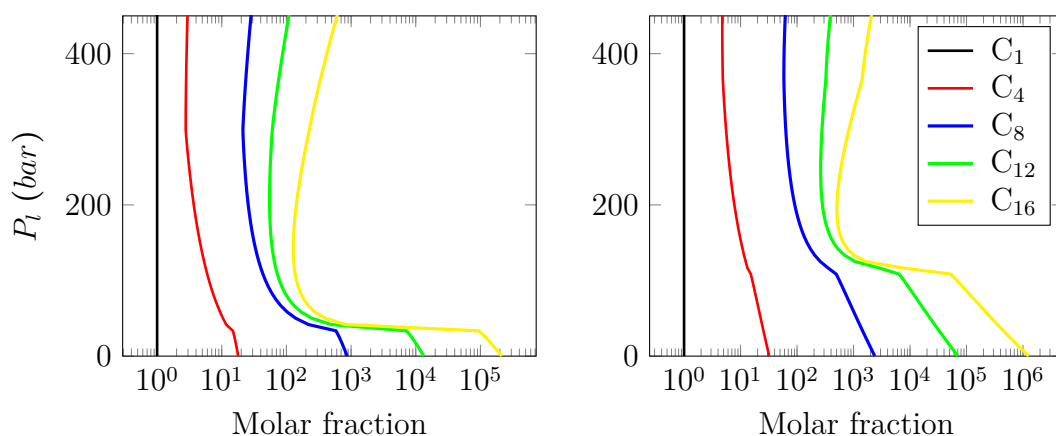


FIGURE 4.19.: Adsorption selectivity with respect to C_1 as a function of the pressure (P_l). [Left] Low-GOR at $T = 400$ K. [Right] High-GOR at $T = 300$ K.

4.4.4. Discussion on Perceived Phase Envelope Changes

We have made two different discussions on the change of the phase envelope under adsorption and capillary effects in Section 4.1 and Section 4.3, respectively, in this chapter. In Section 4.1, the bulk phase composition is assumed constant in the comparison of the phase envelopes; in Section 4.3, the overall composition of all the substance, including the adsorbed phase, is assumed constant. Both comparisons are valid under their specific assumptions but we also need to point out that the phase equilibrium change often discussed in the oil production context can be different from what we discussed earlier. The reason is that during oil production, the comparison is made between the phase envelope estimated using the sampled fluid composition and the actual observed phase envelope/phase change in the field which is determined by all the in-situ composition (If the flowing effects and non-equilibrium effects are neglected for the simplicity of discussion.) If we assume that both capillary effects and adsorption play a role and the sampling happens in an undersaturated reservoir, it is the bulk phase composition will be used for the phase envelope perceived by the engineering using a conventional PVT software (without adsorption and capillary effects.) For the in-situ phase change, the analysis should use the overall composition for all the substance in the pore space, including the adsorbed phase. The algorithm described in section 4.3 should be used to simulate what is going to happen in the reservoir. We note that the two-phase envelopes are calculated based on different compositions. But this analysis better reflects the perceived phase envelope change in the field.

We provide a preliminary analysis of the perceived phase envelope change here. We select an arbitrary reservoir temperature of 400 K and 500 bar for both the low GOR and high GOR system. The equilibrium (physical) bulk phase composition is used as the reservoir sample composition perceived by the reservoir engineer. We calculate its phase envelope without capillary pressure and adsorption (red), and compare the results with the phase envelope using the sampling composition (yellow) and the in-situ correction (orange), using adsorption and capillary effects. The phase envelopes are shown in Figure 4.20 and Figure 4.21.

The estimation of the in-situ composition can be done in one step since we know the composition of the bulk phase ($\mathbf{z}^b =$ reservoir sample composition). The composition of the adsorbed phase is calculated using (Eq. 4.21), and the excess fraction with (Eq. 4.26). Moreover, we can get \mathbf{z}^f using the mass balance in (Eq. 4.19). The results for the modified compositions are presented in Table 4.10

TABLE 4.10.: Molar composition with and without in-situ correction.

Alkane	low-GOR	low-GOR*	high-GOR	high-GOR*
C ₁	0.7000	0.6807	0.8997	0.8808
C ₄	0.1200	0.1169	0.0300	0.0294
C ₈	0.0700	0.0698	0.0297	0.0297
C ₁₂	0.0599	0.0634	0.0232	0.0256
C ₁₆	0.0501	0.0692	0.0174	0.0344

* After in situ approximation

Notice that the composition of the lighter components has reduced, and the one of the heavier components has increased. If we calculate the phase envelope of the new mixtures, we obtain closer phase envelopes to the perceived phase envelope for both systems as shown in 4.21. It can be seen that the saturation point at 400 K for the high-GOR system has increased, and the phase envelope is larger in comparison to the one calculated without applying the correction for the in-situ composition. Moreover, the low-GOR system phase envelope is enlarged to higher temperatures, in comparison to the phase envelope where the in-situ correction is not applied. On the other hand, Figure 4.22 shows that the composition in the single phase region z_b is matched to the perceived composition of the reservoir fluid sample. Moreover it is maintained almost unchanged until the two-phase zone is crossed. Suggesting that the perceived composition might explain the behavior of the reservoir fluid at the beginning of the production, however, deviations may occur as the pressure of the reservoir is lowered.

It should be noted that sampling from shale reservoirs is still an unresolved issue and usually the sampled fluid may not even represent the bulk phase composition. The above discussion is therefore preliminary. It would be better to perform reservoir simulation to generate the perceived reservoir fluid composition and discuss the phase envelope change.

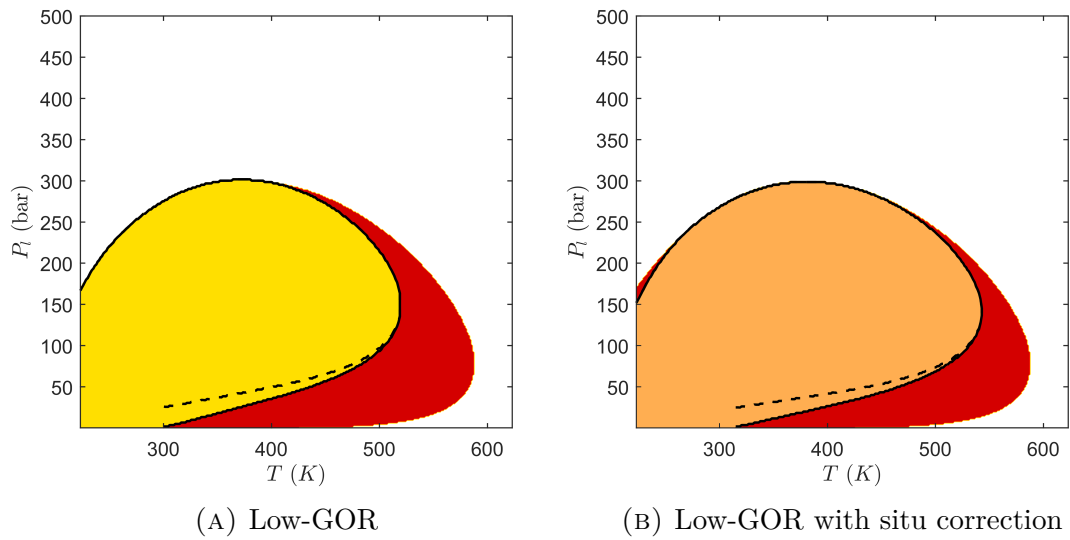


FIGURE 4.20.: Phase envelope comparison for the low-GOR system with and without the in-situ correction. Phase envelope using z^b without capillary and adsorption effects in red.

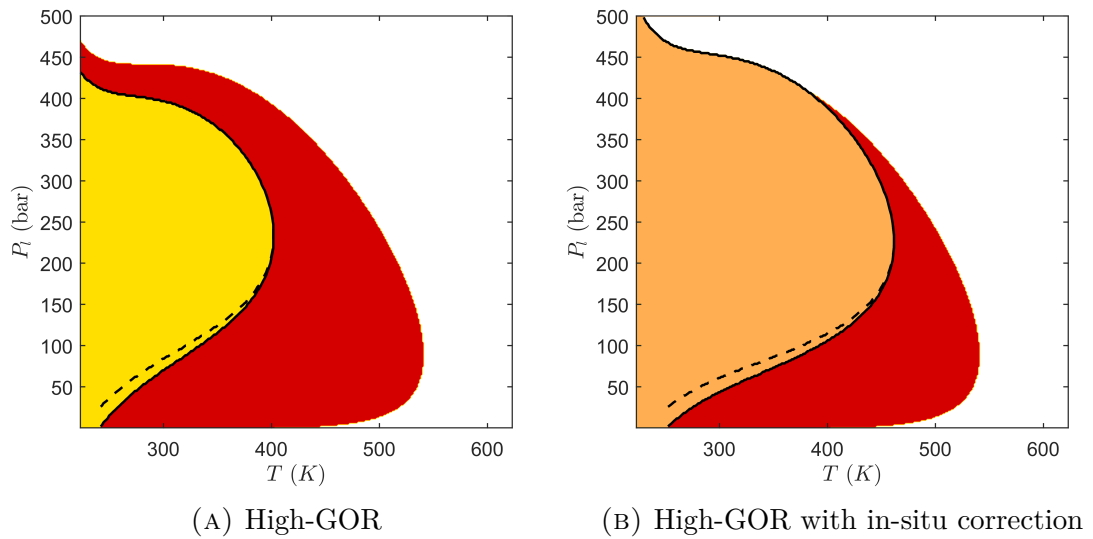


FIGURE 4.21.: Phase envelope comparison for the high-GOR system with and without the in-situ correction. Phase envelope using z^b without capillary and adsorption effects in red.

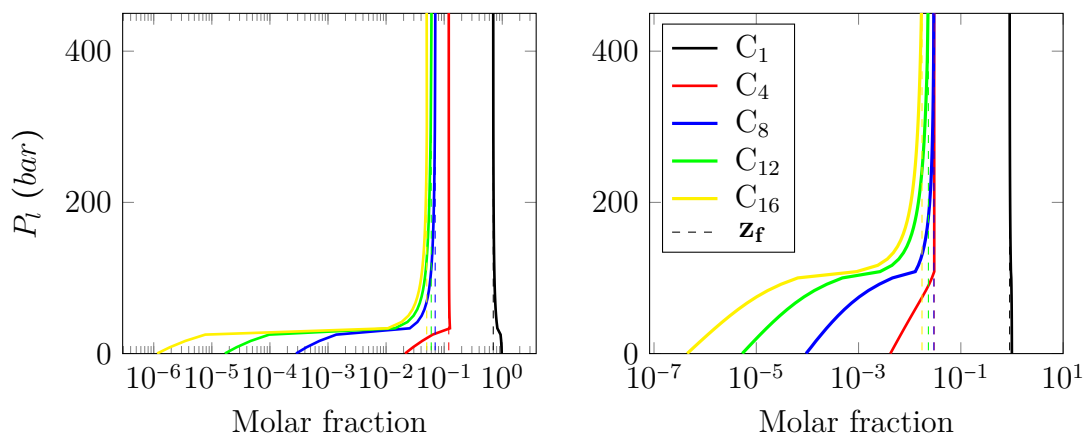


FIGURE 4.22.: Composition profile of the bulk phase (\mathbf{z}_b) as a function of the pressure (P_l). [Left] Low-GOR at $T = 450$ K. [Right] High-GOR at $T = 400$ K.

4.5. Conclusions

In this chapter, the combined effects of capillarity and adsorption were investigated. A modification to include the thickness of the adsorption film in the phase envelope construction is presented. Moreover, a flash algorithm including both capillary pressure and adsorption was developed by alternatingly update the adsorbed phase amount and the phase fugacities in the bulk phases. Furthermore, MPTA was employed as a tool to generate artificial adsorption data at different temperatures for longer hydrocarbons in order to determine the parameters for less theoretical models such as ML, making it possible to investigate the influence of adsorption and compositional changes due to selective adsorption for different systems.

For the adsorption film, an enhancement of the capillary pressure effect due to a reduction of the effective capillary radius was observed. The phase envelope shows that the thickness of the adsorption film becomes relevant far away from the critical point where the interfacial tension and capillary pressure are more pronounced. Near the critical point, the thickness of the adsorption film has a low impact due to the extremely low interfacial tension, showing a negligible impact on the change in phase boundary.

The flash algorithm with capillary pressure and adsorption was used to analyze some representative systems (from binary, ternary to low GOR and high GOR model systems) for the phase equilibrium inside confined spaces. The results show that adsorption and capillary pressure can significantly change the bulk phase composition and thus its corresponding phase envelope. Since the adsorption is different at different temperature and pressure conditions, the extent of change is different. In general, a much shrunk phase envelope with shifted critical point is observed. The adsorption effects are stronger for the gas phase, leading to bigger changes in the gas phase composition and the shift of the dew point curve. The adsorption of heavier components is strongly preferred in the low pressure and high temperature region, while at the high pressure and low temperature region this preference is from low to moderate.

CHAPTER 5

Compositional Reservoir Simulation with Capillary Pressure

The impact of capillary pressure on phase behavior has been presented in previous chapters. The deviation from conventional phase behavior shows to be substantial for systems confined in the nanometer scale. These observations suggest that the oil and gas production from tight reservoirs, with pore sizes comparable to those relevant, will deviate from the conventional production scenario. To study such differences, it is necessary to use advanced tools such as reservoir simulations.

The integration of the capillary pressure effect in phase equilibrium into a reservoir simulator is not entirely trivial. From the black oil simulation perspective, the standard PVT input tables can be generated using modified phase equilibrium calculations that account for capillary pressure effects. The resulting modified tables can be used directly for the simulation. This approach has been used by several authors [18, 19, 72]. Nevertheless, the black oil simulation framework has its own limitations when the capillary pressure of the system is sensitive to compositional changes. In such cases, compositional simulators are preferred.

Compositional simulations give a better description of the underlying phase behavior and are more flexible to test more complex fluids and scenarios. They have been used to study production from shale and tight reservoirs by several authors [73–76]. The reported results show deviations from the conventional case, depending on the use of the capillary pressure and interfacial tension models. The inclusion of capillary pressure effect in phase behavior for such simulations requires additional

efforts in comparison to the black oil simulation case. A previous knowledge of the mathematical and numerical framework of the simulator is required, unlike the black oil case where only the input needs to be altered. Moreover, these modifications will depend on the implicit level of the numerical model of the simulator, with an increasing complexity as the level of implicitness increases.

In general, the standard thermodynamic routines should be modified to allow handling cases where the liquid pressure becomes negative as a result of the high capillary pressures. Additionally, the flash and stability analysis routines involving capillary pressure need an efficient implementation to maintain the safety and speed needed during simulation. Moreover, for the linear solver, the derivatives of the selected pressure models must be obtained and implemented in a consistent way to avoid differences between the capillary pressure model used for phase equilibrium, and the capillary pressure used model for the flow equations.

In this chapter, we discuss the implementation of the capillary pressure effect in phase behavior for the compositional reservoir simulator COSI. Furthermore, we describe the mathematical and numerical framework that COSI uses, and the key modifications made to account for capillarity in phase equilibrium. These added features allowed us to test a natural depletion case of a tight reservoir at various conditions with different capillary pressure models. The case of study consists of a two-dimensional reservoir with ten planar fractures using local grid refinement to capture the fracture-matrix flow exchange. Capillary pressure models using fixed and variable pore sizes were used to study the effect in the production. In general, considerable deviations in the cumulative oil production, producing gas oil ratio, pressure profiles, and saturation profiles were observed for cases with effective capillary radii less than 20 nm. The obtained results are preliminary, and a more extensive analysis using more complex production scenarios should be made in the future. Nevertheless, they serve as a guide to analyze the key differences in oil production from unconventional reservoirs considering capillary pressure effect into phase equilibrium.

5.1. Compositional Reservoir Simulator (COSI)

COSI is an isothermal compositional reservoir simulator that can be used to study a variety of oil and gas production scenarios from conventional depletion and water flooding problems to more complex EOR injection cases. It can handle three-dimensional flow in porous media with an arbitrary number of phases and components. Moreover, it can handle two porous media which can communicate through exchange functions. The mass conservation equations together with the phase saturation equations are used as the primary set of equations in which the fluid flow in porous media is solved. Its numerical formulation relies on an Integral Finite Difference (IFD) method to maintain user flexibility in the construction of the grids. The solution of the volume discretized equations is solved using a Fully Implicit Method (FIM) with the oil pressure and the total mass flows as the set of primary variables. Furthermore, the phase equilibrium calculations are treated using either Peng-Robinson or SRK EoS. A general description, summarized from its manual (*COSI-Formulations and Basic Algorithms, v1.0*), is presented in the following subsections.

5.1.1. Mathematical Model

The formulation given in this section corresponds to a multiple porous media N_m , containing N_p flowing phases conformed by N_c components. It is based upon the mass conservation equations of a multiphase flow system inside porous media.

$$\frac{\partial}{\partial t} \left[\phi_m \sum_j (\rho S C^i)_{jm} \right] + \nabla \cdot \left[\sum_j (\rho C^i \mathbf{u})_{jm} - \phi_m \sum_j (\rho S \{D^i\} \nabla C^i)_{jm} \right] = q_m^i + q_{Sm}^i \quad (5.1)$$

where ϕ is the porosity, ρ the density, S the saturation, C the mass concentration, D the diffusion tensor, \mathbf{u} the velocity, and q_m^i is the production/injection term, q_{Sm}^i the interchange flow rate between two rock media.

$$q_{sm}^i = -a_{12} \sum_j T_{j12}^i (P_m - P_{3-m})_j \quad (5.2)$$

where T_{j12}^i is the source term for the rock media interchange

$$T_{j12}^i = K_{12} \left(\frac{k \rho C^i}{\mu} \right)_{j12} \quad (5.3)$$

Moreover, throughout the chapter, the subscripts $\{i, j, m\}$ will be used to refer to a component, phase, and rock media respectively. They are defined as follows:

$$i = 1, \dots, N_c \quad (5.4)$$

$$j = 1, \dots, N_p \quad (5.5)$$

$$m = 1, \dots, N_m \quad (5.6)$$

Flow in porous media obeys Darcy's law, and it is used to obtain the velocity vector \mathbf{u} for each phase inside the different porous media.

$$\mathbf{u}_{jm} = -\frac{\{Kk_j\}_m}{\mu_{jm}} (\nabla P_{jm} + g\rho_{jm}\nabla H) \quad (5.7)$$

where K is the rock permeability, k the relative permeability, μ the viscosity of the fluid, g the gravity, and H the column height. In total there are $N_c \cdot N_m$ of mass conservation equations. In order to solve them, additional constraints and relationships are needed.

Constraints

Each porous media has to be filled by the contained fluids, therefore the phase saturations and mass/mole concentrations must sum to unity.

$$\sum_j S_{jm} = 1 \quad (5.8)$$

$$\sum_i C_{jm}^i = 1 \quad (5.9)$$

Additionally, an arbitrary equilibrium reference phase, $j_{ref}(m)$ is selected for each porous media and phase pressures are calculated through capillary pressure relations

$$(P_j - P)_m = P_{cjm}, \quad \text{with } j \neq j_{ref}(m) \quad (5.10)$$

For the compositional case, an additional constraint based on the thermodynamic equilibrium of the system should be used. The local thermodynamic equilibrium is a

generally accepted assumption in reservoir simulation [77]. Therefore, an equilibrium constraint based on equality of fugacities can be employed

$$f_{jm}^i = f_{j+1,m}^i \quad (5.11)$$

An equation of state is used to obtain the fugacities and physical properties of each phase. In principle, the equilibrium calculations are performed at the reference pressure $P_{j_{ref}}$ for all the phases. However, in order to consider the capillary pressure effect in the phase equilibrium, (Eq. 5.11) should be coupled with the previous capillary pressure constraints (Eq. 5.10). The implementation procedure to account for such effect in COSI is presented later in this chapter in section 5.2.

5.1.2. Numerical Model

To solve the set of PDEs for the mass conservation equations, a numerical method must be selected. It is of common choice to use a finite difference scheme due to its flexibility in grid construction. COSI uses the integral finite difference method (IFD). The method was first used by MacNeal [78] for solving second order boundary problems and was first classified as an asymmetric finite difference network. The method has demonstrated to be a powerful tool for solving heat transfer and fluid flow in porous media. The central concept of IFD is to discretize the total flow domain into conveniently small N_v sub-domains and evaluate the mass balance in each element k [79].

$$k = 1, \dots, N_v \quad (5.12)$$

Let us call V_k and A_k the volume and surface area, respectively, of cell k . Integrating the mass conservation equations (Eq. 5.1) over the volume of each cell we obtain:

$$\frac{d}{dt} \int_{V_k} m_m^i dV + \int_{V_k} \nabla (\mathbf{F}_m^i + \mathbf{D}_m^i) dV = \int_{V_k} (q + qs)_m^i dV \quad (5.13)$$

where m_m^i , \mathbf{F}_m^i , and \mathbf{D}_m^i have been introduced for convenience. They refer to the specific mass, flux, and diffusion terms, respectively:

$$m_m^i = \phi_m \sum_j (\rho \cdot S \cdot S^i)_{jm} \quad (5.14)$$

$$\mathbf{F}_m^i = \sum_j (\rho C^i \cdot \mathbf{u})_{jm} \quad (5.15)$$

$$\mathbf{D}_m^i = \phi_m \sum_j (\rho S \{D^i\} \nabla C^i)_{jm} \quad (5.16)$$

It is convenient to use surface integrals for the flux and diffusion terms since it is easy to evaluate the flux entering and leaving each element through the polygon faces of the discretized elements. Therefore, we make use of the divergence theorem to convert the second term of the left-hand side to surface integrals as follows,

$$\frac{d}{dt} \int_{V_k} m_m^i dV + \int_{A_k} \mathbf{F}_m^i \cdot \mathbf{n} dA + \int_{A_k} \mathbf{D}_m^i \cdot \mathbf{n} dA = \int_{V_k} (q + q_S)_m^i dV \quad (5.17)$$

Physically the surface integrals are the summation of the fluxes over the surface A_k and indicate the mass rate at which the mass accumulates in cell k . Both, the volume integrals and surface integrals can be expressed as average quantities for each cell k as follows::

$$\int_{V_k} m_m^i dV = (V m_m^i)_k \quad (5.18)$$

$$\int_{A_k} \mathbf{F}_m^i \cdot \mathbf{n} dA = \sum_l (AF_m^i)_{kl} \quad (5.19)$$

$$\int_{A_k} \mathbf{D}_m^i \cdot \mathbf{n} dA = \sum_l (AD_m^i)_{kl} \quad (5.20)$$

$$\int_{V_k} (q + q_S)_m^i dV = (V(q + q_S)_m^i)_k \quad (5.21)$$

where l is the neighboring cell of cell k . Each cell average variable is calculated as follows:

$$F_{mkl}^i = \sum_j (\rho C^i u)_{jmk} \quad (5.22)$$

$$u_{jmk} = \frac{1}{L_{kl}} \left[\frac{K k_j}{\mu_j} \right]_{mkl} [(P_k - P_l)_{jm} + g \Delta(\rho H)_{jmk}] \quad (5.23)$$

$$\Delta(\rho H)_{jmk} = \frac{[V_k \rho_{jmk} + V_l \rho_{jml}](H_k - H_l)}{V_k + V_l} \quad (5.24)$$

$$q_{Smk}^i = -a_{12k} \sum_j [T_{12}^i (P_m - P_{3-m})]_{jk} \quad (5.25)$$

$$T_{j12k}^i = K_{12k} \left(\frac{k \rho C^i}{\mu} \right)_{j12k} \quad (5.26)$$

The discretization of (Eq. 5.1) is now complete. All the average cell and surface values can be obtained from the initial boundary condition of the system. To solve the system of equations over time, a time integration technique is required. The

spatially discretized equations can be written in a compact form as follows:

$$\frac{d}{dt}(m_{mk}^i) = \psi_{mk}^i \quad (5.27)$$

where

$$\psi_{mk}^i = (q + q_S)^i_{mk} - \frac{1}{V_k} \sum_l A_{kl} (F + D)^i_{mkl} \quad (5.28)$$

Then using a discrete time step we can write

$$m_{mk}^{i(n+1)} - m_{mk}^{in} + \Delta t \psi^{i(n+1)}_{mk} = 0 \quad (5.29)$$

where ψ_{mk}^i is evaluated at time $(n+1)$ for a FIM. Other techniques to treat some variables explicitly (time= n) can be used, as it is the case of Implicit Pressure and Explicit Composition method (IMPEC). These methods have some advantages since the system of linear equations to be solved is reduced. However, the stability is affected leading to smaller time-steps during the integration. In general, the time integration has to be done at least in a semi-implicit way to be able to solve the equations. COSI has a fully implicit method formulation (FIM), therefore the time integration in (Eq. 5.29) is employed. The system to be solved at each time step can be written as follows

$$\Psi(\mathbf{y}_p)^{n+1} = \mathbf{0} \quad (5.30)$$

where \mathbf{y}_p is the vector of the primary independent variables (choice dependent), and $\Psi(\mathbf{y})$ is conformed by the set of equations in (Eq. 5.1) and (Eq. 5.8).

$$\Psi = \begin{cases} \Psi_{mk}^{i(n+1)} = (m^{n+1} - m^n)^i_{mk} - \Delta t \psi_{mk}^{i(n+1)} \\ \Psi_{smk}^{n+1} = \sum_j S_{jmk}^{n+1} - 1 \end{cases} = \mathbf{0} \quad (5.31)$$

This system is then solved using Newton's method.

$$\mathbf{J}^n \Delta \mathbf{y}_p^{n+1} + \Psi^n = \mathbf{0} \quad (5.32)$$

where J is the Jacobian matrix of the fully implicit system. Its construction strategy will depend on the choice of primary variables. The time step must be kept under certain conditions to maintain the stability of the solution while getting a specified tolerance for the error. The adjustment is done as follows

$$\Delta t^{n+1} = \Delta t \sqrt{\frac{\epsilon_T}{T^n}} \quad (5.33)$$

where T is the truncation error, and ϵ the specified tolerance.

5.1.3. Choice of Variables

The choice of variables is done in a way to allow modularity during the implementation. COSI is divided into two sets of variables, primary and secondary. In principle, any choice of primary variables is allowed. For the case of COSI, the pressure P and the mass flows m^i are selected as primary variables,

$$\mathbf{y}_p = (P, (m^i, i = 1, \dots, N_c))_{ml} \quad (5.34)$$

the secondary variables are the mass concentrations C^i and phase saturations S_j ,

$$\mathbf{y}_{sv} = ((C^i, i = 1, \dots, N_c), S)_{jmk} \quad (5.35)$$

The primary dependent variables (\mathbf{y}) are the ones used to solve the (FIM) system in (Eq. 5.32). Therefore, the differentiation to obtain the Jacobian is done with respect to the reference pressure P_{jref} and mass flows m^i .

$$\mathbf{J} = \frac{d\Psi}{d\mathbf{y}_p} = \frac{\partial\Psi}{\partial\mathbf{y}_p} + \frac{\partial\Psi}{\partial\mathbf{y}_{sv}} \left(\frac{\partial\mathbf{y}_{sv}}{\partial\mathbf{y}_p} \right) \quad (5.36)$$

where the implicit function theorem was used for the secondary (\mathbf{sv}) variables. The term in parentheses should be obtained using additional relationships. The primary variables are used to determine the secondary variables using the equilibrium fugacity equations (Eq. 5.11), the mass fraction constraints (Eq. 5.9) and the specific mass equation (Eq. 5.14).

$$\Psi_{sv} = \begin{cases} \Psi_{Fmk}^{i(n+1)} = \psi_{jmk}^i - \psi_{j+1,mk}^i \\ \Psi_{Mmk}^{i(n+1)} = m_m^i - \phi_m \sum_j (\rho \cdot S \cdot C^i)_{jm} \\ \Psi_{Cmk}^{n+1} = \sum_i C_{jmk}^i - 1 \end{cases} = \mathbf{0} \quad (5.37)$$

using this set of equations and the implicit function theorem (i.e. $\mathbf{y}_p = \mathbf{y}_p(\mathbf{y}_{sv})$) we can determine,

$$\frac{\partial\mathbf{y}_{sv}}{\partial\mathbf{y}_p} = - \left(\frac{\partial\Psi_{sv}}{\partial\mathbf{y}_{sv}} \right)^{-1} \frac{\partial\Psi_{sv}}{\partial\mathbf{y}_p} \quad (5.38)$$

Furthermore, the calculation of the contribution of the tertiary variables $\partial \mathbf{y}_{\text{tv}} / \partial \mathbf{y}_{\text{p}}$ are obtained in the same manner, using relationships for the cell average variables, cell boundary variables, and rock media interfaces variables:

Cell Average Variables

- The phase densities and its derivatives with respect the reference pressure and mass flows are obtained from the selected Equation of State (EoS). In principle, any EoS of state can be implemented due to the modularity of COSI. For this study, Peng-Robinson EoS was employed.
- The viscosity is computed through correlations, in the default case, by the compositional viscosity correlation proposed by Lorenz, Bray, and Clark (LBC) [80].
- Porosity and rock compressibility values and its derivatives, are calculated straightforward from $\phi_m = \phi_m(P_m)$ and $\{K\}_m = \{K(P_m)\}$.
- Capillary pressure is obtained from phase saturation and interfacial tension by interpolation in a table. Afterward, the phase pressures are updated using the capillary pressure constraints in (Eq. 5.10). For the case of gas-oil pressure, the interfacial tension is dependent on the phase pressures and mass flows. For this study, the parachor model is used for computing $\sigma_{j\bar{j}}$ and obtaining the respective derivatives.

Cell Boundary Variables

The boundary variables are defined from the cell average variables values. And depending on the choice, the accuracy and stability will vary. The general approach is to get a type of average value from the cells that share the boundary. The most simple approach is to use the upstream cell average variable. This is called single-point upstream weighting method. Single-point weighting leads to a numerically stable finite-differences scheme if the mobilities are evaluated at the current time step, and conditionally stable if evaluated at the previous time step [81]. Therefore, using it for FIM is appropriate.

5.2. Integration of Capillary Pressure Effect on Phase Behavior in COSI

In the context of reservoir simulation, phase equilibrium calculations are generally performed at the reference pressure P_{ref} for all the phases. After reaching equilibrium, the capillary pressure values and derivatives are updated externally using the phase densities and saturation. However, as shown in Chapter 2, the capillary pressure between the oil and gas phase has an important effect on the phase equilibrium. Therefore it is convenient to consider the capillary effect during phase split calculations in relevant cases such as in production from tight reservoirs.

The central idea of integrating the capillary pressure effect in phase equilibrium into a FIM reservoir simulation is to couple (Eq. 5.11) with (Eq. 5.10) as follows,

$$f_{jref}^i(P_{jref}, \mathbf{C}_{jref}) = f_j^i(P_j, \mathbf{C}_j) \quad (5.39)$$

This corresponds to the flash procedure described in Section 2.2 of Chapter 2. The coupling of these constraints has to be done in a consistent way and additional considerations have to be taken into account. The following sections describe such changes and give some recommendations in its implementation.

5.2.1. Change of Variables in Thermodynamic Subroutines

In order to work with a capillary pressure difference in phase equilibrium, modifications in the standard thermodynamic routines are needed. By considering a capillary pressure difference into the system, negative pressures can be encountered for the liquid phase in cases where the gas pressure is selected as the reference pressure. A suggested modification is the change of variable from the fugacity coefficients to its multiplication with the phase pressure ($\varphi_i \rightarrow \varphi_i P$). This avoids obtaining undefined values when determining its logarithm as it is done in standard practice

$$RT \ln \varphi_i = -\frac{\partial}{\partial n_i} \left(\int_{\infty}^V \left(P - \frac{nRT}{V} \right) dV \right) - RT \ln Z \quad (5.40)$$

adding $(RT \ln P)$ in both sides of the equation yields

$$RT \ln(\varphi_i P) = -\frac{\partial}{\partial n_i} \left(\int_{\infty}^V \left(P - \frac{nRT}{V} \right) dV \right) - RT \ln \left(\frac{Z}{P} \right) \quad (5.41)$$

this allows us to compute the new variable at any pressure. The first term on the right-hand side can always be calculated no matter the pressure is positive or not. The second term always have the same sign for Z and P . Hence, its ratio is always positive and the logarithm of the ratio can be calculated at any pressure. The overall expression therefore has no problem even at negative liquid pressures. The necessary derivatives of the new variable ($F = \varphi_i P$) need to be determined. Fortunately, the new derivatives can be easily related to the derivatives of the fugacity coefficient.

$$\frac{\partial \ln F_i}{\partial T} = \frac{\partial \ln \varphi_i}{\partial T} \quad (5.42)$$

$$\frac{\partial \ln F_i}{\partial P} = \frac{\partial \ln \varphi_i}{\partial P} + \frac{1}{P} \quad (5.43)$$

$$\frac{\partial \ln F_i}{\partial n_j} = \frac{\partial \ln \varphi_i}{\partial n_j} \quad (5.44)$$

The new set of variables is more advantageous for calculations that involve negative pressures, and it is straightforward to implement into thermodynamic routines.

5.2.2. The Capillary Pressure Model

One important consideration when coupling the capillary pressure is to maintain consistency between the chosen capillary pressure model for phase equilibrium and the one chosen to update the phase pressure and derivatives for the flow equations. For instance, it is not recommended to use a Young-Laplace equation at a constant capillary radius for the phase equilibrium calculations together with a J-function approach for the update of the phase pressures and derivatives for the mass conservation equations. If a Young-Laplace model at a constant capillary radius is chosen, the equivalent choice of J-function would be a constant. Therefore, the capillary pressure and its derivatives will entirely depend on the interfacial tension. If a J-function model is selected, the coupling with the phase equilibrium calculations must be done accordingly. This may introduce additional difficulties in the flash procedure. Such difficulties, will be discussed later in Section 5.3.2.

In order to account for the contribution of the capillary pressure in the Jacobian matrix in (Eq. 5.36), the derivatives of the selected model must be obtained. The derivatives of the capillary pressure with respect to the primary variables must be calculated after obtaining the values from the phase split calculations. These will

depend on the choice of capillary pressure model. Let us assume a somehow general expression of the capillary pressure model as follows,

$$P_{cj} = \frac{\sigma_j(P, P_g, \mathbf{C}, \mathbf{C}_g)}{R(S_j)} \quad (5.45)$$

where the subscript *jref* is dropped for the oil phase, and the *j* phase corresponds to the gas phase for convenience. Moreover, it is assumed that the interfacial tension is a function of the phase pressures and concentrations, and the effective curvature is a function of the saturation (i.e. variable pore size). The derivatives with respect to the primary variables can be written as follows:

$$\frac{\partial P_{cj}}{\partial P} = \frac{1}{R(S_j)} \frac{\partial \sigma_j}{\partial P} - \frac{\sigma_{cj}}{R^2(S_j)} \frac{\partial R(S_j)}{\partial S_j} \frac{\partial S_j}{\partial P} \quad (5.46)$$

$$\frac{\partial P_{cj}}{\partial m^i} = \frac{1}{R(S_j)} \frac{\partial \sigma_j}{\partial m^i} - \frac{\sigma_{cj}}{R^2(S_j)} \frac{\partial R(S_j)}{\partial S_j} \frac{\partial S_j}{\partial m^i} \quad (5.47)$$

where the second term on the right-hand side vanishes in cases where the pore radius is assumed to be constant. Moreover, the phase pressure derivatives with respect to the primary variables can be written as a function of the capillary pressure derivatives.

$$\frac{\partial P_j}{\partial P} = 1 + \frac{\partial P_{cj}}{\partial P} \quad (5.48)$$

$$\frac{\partial P_j}{\partial m^i} = \frac{\partial P_{cj}}{\partial m^i} \quad (5.49)$$

Furthermore, the capillary pressure difference is also a function of the secondary dependent variables. The phase pressure derivatives can be related as follows,

$$\frac{\partial P_j}{\partial C_j^i} = \frac{\partial P_{cj}}{\partial \sigma_j} \left(\frac{\partial \sigma_j}{\partial C_j^i} \right)_S \quad (5.50)$$

$$\frac{\partial P_j}{\partial S} = \frac{\partial P_{cj}}{\partial S} \quad (5.51)$$

We can further expand the required derivatives using a defined interfacial tension model. The modification implemented in COSI corresponds to the parachor model

$$\sigma^{1/E} = \sum_{i=1}^{N_c} \chi_i (x_i \tilde{\rho}^l - y_i \tilde{\rho}^g) \quad (5.52)$$

where χ_i are the parachor constants, $\tilde{\rho}$ is the molar density and x_i and y_i the molar

fractions of the oil and gas phases respectively. We can recall some useful derivatives of the parachor model with respect to the phase pressures and molar fractions from Chapter 2

$$\frac{\partial \sigma_j}{\partial P_l} = -E \sigma^{\frac{E-1}{E}} \sum_{i=1}^{N_c} \chi_i \left[\frac{x_i}{V_l^2} \frac{\partial V_l}{\partial P_l} \right] \quad (5.53)$$

$$\frac{\partial \sigma_j}{\partial P_g} = E \sigma^{\frac{E-1}{E}} \sum_{i=1}^{N_c} \chi_i \left[\frac{y_i}{V_g^2} \frac{\partial V_g}{\partial P_g} \right] \quad (5.54)$$

$$\frac{\partial \sigma_j}{\partial x_i} = -E \sigma^{\frac{E-1}{E}} \left[\frac{\chi_i}{V_l} + \frac{V_l - V_{li}}{V_l^2} \sum_k^{N_c} \chi_k x_k \right] \quad (5.55)$$

$$\frac{\partial \sigma_j}{\partial y_i} = E \sigma^{\frac{E-1}{E}} \left[\frac{\chi_i}{V_g} + \frac{V_g - V_{gi}}{V_g^2} \sum_k^{N_c} \chi_k y_k \right] \quad (5.56)$$

The derivatives with respect the phase pressure can be directly used in (Eq. 5.46). The last step is to relate these derivatives to the required ones with respect to the remaining primary and secondary variables. The molar fraction derivatives can be related to the concentration derivatives using the molecular weights

$$\frac{\partial \sigma_j}{\partial C_g^i} = \left(\frac{\bar{W}_g}{W^i} \right) \frac{\partial \sigma_j}{\partial y^i}, \quad \frac{\partial \sigma_j}{\partial C_l^i} = \left(\frac{\bar{W}_l}{W^i} \right) \frac{\partial \sigma_j}{\partial x^i} \quad (5.57)$$

where W^i is the molar weight of component i , and \bar{W} is the average molar weight of the phase. Finally, these derivatives can be related to the total mass flows to obtain the interfacial tension derivative.

$$\frac{\partial \sigma_j}{\partial m^i} = \sum_k \frac{\partial \sigma_j}{\partial C_k^i} \frac{\partial C_k^i}{\partial m^i} \quad (5.58)$$

The remaining derivatives of effective curvature $R(S)$ can be obtained from the choice of variable pore size model. For a constant pore radius, these derivatives are going to vanish. However, if a function such as the Leverett J-function is chosen, the effective curvature as a function of the phase saturation can be written as follows

$$R(S) = \frac{\sqrt{k/\phi}}{J(S)} \quad (5.59)$$

the remaining derivative will depend on the selected J-function and can be obtained straightforward

$$\frac{\partial R(S)}{\partial S} = -\frac{J'(S)}{J^2(S)}\sqrt{k/\phi} \quad (5.60)$$

With this last relationship, we have now all the necessary derivatives to evaluate the terms in (Eq. 5.46) and (Eq. 5.47). The remaining relationships and derivatives between the primary and secondary variables can be obtained using (Eq. 5.38).

5.3. Case of Study

A two-dimensional reservoir with a total of 10 planar fractures along a horizontal well was selected to emulate a natural depletion of a tight reservoir using the compositional simulator COSI. Local grid refinement (LGR) was applied to accurately model the fracture-matrix flow exchange. The dimensions used were similar to those from Whitson and Sunjerga [44], and Lei et al. [82]. A schematic view of the grid is presented in Figure 5.1. The grid dimensions are presented in Table 5.1 and Table 5.2. The grid along the fracture direction corresponds to half of the reservoir, being the horizontal well the middle of the reservoir in y -direction. The grid along the well (x -direction), corresponds to a fracture length and should be repeated periodically to construct all ten fractures.

The initial temperature and pressure of the reservoir are 400 K and 300 bar respectively. The porosity of the matrix is 0.04 and the one of the fractures is 0.25. The conductivity of the fracture is 1000 (mD/ft), and the fracture half length is 45.72 m (150 ft). The wellbore diameter is 0.127 m (5 inch), and the operation bottomhole pressure is 50 bar. The simulation is performed for a total of 30 years, which corresponds to a similar production time used in Zhang et al. [19].

A fluid from the Bakken field was used for all the simulation scenarios. The description is given in Table 5.3 and was taken from Nojabaei et al. [32]. Peng-Robinson EoS was used for the fluid description. Moreover, the LBC correlation was used to calculate the viscosity of the gas and oil phases.

The oil-gas relative permeability curves were taken from Yu et al. [83]. They were obtained by means of history matching with a field production well from the Middle Bakken [84]. The curves are used for all the cases, and are presented in Figure 5.2.

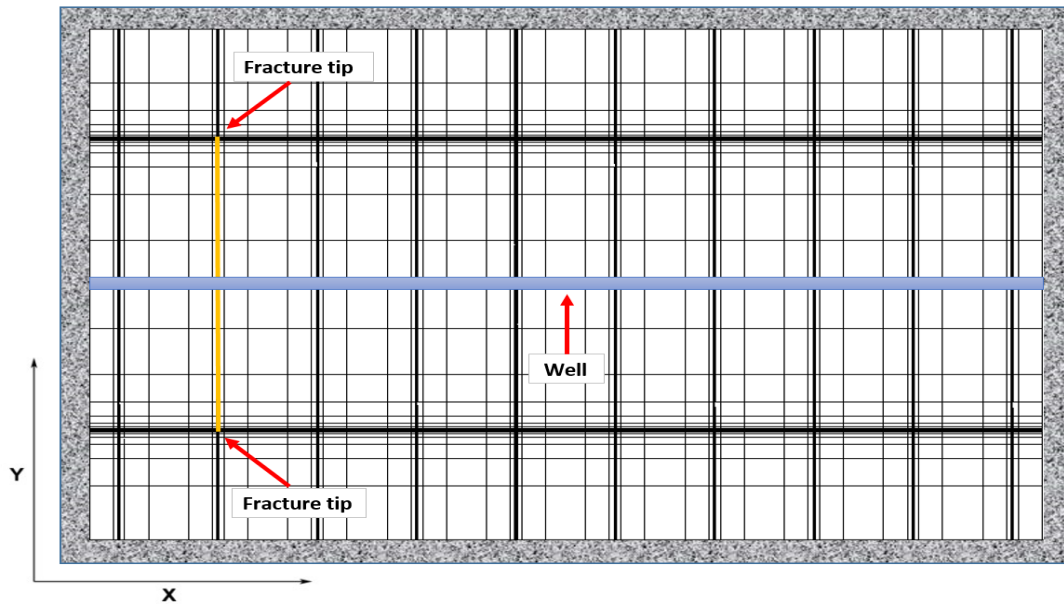


FIGURE 5.1.: Top view of the two-dimensional reservoir with 10 planar fractures. x-length = 914.4m (3000 ft), y-length = 182.9m (600 ft), z-thickness = 76.2 m (250 ft).

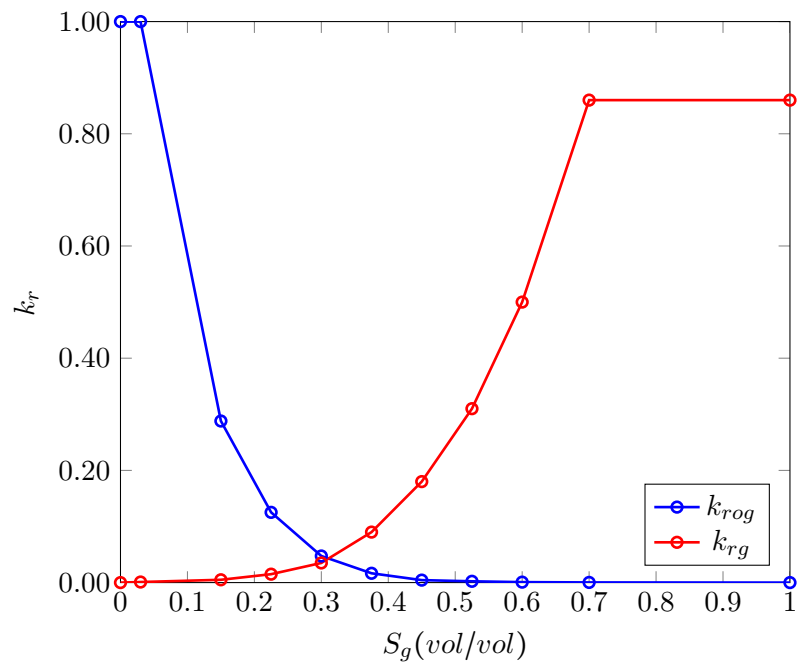


FIGURE 5.2.: Relative permeability curves for the oil and gas phases. Data obtained from Yu et al. [83]

TABLE 5.1.: Gridding along the Y-axis (along the fracture). See Figure 5.1 for reference.

Y-cell index	$\Delta Y(m)$	Cell name
1	22.605	
2	11.435	
3	5.784	
4	2.926	
5	1.480	
6	0.749	
7	0.379	
8	0.192	
9	0.097	
10	0.049	
11	0.025	Matrix
12	0.025	Tip of the fracture
13	0.049	
14	0.097	
15	0.192	
16	0.379	
17	0.749	
18	1.480	
19	2.926	
20	5.784	
21	11.435	
22	17.605	
23	10.000	Well

TABLE 5.2.: Periodic gridding along the X-axis (along the well). See Figure 5.1 for reference.

X-cell index	$\Delta X(m)$	Cell name
1	36.832	
2	7.160	
3	1.392	
4	0.271	
5	0.053	
6	0.025	Fracture Cell
7	0.053	
8	0.271	
9	1.392	
10	7.160	
11	36.832	

TABLE 5.3.: Compositional data for Bakken oil

Component	Composition	P_{crit} (bar)	T_{crit} (K)	ω	Parachor
C ₁	0.36736	45.162	186.297	0.0102	74.8
C ₂	0.14885	49.779	305.538	0.1028	107.7
C ₃	0.09334	42.455	369.983	0.1520	151.9
C ₄	0.05751	37.677	421.782	0.1894	189.6
C ₅ -C ₆	0.06406	31.804	486.377	0.2684	250.2
C ₇ -C ₁₂	0.15854	25.051	585.138	0.4291	350.2
C ₁₃ -C ₂₁	0.0733	17.210	740.052	0.7203	590.0
C ₂₂ -C ₈₀	0.03704	13.108	1024.717	1.0159	1216.8

5.3.1. Fixed Pore Size

Different pore sizes are tested to examine the impact of the capillary pressure. A pore geometry of interconnected capillary tubes with a constant radius is assumed. Therefore, the Young-Laplace equation inside a tube is chosen

$$P_c = \frac{2\sigma \cos \theta}{r_c} \quad (5.61)$$

where σ is calculated using the parachor model in (Eq. 5.52) using $E = 4$ for the scaling exponent. The parachor values are presented in Table 5.3. We are aware that assuming a fixed pore radius is a simplification of the matrix nature. However, evaluating the oil production at different capillary radii is useful to evaluate the magnitude of change in the results.

5.3.2. Variable Pore Size

In general, porous materials are more complex than a network of capillary tubes with a constant radius. Instead, they are conformed by different pore sizes determined by a particular pore size distribution. For instance, shale reservoirs have pore size distributions that range in the nanometer scale. In general, the heterogeneity nature of a pore size distribution makes several properties to be function of the phase saturation. One important property, is the capillary pressure. The Leverett J-function curves are employed to account for this pore size distribution in the capillary pressure [85]. The J-function is a function of the phase saturation, rock porosity, and permeability. It can be written as follows:

$$J(S) = \frac{P_c(S)\sqrt{k/\phi}}{\sigma \cos \theta} \quad (5.62)$$

where ϕ is the rock porosity, k is the rock permeability in (m^{-2}), and θ the contact angle. This is equivalent to consider an effective capillary radius as a function of the saturation. Moreover, this relationship can be obtained by replacing the Young-Laplace equation inside a capillary tube for P_c in (Eq. 5.62) as follows:

$$J(S) = \frac{2\sqrt{k/\phi}}{r_c(S)} \rightarrow r_c(S) = \frac{2\sqrt{k/\phi}}{J(S)} \quad (5.63)$$

If we assume a constant capillary radius, the J-function is reduced to a constant value, corresponding to the particular case of the Young-Laplace equation in a capillary tube. In our case, by using the J-function, we are indirectly considering that effective pore size decreases as the oil saturation decreases. Moreover, the capillary radius at $S_{oil} = 1$, corresponds to the effective capillary radius at the bubble point. Hence, the bubble point transition occurs in the biggest pores. However, as we decrease the oil saturation the effective capillary radius becomes smaller as seen in Figure 5.3, therefore, higher deviations from conventional phase equilibrium are expected.

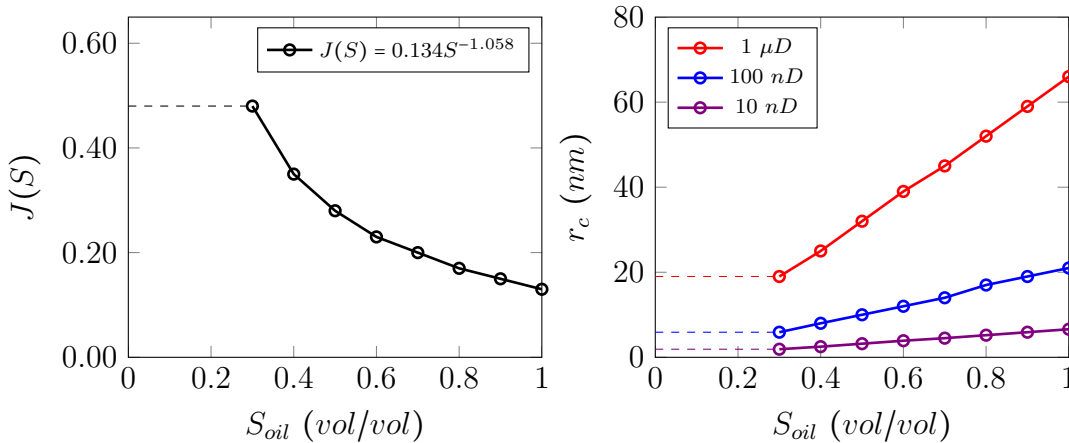


FIGURE 5.3.: [Left] J-function (taken from Brooks and Corey [86]). [Right] Effective capillary radius based on J-function at different rock permeability.

A J-function approach appears easier to implement into reservoir simulators, since the capability is already there. In reality, this only increases the difficulty of the problem because a more complex capillary pressure model needs to couple with phase equilibrium calculations. In general, it is important to maintain consistency in the capillary pressure model used to update the phase pressures during the simulation, and the capillary pressure model used for the phase equilibrium calculations. For instance, if a constant capillary radius is used, the equivalent J-function would be a

constant and the capillary pressure will be subjected only to changes in the interfacial tension. On the other hand, if a J-function approach is chosen, the effective capillary radius is now a function of the phase fraction, which at the same time is the solution of the flash problem (i.e. β). Hence, the level of implicitness of the problem makes the calculations more costly.

As shown in Chapter 2, the flash problem considering capillary pressure finds the solution to the following equations

$$\mathbf{FP}_1 = \begin{cases} \ln f_i^g(P_g, \mathbf{y}) - \ln f_i^l(P_l, \mathbf{x}) \\ z_i - \beta y_i - (1 - \beta)x_i \\ P_g - P_l - \frac{2\sigma(P_l, P_g, \mathbf{x}, \mathbf{y})}{r_c(\beta)} \end{cases} = \mathbf{0} \quad (5.64)$$

where complete wetting of the oil phase is assumed ($\theta = 0$). Unlike the calculations done at a constant capillary radius, the solution of capillary pressure not only depends on the final phase pressures and compositions, but also on the phase saturation. As a result, the successive substitution procedure on the capillary pressure will be much slower in comparison to a constant capillary radius approach. Nevertheless, the same procedure as in Section 2.2 of Chapter 2 was implemented without having additional problems except for the slower convergence.

The modified stability analysis requires also some slight modifications. In contrast to the flash procedure, this modifications does not impact on the convergence. Since the effective capillary radius at the bubble point is $r_c(S_{oil} = 1)$, a constant capillary radius is used at this value when the feed phase is assumed liquid and the trial phase a vapor. For the case where the feed phase is assumed vapor, and the trial phase a liquid, we need to use an effective capillary radius at $r_c(S_{oil} = 0)$. However, the J-function is not defined at such phase fraction, therefore, a cut off value must be introduced as an approximation. For the case of Figure 5.3, $r_c(S_{oil} = 0)$ would correspond to $r_c(S_{oil} \approx 0.3)$. Nevertheless, this approximation is not relevant for the depletion scenarios considered in this study since only stability analysis close to the bubble point is needed.

5.4. Results

Different capillary radii ranging from 5 nm to 100 nm were used to evaluate the impact of the capillary pressure in phase equilibrium for the accumulated oil and gas production, solution gas oil ratio, pressure profiles, and saturation profiles. Additionally, a variable capillary radius based on the Leverett J-function was tested at two different rock permeabilities (Figure 5.3 with $1\mu D$ and $100nD$). Table 5.4 shows the different tested scenarios.

TABLE 5.4.: Simulation scenarios. Labeling given by letter and subscript.

r_c (nm)	$k = 1\mu D$	$k = 100nD$	Color code
∞ (=bulk)	A_1	A_2	—
5	B_1	-	---
10	C_1	C_2	---
20	D_1	-	---
100	E_1	-	---
$r_c(S)$	F_1	F_2	---

Results are shown from Figure 5.4 to Figure 5.18. Production without using the effect of capillary pressure in phase equilibrium is considerably different from those when the effective capillary radius is less than 20 nm. Figure 5.4 and 5.5 show the cumulative oil and gas production of 30 years for a reservoir of rock permeability of $1\mu D$ for cases A_1 to F_1 . In general, an increase in both gas and oil production can be observed as the capillary radius decreases. Furthermore, approximately 8% more oil is produced from case B_1 in comparison to the oil produced from case A_1 (no P_c). The difference is smaller for the accumulated gas production ($\approx 2.7\%$) and Figure 5.5 suggests that this difference may decrease over time. On the other hand, cases E_1 and F_1 have a negligible impact, and the impact of cases C_1 and D_1 can be considered moderate, and should not be neglected. Figure 5.6 and Figure 5.7 illustrate the oil saturation inside the reservoir after 30 years of production for cases A_1 and C_1 . Saturation map for the case A_1 is slightly lower in comparison to the saturation map for the case C_1 . This seems contradictory with the results observed from the accumulated oil production together with the fact that we are using the same reservoir fluid. However, this can be explained by the capillary pressure effect on phase behavior. The bubble point is suppressed, and this is translated to a delayed two-phase region that allows a longer production from the single-phase liquid region. Figure 5.8 illustrates the shift of the bubble point of case A_1 and C_1 . Similar to the bubble point shift, the saturation lines are also shifted to lower pressures, delaying the gas saturation of the reservoir.

The impact of the suppression of the bubble point can also be observed in the reservoir solution gas-oil ratio (R_s) in Figure 5.9. In general, when the capillary pressure effect is considered in the phase behavior, a longer region with a constant GOR is obtained as seen in Fig 5.9. Once more, the most relevant cases are B_1 , C_1 and D_1 . As the capillary radius is reduced, this region becomes bigger. Moreover, the producing (GOR) has different behavior over the time for the different cases as shown in Figure 5.10. In the first five years, case A_1 has a slightly lower GOR than the rest of the cases. Furthermore, after the fifth year the GOR for the case A_1 increases much faster than the other cases considering capillary pressure on the phase behavior. This difference keeps increasing over time, and all the cases (B_1 to F_1) have a noticeable effect that cannot be neglected. In specific, cases B_1 and C_1 have approximately 10% and 16% lower producing GOR after 30 years of production. In general, a lighter fluid with higher methane composition is produced at the beginning of the first years yielding slightly higher GOR as shown in Figure 5.11. This implies that lighter components will be present in the liquid phase when capillary pressure effect is considered. Furthermore, while cases B_1 to E_1 show a tendency on the changes as the capillary radius is reduced, F_1 shows a more unusual behavior due to the heterogeneity of the pore size distribution.

The pressure behavior inside the reservoir, as well as the oil production and GOR, show some differences when the capillary pressure effect is considered. Figure 5.12 shows the pressure drop of the reservoir over time for all the cases. It can be observed that as the capillary radius decreases the pressure drop is higher. This is a direct consequence of the suppression of the bubble point due to capillarity. When the bubble point is shifted to lower pressures, the reservoir is maintained in the single phase for a longer period than the conventional case (A_1), having a further pressure drop before the pressure is stabilized by the appearance of the incipient gas phase. After a two-phase region is reached in all the reservoir, the pressure drop becomes very slow over the time. Figure 5.13 and 5.14 show the pressure map after 30 years of production for cases A_1 and C_1 . Unlike the differences in the saturation map, the differences in the pressure map are more pronounced. It can be observed that the pressure after 30 years is lower in C_1 than A_1 , especially close to the fractures and the horizontal well. On average, as shown in Figure 5.12, the pressure drop is close to 5 bar, however, the pressure map shows that in some areas this pressure difference can be higher.

A more tight reservoir with a rock permeability of 100 nD was tested to observe the main differences between the use of a variable pore size and a fixed pore size. The

use of the J-function gives a variable pore size that ranges from 10 nm to 20 nm as shown in Figure 5.3. The most appropriate comparison would be with one of a fixed pore radius of 10 nm and another one of 20 nm (C_2 and D_2). The results are shown from Figure 5.15 to Figure 5.18. In general the behavior of a variable pore size, case F_2 , is more similar to D_2 than C_2 . Moreover, the accumulated oil production, solution gas-oil ratio, and pressure profile are almost identical. The only perceived difference is encountered at the first years for the producing GOR, however, after the third year F_2 follows the same behavior as D_2 . This suggests that for a natural depletion case, the effective pore size at the bubble point $r_c(\beta = 0)$, will have the biggest influence on the production profile since the production is quite slow, and the saturation values are close to the unity. This is not expected to change under the same conditions unless we run the simulation for several more years. Nevertheless, this may not be the case for other production scenarios where low oil saturation values can be encountered such as gas injection scenarios. Furthermore, the choice of J-function may influence the results. Therefore, it is recommended to study different production scenarios and different choices of J-function in the future in order to make a complete assessment.

5.5. Conclusions

In this chapter, we presented a procedure to include the capillary pressure effect on phase behavior into a fully implicit compositional reservoir simulator. General guidelines are given in order to modify thermodynamic subroutines that can handle cases with negative liquid pressures that may be potentially encountered during simulation involving high capillary pressures. Moreover, details and recommendations on how to integrate the capillary pressure model into the numerical framework in a consistent way are presented. In general, including the capillary pressure difference requires a modification on how the flash calculations for phase splitting are made and how the phase pressures are updated in the different parts of the simulator. Moreover, derivatives of the capillary pressure model with respect to the primary and secondary variables are required to include the contributions in the general Jacobian matrix. Its implementation will depend on the complexity of the capillary pressure model and the implicit level of the numerical model.

A natural depletion case of a tight reservoir was used to test the features added to the simulator. The case consists of a two-dimensional reservoir with a series of planar fractures along a horizontal well. It uses a single porosity media with local

grid refinement in the x and y direction along to the fractures to capture the flow interchange with a low permeable matrix of $1\mu D$ and $100nD$. The simulator is able to handle different capillary pressure models with fixed and variable effective capillary radius. Moreover, tests were performed to analyze the effect of capillary pressure in phase behavior in the context of reservoir simulation. In general, the simulated oil and gas production considering capillary pressure differs from that using the conventional approach where capillary pressure is not included in phase equilibrium. The accumulated oil production increases due to the delay single liquid phase production window caused by the suppression of the bubble point. This has a direct impact on the pressure production profile and on the pressure distribution at the end of the production period. Moreover, the producing GOR after 30 years is considerably lower for cases with capillary radii less than 20 nm. On the other hand, a variable pore size capillary pressure model shows similar results to those obtained at fixed capillary radius. In the long term, the results are closer to a fixed pore size calculated at the bubble point ($r_c(S_{oil} = 1)$). However, for the first years of production, some deviations can be noticed, especially in the producing GOR. The obtained results are preliminary, and a more extensive analysis using different production scenarios and reservoir fluids is recommended for the future work.

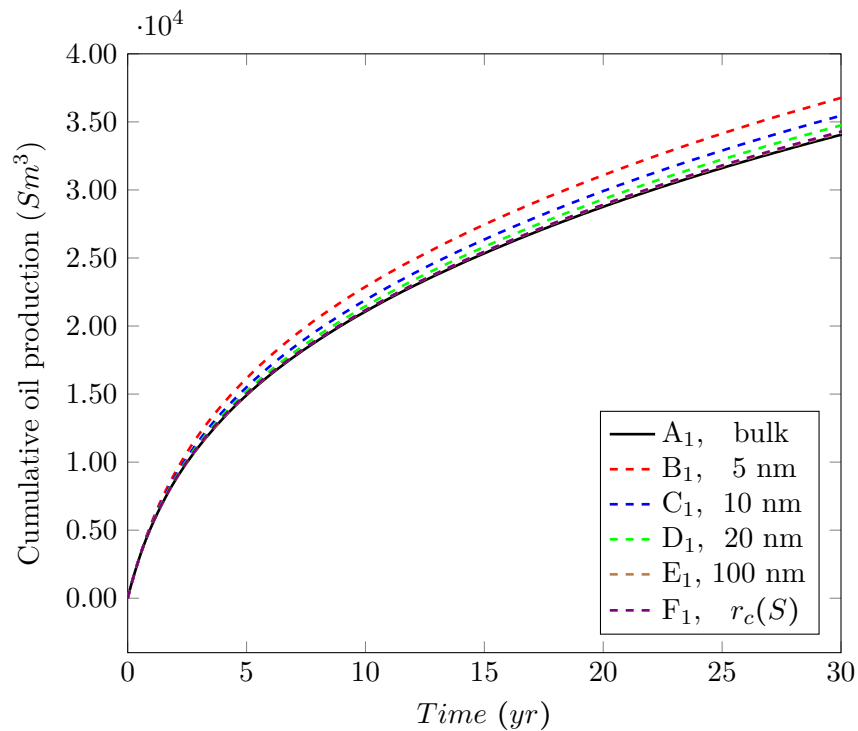


FIGURE 5.4.: Cumulative oil production. Rock permeability $K = 1\mu D$

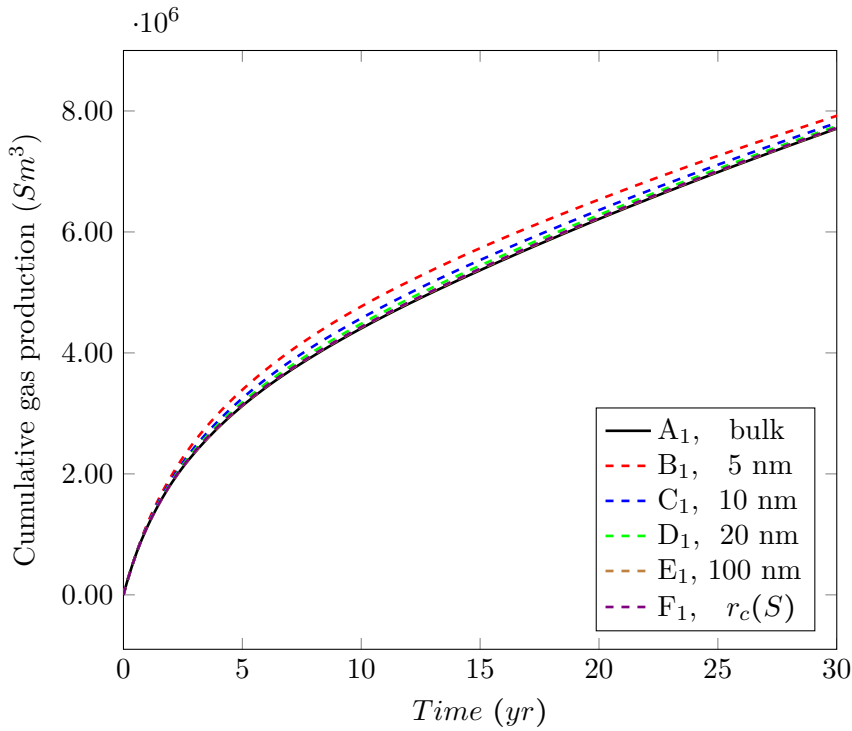


FIGURE 5.5.: Cumulative gas production. Rock permeability $K = 1\mu D$. Cases A_1 to F_1

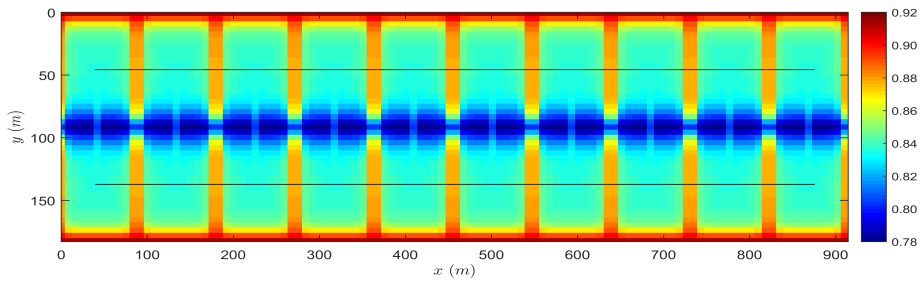


FIGURE 5.6.: Oil saturation map at $yr = 30$ for case A_1 . Solid lines (—) indicate the tip of the fractures

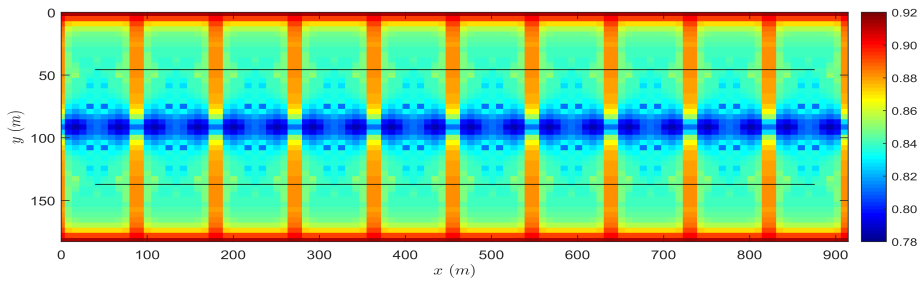
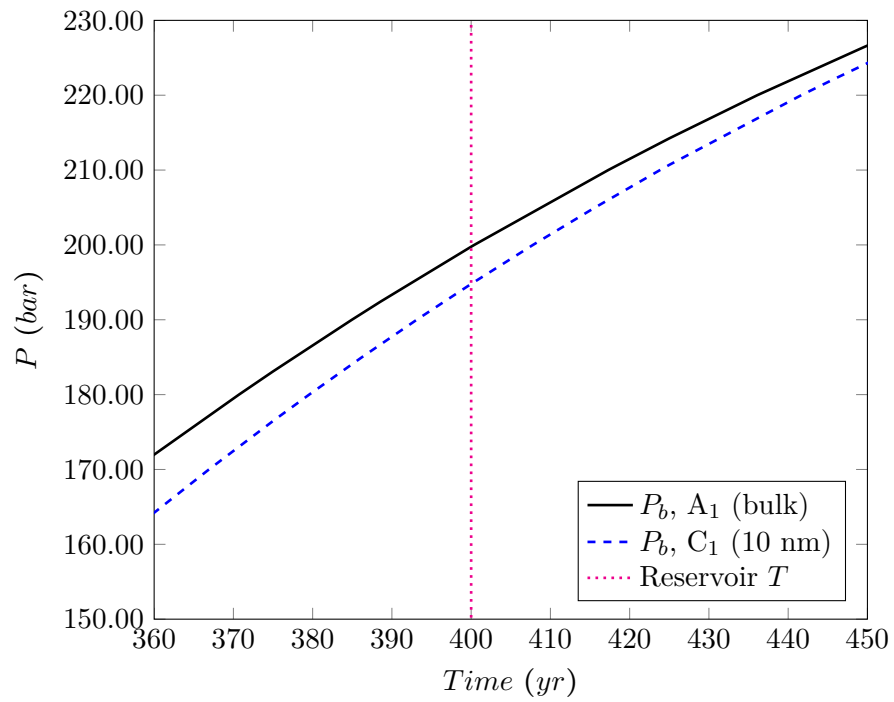
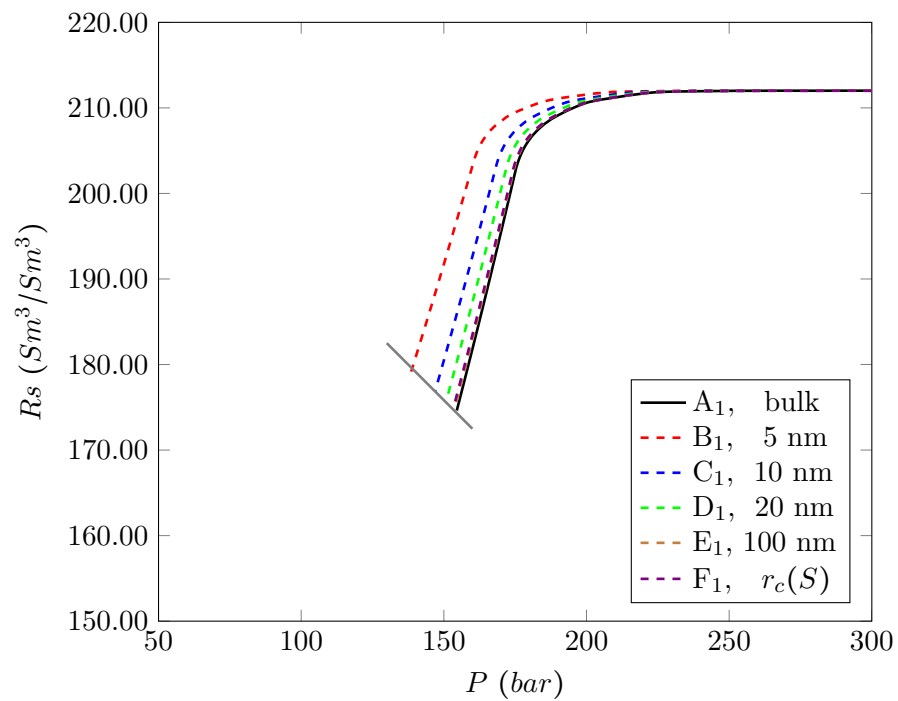


FIGURE 5.7.: Oil saturation map at $yr = 30$ for case C_1 . Solid lines (—) indicate the tip of the fractures

FIGURE 5.8.: Bubble point of the Bakken fluid for cases A_1 and C_1 FIGURE 5.9.: Solution Gas-Oil ratio (R_s) as function of the average pressure of the reservoir. Cases A_1 to F_1

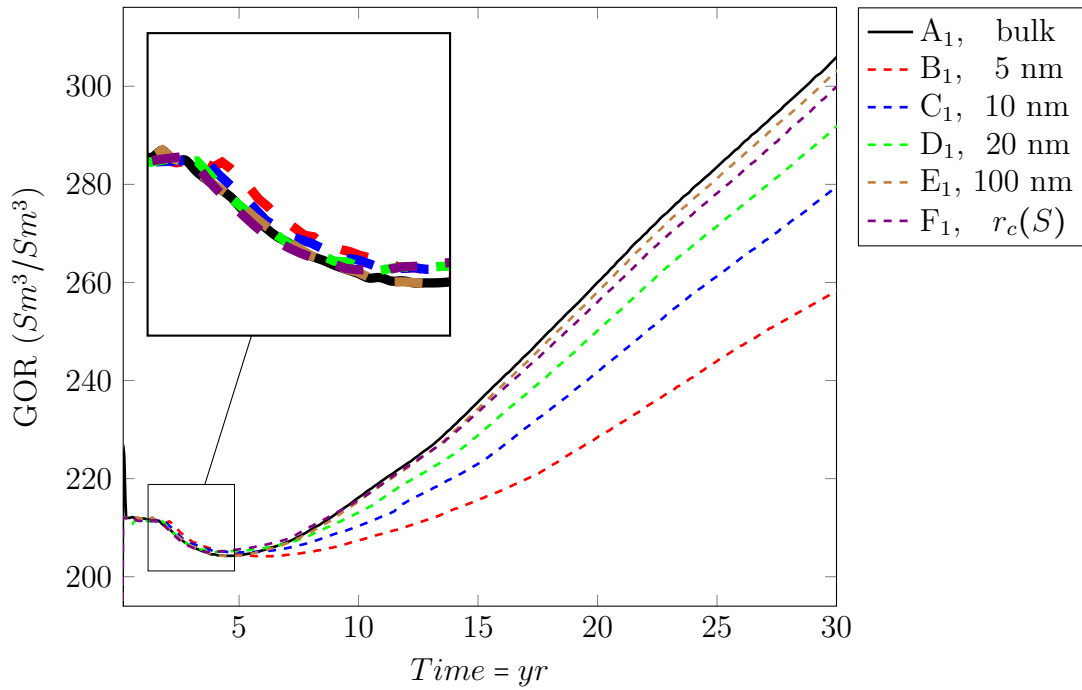


FIGURE 5.10.: Producing Gas-Oil ratio over time. Cases A_1 to F_1

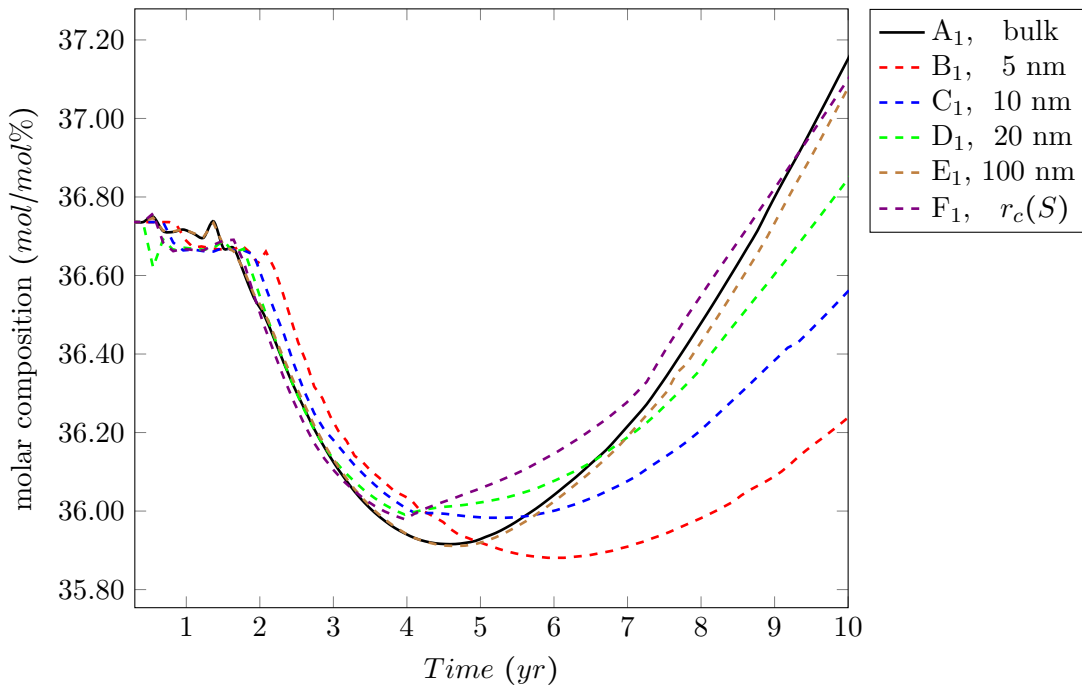


FIGURE 5.11.: C_1 molar composition at production. Rock permeability $K = 1\mu D$. Cases A_1 to F_1 .

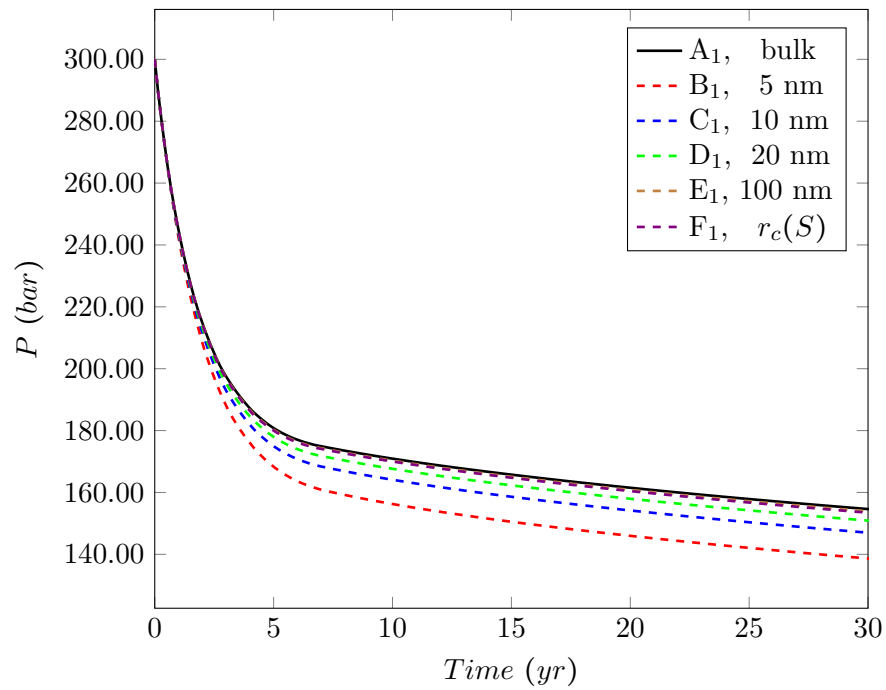


FIGURE 5.12.: Average pressure profile of the reservoir. Rock permeability $K = 1 \mu D$. Cases A_1 to F_1

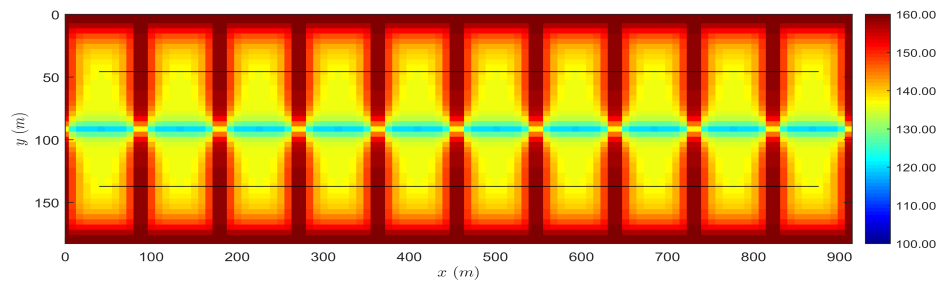


FIGURE 5.13.: Pressure map at $yr = 30$ for case A_1 . Solid lines (—) indicate the tip of the fractures

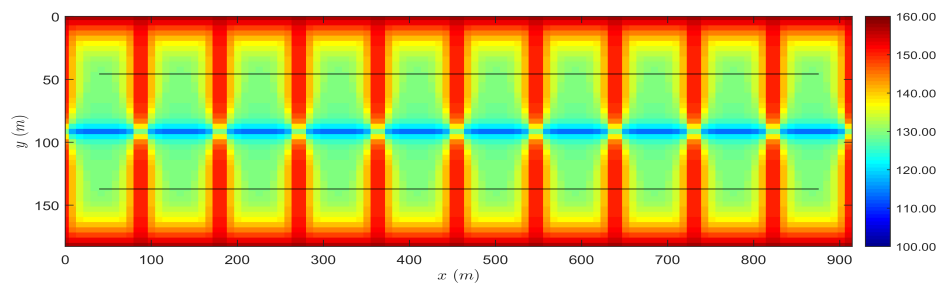


FIGURE 5.14.: Pressure map at $yr = 30$ for case C_1 . Solid lines (—) indicate the tip of the fractures

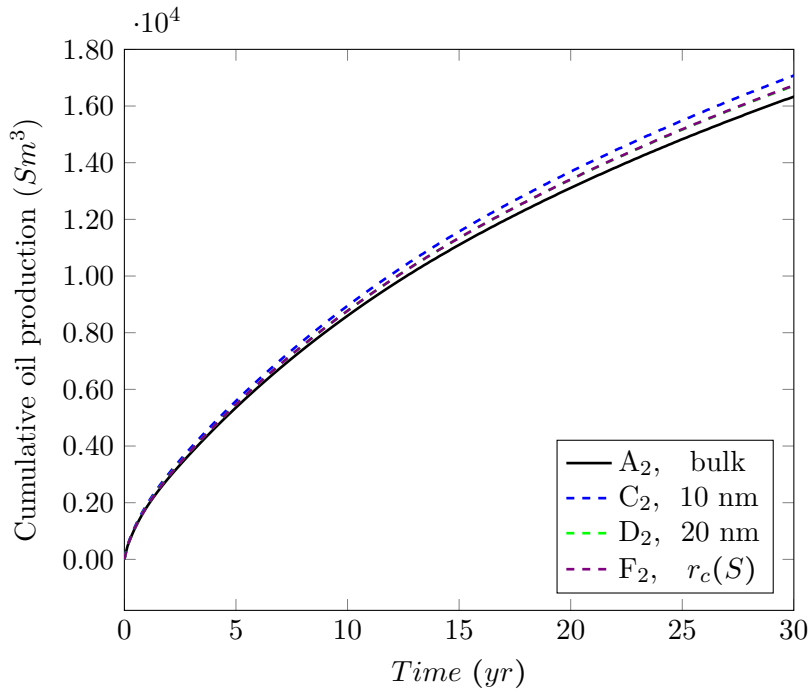


FIGURE 5.15.: Cumulative oil production. Rock permeability $K = 100$ nD. Cases A_2 to F_2

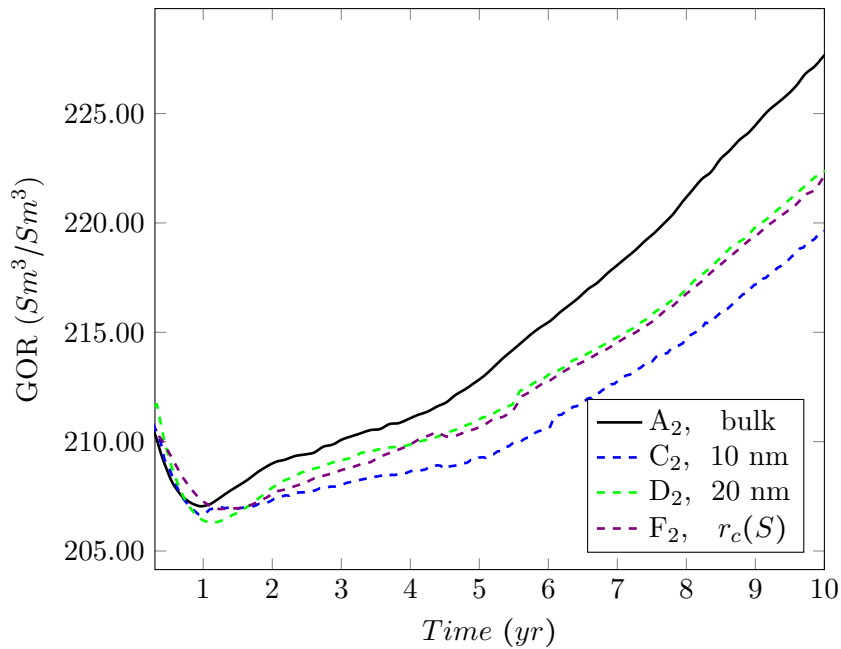


FIGURE 5.16.: Producing Gas-Oil ratio over time. Cases A_2 to F_2 .

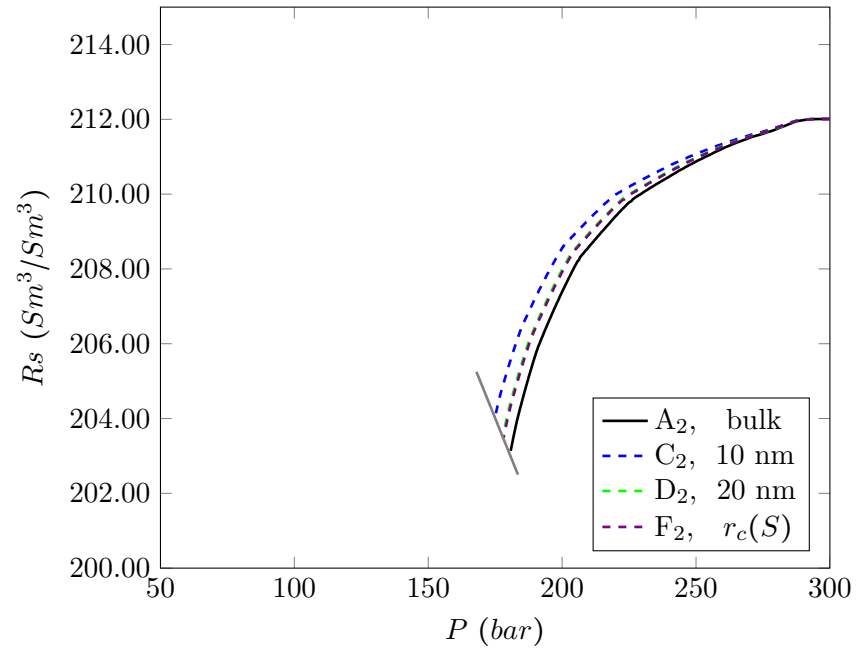


FIGURE 5.17.: Solution Gas-Oil ratio (R_s) as function of the average reservoir pressure. Cases A_2 to F_2

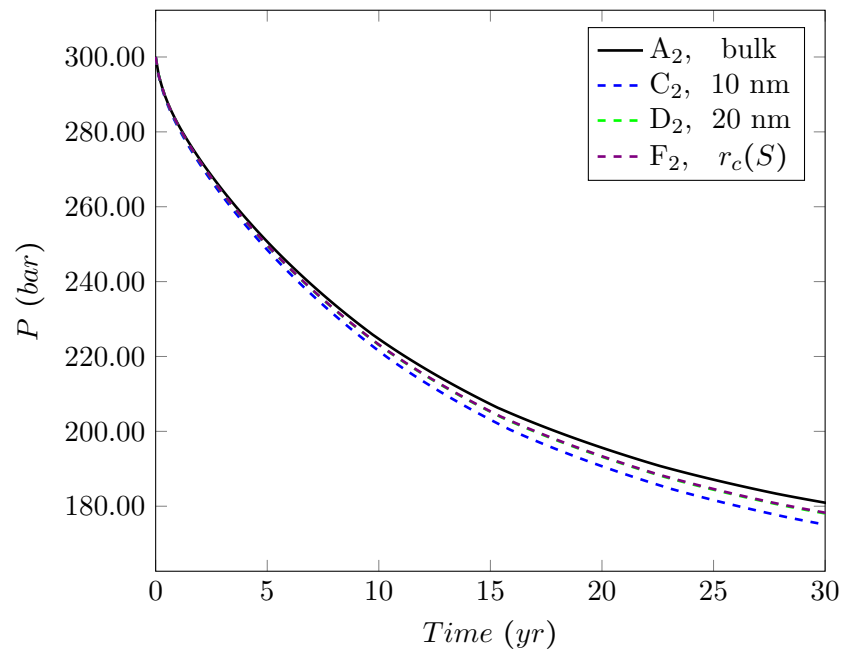


FIGURE 5.18.: Average pressure profile of the reservoir. Cases A_2 to F_2

CHAPTER 6

Conclusions

This thesis has focused on phase equilibrium modeling of capillary and adsorption effects in porous media which is a central issue in the shale production. Several phase equilibrium calculation tools have been developed by combining equations of state based thermodynamic modeling with capillary pressure expressions and adsorption models of different complexities. The tools serve two major purposes: first, they are used to analyze the capillary and adsorption effects at a wide range of temperature, pressure and composition conditions; second, some of the tools can be used as modules in compositional reservoir simulation. To serve these purposes, robustness and efficiency have been emphasized on the algorithmic aspect of the developed tools. In addition, the thesis has dealt with theoretical analysis of phase envelope shift under capillarity, evaluation of adsorption models for shale, and development of compositional reservoir simulation with capillary pressure. The detailed conclusions are summarized below.

For the capillary pressure effect alone, two algorithms were developed: one for tracing the phase envelope and another one for isothermal flash calculations. Additionally, a mathematical analysis of the changes in the phase envelope was provided. The phase envelope algorithm shows to be efficient and robust. It can automatically trace the phase boundary of a multicomponent mixture under a capillary pressure difference. A shift in the entire phase envelope is observed except at the critical point. Specifically, the bubble point pressure and the lower dew point pressure are suppressed, and the upper dew point pressure and temperature of the criconden-therm are increased. The observed changes are enhanced as the capillary radius

decreases. On the other hand, the flash algorithms, both P_g and P_l specifications, showed to be convergent in all the temperature and pressure range tested. The increase of the computational cost associated with capillary pressure effect in flash calculations is around 40% for the tested systems. Moreover, a stability analysis, based on a modified tangent plane distance considering capillary pressure, was used to check the correctness of the results obtained by the flash algorithm. Furthermore, the linear relationships derived from the mathematical analysis, are used to predict the direction of the shift of the phase envelope, prior to solving the system of equations for phase equilibrium. In some cases, they can estimate with accuracy the magnitude of the shift in bubble point and upper dew point.

A model comparison for adsorption of pure components and binary mixtures in shale at high-pressures was presented. It was found that for pure components, the models tested can fit with similar accuracy the adsorption isotherm data. Langmuir, Toth, and MPTA-DRA yield absolute average deviations lower than 10%. However, MPTA+DRA is able to achieve the same results with fewer parameters. The reason behind is the temperature independence on the model parameters, which makes MPTA+DRA a flexible predictive model. For multicomponent systems, MPTA+DRA shows the best prediction for the adsorbed amounts with an absolute average deviation of 17.9% followed by ML and IAST+Langmuir with 26.1% and 27.0%, respectively. Furthermore, the binary system C_1 - CO_2 shows to be more challenging than the C_1 - C_2 system. Large differences in the individual pure component isotherms between C_1 and CO_2 partly explains the low accuracy of all the models in the prediction of this binary mixture.

The combined effect of capillary pressure and adsorption was also studied. A modification of the algorithm for phase envelope calculations was used to include the effect of the adsorption film thickness. The modification of the capillary radius enhances the capillarity of the system. The effects were found to be negligible close to the critical point, and moderate far away from it. The magnitude of the calculated adsorption film thickness along the phase envelope, suggests that adsorbed phase is approximately a single layer. Therefore, the changes in the capillary radius will be of importance only at very low pore sizes. Moreover, a flash algorithm that accounts for both capillary pressure and adsorption was developed. It was used to test various systems, from a binary system to a five-component mixture representative of a reservoir fluid. MPTA was used as a tool to generate artificial adsorption data for different hydrocarbons. The data was then used to determine model parameters of ML to model the adsorbed phase. The results obtained from the tested systems

show that adsorption and capillary pressure can significantly change the bulk phase composition and thus its corresponding phase envelope. In general, a much shrunk phase envelope with shifted critical point is observed. Adsorption in the liquid phase appears to be moderate, thus, obtaining small deviations in the bubble point region. On the other hand, effects at low pressures and high temperatures are more pronounced due to strong adsorption selectivity towards heavier components. As a result, changes in the dew point region are abrupt.

Finally, the integration of capillary pressure effects into a fully implicit compositional simulator was accomplished. Recommendations on how to consistently integrate the capillary pressure on phase behavior and flow equations are given. The added capability was used to test the impact of the capillary pressure on phase behavior in reservoir simulation and oil production from tight reservoirs in general. A natural depletion case consisting of a two-dimensional reservoir with a series of planar fractures along a horizontal well was used as a test case. Different permeability and capillary pressure functions were evaluated. In general, when considering capillary pressure on phase behavior, the accumulated oil production increases. One of the reasons is the extension of the single liquid phase production window caused by the suppression of the bubble point. This has a direct impact on the pressure production profile and on the pressure distribution at the end of the production period. Moreover, the producing GOR after 30 years is considerably lower for cases with capillary radii less than 20 nm than for the case without considering capillarity. On the other hand, a variable pore size capillary pressure model show similar results to those obtained at fixed capillary radius, suggesting that the bigger pores of the distribution play a major role during the production of an oil reservoir. The simulation results are preliminary, and a more extensive analysis using different production scenarios and reservoir fluids are recommended.

APPENDIX *A***Artificial Adsorption Data of Alkanes
on Shale Using MPTA**

TABLE A.1.: Summary of Langmuir fittings for the artificial data.

Alkane	T (K)	n^{max}	b (bar ⁻¹)	RMS ($\frac{mmol}{g}$)	AAD
C ₁	223.15	$3.37 \cdot 10^{-1}$	$8.16 \cdot 10^{-2}$	$1.24 \cdot 10^{-2}$	9.4%
	323.15	$2.85 \cdot 10^{-1}$	$1.93 \cdot 10^{-2}$	$7.14 \cdot 10^{-3}$	15.5%
	373.15	$2.71 \cdot 10^{-1}$	$1.15 \cdot 10^{-2}$	$5.21 \cdot 10^{-3}$	17.5%
	423.15	$2.61 \cdot 10^{-1}$	$7.60 \cdot 10^{-3}$	$3.66 \cdot 10^{-3}$	17.8%
	473.15	$2.53 \cdot 10^{-1}$	$5.49 \cdot 10^{-3}$	$2.53 \cdot 10^{-3}$	16.8%
573.15	$2.16 \cdot 10^{-1}$	$4.15 \cdot 10^{-3}$	$1.83 \cdot 10^{-3}$	9.0%	
C ₂	223.15	$2.46 \cdot 10^{-1}$	$2.05 \cdot 10^0$	$1.37 \cdot 10^{-2}$	7.0%
	323.15	$2.34 \cdot 10^{-1}$	$9.86 \cdot 10^{-2}$	$7.81 \cdot 10^{-3}$	7.8%
	373.15	$2.19 \cdot 10^{-1}$	$5.07 \cdot 10^{-2}$	$6.32 \cdot 10^{-3}$	10.5%
	423.15	$2.06 \cdot 10^{-1}$	$3.01 \cdot 10^{-2}$	$5.25 \cdot 10^{-3}$	12.6%
	473.15	$1.95 \cdot 10^{-1}$	$1.93 \cdot 10^{-2}$	$4.38 \cdot 10^{-3}$	14.5%
573.15	$1.81 \cdot 10^{-1}$	$9.58 \cdot 10^{-3}$	$2.83 \cdot 10^{-3}$	17.0%	
C ₄	323.15	$1.40 \cdot 10^{-1}$	$2.26 \cdot 10^0$	$5.82 \cdot 10^{-3}$	2.5%
	373.15	$1.37 \cdot 10^{-1}$	$5.07 \cdot 10^{-1}$	$5.65 \cdot 10^{-3}$	3.3%
	423.15	$1.32 \cdot 10^{-1}$	$2.16 \cdot 10^{-1}$	$5.45 \cdot 10^{-3}$	6.0%
	473.15	$1.26 \cdot 10^{-1}$	$1.19 \cdot 10^{-1}$	$4.99 \cdot 10^{-3}$	8.2%
	573.15	$1.13 \cdot 10^{-1}$	$5.31 \cdot 10^{-2}$	$3.87 \cdot 10^{-3}$	11.4%
C ₈	323.15	$7.09 \cdot 10^{-2}$	$3.97 \cdot 10^2$	$4.58 \cdot 10^{-3}$	4.0%
	373.15	$6.95 \cdot 10^{-2}$	$6.61 \cdot 10^1$	$8.66 \cdot 10^{-3}$	16.8%
	423.15	$6.79 \cdot 10^{-2}$	$1.88 \cdot 10^1$	$8.18 \cdot 10^{-3}$	25.3%
	473.15	$6.64 \cdot 10^{-2}$	$6.72 \cdot 10^0$	$6.75 \cdot 10^{-3}$	21.9%
	573.15	$6.26 \cdot 10^{-2}$	$1.86 \cdot 10^0$	$6.01 \cdot 10^{-3}$	38.7%
C ₁₀	323.15	$5.69 \cdot 10^{-2}$	$2.26 \cdot 10^3$	$1.03 \cdot 10^{-3}$	1.7%
	373.15	$5.49 \cdot 10^{-2}$	$4.66 \cdot 10^2$	$3.80 \cdot 10^{-3}$	5.1%
	423.15	$5.41 \cdot 10^{-2}$	$1.09 \cdot 10^2$	$6.78 \cdot 10^{-3}$	16.1%
	473.15	$5.31 \cdot 10^{-2}$	$2.09 \cdot 10^1$	$5.45 \cdot 10^{-3}$	14.6%
	573.15	$5.10 \cdot 10^{-2}$	$6.50 \cdot 10^0$	$5.60 \cdot 10^{-3}$	22.9%
C ₁₂	323.15	$4.60 \cdot 10^{-2}$	$2.20 \cdot 10^4$	$9.60 \cdot 10^{-4}$	1.6%
	373.15	$4.53 \cdot 10^{-2}$	$3.69 \cdot 10^3$	$4.37 \cdot 10^{-3}$	8.4%
	423.15	$4.48 \cdot 10^{-2}$	$3.41 \cdot 10^2$	$4.02 \cdot 10^{-3}$	7.8%
	473.15	$4.43 \cdot 10^{-2}$	$4.86 \cdot 10^1$	$4.81 \cdot 10^{-3}$	10.9%
	573.15	$4.31 \cdot 10^{-2}$	$1.22 \cdot 10^1$	$4.92 \cdot 10^{-3}$	20.2%
C ₁₆	323.15	$3.23 \cdot 10^{-2}$	$1.44 \cdot 10^6$	$1.20 \cdot 10^{-3}$	1.5%
	373.15	$3.22 \cdot 10^{-2}$	$2.96 \cdot 10^4$	$4.10 \cdot 10^{-3}$	7.5%
	423.15	$3.19 \cdot 10^{-2}$	$4.63 \cdot 10^3$	$6.18 \cdot 10^{-3}$	21.5%
	473.15	$3.16 \cdot 10^{-2}$	$1.41 \cdot 10^3$	$5.87 \cdot 10^{-3}$	31.6%
	573.15	$3.10 \cdot 10^{-2}$	$2.98 \cdot 10^2$	$4.83 \cdot 10^{-3}$	48.1%

P (bar)	f (bar)	n^{exp} $\left(\frac{mmol}{g}\right)$	n^L $\left(\frac{mmol}{g}\right)$
0.10	0.10	$1.82 \cdot 10^{-2}$	$2.72 \cdot 10^{-3}$
1.00	0.99	$5.16 \cdot 10^{-2}$	$2.53 \cdot 10^{-2}$
2.00	1.98	$7.02 \cdot 10^{-2}$	$4.68 \cdot 10^{-2}$
3.00	2.95	$8.38 \cdot 10^{-2}$	$6.53 \cdot 10^{-2}$
4.00	3.92	$9.49 \cdot 10^{-2}$	$8.15 \cdot 10^{-2}$
5.00	4.87	$1.04 \cdot 10^{-1}$	$9.57 \cdot 10^{-2}$
6.00	5.81	$1.13 \cdot 10^{-1}$	$1.08 \cdot 10^{-1}$
7.00	6.74	$1.20 \cdot 10^{-1}$	$1.19 \cdot 10^{-1}$
8.00	7.66	$1.27 \cdot 10^{-1}$	$1.30 \cdot 10^{-1}$
10.00	9.48	$1.39 \cdot 10^{-1}$	$1.47 \cdot 10^{-1}$
12.00	11.25	$1.50 \cdot 10^{-1}$	$1.61 \cdot 10^{-1}$
15.00	13.83	$1.63 \cdot 10^{-1}$	$1.78 \cdot 10^{-1}$
20.00	17.95	$1.82 \cdot 10^{-1}$	$2.00 \cdot 10^{-1}$
50.00	37.91	$2.44 \cdot 10^{-1}$	$2.54 \cdot 10^{-1}$
100.00	57.28	$2.78 \cdot 10^{-1}$	$2.77 \cdot 10^{-1}$
150.00	70.22	$2.89 \cdot 10^{-1}$	$2.87 \cdot 10^{-1}$
200.00	82.63	$2.97 \cdot 10^{-1}$	$2.93 \cdot 10^{-1}$
250.00	95.55	$3.03 \cdot 10^{-1}$	$2.98 \cdot 10^{-1}$
300.00	109.40	$3.08 \cdot 10^{-1}$	$3.03 \cdot 10^{-1}$
400.00	140.50	$3.15 \cdot 10^{-1}$	$3.10 \cdot 10^{-1}$

TABLE A.2.: Artificial MPTA data (n^{exp}), and Langmuir fit (n^L) for C₁ at 223 K.

P (bar)	f (bar)	n^{exp} $\left(\frac{mmol}{g}\right)$	n^L $\left(\frac{mmol}{g}\right)$
0.10	0.10	$2.73 \cdot 10^{-3}$	$5.50 \cdot 10^{-4}$
1.00	1.00	$1.22 \cdot 10^{-2}$	$5.40 \cdot 10^{-3}$
2.00	1.99	$1.89 \cdot 10^{-2}$	$1.06 \cdot 10^{-2}$
3.00	2.99	$2.44 \cdot 10^{-2}$	$1.56 \cdot 10^{-2}$
4.00	3.97	$2.91 \cdot 10^{-2}$	$2.03 \cdot 10^{-2}$
5.00	4.96	$3.34 \cdot 10^{-2}$	$2.49 \cdot 10^{-2}$
6.00	5.94	$3.73 \cdot 10^{-2}$	$2.94 \cdot 10^{-2}$
7.00	6.92	$4.09 \cdot 10^{-2}$	$3.36 \cdot 10^{-2}$
8.00	7.89	$4.44 \cdot 10^{-2}$	$3.77 \cdot 10^{-2}$
10.00	9.83	$5.06 \cdot 10^{-2}$	$4.55 \cdot 10^{-2}$
12.00	11.76	$5.64 \cdot 10^{-2}$	$5.28 \cdot 10^{-2}$
15.00	14.63	$6.41 \cdot 10^{-2}$	$6.29 \cdot 10^{-2}$
20.00	19.35	$7.55 \cdot 10^{-2}$	$7.76 \cdot 10^{-2}$
50.00	46.17	$1.22 \cdot 10^{-1}$	$1.35 \cdot 10^{-1}$
100.00	86.25	$1.67 \cdot 10^{-1}$	$1.78 \cdot 10^{-1}$
150.00	122.40	$1.94 \cdot 10^{-1}$	$2.01 \cdot 10^{-1}$
200.00	156.60	$2.12 \cdot 10^{-1}$	$2.14 \cdot 10^{-1}$
250.00	190.10	$2.26 \cdot 10^{-1}$	$2.24 \cdot 10^{-1}$
300.00	223.90	$2.37 \cdot 10^{-1}$	$2.32 \cdot 10^{-1}$
400.00	294.80	$2.53 \cdot 10^{-1}$	$2.43 \cdot 10^{-1}$

TABLE A.3.: Artificial MPTA data (n^{exp}), and Langmuir fit (n^L) for C₁ at 323 K.

P (bar)	f (bar)	n^{exp} ($\frac{mmol}{g}$)	n^L ($\frac{mmol}{g}$)
0.10	0.10	$1.21 \cdot 10^{-3}$	$3.11 \cdot 10^{-4}$
1.00	1.00	$6.61 \cdot 10^{-3}$	$3.08 \cdot 10^{-3}$
2.00	2.00	$1.09 \cdot 10^{-2}$	$6.08 \cdot 10^{-3}$
3.00	2.99	$1.45 \cdot 10^{-2}$	$9.01 \cdot 10^{-3}$
4.00	3.98	$1.77 \cdot 10^{-2}$	$1.19 \cdot 10^{-2}$
5.00	4.98	$2.07 \cdot 10^{-2}$	$1.47 \cdot 10^{-2}$
6.00	5.97	$2.35 \cdot 10^{-2}$	$1.74 \cdot 10^{-2}$
7.00	6.95	$2.61 \cdot 10^{-2}$	$2.01 \cdot 10^{-2}$
8.00	7.94	$2.85 \cdot 10^{-2}$	$2.27 \cdot 10^{-2}$
10.00	9.90	$3.31 \cdot 10^{-2}$	$2.77 \cdot 10^{-2}$
12.00	11.86	$3.74 \cdot 10^{-2}$	$3.25 \cdot 10^{-2}$
15.00	14.79	$4.33 \cdot 10^{-2}$	$3.94 \cdot 10^{-2}$
20.00	19.62	$5.21 \cdot 10^{-2}$	$4.99 \cdot 10^{-2}$
50.00	47.79	$9.07 \cdot 10^{-2}$	$9.61 \cdot 10^{-2}$
100.00	92.10	$1.31 \cdot 10^{-1}$	$1.39 \cdot 10^{-1}$
150.00	134.20	$1.58 \cdot 10^{-1}$	$1.64 \cdot 10^{-1}$
200.00	175.30	$1.78 \cdot 10^{-1}$	$1.81 \cdot 10^{-1}$
250.00	216.10	$1.93 \cdot 10^{-1}$	$1.93 \cdot 10^{-1}$
300.00	257.50	$2.05 \cdot 10^{-1}$	$2.03 \cdot 10^{-1}$
400.00	343.70	$2.24 \cdot 10^{-1}$	$2.16 \cdot 10^{-1}$

TABLE A.4.: Artificial MPTA data (n^{exp}), and Langmuir fit (n^L) for C₁ at 373 K.

P (bar)	f (bar)	n^{exp} ($\frac{mmol}{g}$)	n^L ($\frac{mmol}{g}$)
0.10	0.10	$5.93 \cdot 10^{-4}$	$1.98 \cdot 10^{-4}$
1.00	1.00	$3.87 \cdot 10^{-3}$	$1.97 \cdot 10^{-3}$
2.00	2.00	$6.68 \cdot 10^{-3}$	$3.91 \cdot 10^{-3}$
3.00	3.00	$9.16 \cdot 10^{-3}$	$5.81 \cdot 10^{-3}$
4.00	3.99	$1.14 \cdot 10^{-2}$	$7.69 \cdot 10^{-3}$
5.00	4.99	$1.36 \cdot 10^{-2}$	$9.53 \cdot 10^{-3}$
6.00	5.98	$1.56 \cdot 10^{-2}$	$1.14 \cdot 10^{-2}$
7.00	6.97	$1.75 \cdot 10^{-2}$	$1.31 \cdot 10^{-2}$
8.00	7.97	$1.93 \cdot 10^{-2}$	$1.49 \cdot 10^{-2}$
10.00	9.95	$2.28 \cdot 10^{-2}$	$1.84 \cdot 10^{-2}$
12.00	11.92	$2.60 \cdot 10^{-2}$	$2.17 \cdot 10^{-2}$
15.00	14.88	$3.06 \cdot 10^{-2}$	$2.65 \cdot 10^{-2}$
20.00	19.79	$3.75 \cdot 10^{-2}$	$3.41 \cdot 10^{-2}$
50.00	48.77	$6.93 \cdot 10^{-2}$	$7.06 \cdot 10^{-2}$
100.00	95.70	$1.05 \cdot 10^{-1}$	$1.10 \cdot 10^{-1}$
150.00	141.60	$1.31 \cdot 10^{-1}$	$1.35 \cdot 10^{-1}$
200.00	187.20	$1.50 \cdot 10^{-1}$	$1.53 \cdot 10^{-1}$
250.00	233.10	$1.66 \cdot 10^{-1}$	$1.67 \cdot 10^{-1}$
300.00	279.80	$1.79 \cdot 10^{-1}$	$1.78 \cdot 10^{-1}$
400.00	377.20	$1.99 \cdot 10^{-1}$	$1.94 \cdot 10^{-1}$

TABLE A.5.: Artificial MPTA data (n^{exp}), and Langmuir fit (n^L) for C₁ at 423 K.

P (bar)	f (bar)	n^{exp} $\left(\frac{mmol}{g}\right)$	n^L $\left(\frac{mmol}{g}\right)$
0.10	0.10	$3.24 \cdot 10^{-4}$	$1.39 \cdot 10^{-4}$
1.00	1.00	$2.43 \cdot 10^{-3}$	$1.38 \cdot 10^{-3}$
2.00	2.00	$4.38 \cdot 10^{-3}$	$2.75 \cdot 10^{-3}$
3.00	3.00	$6.14 \cdot 10^{-3}$	$4.10 \cdot 10^{-3}$
4.00	4.00	$7.79 \cdot 10^{-3}$	$5.43 \cdot 10^{-3}$
5.00	4.99	$9.36 \cdot 10^{-3}$	$6.75 \cdot 10^{-3}$
6.00	5.99	$1.09 \cdot 10^{-2}$	$8.06 \cdot 10^{-3}$
7.00	6.99	$1.23 \cdot 10^{-2}$	$9.35 \cdot 10^{-3}$
8.00	7.98	$1.37 \cdot 10^{-2}$	$1.06 \cdot 10^{-2}$
10.00	9.97	$1.63 \cdot 10^{-2}$	$1.31 \cdot 10^{-2}$
12.00	11.96	$1.89 \cdot 10^{-2}$	$1.56 \cdot 10^{-2}$
15.00	14.94	$2.24 \cdot 10^{-2}$	$1.92 \cdot 10^{-2}$
20.00	19.89	$2.80 \cdot 10^{-2}$	$2.49 \cdot 10^{-2}$
50.00	49.40	$5.45 \cdot 10^{-2}$	$5.40 \cdot 10^{-2}$
100.00	98.00	$8.61 \cdot 10^{-2}$	$8.86 \cdot 10^{-2}$
150.00	146.40	$1.10 \cdot 10^{-1}$	$1.13 \cdot 10^{-1}$
200.00	195.00	$1.28 \cdot 10^{-1}$	$1.31 \cdot 10^{-1}$
250.00	244.30	$1.44 \cdot 10^{-1}$	$1.45 \cdot 10^{-1}$
300.00	294.70	$1.57 \cdot 10^{-1}$	$1.57 \cdot 10^{-1}$
400.00	399.90	$1.78 \cdot 10^{-1}$	$1.74 \cdot 10^{-1}$

TABLE A.6.: Artificial MPTA data (n^{exp}), and Langmuir fit (n^L) for C₁ at 473 K.

P (bar)	f (bar)	n^{exp} $\left(\frac{mmol}{g}\right)$	n^L $\left(\frac{mmol}{g}\right)$
0.10	0.10	$1.31 \cdot 10^{-4}$	$8.96 \cdot 10^{-5}$
1.00	1.00	$1.17 \cdot 10^{-3}$	$8.92 \cdot 10^{-4}$
2.00	2.00	$2.22 \cdot 10^{-3}$	$1.78 \cdot 10^{-3}$
3.00	3.00	$3.22 \cdot 10^{-3}$	$2.66 \cdot 10^{-3}$
4.00	4.00	$4.18 \cdot 10^{-3}$	$3.53 \cdot 10^{-3}$
5.00	5.00	$5.12 \cdot 10^{-3}$	$4.39 \cdot 10^{-3}$
6.00	6.00	$6.02 \cdot 10^{-3}$	$5.25 \cdot 10^{-3}$
7.00	7.00	$6.91 \cdot 10^{-3}$	$6.10 \cdot 10^{-3}$
8.00	8.00	$7.77 \cdot 10^{-3}$	$6.94 \cdot 10^{-3}$
10.00	10.00	$9.46 \cdot 10^{-3}$	$8.61 \cdot 10^{-3}$
12.00	12.00	$1.11 \cdot 10^{-2}$	$1.02 \cdot 10^{-2}$
15.00	15.00	$1.34 \cdot 10^{-2}$	$1.27 \cdot 10^{-2}$
20.00	20.01	$1.72 \cdot 10^{-2}$	$1.66 \cdot 10^{-2}$
50.00	50.07	$3.62 \cdot 10^{-2}$	$3.72 \cdot 10^{-2}$
100.00	100.50	$6.08 \cdot 10^{-2}$	$6.36 \cdot 10^{-2}$
150.00	151.60	$8.05 \cdot 10^{-2}$	$8.34 \cdot 10^{-2}$
200.00	203.60	$9.69 \cdot 10^{-2}$	$9.89 \cdot 10^{-2}$
250.00	256.80	$1.11 \cdot 10^{-1}$	$1.12 \cdot 10^{-1}$
300.00	311.40	$1.23 \cdot 10^{-1}$	$1.22 \cdot 10^{-1}$
400.00	425.60	$1.44 \cdot 10^{-1}$	$1.38 \cdot 10^{-1}$

TABLE A.7.: Artificial MPTA data (n^{exp}), and Langmuir fit (n^L) for C₁ at 573 K.

P (bar)	f (bar)	n^{exp} ($\frac{mmol}{g}$)	n^L ($\frac{mmol}{g}$)
0.05	0.05	$5.59 \cdot 10^{-2}$	$2.29 \cdot 10^{-2}$
0.10	0.10	$6.96 \cdot 10^{-2}$	$4.18 \cdot 10^{-2}$
0.20	0.20	$8.65 \cdot 10^{-2}$	$7.14 \cdot 10^{-2}$
0.30	0.30	$9.81 \cdot 10^{-2}$	$9.34 \cdot 10^{-2}$
0.40	0.40	$1.07 \cdot 10^{-1}$	$1.10 \cdot 10^{-1}$
0.50	0.50	$1.14 \cdot 10^{-1}$	$1.24 \cdot 10^{-1}$
1.00	0.98	$1.41 \cdot 10^{-1}$	$1.64 \cdot 10^{-1}$
2.00	1.93	$1.74 \cdot 10^{-1}$	$1.96 \cdot 10^{-1}$
3.00	2.84	$1.96 \cdot 10^{-1}$	$2.10 \cdot 10^{-1}$
4.00	3.71	$2.12 \cdot 10^{-1}$	$2.18 \cdot 10^{-1}$
5.00	4.55	$2.25 \cdot 10^{-1}$	$2.22 \cdot 10^{-1}$
6.00	4.98	$2.31 \cdot 10^{-1}$	$2.24 \cdot 10^{-1}$
7.00	4.99	$2.31 \cdot 10^{-1}$	$2.24 \cdot 10^{-1}$
8.00	5.01	$2.31 \cdot 10^{-1}$	$2.24 \cdot 10^{-1}$
9.00	5.02	$2.31 \cdot 10^{-1}$	$2.24 \cdot 10^{-1}$
10.00	5.04	$2.31 \cdot 10^{-1}$	$2.24 \cdot 10^{-1}$
50.00	5.69	$2.32 \cdot 10^{-1}$	$2.27 \cdot 10^{-1}$
100.00	6.60	$2.33 \cdot 10^{-1}$	$2.29 \cdot 10^{-1}$
300.00	11.71	$2.38 \cdot 10^{-1}$	$2.36 \cdot 10^{-1}$
400.00	15.45	$2.39 \cdot 10^{-1}$	$2.39 \cdot 10^{-1}$

TABLE A.8.: Artificial MPTA data (n^{exp}), and Langmuir fit (n^L) for C₂ at 223 K.

P (bar)	f (bar)	n^{exp} ($\frac{mmol}{g}$)	n^L ($\frac{mmol}{g}$)
0.10	0.10	$1.36 \cdot 10^{-2}$	$2.28 \cdot 10^{-3}$
1.00	0.99	$3.89 \cdot 10^{-2}$	$2.09 \cdot 10^{-2}$
2.00	1.97	$5.31 \cdot 10^{-2}$	$3.81 \cdot 10^{-2}$
3.00	2.94	$6.35 \cdot 10^{-2}$	$5.26 \cdot 10^{-2}$
4.00	3.90	$7.20 \cdot 10^{-2}$	$6.49 \cdot 10^{-2}$
5.00	4.84	$7.93 \cdot 10^{-2}$	$7.55 \cdot 10^{-2}$
6.00	5.77	$8.57 \cdot 10^{-2}$	$8.48 \cdot 10^{-2}$
7.00	6.68	$9.14 \cdot 10^{-2}$	$9.29 \cdot 10^{-2}$
8.00	7.58	$9.66 \cdot 10^{-2}$	$1.00 \cdot 10^{-1}$
10.00	9.35	$1.06 \cdot 10^{-1}$	$1.12 \cdot 10^{-1}$
12.00	11.07	$1.14 \cdot 10^{-1}$	$1.22 \cdot 10^{-1}$
15.00	13.55	$1.24 \cdot 10^{-1}$	$1.34 \cdot 10^{-1}$
20.00	17.45	$1.38 \cdot 10^{-1}$	$1.48 \cdot 10^{-1}$
50.00	34.83	$1.81 \cdot 10^{-1}$	$1.81 \cdot 10^{-1}$
100.00	46.33	$1.95 \cdot 10^{-1}$	$1.92 \cdot 10^{-1}$
150.00	54.57	$2.00 \cdot 10^{-1}$	$1.97 \cdot 10^{-1}$
200.00	63.07	$2.04 \cdot 10^{-1}$	$2.02 \cdot 10^{-1}$
250.00	72.16	$2.07 \cdot 10^{-1}$	$2.05 \cdot 10^{-1}$
300.00	82.01	$2.10 \cdot 10^{-1}$	$2.08 \cdot 10^{-1}$
400.00	104.50	$2.14 \cdot 10^{-1}$	$2.13 \cdot 10^{-1}$

TABLE A.9.: Artificial MPTA data (n^{exp}), and Langmuir fit (n^L) for C₂ at 323 K.

$P(\text{bar})$	$f(\text{bar})$	$n^{exp} \left(\frac{\text{mmol}}{\text{g}} \right)$	$n^L \left(\frac{\text{mmol}}{\text{g}} \right)$
0.10	0.10	$6.48 \cdot 10^{-3}$	$1.11 \cdot 10^{-3}$
1.00	1.00	$2.19 \cdot 10^{-2}$	$1.05 \cdot 10^{-2}$
2.00	1.98	$3.14 \cdot 10^{-2}$	$2.00 \cdot 10^{-2}$
3.00	2.96	$3.86 \cdot 10^{-2}$	$2.86 \cdot 10^{-2}$
4.00	3.93	$4.47 \cdot 10^{-2}$	$3.64 \cdot 10^{-2}$
5.00	4.89	$5.00 \cdot 10^{-2}$	$4.36 \cdot 10^{-2}$
6.00	5.85	$5.47 \cdot 10^{-2}$	$5.01 \cdot 10^{-2}$
7.00	6.79	$5.90 \cdot 10^{-2}$	$5.62 \cdot 10^{-2}$
8.00	7.73	$6.29 \cdot 10^{-2}$	$6.17 \cdot 10^{-2}$
10.00	9.58	$7.01 \cdot 10^{-2}$	$7.17 \cdot 10^{-2}$
12.00	11.39	$7.63 \cdot 10^{-2}$	$8.03 \cdot 10^{-2}$
15.00	14.06	$8.46 \cdot 10^{-2}$	$9.12 \cdot 10^{-2}$
20.00	18.34	$9.62 \cdot 10^{-2}$	$1.06 \cdot 10^{-1}$
50.00	40.25	$1.38 \cdot 10^{-1}$	$1.47 \cdot 10^{-1}$
100.00	65.19	$1.66 \cdot 10^{-1}$	$1.68 \cdot 10^{-1}$
150.00	82.61	$1.78 \cdot 10^{-1}$	$1.77 \cdot 10^{-1}$
200.00	98.26	$1.85 \cdot 10^{-1}$	$1.83 \cdot 10^{-1}$
250.00	114.00	$1.89 \cdot 10^{-1}$	$1.87 \cdot 10^{-1}$
300.00	130.50	$1.93 \cdot 10^{-1}$	$1.91 \cdot 10^{-1}$
400.00	166.80	$2.00 \cdot 10^{-1}$	$1.96 \cdot 10^{-1}$

TABLE A.10.: Artificial MPTA data (n^{exp}), and Langmuir fit (n^L) for C_2 at 373 K.

$P(\text{bar})$	$f(\text{bar})$	$n^{exp} \left(\frac{\text{mmol}}{\text{g}} \right)$	$n^L \left(\frac{\text{mmol}}{\text{g}} \right)$
0.10	0.10	$3.26 \cdot 10^{-3}$	$6.17 \cdot 10^{-4}$
1.00	1.00	$1.29 \cdot 10^{-2}$	$5.99 \cdot 10^{-3}$
2.00	1.99	$1.94 \cdot 10^{-2}$	$1.16 \cdot 10^{-2}$
3.00	2.97	$2.45 \cdot 10^{-2}$	$1.69 \cdot 10^{-2}$
4.00	3.95	$2.89 \cdot 10^{-2}$	$2.19 \cdot 10^{-2}$
5.00	4.93	$3.28 \cdot 10^{-2}$	$2.66 \cdot 10^{-2}$
6.00	5.90	$3.63 \cdot 10^{-2}$	$3.10 \cdot 10^{-2}$
7.00	6.86	$3.96 \cdot 10^{-2}$	$3.52 \cdot 10^{-2}$
8.00	7.82	$4.26 \cdot 10^{-2}$	$3.92 \cdot 10^{-2}$
10.00	9.72	$4.81 \cdot 10^{-2}$	$4.65 \cdot 10^{-2}$
12.00	11.60	$5.31 \cdot 10^{-2}$	$5.32 \cdot 10^{-2}$
15.00	14.37	$5.97 \cdot 10^{-2}$	$6.21 \cdot 10^{-2}$
20.00	18.90	$6.92 \cdot 10^{-2}$	$7.46 \cdot 10^{-2}$
50.00	43.49	$1.06 \cdot 10^{-1}$	$1.17 \cdot 10^{-1}$
100.00	76.67	$1.37 \cdot 10^{-1}$	$1.44 \cdot 10^{-1}$
150.00	103.60	$1.54 \cdot 10^{-1}$	$1.56 \cdot 10^{-1}$
200.00	127.90	$1.64 \cdot 10^{-1}$	$1.63 \cdot 10^{-1}$
250.00	151.40	$1.71 \cdot 10^{-1}$	$1.69 \cdot 10^{-1}$
300.00	175.40	$1.76 \cdot 10^{-1}$	$1.73 \cdot 10^{-1}$
400.00	226.80	$1.85 \cdot 10^{-1}$	$1.80 \cdot 10^{-1}$

TABLE A.11.: Artificial MPTA data (n^{exp}), and Langmuir fit (n^L) for C_2 at 423 K.

P (bar)	f (bar)	n^{exp} ($\frac{mmol}{g}$)	n^L ($\frac{mmol}{g}$)
0.10	0.10	$1.73 \cdot 10^{-3}$	$3.76 \cdot 10^{-4}$
1.00	1.00	$7.97 \cdot 10^{-3}$	$3.69 \cdot 10^{-3}$
2.00	1.99	$1.25 \cdot 10^{-2}$	$7.24 \cdot 10^{-3}$
3.00	2.98	$1.62 \cdot 10^{-2}$	$1.06 \cdot 10^{-2}$
4.00	3.97	$1.94 \cdot 10^{-2}$	$1.39 \cdot 10^{-2}$
5.00	4.95	$2.23 \cdot 10^{-2}$	$1.70 \cdot 10^{-2}$
6.00	5.93	$2.50 \cdot 10^{-2}$	$2.01 \cdot 10^{-2}$
7.00	6.91	$2.75 \cdot 10^{-2}$	$2.30 \cdot 10^{-2}$
8.00	7.88	$2.99 \cdot 10^{-2}$	$2.58 \cdot 10^{-2}$
10.00	9.81	$3.42 \cdot 10^{-2}$	$3.11 \cdot 10^{-2}$
12.00	11.73	$3.81 \cdot 10^{-2}$	$3.61 \cdot 10^{-2}$
15.00	14.58	$4.35 \cdot 10^{-2}$	$4.29 \cdot 10^{-2}$
20.00	19.25	$5.13 \cdot 10^{-2}$	$5.29 \cdot 10^{-2}$
50.00	45.61	$8.36 \cdot 10^{-2}$	$9.14 \cdot 10^{-2}$
100.00	84.19	$1.14 \cdot 10^{-1}$	$1.21 \cdot 10^{-1}$
150.00	118.30	$1.32 \cdot 10^{-1}$	$1.36 \cdot 10^{-1}$
200.00	150.10	$1.44 \cdot 10^{-1}$	$1.45 \cdot 10^{-1}$
250.00	181.20	$1.53 \cdot 10^{-1}$	$1.52 \cdot 10^{-1}$
300.00	212.50	$1.60 \cdot 10^{-1}$	$1.57 \cdot 10^{-1}$
400.00	278.40	$1.70 \cdot 10^{-1}$	$1.64 \cdot 10^{-1}$

TABLE A.12.: Artificial MPTA data (n^{exp}), and Langmuir fit (n^L) for C_2 at 473 K.

P (bar)	f (bar)	n^{exp} ($\frac{mmol}{g}$)	n^L ($\frac{mmol}{g}$)
0.10	0.10	$5.67 \cdot 10^{-4}$	$1.73 \cdot 10^{-4}$
1.00	1.00	$3.43 \cdot 10^{-3}$	$1.71 \cdot 10^{-3}$
2.00	2.00	$5.81 \cdot 10^{-3}$	$3.39 \cdot 10^{-3}$
3.00	2.99	$7.87 \cdot 10^{-3}$	$5.03 \cdot 10^{-3}$
4.00	3.99	$9.74 \cdot 10^{-3}$	$6.64 \cdot 10^{-3}$
5.00	4.98	$1.15 \cdot 10^{-2}$	$8.22 \cdot 10^{-3}$
6.00	5.97	$1.31 \cdot 10^{-2}$	$9.76 \cdot 10^{-3}$
7.00	6.96	$1.46 \cdot 10^{-2}$	$1.13 \cdot 10^{-2}$
8.00	7.95	$1.61 \cdot 10^{-2}$	$1.28 \cdot 10^{-2}$
10.00	9.91	$1.89 \cdot 10^{-2}$	$1.57 \cdot 10^{-2}$
12.00	11.88	$2.14 \cdot 10^{-2}$	$1.84 \cdot 10^{-2}$
15.00	14.81	$2.50 \cdot 10^{-2}$	$2.24 \cdot 10^{-2}$
20.00	19.66	$3.04 \cdot 10^{-2}$	$2.86 \cdot 10^{-2}$
50.00	48.03	$5.46 \cdot 10^{-2}$	$5.69 \cdot 10^{-2}$
100.00	92.99	$8.07 \cdot 10^{-2}$	$8.50 \cdot 10^{-2}$
150.00	136.10	$9.85 \cdot 10^{-2}$	$1.02 \cdot 10^{-1}$
200.00	178.30	$1.12 \cdot 10^{-1}$	$1.14 \cdot 10^{-1}$
250.00	220.50	$1.22 \cdot 10^{-1}$	$1.23 \cdot 10^{-1}$
300.00	263.30	$1.31 \cdot 10^{-1}$	$1.29 \cdot 10^{-1}$
400.00	352.70	$1.44 \cdot 10^{-1}$	$1.39 \cdot 10^{-1}$

TABLE A.13.: Artificial MPTA data (n^{exp}), and Langmuir fit (n^L) for C_2 at 573 K.

P (bar)	f (bar)	n^{exp} ($\frac{mmol}{g}$)	n^L ($\frac{mmol}{g}$)
0.10	0.10	$4.504 \cdot 10^{-2}$	$2.570 \cdot 10^{-2}$
1.00	0.98	$8.581 \cdot 10^{-2}$	$9.623 \cdot 10^{-2}$
2.00	1.91	$1.034 \cdot 10^{-1}$	$1.135 \cdot 10^{-1}$
3.00	2.81	$1.146 \cdot 10^{-1}$	$1.207 \cdot 10^{-1}$
4.00	3.65	$1.233 \cdot 10^{-1}$	$1.247 \cdot 10^{-1}$
5.00	4.42	$1.295 \cdot 10^{-1}$	$1.271 \cdot 10^{-1}$
6.00	4.44	$1.295 \cdot 10^{-1}$	$1.271 \cdot 10^{-1}$
7.00	4.46	$1.295 \cdot 10^{-1}$	$1.272 \cdot 10^{-1}$
8.00	4.47	$1.296 \cdot 10^{-1}$	$1.272 \cdot 10^{-1}$
9.00	4.49	$1.296 \cdot 10^{-1}$	$1.273 \cdot 10^{-1}$
10.00	4.51	$1.296 \cdot 10^{-1}$	$1.273 \cdot 10^{-1}$
12.00	4.54	$1.297 \cdot 10^{-1}$	$1.274 \cdot 10^{-1}$
15.00	4.59	$1.297 \cdot 10^{-1}$	$1.275 \cdot 10^{-1}$
20.00	4.68	$1.298 \cdot 10^{-1}$	$1.277 \cdot 10^{-1}$
50.00	5.24	$1.304 \cdot 10^{-1}$	$1.289 \cdot 10^{-1}$
100.00	6.30	$1.313 \cdot 10^{-1}$	$1.306 \cdot 10^{-1}$
150.00	7.54	$1.321 \cdot 10^{-1}$	$1.321 \cdot 10^{-1}$
200.00	9.01	$1.327 \cdot 10^{-1}$	$1.333 \cdot 10^{-1}$
250.00	10.72	$1.334 \cdot 10^{-1}$	$1.343 \cdot 10^{-1}$
300.00	12.74	$1.340 \cdot 10^{-1}$	$1.351 \cdot 10^{-1}$

TABLE A.14.: Artificial MPTA data (n^{exp}), and Langmuir fit (n^L) for C₄ at 323 K.

P (bar)	f (bar)	n^{exp} ($\frac{mmol}{g}$)	n^L ($\frac{mmol}{g}$)
0.10	0.10	$2.613 \cdot 10^{-2}$	$6.619 \cdot 10^{-3}$
1.00	0.99	$5.586 \cdot 10^{-2}$	$4.576 \cdot 10^{-2}$
2.00	1.94	$6.938 \cdot 10^{-2}$	$6.814 \cdot 10^{-2}$
3.00	2.87	$7.877 \cdot 10^{-2}$	$8.140 \cdot 10^{-2}$
4.00	3.77	$8.558 \cdot 10^{-2}$	$9.016 \cdot 10^{-2}$
5.00	4.64	$9.157 \cdot 10^{-2}$	$9.638 \cdot 10^{-2}$
6.00	5.48	$9.650 \cdot 10^{-2}$	$1.010 \cdot 10^{-1}$
7.00	6.30	$1.008 \cdot 10^{-1}$	$1.046 \cdot 10^{-1}$
8.00	7.08	$1.043 \cdot 10^{-1}$	$1.074 \cdot 10^{-1}$
9.00	7.84	$1.075 \cdot 10^{-1}$	$1.097 \cdot 10^{-1}$
10.00	8.57	$1.107 \cdot 10^{-1}$	$1.117 \cdot 10^{-1}$
12.00	9.95	$1.156 \cdot 10^{-1}$	$1.146 \cdot 10^{-1}$
15.00	11.80	$1.215 \cdot 10^{-1}$	$1.177 \cdot 10^{-1}$
20.00	12.23	$1.224 \cdot 10^{-1}$	$1.183 \cdot 10^{-1}$
50.00	13.74	$1.235 \cdot 10^{-1}$	$1.201 \cdot 10^{-1}$
100.00	16.50	$1.250 \cdot 10^{-1}$	$1.227 \cdot 10^{-1}$
150.00	19.66	$1.262 \cdot 10^{-1}$	$1.248 \cdot 10^{-1}$
200.00	23.28	$1.273 \cdot 10^{-1}$	$1.266 \cdot 10^{-1}$
250.00	27.45	$1.282 \cdot 10^{-1}$	$1.281 \cdot 10^{-1}$
300.00	32.25	$1.291 \cdot 10^{-1}$	$1.294 \cdot 10^{-1}$

TABLE A.15.: Artificial MPTA data (n^{exp}), and Langmuir fit (n^L) for C₄ at 373 K.

P (bar)	f (bar)	n^{exp} ($\frac{mmol}{g}$)	n^L ($\frac{mmol}{g}$)
0.10	0.10	$1.568 \cdot 10^{-2}$	$2.772 \cdot 10^{-3}$
1.00	0.99	$3.699 \cdot 10^{-2}$	$2.312 \cdot 10^{-2}$
2.00	1.96	$4.748 \cdot 10^{-2}$	$3.905 \cdot 10^{-2}$
3.00	2.91	$5.486 \cdot 10^{-2}$	$5.068 \cdot 10^{-2}$
4.00	3.84	$6.066 \cdot 10^{-2}$	$5.955 \cdot 10^{-2}$
5.00	4.75	$6.557 \cdot 10^{-2}$	$6.652 \cdot 10^{-2}$
6.00	5.64	$6.973 \cdot 10^{-2}$	$7.216 \cdot 10^{-2}$
7.00	6.51	$7.338 \cdot 10^{-2}$	$7.679 \cdot 10^{-2}$
8.00	7.37	$7.661 \cdot 10^{-2}$	$8.068 \cdot 10^{-2}$
9.00	8.20	$7.958 \cdot 10^{-2}$	$8.398 \cdot 10^{-2}$
10.00	9.01	$8.224 \cdot 10^{-2}$	$8.681 \cdot 10^{-2}$
12.00	10.58	$8.693 \cdot 10^{-2}$	$9.143 \cdot 10^{-2}$
15.00	12.80	$9.282 \cdot 10^{-2}$	$9.653 \cdot 10^{-2}$
20.00	16.13	$1.003 \cdot 10^{-1}$	$1.021 \cdot 10^{-1}$
50.00	25.57	$1.146 \cdot 10^{-1}$	$1.113 \cdot 10^{-1}$
100.00	31.48	$1.175 \cdot 10^{-1}$	$1.146 \cdot 10^{-1}$
150.00	37.77	$1.195 \cdot 10^{-1}$	$1.171 \cdot 10^{-1}$
200.00	44.77	$1.212 \cdot 10^{-1}$	$1.192 \cdot 10^{-1}$
250.00	52.64	$1.225 \cdot 10^{-1}$	$1.209 \cdot 10^{-1}$
300.00	61.55	$1.237 \cdot 10^{-1}$	$1.223 \cdot 10^{-1}$

TABLE A.16.: Artificial MPTA data (n^{exp}), and Langmuir fit (n^L) for C₄ at 423 K.

P (bar)	f (bar)	n^{exp} ($\frac{mmol}{g}$)	n^L ($\frac{mmol}{g}$)
0.10	0.10	$9.593 \cdot 10^{-3}$	$1.473 \cdot 10^{-3}$
1.00	0.99	$2.510 \cdot 10^{-2}$	$1.325 \cdot 10^{-2}$
2.00	1.97	$3.331 \cdot 10^{-2}$	$2.384 \cdot 10^{-2}$
3.00	2.94	$3.920 \cdot 10^{-2}$	$3.249 \cdot 10^{-2}$
4.00	3.89	$4.393 \cdot 10^{-2}$	$3.969 \cdot 10^{-2}$
5.00	4.82	$4.792 \cdot 10^{-2}$	$4.577 \cdot 10^{-2}$
6.00	5.75	$5.141 \cdot 10^{-2}$	$5.098 \cdot 10^{-2}$
7.00	6.66	$5.451 \cdot 10^{-2}$	$5.549 \cdot 10^{-2}$
8.00	7.55	$5.730 \cdot 10^{-2}$	$5.943 \cdot 10^{-2}$
9.00	8.43	$5.986 \cdot 10^{-2}$	$6.290 \cdot 10^{-2}$
10.00	9.30	$6.220 \cdot 10^{-2}$	$6.598 \cdot 10^{-2}$
12.00	11.00	$6.640 \cdot 10^{-2}$	$7.121 \cdot 10^{-2}$
15.00	13.44	$7.174 \cdot 10^{-2}$	$7.732 \cdot 10^{-2}$
20.00	17.27	$7.886 \cdot 10^{-2}$	$8.453 \cdot 10^{-2}$
50.00	34.12	$1.000 \cdot 10^{-1}$	$1.009 \cdot 10^{-1}$
100.00	47.85	$1.084 \cdot 10^{-1}$	$1.070 \cdot 10^{-1}$
150.00	58.92	$1.119 \cdot 10^{-1}$	$1.101 \cdot 10^{-1}$
200.00	70.54	$1.144 \cdot 10^{-1}$	$1.124 \cdot 10^{-1}$
250.00	83.24	$1.163 \cdot 10^{-1}$	$1.142 \cdot 10^{-1}$
300.00	97.33	$1.179 \cdot 10^{-1}$	$1.158 \cdot 10^{-1}$

TABLE A.17.: Artificial MPTA data (n^{exp}), and Langmuir fit (n^L) for C₄ at 473 K.

P (bar)	f (bar)	n^{exp} ($\frac{mmol}{g}$)	n^L ($\frac{mmol}{g}$)
0.10	0.10	$3.859 \cdot 10^{-3}$	$5.977 \cdot 10^{-4}$
1.00	1.00	$1.238 \cdot 10^{-2}$	$5.688 \cdot 10^{-3}$
2.00	1.99	$1.746 \cdot 10^{-2}$	$1.079 \cdot 10^{-2}$
3.00	2.97	$2.128 \cdot 10^{-2}$	$1.541 \cdot 10^{-2}$
4.00	3.94	$2.445 \cdot 10^{-2}$	$1.959 \cdot 10^{-2}$
5.00	4.91	$2.720 \cdot 10^{-2}$	$2.340 \cdot 10^{-2}$
6.00	5.87	$2.964 \cdot 10^{-2}$	$2.689 \cdot 10^{-2}$
7.00	6.82	$3.186 \cdot 10^{-2}$	$3.010 \cdot 10^{-2}$
8.00	7.77	$3.389 \cdot 10^{-2}$	$3.305 \cdot 10^{-2}$
9.00	8.70	$3.578 \cdot 10^{-2}$	$3.579 \cdot 10^{-2}$
10.00	9.63	$3.753 \cdot 10^{-2}$	$3.832 \cdot 10^{-2}$
12.00	11.48	$4.074 \cdot 10^{-2}$	$4.287 \cdot 10^{-2}$
15.00	14.19	$4.494 \cdot 10^{-2}$	$4.865 \cdot 10^{-2}$
20.00	18.57	$5.080 \cdot 10^{-2}$	$5.623 \cdot 10^{-2}$
50.00	41.77	$7.184 \cdot 10^{-2}$	$7.807 \cdot 10^{-2}$
100.00	71.79	$8.725 \cdot 10^{-2}$	$8.973 \cdot 10^{-2}$
150.00	96.67	$9.475 \cdot 10^{-2}$	$9.481 \cdot 10^{-2}$
200.00	120.50	$9.947 \cdot 10^{-2}$	$9.797 \cdot 10^{-2}$
250.00	145.20	$1.029 \cdot 10^{-1}$	$1.003 \cdot 10^{-1}$
300.00	171.50	$1.057 \cdot 10^{-1}$	$1.021 \cdot 10^{-1}$

TABLE A.18.: Artificial MPTA data (n^{exp}), and Langmuir fit (n^L) for C₄ at 573 K

P (bar)	f (bar)	n^{exp} ($\frac{mmol}{g}$)	n^L ($\frac{mmol}{g}$)
$1.00 \cdot 10^{-3}$	$1.00 \cdot 10^{-3}$	$3.567 \cdot 10^{-2}$	$2.012 \cdot 10^{-2}$
$2.00 \cdot 10^{-3}$	$2.00 \cdot 10^{-3}$	$3.978 \cdot 10^{-2}$	$3.134 \cdot 10^{-2}$
$3.00 \cdot 10^{-3}$	$3.00 \cdot 10^{-3}$	$4.261 \cdot 10^{-2}$	$3.850 \cdot 10^{-2}$
$4.00 \cdot 10^{-3}$	$4.00 \cdot 10^{-3}$	$4.451 \cdot 10^{-2}$	$4.346 \cdot 10^{-2}$
$5.00 \cdot 10^{-3}$	$5.00 \cdot 10^{-3}$	$4.609 \cdot 10^{-2}$	$4.711 \cdot 10^{-2}$
$1.00 \cdot 10^{-2}$	$9.99 \cdot 10^{-3}$	$5.146 \cdot 10^{-2}$	$5.659 \cdot 10^{-2}$
$2.00 \cdot 10^{-2}$	$2.00 \cdot 10^{-2}$	$5.746 \cdot 10^{-2}$	$6.293 \cdot 10^{-2}$
$3.00 \cdot 10^{-2}$	$2.99 \cdot 10^{-2}$	$6.125 \cdot 10^{-2}$	$6.537 \cdot 10^{-2}$
$4.00 \cdot 10^{-2}$	$3.99 \cdot 10^{-2}$	$6.380 \cdot 10^{-2}$	$6.666 \cdot 10^{-2}$
$5.00 \cdot 10^{-2}$	$4.98 \cdot 10^{-2}$	$6.602 \cdot 10^{-2}$	$6.746 \cdot 10^{-2}$
$7.50 \cdot 10^{-2}$	$6.84 \cdot 10^{-2}$	$6.933 \cdot 10^{-2}$	$6.836 \cdot 10^{-2}$
$1.00 \cdot 10^{-1}$	$6.84 \cdot 10^{-2}$	$6.934 \cdot 10^{-2}$	$6.836 \cdot 10^{-2}$
$5.00 \cdot 10^{-1}$	$6.86 \cdot 10^{-2}$	$6.934 \cdot 10^{-2}$	$6.837 \cdot 10^{-2}$
$1.00 \cdot 10^0$	$6.88 \cdot 10^{-2}$	$6.934 \cdot 10^{-2}$	$6.837 \cdot 10^{-2}$
$1.00 \cdot 10^1$	$7.29 \cdot 10^{-2}$	$6.938 \cdot 10^{-2}$	$6.851 \cdot 10^{-2}$
$5.00 \cdot 10^1$	$9.42 \cdot 10^{-2}$	$6.955 \cdot 10^{-2}$	$6.903 \cdot 10^{-2}$
$1.00 \cdot 10^2$	$1.30 \cdot 10^{-1}$	$6.975 \cdot 10^{-2}$	$6.953 \cdot 10^{-2}$
$1.50 \cdot 10^2$	$1.78 \cdot 10^{-1}$	$6.994 \cdot 10^{-2}$	$6.989 \cdot 10^{-2}$
$2.00 \cdot 10^2$	$2.43 \cdot 10^{-1}$	$7.011 \cdot 10^{-2}$	$7.015 \cdot 10^{-2}$
$3.00 \cdot 10^2$	$4.53 \cdot 10^{-1}$	$7.042 \cdot 10^{-2}$	$7.049 \cdot 10^{-2}$

TABLE A.19.: Artificial MPTA data (n^{exp}), and Langmuir fit (n^L) for C₈ at 323 K

P (bar)	f (bar)	n^{exp} ($\frac{mmol}{g}$)	n^L ($\frac{mmol}{g}$)
$1.00 \cdot 10^{-3}$	$1.00 \cdot 10^{-3}$	$2.186 \cdot 10^{-2}$	$4.309 \cdot 10^{-3}$
$2.00 \cdot 10^{-3}$	$2.00 \cdot 10^{-3}$	$2.494 \cdot 10^{-2}$	$8.115 \cdot 10^{-3}$
$3.00 \cdot 10^{-3}$	$3.00 \cdot 10^{-3}$	$2.680 \cdot 10^{-2}$	$1.150 \cdot 10^{-2}$
$4.00 \cdot 10^{-3}$	$4.00 \cdot 10^{-3}$	$2.833 \cdot 10^{-2}$	$1.453 \cdot 10^{-2}$
$5.00 \cdot 10^{-3}$	$5.00 \cdot 10^{-3}$	$2.956 \cdot 10^{-2}$	$1.726 \cdot 10^{-2}$
$1.00 \cdot 10^{-2}$	$1.00 \cdot 10^{-2}$	$3.357 \cdot 10^{-2}$	$2.765 \cdot 10^{-2}$
$2.00 \cdot 10^{-2}$	$2.00 \cdot 10^{-2}$	$3.819 \cdot 10^{-2}$	$3.956 \cdot 10^{-2}$
$3.00 \cdot 10^{-2}$	$3.00 \cdot 10^{-2}$	$4.126 \cdot 10^{-2}$	$4.618 \cdot 10^{-2}$
$4.00 \cdot 10^{-2}$	$3.99 \cdot 10^{-2}$	$4.343 \cdot 10^{-2}$	$5.040 \cdot 10^{-2}$
$5.00 \cdot 10^{-2}$	$4.99 \cdot 10^{-2}$	$4.527 \cdot 10^{-2}$	$5.333 \cdot 10^{-2}$
$7.50 \cdot 10^{-2}$	$7.47 \cdot 10^{-2}$	$4.895 \cdot 10^{-2}$	$5.780 \cdot 10^{-2}$
$1.00 \cdot 10^{-1}$	$9.95 \cdot 10^{-2}$	$5.143 \cdot 10^{-2}$	$6.033 \cdot 10^{-2}$
$5.00 \cdot 10^{-1}$	$4.58 \cdot 10^{-1}$	$6.761 \cdot 10^{-2}$	$6.728 \cdot 10^{-2}$
$1.00 \cdot 10^0$	$4.59 \cdot 10^{-1}$	$6.761 \cdot 10^{-2}$	$6.729 \cdot 10^{-2}$
$1.00 \cdot 10^1$	$4.84 \cdot 10^{-1}$	$6.768 \cdot 10^{-2}$	$6.740 \cdot 10^{-2}$
$5.00 \cdot 10^1$	$6.12 \cdot 10^{-1}$	$6.793 \cdot 10^{-2}$	$6.783 \cdot 10^{-2}$
$1.00 \cdot 10^2$	$8.17 \cdot 10^{-1}$	$6.822 \cdot 10^{-2}$	$6.825 \cdot 10^{-2}$
$1.50 \cdot 10^2$	$1.09 \cdot 10^0$	$6.848 \cdot 10^{-2}$	$6.856 \cdot 10^{-2}$
$2.00 \cdot 10^2$	$1.44 \cdot 10^0$	$6.872 \cdot 10^{-2}$	$6.879 \cdot 10^{-2}$
$3.00 \cdot 10^2$	$2.52 \cdot 10^0$	$6.914 \cdot 10^{-2}$	$6.910 \cdot 10^{-2}$

TABLE A.20.: Artificial MPTA data (n^{exp}), and Langmuir fit (n^L) for C₈ at 373 K

P (bar)	f (bar)	n^{exp} ($\frac{mmol}{g}$)	n^L ($\frac{mmol}{g}$)
$1.00 \cdot 10^{-3}$	$1.00 \cdot 10^{-3}$	$1.375 \cdot 10^{-2}$	$1.253 \cdot 10^{-3}$
$2.00 \cdot 10^{-3}$	$2.00 \cdot 10^{-3}$	$1.585 \cdot 10^{-2}$	$2.461 \cdot 10^{-3}$
$3.00 \cdot 10^{-3}$	$3.00 \cdot 10^{-3}$	$1.734 \cdot 10^{-2}$	$3.626 \cdot 10^{-3}$
$4.00 \cdot 10^{-3}$	$4.00 \cdot 10^{-3}$	$1.827 \cdot 10^{-2}$	$4.749 \cdot 10^{-3}$
$5.00 \cdot 10^{-3}$	$5.00 \cdot 10^{-3}$	$1.916 \cdot 10^{-2}$	$5.835 \cdot 10^{-3}$
$1.00 \cdot 10^{-2}$	$1.00 \cdot 10^{-2}$	$2.242 \cdot 10^{-2}$	$1.074 \cdot 10^{-2}$
$2.00 \cdot 10^{-2}$	$2.00 \cdot 10^{-2}$	$2.600 \cdot 10^{-2}$	$1.855 \cdot 10^{-2}$
$3.00 \cdot 10^{-2}$	$3.00 \cdot 10^{-2}$	$2.813 \cdot 10^{-2}$	$2.447 \cdot 10^{-2}$
$4.00 \cdot 10^{-2}$	$3.99 \cdot 10^{-2}$	$2.992 \cdot 10^{-2}$	$2.913 \cdot 10^{-2}$
$5.00 \cdot 10^{-2}$	$4.99 \cdot 10^{-2}$	$3.141 \cdot 10^{-2}$	$3.288 \cdot 10^{-2}$
$7.50 \cdot 10^{-2}$	$7.48 \cdot 10^{-2}$	$3.412 \cdot 10^{-2}$	$3.969 \cdot 10^{-2}$
$1.00 \cdot 10^{-1}$	$9.96 \cdot 10^{-2}$	$3.622 \cdot 10^{-2}$	$4.428 \cdot 10^{-2}$
$5.00 \cdot 10^{-1}$	$4.91 \cdot 10^{-1}$	$5.056 \cdot 10^{-2}$	$6.127 \cdot 10^{-2}$
$1.00 \cdot 10^0$	$9.62 \cdot 10^{-1}$	$5.828 \cdot 10^{-2}$	$6.436 \cdot 10^{-2}$
$1.00 \cdot 10^1$	$1.85 \cdot 10^0$	$6.569 \cdot 10^{-2}$	$6.602 \cdot 10^{-2}$
$5.00 \cdot 10^1$	$2.31 \cdot 10^0$	$6.608 \cdot 10^{-2}$	$6.639 \cdot 10^{-2}$
$1.00 \cdot 10^2$	$3.03 \cdot 10^0$	$6.650 \cdot 10^{-2}$	$6.674 \cdot 10^{-2}$
$1.50 \cdot 10^2$	$3.95 \cdot 10^0$	$6.687 \cdot 10^{-2}$	$6.701 \cdot 10^{-2}$
$2.00 \cdot 10^2$	$5.13 \cdot 10^0$	$6.719 \cdot 10^{-2}$	$6.722 \cdot 10^{-2}$
$3.00 \cdot 10^2$	$8.58 \cdot 10^0$	$6.776 \cdot 10^{-2}$	$6.750 \cdot 10^{-2}$

TABLE A.21.: Artificial MPTA data (n^{exp}), and Langmuir fit (n^L) for C₈ at 423 K.

P (bar)	f (bar)	n^{exp} ($\frac{mmol}{g}$)	n^L ($\frac{mmol}{g}$)
$1.00 \cdot 10^{-3}$	$1.00 \cdot 10^{-3}$	$8.679 \cdot 10^{-3}$	$4.431 \cdot 10^{-4}$
$5.00 \cdot 10^{-3}$	$5.00 \cdot 10^{-3}$	$1.274 \cdot 10^{-2}$	$2.158 \cdot 10^{-3}$
$1.00 \cdot 10^{-2}$	$1.00 \cdot 10^{-2}$	$1.505 \cdot 10^{-2}$	$4.179 \cdot 10^{-3}$
$2.00 \cdot 10^{-2}$	$2.00 \cdot 10^{-2}$	$1.768 \cdot 10^{-2}$	$7.861 \cdot 10^{-3}$
$3.00 \cdot 10^{-2}$	$3.00 \cdot 10^{-2}$	$1.943 \cdot 10^{-2}$	$1.113 \cdot 10^{-2}$
$4.00 \cdot 10^{-2}$	$4.00 \cdot 10^{-2}$	$2.087 \cdot 10^{-2}$	$1.405 \cdot 10^{-2}$
$5.00 \cdot 10^{-2}$	$4.99 \cdot 10^{-2}$	$2.202 \cdot 10^{-2}$	$1.668 \cdot 10^{-2}$
$6.00 \cdot 10^{-2}$	$5.99 \cdot 10^{-2}$	$2.291 \cdot 10^{-2}$	$1.905 \cdot 10^{-2}$
$7.00 \cdot 10^{-2}$	$6.99 \cdot 10^{-2}$	$2.378 \cdot 10^{-2}$	$2.121 \cdot 10^{-2}$
$8.00 \cdot 10^{-2}$	$7.98 \cdot 10^{-2}$	$2.462 \cdot 10^{-2}$	$2.317 \cdot 10^{-2}$
$9.00 \cdot 10^{-2}$	$8.98 \cdot 10^{-2}$	$2.523 \cdot 10^{-2}$	$2.498 \cdot 10^{-2}$
$1.00 \cdot 10^{-1}$	$9.97 \cdot 10^{-2}$	$2.604 \cdot 10^{-2}$	$2.663 \cdot 10^{-2}$
$5.00 \cdot 10^{-1}$	$4.93 \cdot 10^{-1}$	$3.790 \cdot 10^{-2}$	$5.098 \cdot 10^{-2}$
$1.00 \cdot 10^0$	$9.73 \cdot 10^{-1}$	$4.428 \cdot 10^{-2}$	$5.755 \cdot 10^{-2}$
$1.00 \cdot 10^1$	$4.83 \cdot 10^0$	$6.334 \cdot 10^{-2}$	$6.437 \cdot 10^{-2}$
$5.00 \cdot 10^1$	$6.03 \cdot 10^0$	$6.394 \cdot 10^{-2}$	$6.476 \cdot 10^{-2}$
$1.00 \cdot 10^2$	$7.85 \cdot 10^0$	$6.455 \cdot 10^{-2}$	$6.512 \cdot 10^{-2}$
$1.50 \cdot 10^2$	$1.01 \cdot 10^1$	$6.507 \cdot 10^{-2}$	$6.539 \cdot 10^{-2}$
$2.00 \cdot 10^2$	$1.30 \cdot 10^1$	$6.552 \cdot 10^{-2}$	$6.560 \cdot 10^{-2}$
$3.00 \cdot 10^2$	$2.10 \cdot 10^1$	$6.627 \cdot 10^{-2}$	$6.589 \cdot 10^{-2}$

TABLE A.22.: Artificial MPTA data (n^{exp}), and Langmuir fit (n^L) for C₈ at 473 K.

P (bar)	f (bar)	n^{exp} ($\frac{mmol}{g}$)	n^L ($\frac{mmol}{g}$)
$1.00 \cdot 10^{-3}$	$1.00 \cdot 10^{-3}$	$3.618 \cdot 10^{-3}$	$1.158 \cdot 10^{-4}$
$5.00 \cdot 10^{-3}$	$5.00 \cdot 10^{-3}$	$5.750 \cdot 10^{-3}$	$5.748 \cdot 10^{-4}$
$1.00 \cdot 10^{-2}$	$1.00 \cdot 10^{-2}$	$7.056 \cdot 10^{-3}$	$1.139 \cdot 10^{-3}$
$2.00 \cdot 10^{-2}$	$2.00 \cdot 10^{-2}$	$8.647 \cdot 10^{-3}$	$2.237 \cdot 10^{-3}$
$3.00 \cdot 10^{-2}$	$3.00 \cdot 10^{-2}$	$9.730 \cdot 10^{-3}$	$3.296 \cdot 10^{-3}$
$4.00 \cdot 10^{-2}$	$4.00 \cdot 10^{-2}$	$1.057 \cdot 10^{-2}$	$4.319 \cdot 10^{-3}$
$5.00 \cdot 10^{-2}$	$5.00 \cdot 10^{-2}$	$1.130 \cdot 10^{-2}$	$5.306 \cdot 10^{-3}$
$6.00 \cdot 10^{-2}$	$6.00 \cdot 10^{-2}$	$1.190 \cdot 10^{-2}$	$6.260 \cdot 10^{-3}$
$7.00 \cdot 10^{-2}$	$6.99 \cdot 10^{-2}$	$1.244 \cdot 10^{-2}$	$7.183 \cdot 10^{-3}$
$8.00 \cdot 10^{-2}$	$7.99 \cdot 10^{-2}$	$1.294 \cdot 10^{-2}$	$8.075 \cdot 10^{-3}$
$9.00 \cdot 10^{-2}$	$8.99 \cdot 10^{-2}$	$1.340 \cdot 10^{-2}$	$8.939 \cdot 10^{-3}$
$1.00 \cdot 10^{-1}$	$9.99 \cdot 10^{-2}$	$1.380 \cdot 10^{-2}$	$9.776 \cdot 10^{-3}$
$5.00 \cdot 10^{-1}$	$4.96 \cdot 10^{-1}$	$2.191 \cdot 10^{-2}$	$2.998 \cdot 10^{-2}$
$1.00 \cdot 10^0$	$9.85 \cdot 10^{-1}$	$2.665 \cdot 10^{-2}$	$4.043 \cdot 10^{-2}$
$1.00 \cdot 10^1$	$8.57 \cdot 10^0$	$4.850 \cdot 10^{-2}$	$5.885 \cdot 10^{-2}$
$5.00 \cdot 10^1$	$1.99 \cdot 10^1$	$5.841 \cdot 10^{-2}$	$6.090 \cdot 10^{-2}$
$1.00 \cdot 10^2$	$2.66 \cdot 10^1$	$5.988 \cdot 10^{-2}$	$6.131 \cdot 10^{-2}$
$1.50 \cdot 10^2$	$3.43 \cdot 10^1$	$6.090 \cdot 10^{-2}$	$6.158 \cdot 10^{-2}$
$2.00 \cdot 10^2$	$4.36 \cdot 10^1$	$6.171 \cdot 10^{-2}$	$6.179 \cdot 10^{-2}$
$3.00 \cdot 10^2$	$6.84 \cdot 10^1$	$6.297 \cdot 10^{-2}$	$6.206 \cdot 10^{-2}$

TABLE A.23.: Artificial MPTA data (n^{exp}), and Langmuir fit (n^L) for C₈ at 573 K.

P (bar)	f (bar)	n^{exp} ($\frac{mmol}{g}$)	n^L ($\frac{mmol}{g}$)
$1.00 \cdot 10^{-3}$	$1.00 \cdot 10^{-3}$	$4.124 \cdot 10^{-2}$	$3.941 \cdot 10^{-2}$
$2.00 \cdot 10^{-3}$	$2.00 \cdot 10^{-3}$	$4.525 \cdot 10^{-2}$	$4.656 \cdot 10^{-2}$
$3.00 \cdot 10^{-3}$	$3.00 \cdot 10^{-3}$	$4.776 \cdot 10^{-2}$	$4.955 \cdot 10^{-2}$
$4.00 \cdot 10^{-3}$	$4.00 \cdot 10^{-3}$	$4.928 \cdot 10^{-2}$	$5.119 \cdot 10^{-2}$
$5.00 \cdot 10^{-3}$	$5.00 \cdot 10^{-3}$	$5.078 \cdot 10^{-2}$	$5.224 \cdot 10^{-2}$
$1.00 \cdot 10^{-2}$	$9.35 \cdot 10^{-3}$	$5.504 \cdot 10^{-2}$	$5.429 \cdot 10^{-2}$
$2.00 \cdot 10^{-2}$	$9.35 \cdot 10^{-3}$	$5.504 \cdot 10^{-2}$	$5.429 \cdot 10^{-2}$
$3.00 \cdot 10^{-2}$	$9.36 \cdot 10^{-3}$	$5.504 \cdot 10^{-2}$	$5.429 \cdot 10^{-2}$
$4.00 \cdot 10^{-2}$	$9.36 \cdot 10^{-3}$	$5.504 \cdot 10^{-2}$	$5.429 \cdot 10^{-2}$
$5.00 \cdot 10^{-2}$	$9.36 \cdot 10^{-3}$	$5.504 \cdot 10^{-2}$	$5.429 \cdot 10^{-2}$
$7.50 \cdot 10^{-2}$	$9.36 \cdot 10^{-3}$	$5.504 \cdot 10^{-2}$	$5.429 \cdot 10^{-2}$
$1.00 \cdot 10^{-1}$	$9.36 \cdot 10^{-3}$	$5.504 \cdot 10^{-2}$	$5.429 \cdot 10^{-2}$
$5.00 \cdot 10^{-1}$	$9.39 \cdot 10^{-3}$	$5.504 \cdot 10^{-2}$	$5.430 \cdot 10^{-2}$
$1.00 \cdot 10^0$	$9.43 \cdot 10^{-3}$	$5.505 \cdot 10^{-2}$	$5.431 \cdot 10^{-2}$
$1.00 \cdot 10^1$	$1.01 \cdot 10^{-2}$	$5.507 \cdot 10^{-2}$	$5.448 \cdot 10^{-2}$
$5.00 \cdot 10^1$	$1.39 \cdot 10^{-2}$	$5.518 \cdot 10^{-2}$	$5.511 \cdot 10^{-2}$
$1.00 \cdot 10^2$	$2.07 \cdot 10^{-2}$	$5.531 \cdot 10^{-2}$	$5.567 \cdot 10^{-2}$
$1.50 \cdot 10^2$	$3.07 \cdot 10^{-2}$	$5.543 \cdot 10^{-2}$	$5.605 \cdot 10^{-2}$
$2.00 \cdot 10^2$	$4.55 \cdot 10^{-2}$	$5.554 \cdot 10^{-2}$	$5.631 \cdot 10^{-2}$
$3.00 \cdot 10^2$	$9.91 \cdot 10^{-2}$	$5.574 \cdot 10^{-2}$	$5.661 \cdot 10^{-2}$

TABLE A.24.: Artificial MPTA data (n^{exp}), and Langmuir fit (n^L) for C₁₀ at 323 K.

P (bar)	f (bar)	n^{exp} ($\frac{mmol}{g}$)	n^L ($\frac{mmol}{g}$)
$1.00 \cdot 10^{-3}$	$1.00 \cdot 10^{-3}$	$2.715 \cdot 10^{-2}$	$1.746 \cdot 10^{-2}$
$2.00 \cdot 10^{-3}$	$2.00 \cdot 10^{-3}$	$3.010 \cdot 10^{-2}$	$2.650 \cdot 10^{-2}$
$3.00 \cdot 10^{-3}$	$3.00 \cdot 10^{-3}$	$3.207 \cdot 10^{-2}$	$3.202 \cdot 10^{-2}$
$4.00 \cdot 10^{-3}$	$4.00 \cdot 10^{-3}$	$3.354 \cdot 10^{-2}$	$3.575 \cdot 10^{-2}$
$5.00 \cdot 10^{-3}$	$5.00 \cdot 10^{-3}$	$3.454 \cdot 10^{-2}$	$3.843 \cdot 10^{-2}$
$1.00 \cdot 10^{-2}$	$9.99 \cdot 10^{-3}$	$3.846 \cdot 10^{-2}$	$4.522 \cdot 10^{-2}$
$2.00 \cdot 10^{-2}$	$2.00 \cdot 10^{-2}$	$4.287 \cdot 10^{-2}$	$4.960 \cdot 10^{-2}$
$3.00 \cdot 10^{-2}$	$2.99 \cdot 10^{-2}$	$4.535 \cdot 10^{-2}$	$5.126 \cdot 10^{-2}$
$4.00 \cdot 10^{-2}$	$3.99 \cdot 10^{-2}$	$4.732 \cdot 10^{-2}$	$5.212 \cdot 10^{-2}$
$5.00 \cdot 10^{-2}$	$4.98 \cdot 10^{-2}$	$4.926 \cdot 10^{-2}$	$5.266 \cdot 10^{-2}$
$7.50 \cdot 10^{-2}$	$7.45 \cdot 10^{-2}$	$5.222 \cdot 10^{-2}$	$5.339 \cdot 10^{-2}$
$1.00 \cdot 10^{-1}$	$9.66 \cdot 10^{-2}$	$5.396 \cdot 10^{-2}$	$5.374 \cdot 10^{-2}$
$5.00 \cdot 10^{-1}$	$9.68 \cdot 10^{-2}$	$5.396 \cdot 10^{-2}$	$5.374 \cdot 10^{-2}$
$1.00 \cdot 10^0$	$9.72 \cdot 10^{-2}$	$5.396 \cdot 10^{-2}$	$5.374 \cdot 10^{-2}$
$1.00 \cdot 10^1$	$1.04 \cdot 10^{-1}$	$5.400 \cdot 10^{-2}$	$5.382 \cdot 10^{-2}$
$5.00 \cdot 10^1$	$1.38 \cdot 10^{-1}$	$5.416 \cdot 10^{-2}$	$5.409 \cdot 10^{-2}$
$1.00 \cdot 10^2$	$1.97 \cdot 10^{-1}$	$5.434 \cdot 10^{-2}$	$5.434 \cdot 10^{-2}$
$1.50 \cdot 10^2$	$2.81 \cdot 10^{-1}$	$5.451 \cdot 10^{-2}$	$5.451 \cdot 10^{-2}$
$2.00 \cdot 10^2$	$3.99 \cdot 10^{-1}$	$5.466 \cdot 10^{-2}$	$5.464 \cdot 10^{-2}$
$3.00 \cdot 10^2$	$7.98 \cdot 10^{-1}$	$5.493 \cdot 10^{-2}$	$5.478 \cdot 10^{-2}$

TABLE A.25.: Artificial MPTA data (n^{exp}), and Langmuir fit (n^L) for C₁₀ at 373 K.

P (bar)	f (bar)	n^{exp} ($\frac{mmol}{g}$)	n^L ($\frac{mmol}{g}$)
$1.00 \cdot 10^{-3}$	$1.00 \cdot 10^{-3}$	$1.790 \cdot 10^{-2}$	$5.298 \cdot 10^{-3}$
$2.00 \cdot 10^{-3}$	$2.00 \cdot 10^{-3}$	$2.030 \cdot 10^{-2}$	$9.649 \cdot 10^{-3}$
$3.00 \cdot 10^{-3}$	$3.00 \cdot 10^{-3}$	$2.174 \cdot 10^{-2}$	$1.329 \cdot 10^{-2}$
$4.00 \cdot 10^{-3}$	$4.00 \cdot 10^{-3}$	$2.315 \cdot 10^{-2}$	$1.637 \cdot 10^{-2}$
$5.00 \cdot 10^{-3}$	$5.00 \cdot 10^{-3}$	$2.410 \cdot 10^{-2}$	$1.903 \cdot 10^{-2}$
$1.00 \cdot 10^{-2}$	$9.99 \cdot 10^{-3}$	$2.701 \cdot 10^{-2}$	$2.814 \cdot 10^{-2}$
$2.00 \cdot 10^{-2}$	$2.00 \cdot 10^{-2}$	$3.038 \cdot 10^{-2}$	$3.701 \cdot 10^{-2}$
$3.00 \cdot 10^{-2}$	$3.00 \cdot 10^{-2}$	$3.276 \cdot 10^{-2}$	$4.135 \cdot 10^{-2}$
$4.00 \cdot 10^{-2}$	$3.99 \cdot 10^{-2}$	$3.422 \cdot 10^{-2}$	$4.393 \cdot 10^{-2}$
$5.00 \cdot 10^{-2}$	$4.99 \cdot 10^{-2}$	$3.565 \cdot 10^{-2}$	$4.563 \cdot 10^{-2}$
$7.50 \cdot 10^{-2}$	$7.47 \cdot 10^{-2}$	$3.807 \cdot 10^{-2}$	$4.813 \cdot 10^{-2}$
$1.00 \cdot 10^{-1}$	$9.94 \cdot 10^{-2}$	$3.999 \cdot 10^{-2}$	$4.948 \cdot 10^{-2}$
$5.00 \cdot 10^{-1}$	$4.85 \cdot 10^{-1}$	$5.245 \cdot 10^{-2}$	$5.305 \cdot 10^{-2}$
$1.00 \cdot 10^0$	$5.12 \cdot 10^{-1}$	$5.272 \cdot 10^{-2}$	$5.311 \cdot 10^{-2}$
$1.00 \cdot 10^1$	$5.44 \cdot 10^{-1}$	$5.277 \cdot 10^{-2}$	$5.316 \cdot 10^{-2}$
$5.00 \cdot 10^1$	$7.11 \cdot 10^{-1}$	$5.300 \cdot 10^{-2}$	$5.337 \cdot 10^{-2}$
$1.00 \cdot 10^2$	$9.88 \cdot 10^{-1}$	$5.326 \cdot 10^{-2}$	$5.356 \cdot 10^{-2}$
$1.50 \cdot 10^2$	$1.37 \cdot 10^0$	$5.349 \cdot 10^{-2}$	$5.370 \cdot 10^{-2}$
$2.00 \cdot 10^2$	$1.88 \cdot 10^0$	$5.370 \cdot 10^{-2}$	$5.380 \cdot 10^{-2}$
$3.00 \cdot 10^2$	$3.54 \cdot 10^0$	$5.406 \cdot 10^{-2}$	$5.392 \cdot 10^{-2}$

TABLE A.26.: Artificial MPTA data (n^{exp}), and Langmuir fit (n^L) for C₁₀ at 423 K.

P (bar)	f (bar)	n^{exp} ($\frac{mmol}{g}$)	n^L ($\frac{mmol}{g}$)
$1.00 \cdot 10^{-3}$	$1.00 \cdot 10^{-3}$	$1.226 \cdot 10^{-2}$	$1.086 \cdot 10^{-3}$
$5.00 \cdot 10^{-3}$	$5.00 \cdot 10^{-3}$	$1.651 \cdot 10^{-2}$	$5.018 \cdot 10^{-3}$
$1.00 \cdot 10^{-2}$	$1.00 \cdot 10^{-2}$	$1.926 \cdot 10^{-2}$	$9.168 \cdot 10^{-3}$
$2.00 \cdot 10^{-2}$	$2.00 \cdot 10^{-2}$	$2.206 \cdot 10^{-2}$	$1.563 \cdot 10^{-2}$
$3.00 \cdot 10^{-2}$	$3.00 \cdot 10^{-2}$	$2.353 \cdot 10^{-2}$	$2.043 \cdot 10^{-2}$
$4.00 \cdot 10^{-2}$	$3.99 \cdot 10^{-2}$	$2.492 \cdot 10^{-2}$	$2.414 \cdot 10^{-2}$
$5.00 \cdot 10^{-2}$	$4.99 \cdot 10^{-2}$	$2.628 \cdot 10^{-2}$	$2.709 \cdot 10^{-2}$
$6.00 \cdot 10^{-2}$	$5.99 \cdot 10^{-2}$	$2.721 \cdot 10^{-2}$	$2.950 \cdot 10^{-2}$
$7.00 \cdot 10^{-2}$	$6.98 \cdot 10^{-2}$	$2.774 \cdot 10^{-2}$	$3.149 \cdot 10^{-2}$
$8.00 \cdot 10^{-2}$	$7.97 \cdot 10^{-2}$	$2.864 \cdot 10^{-2}$	$3.317 \cdot 10^{-2}$
$9.00 \cdot 10^{-2}$	$8.97 \cdot 10^{-2}$	$2.914 \cdot 10^{-2}$	$3.461 \cdot 10^{-2}$
$1.00 \cdot 10^{-1}$	$9.96 \cdot 10^{-2}$	$3.002 \cdot 10^{-2}$	$3.586 \cdot 10^{-2}$
$5.00 \cdot 10^{-1}$	$4.89 \cdot 10^{-1}$	$4.075 \cdot 10^{-2}$	$4.837 \cdot 10^{-2}$
$1.00 \cdot 10^0$	$9.58 \cdot 10^{-1}$	$4.593 \cdot 10^{-2}$	$5.058 \cdot 10^{-2}$
$1.00 \cdot 10^1$	$1.82 \cdot 10^0$	$5.135 \cdot 10^{-2}$	$5.175 \cdot 10^{-2}$
$5.00 \cdot 10^1$	$2.36 \cdot 10^0$	$5.169 \cdot 10^{-2}$	$5.205 \cdot 10^{-2}$
$1.00 \cdot 10^2$	$3.22 \cdot 10^0$	$5.205 \cdot 10^{-2}$	$5.233 \cdot 10^{-2}$
$1.50 \cdot 10^2$	$4.37 \cdot 10^0$	$5.236 \cdot 10^{-2}$	$5.253 \cdot 10^{-2}$
$2.00 \cdot 10^2$	$5.90 \cdot 10^0$	$5.264 \cdot 10^{-2}$	$5.268 \cdot 10^{-2}$
$3.00 \cdot 10^2$	$1.06 \cdot 10^1$	$5.311 \cdot 10^{-2}$	$5.287 \cdot 10^{-2}$

TABLE A.27.: Artificial MPTA data (n^{exp}), and Langmuir fit (n^L) for C₁₀ at 473 K.

P (bar)	f (bar)	n^{exp} ($\frac{mmol}{g}$)	n^L ($\frac{mmol}{g}$)
$1.00 \cdot 10^{-3}$	$1.00 \cdot 10^{-3}$	$5.778 \cdot 10^{-3}$	$3.296 \cdot 10^{-4}$
$5.00 \cdot 10^{-3}$	$5.00 \cdot 10^{-3}$	$8.439 \cdot 10^{-3}$	$1.607 \cdot 10^{-3}$
$1.00 \cdot 10^{-2}$	$1.00 \cdot 10^{-2}$	$9.841 \cdot 10^{-3}$	$3.115 \cdot 10^{-3}$
$2.00 \cdot 10^{-2}$	$2.00 \cdot 10^{-2}$	$1.161 \cdot 10^{-2}$	$5.870 \cdot 10^{-3}$
$3.00 \cdot 10^{-2}$	$3.00 \cdot 10^{-2}$	$1.287 \cdot 10^{-2}$	$8.324 \cdot 10^{-3}$
$4.00 \cdot 10^{-2}$	$4.00 \cdot 10^{-2}$	$1.377 \cdot 10^{-2}$	$1.052 \cdot 10^{-2}$
$5.00 \cdot 10^{-2}$	$4.99 \cdot 10^{-2}$	$1.459 \cdot 10^{-2}$	$1.251 \cdot 10^{-2}$
$6.00 \cdot 10^{-2}$	$5.99 \cdot 10^{-2}$	$1.512 \cdot 10^{-2}$	$1.431 \cdot 10^{-2}$
$7.00 \cdot 10^{-2}$	$6.99 \cdot 10^{-2}$	$1.586 \cdot 10^{-2}$	$1.594 \cdot 10^{-2}$
$8.00 \cdot 10^{-2}$	$7.99 \cdot 10^{-2}$	$1.633 \cdot 10^{-2}$	$1.744 \cdot 10^{-2}$
$9.00 \cdot 10^{-2}$	$8.98 \cdot 10^{-2}$	$1.678 \cdot 10^{-2}$	$1.881 \cdot 10^{-2}$
$1.00 \cdot 10^{-1}$	$9.98 \cdot 10^{-2}$	$1.721 \cdot 10^{-2}$	$2.008 \cdot 10^{-2}$
$5.00 \cdot 10^{-1}$	$4.94 \cdot 10^{-1}$	$2.509 \cdot 10^{-2}$	$3.891 \cdot 10^{-2}$
$1.00 \cdot 10^0$	$9.77 \cdot 10^{-1}$	$2.943 \cdot 10^{-2}$	$4.408 \cdot 10^{-2}$
$1.00 \cdot 10^1$	$7.76 \cdot 10^0$	$4.664 \cdot 10^{-2}$	$5.003 \cdot 10^{-2}$
$5.00 \cdot 10^1$	$1.11 \cdot 10^1$	$4.843 \cdot 10^{-2}$	$5.032 \cdot 10^{-2}$
$1.00 \cdot 10^2$	$1.51 \cdot 10^1$	$4.919 \cdot 10^{-2}$	$5.051 \cdot 10^{-2}$
$1.50 \cdot 10^2$	$2.02 \cdot 10^1$	$4.977 \cdot 10^{-2}$	$5.063 \cdot 10^{-2}$
$2.00 \cdot 10^2$	$2.67 \cdot 10^1$	$5.025 \cdot 10^{-2}$	$5.073 \cdot 10^{-2}$
$3.00 \cdot 10^2$	$4.54 \cdot 10^1$	$5.102 \cdot 10^{-2}$	$5.085 \cdot 10^{-2}$

TABLE A.28.: Artificial MPTA data (n^{exp}), and Langmuir fit (n^L) for C₁₀ at 573 K

P (bar)	f (bar)	n^{exp} ($\frac{mmol}{g}$)	n^L ($\frac{mmol}{g}$)
$1.00 \cdot 10^{-4}$	$1.00 \cdot 10^{-4}$	$3.388 \cdot 10^{-2}$	$3.159 \cdot 10^{-2}$
$2.00 \cdot 10^{-4}$	$2.00 \cdot 10^{-4}$	$3.656 \cdot 10^{-2}$	$3.745 \cdot 10^{-2}$
$3.00 \cdot 10^{-4}$	$3.00 \cdot 10^{-4}$	$3.820 \cdot 10^{-2}$	$3.992 \cdot 10^{-2}$
$4.00 \cdot 10^{-4}$	$4.00 \cdot 10^{-4}$	$3.943 \cdot 10^{-2}$	$4.128 \cdot 10^{-2}$
$5.00 \cdot 10^{-4}$	$5.00 \cdot 10^{-4}$	$4.046 \cdot 10^{-2}$	$4.214 \cdot 10^{-2}$
$1.00 \cdot 10^{-3}$	$1.00 \cdot 10^{-3}$	$4.355 \cdot 10^{-2}$	$4.398 \cdot 10^{-2}$
$2.00 \cdot 10^{-3}$	$1.38 \cdot 10^{-3}$	$4.509 \cdot 10^{-2}$	$4.451 \cdot 10^{-2}$
$3.00 \cdot 10^{-3}$	$1.38 \cdot 10^{-3}$	$4.509 \cdot 10^{-2}$	$4.451 \cdot 10^{-2}$
$4.00 \cdot 10^{-3}$	$1.38 \cdot 10^{-3}$	$4.509 \cdot 10^{-2}$	$4.451 \cdot 10^{-2}$
$5.00 \cdot 10^{-3}$	$1.38 \cdot 10^{-3}$	$4.509 \cdot 10^{-2}$	$4.451 \cdot 10^{-2}$
$7.50 \cdot 10^{-3}$	$1.38 \cdot 10^{-3}$	$4.509 \cdot 10^{-2}$	$4.451 \cdot 10^{-2}$
$1.00 \cdot 10^{-2}$	$1.38 \cdot 10^{-3}$	$4.509 \cdot 10^{-2}$	$4.451 \cdot 10^{-2}$
$5.00 \cdot 10^{-2}$	$1.39 \cdot 10^{-3}$	$4.509 \cdot 10^{-2}$	$4.452 \cdot 10^{-2}$
$1.00 \cdot 10^{-1}$	$1.39 \cdot 10^{-3}$	$4.509 \cdot 10^{-2}$	$4.452 \cdot 10^{-2}$
$1.00 \cdot 10^0$	$1.40 \cdot 10^{-3}$	$4.509 \cdot 10^{-2}$	$4.453 \cdot 10^{-2}$
$5.00 \cdot 10^1$	$2.24 \cdot 10^{-3}$	$4.519 \cdot 10^{-2}$	$4.506 \cdot 10^{-2}$
$1.00 \cdot 10^2$	$3.63 \cdot 10^{-3}$	$4.528 \cdot 10^{-2}$	$4.541 \cdot 10^{-2}$
$1.50 \cdot 10^2$	$5.85 \cdot 10^{-3}$	$4.536 \cdot 10^{-2}$	$4.562 \cdot 10^{-2}$
$2.00 \cdot 10^2$	$9.41 \cdot 10^{-3}$	$4.544 \cdot 10^{-2}$	$4.576 \cdot 10^{-2}$
$5.00 \cdot 10^2$	$1.58 \cdot 10^{-1}$	$4.581 \cdot 10^{-2}$	$4.597 \cdot 10^{-2}$

TABLE A.29.: Artificial MPTA data (n^{exp}), and Langmuir fit (n^L) for C₁₂ at 323 K.

P (bar)	f (bar)	n^{exp} ($\frac{mmol}{g}$)	n^L ($\frac{mmol}{g}$)
$1.00 \cdot 10^{-4}$	$1.00 \cdot 10^{-4}$	$2.241 \cdot 10^{-2}$	$1.223 \cdot 10^{-2}$
$2.00 \cdot 10^{-4}$	$2.00 \cdot 10^{-4}$	$2.444 \cdot 10^{-2}$	$1.926 \cdot 10^{-2}$
$3.00 \cdot 10^{-4}$	$3.00 \cdot 10^{-4}$	$2.584 \cdot 10^{-2}$	$2.382 \cdot 10^{-2}$
$4.00 \cdot 10^{-4}$	$4.00 \cdot 10^{-4}$	$2.666 \cdot 10^{-2}$	$2.703 \cdot 10^{-2}$
$5.00 \cdot 10^{-4}$	$5.00 \cdot 10^{-4}$	$2.747 \cdot 10^{-2}$	$2.940 \cdot 10^{-2}$
$1.00 \cdot 10^{-3}$	$1.00 \cdot 10^{-3}$	$3.009 \cdot 10^{-2}$	$3.567 \cdot 10^{-2}$
$2.00 \cdot 10^{-3}$	$2.00 \cdot 10^{-3}$	$3.292 \cdot 10^{-2}$	$3.992 \cdot 10^{-2}$
$3.00 \cdot 10^{-3}$	$3.00 \cdot 10^{-3}$	$3.473 \cdot 10^{-2}$	$4.158 \cdot 10^{-2}$
$4.00 \cdot 10^{-3}$	$4.00 \cdot 10^{-3}$	$3.595 \cdot 10^{-2}$	$4.245 \cdot 10^{-2}$
$5.00 \cdot 10^{-3}$	$5.00 \cdot 10^{-3}$	$3.696 \cdot 10^{-2}$	$4.300 \cdot 10^{-2}$
$7.50 \cdot 10^{-3}$	$7.49 \cdot 10^{-3}$	$3.898 \cdot 10^{-2}$	$4.375 \cdot 10^{-2}$
$1.00 \cdot 10^{-2}$	$9.99 \cdot 10^{-3}$	$4.040 \cdot 10^{-2}$	$4.413 \cdot 10^{-2}$
$5.00 \cdot 10^{-2}$	$2.16 \cdot 10^{-2}$	$4.435 \cdot 10^{-2}$	$4.477 \cdot 10^{-2}$
$1.00 \cdot 10^{-1}$	$2.16 \cdot 10^{-2}$	$4.435 \cdot 10^{-2}$	$4.477 \cdot 10^{-2}$
$1.00 \cdot 10^0$	$2.18 \cdot 10^{-2}$	$4.435 \cdot 10^{-2}$	$4.477 \cdot 10^{-2}$
$5.00 \cdot 10^1$	$3.33 \cdot 10^{-2}$	$4.449 \cdot 10^{-2}$	$4.496 \cdot 10^{-2}$
$1.00 \cdot 10^2$	$5.12 \cdot 10^{-2}$	$4.462 \cdot 10^{-2}$	$4.509 \cdot 10^{-2}$
$1.50 \cdot 10^2$	$7.83 \cdot 10^{-2}$	$4.473 \cdot 10^{-2}$	$4.517 \cdot 10^{-2}$
$2.00 \cdot 10^2$	$1.20 \cdot 10^{-1}$	$4.484 \cdot 10^{-2}$	$4.523 \cdot 10^{-2}$
$5.00 \cdot 10^2$	$1.45 \cdot 10^0$	$4.533 \cdot 10^{-2}$	$4.532 \cdot 10^{-2}$

TABLE A.30.: Artificial MPTA data (n^{exp}), and Langmuir fit (n^L) for C₁₂ at 373 K.

P (bar)	f (bar)	n^{exp} ($\frac{mmol}{g}$)	n^L ($\frac{mmol}{g}$)
$1.00 \cdot 10^{-3}$	$1.00 \cdot 10^{-3}$	$2.099 \cdot 10^{-2}$	$1.140 \cdot 10^{-2}$
$2.00 \cdot 10^{-3}$	$2.00 \cdot 10^{-3}$	$2.318 \cdot 10^{-2}$	$1.818 \cdot 10^{-2}$
$3.00 \cdot 10^{-3}$	$3.00 \cdot 10^{-3}$	$2.457 \cdot 10^{-2}$	$2.267 \cdot 10^{-2}$
$4.00 \cdot 10^{-3}$	$4.00 \cdot 10^{-3}$	$2.575 \cdot 10^{-2}$	$2.587 \cdot 10^{-2}$
$5.00 \cdot 10^{-3}$	$5.00 \cdot 10^{-3}$	$2.655 \cdot 10^{-2}$	$2.826 \cdot 10^{-2}$
$1.00 \cdot 10^{-2}$	$9.99 \cdot 10^{-3}$	$2.933 \cdot 10^{-2}$	$3.466 \cdot 10^{-2}$
$2.00 \cdot 10^{-2}$	$2.00 \cdot 10^{-2}$	$3.249 \cdot 10^{-2}$	$3.909 \cdot 10^{-2}$
$3.00 \cdot 10^{-2}$	$2.99 \cdot 10^{-2}$	$3.447 \cdot 10^{-2}$	$4.083 \cdot 10^{-2}$
$4.00 \cdot 10^{-2}$	$3.99 \cdot 10^{-2}$	$3.587 \cdot 10^{-2}$	$4.176 \cdot 10^{-2}$
$5.00 \cdot 10^{-2}$	$4.98 \cdot 10^{-2}$	$3.706 \cdot 10^{-2}$	$4.234 \cdot 10^{-2}$
$7.50 \cdot 10^{-2}$	$7.45 \cdot 10^{-2}$	$3.924 \cdot 10^{-2}$	$4.313 \cdot 10^{-2}$
$1.00 \cdot 10^{-1}$	$9.91 \cdot 10^{-2}$	$4.083 \cdot 10^{-2}$	$4.354 \cdot 10^{-2}$
$5.00 \cdot 10^{-1}$	$1.55 \cdot 10^{-1}$	$4.351 \cdot 10^{-2}$	$4.400 \cdot 10^{-2}$
$1.00 \cdot 10^0$	$1.56 \cdot 10^{-1}$	$4.351 \cdot 10^{-2}$	$4.400 \cdot 10^{-2}$
$1.00 \cdot 10^1$	$1.67 \cdot 10^{-1}$	$4.355 \cdot 10^{-2}$	$4.406 \cdot 10^{-2}$
$5.00 \cdot 10^1$	$2.30 \cdot 10^{-1}$	$4.370 \cdot 10^{-2}$	$4.427 \cdot 10^{-2}$
$1.00 \cdot 10^2$	$3.41 \cdot 10^{-1}$	$4.388 \cdot 10^{-2}$	$4.445 \cdot 10^{-2}$
$1.50 \cdot 10^2$	$5.02 \cdot 10^{-1}$	$4.404 \cdot 10^{-2}$	$4.457 \cdot 10^{-2}$
$2.00 \cdot 10^2$	$7.37 \cdot 10^{-1}$	$4.418 \cdot 10^{-2}$	$4.465 \cdot 10^{-2}$
$5.00 \cdot 10^2$	$7.00 \cdot 10^0$	$4.483 \cdot 10^{-2}$	$4.481 \cdot 10^{-2}$

TABLE A.31.: Artificial MPTA data (n^{exp}), and Langmuir fit (n^L) for C₁₂ at 423 K.

P (bar)	f (bar)	n^{exp} ($\frac{mmol}{g}$)	n^L ($\frac{mmol}{g}$)
$1.00 \cdot 10^{-3}$	$1.00 \cdot 10^{-3}$	$1.473 \cdot 10^{-2}$	$2.052 \cdot 10^{-3}$
$5.00 \cdot 10^{-3}$	$5.00 \cdot 10^{-3}$	$1.936 \cdot 10^{-2}$	$8.653 \cdot 10^{-3}$
$1.00 \cdot 10^{-2}$	$9.99 \cdot 10^{-3}$	$2.169 \cdot 10^{-2}$	$1.447 \cdot 10^{-2}$
$2.00 \cdot 10^{-2}$	$2.00 \cdot 10^{-2}$	$2.422 \cdot 10^{-2}$	$2.181 \cdot 10^{-2}$
$3.00 \cdot 10^{-2}$	$2.99 \cdot 10^{-2}$	$2.595 \cdot 10^{-2}$	$2.624 \cdot 10^{-2}$
$4.00 \cdot 10^{-2}$	$3.99 \cdot 10^{-2}$	$2.713 \cdot 10^{-2}$	$2.921 \cdot 10^{-2}$
$5.00 \cdot 10^{-2}$	$4.99 \cdot 10^{-2}$	$2.810 \cdot 10^{-2}$	$3.134 \cdot 10^{-2}$
$6.00 \cdot 10^{-2}$	$5.98 \cdot 10^{-2}$	$2.906 \cdot 10^{-2}$	$3.294 \cdot 10^{-2}$
$7.00 \cdot 10^{-2}$	$6.97 \cdot 10^{-2}$	$2.966 \cdot 10^{-2}$	$3.419 \cdot 10^{-2}$
$8.00 \cdot 10^{-2}$	$7.96 \cdot 10^{-2}$	$3.042 \cdot 10^{-2}$	$3.518 \cdot 10^{-2}$
$9.00 \cdot 10^{-2}$	$8.95 \cdot 10^{-2}$	$3.100 \cdot 10^{-2}$	$3.600 \cdot 10^{-2}$
$1.00 \cdot 10^{-1}$	$9.94 \cdot 10^{-2}$	$3.157 \cdot 10^{-2}$	$3.668 \cdot 10^{-2}$
$5.00 \cdot 10^{-1}$	$4.85 \cdot 10^{-1}$	$4.051 \cdot 10^{-2}$	$4.248 \cdot 10^{-2}$
$1.00 \cdot 10^0$	$6.59 \cdot 10^{-1}$	$4.254 \cdot 10^{-2}$	$4.294 \cdot 10^{-2}$
$1.00 \cdot 10^1$	$7.06 \cdot 10^{-1}$	$4.259 \cdot 10^{-2}$	$4.303 \cdot 10^{-2}$
$5.00 \cdot 10^1$	$9.53 \cdot 10^{-1}$	$4.282 \cdot 10^{-2}$	$4.334 \cdot 10^{-2}$
$1.00 \cdot 10^2$	$1.38 \cdot 10^0$	$4.306 \cdot 10^{-2}$	$4.363 \cdot 10^{-2}$
$1.50 \cdot 10^2$	$1.98 \cdot 10^0$	$4.327 \cdot 10^{-2}$	$4.382 \cdot 10^{-2}$
$2.00 \cdot 10^2$	$2.82 \cdot 10^0$	$4.346 \cdot 10^{-2}$	$4.396 \cdot 10^{-2}$
$5.00 \cdot 10^2$	$2.23 \cdot 10^1$	$4.428 \cdot 10^{-2}$	$4.424 \cdot 10^{-2}$

TABLE A.32.: Artificial MPTA data (n^{exp}), and Langmuir fit (n^L) for C₁₂ at 473 K.

P (bar)	f (bar)	n^{exp} ($\frac{mmol}{g}$)	n^L ($\frac{mmol}{g}$)
$1.00 \cdot 10^{-3}$	$1.00 \cdot 10^{-3}$	$7.539 \cdot 10^{-3}$	$5.186 \cdot 10^{-4}$
$5.00 \cdot 10^{-3}$	$5.00 \cdot 10^{-3}$	$1.047 \cdot 10^{-2}$	$2.474 \cdot 10^{-3}$
$1.00 \cdot 10^{-2}$	$1.00 \cdot 10^{-2}$	$1.210 \cdot 10^{-2}$	$4.678 \cdot 10^{-3}$
$2.00 \cdot 10^{-2}$	$2.00 \cdot 10^{-2}$	$1.393 \cdot 10^{-2}$	$8.438 \cdot 10^{-3}$
$3.00 \cdot 10^{-2}$	$3.00 \cdot 10^{-2}$	$1.506 \cdot 10^{-2}$	$1.153 \cdot 10^{-2}$
$4.00 \cdot 10^{-2}$	$4.00 \cdot 10^{-2}$	$1.597 \cdot 10^{-2}$	$1.411 \cdot 10^{-2}$
$5.00 \cdot 10^{-2}$	$4.99 \cdot 10^{-2}$	$1.670 \cdot 10^{-2}$	$1.630 \cdot 10^{-2}$
$6.00 \cdot 10^{-2}$	$5.99 \cdot 10^{-2}$	$1.727 \cdot 10^{-2}$	$1.818 \cdot 10^{-2}$
$7.00 \cdot 10^{-2}$	$6.98 \cdot 10^{-2}$	$1.782 \cdot 10^{-2}$	$1.981 \cdot 10^{-2}$
$8.00 \cdot 10^{-2}$	$7.98 \cdot 10^{-2}$	$1.835 \cdot 10^{-2}$	$2.125 \cdot 10^{-2}$
$9.00 \cdot 10^{-2}$	$8.97 \cdot 10^{-2}$	$1.874 \cdot 10^{-2}$	$2.251 \cdot 10^{-2}$
$1.00 \cdot 10^{-1}$	$9.97 \cdot 10^{-2}$	$1.912 \cdot 10^{-2}$	$2.364 \cdot 10^{-2}$
$5.00 \cdot 10^{-1}$	$4.92 \cdot 10^{-1}$	$2.627 \cdot 10^{-2}$	$3.695 \cdot 10^{-2}$
$1.00 \cdot 10^0$	$9.67 \cdot 10^{-1}$	$3.008 \cdot 10^{-2}$	$3.974 \cdot 10^{-2}$
$1.00 \cdot 10^1$	$4.59 \cdot 10^0$	$4.018 \cdot 10^{-2}$	$4.236 \cdot 10^{-2}$
$5.00 \cdot 10^1$	$6.17 \cdot 10^0$	$4.067 \cdot 10^{-2}$	$4.255 \cdot 10^{-2}$
$1.00 \cdot 10^2$	$8.73 \cdot 10^0$	$4.114 \cdot 10^{-2}$	$4.272 \cdot 10^{-2}$
$1.50 \cdot 10^2$	$1.22 \cdot 10^1$	$4.152 \cdot 10^{-2}$	$4.283 \cdot 10^{-2}$
$2.00 \cdot 10^2$	$1.68 \cdot 10^1$	$4.184 \cdot 10^{-2}$	$4.291 \cdot 10^{-2}$
$5.00 \cdot 10^2$	$1.03 \cdot 10^2$	$4.312 \cdot 10^{-2}$	$4.309 \cdot 10^{-2}$

TABLE A.33.: Artificial MPTA data (n^{exp}), and Langmuir fit (n^L) for C₁₂ at 573 K

P (bar)	f (bar)	n^{exp} ($\frac{mmol}{g}$)	n^L ($\frac{mmol}{g}$)
$1.00 \cdot 10^{-6}$	$1.00 \cdot 10^{-6}$	$2.363 \cdot 10^{-2}$	$1.902 \cdot 10^{-2}$
$2.00 \cdot 10^{-6}$	$2.00 \cdot 10^{-6}$	$2.509 \cdot 10^{-2}$	$2.395 \cdot 10^{-2}$
$3.00 \cdot 10^{-6}$	$3.00 \cdot 10^{-6}$	$2.596 \cdot 10^{-2}$	$2.621 \cdot 10^{-2}$
$4.00 \cdot 10^{-6}$	$4.00 \cdot 10^{-6}$	$2.655 \cdot 10^{-2}$	$2.751 \cdot 10^{-2}$
$5.00 \cdot 10^{-6}$	$5.00 \cdot 10^{-6}$	$2.713 \cdot 10^{-2}$	$2.835 \cdot 10^{-2}$
$1.00 \cdot 10^{-5}$	$1.00 \cdot 10^{-5}$	$2.874 \cdot 10^{-2}$	$3.021 \cdot 10^{-2}$
$2.00 \cdot 10^{-5}$	$2.00 \cdot 10^{-5}$	$3.035 \cdot 10^{-2}$	$3.123 \cdot 10^{-2}$
$3.00 \cdot 10^{-5}$	$3.00 \cdot 10^{-5}$	$3.137 \cdot 10^{-2}$	$3.158 \cdot 10^{-2}$
$4.00 \cdot 10^{-5}$	$3.79 \cdot 10^{-5}$	$3.202 \cdot 10^{-2}$	$3.173 \cdot 10^{-2}$
$5.00 \cdot 10^{-5}$	$3.79 \cdot 10^{-5}$	$3.202 \cdot 10^{-2}$	$3.173 \cdot 10^{-2}$
$7.50 \cdot 10^{-5}$	$3.79 \cdot 10^{-5}$	$3.202 \cdot 10^{-2}$	$3.173 \cdot 10^{-2}$
$1.00 \cdot 10^{-4}$	$3.79 \cdot 10^{-5}$	$3.202 \cdot 10^{-2}$	$3.173 \cdot 10^{-2}$
$5.00 \cdot 10^{-4}$	$3.79 \cdot 10^{-5}$	$3.202 \cdot 10^{-2}$	$3.173 \cdot 10^{-2}$
$1.00 \cdot 10^{-2}$	$3.80 \cdot 10^{-5}$	$3.202 \cdot 10^{-2}$	$3.173 \cdot 10^{-2}$
$1.00 \cdot 10^0$	$3.85 \cdot 10^{-5}$	$3.203 \cdot 10^{-2}$	$3.174 \cdot 10^{-2}$
$5.00 \cdot 10^1$	$7.44 \cdot 10^{-5}$	$3.208 \cdot 10^{-2}$	$3.202 \cdot 10^{-2}$
$1.00 \cdot 10^2$	$1.45 \cdot 10^{-4}$	$3.213 \cdot 10^{-2}$	$3.216 \cdot 10^{-2}$
$1.50 \cdot 10^2$	$2.84 \cdot 10^{-4}$	$3.218 \cdot 10^{-2}$	$3.224 \cdot 10^{-2}$
$2.00 \cdot 10^2$	$5.52 \cdot 10^{-4}$	$3.223 \cdot 10^{-2}$	$3.228 \cdot 10^{-2}$
$3.00 \cdot 10^2$	$2.08 \cdot 10^{-3}$	$3.231 \cdot 10^{-2}$	$3.231 \cdot 10^{-2}$

TABLE A.34.: Artificial MPTA data (n^{exp}), and Langmuir fit (n^L) for C₁₆ at 323 K.

P (bar)	f (bar)	n^{exp} ($\frac{mmol}{g}$)	n^L ($\frac{mmol}{g}$)
$1.00 \cdot 10^{-5}$	$1.00 \cdot 10^{-5}$	$1.973 \cdot 10^{-2}$	$7.352 \cdot 10^{-3}$
$2.00 \cdot 10^{-5}$	$2.00 \cdot 10^{-5}$	$2.117 \cdot 10^{-2}$	$1.197 \cdot 10^{-2}$
$3.00 \cdot 10^{-5}$	$3.00 \cdot 10^{-5}$	$2.204 \cdot 10^{-2}$	$1.514 \cdot 10^{-2}$
$4.00 \cdot 10^{-5}$	$4.00 \cdot 10^{-5}$	$2.261 \cdot 10^{-2}$	$1.745 \cdot 10^{-2}$
$5.00 \cdot 10^{-5}$	$5.00 \cdot 10^{-5}$	$2.319 \cdot 10^{-2}$	$1.921 \cdot 10^{-2}$
$1.00 \cdot 10^{-4}$	$1.00 \cdot 10^{-4}$	$2.478 \cdot 10^{-2}$	$2.406 \cdot 10^{-2}$
$2.00 \cdot 10^{-4}$	$2.00 \cdot 10^{-4}$	$2.651 \cdot 10^{-2}$	$2.754 \cdot 10^{-2}$
$3.00 \cdot 10^{-4}$	$3.00 \cdot 10^{-4}$	$2.752 \cdot 10^{-2}$	$2.893 \cdot 10^{-2}$
$4.00 \cdot 10^{-4}$	$4.00 \cdot 10^{-4}$	$2.838 \cdot 10^{-2}$	$2.968 \cdot 10^{-2}$
$5.00 \cdot 10^{-4}$	$5.00 \cdot 10^{-4}$	$2.896 \cdot 10^{-2}$	$3.015 \cdot 10^{-2}$
$7.50 \cdot 10^{-4}$	$7.50 \cdot 10^{-4}$	$3.011 \cdot 10^{-2}$	$3.080 \cdot 10^{-2}$
$1.00 \cdot 10^{-3}$	$1.00 \cdot 10^{-3}$	$3.097 \cdot 10^{-2}$	$3.114 \cdot 10^{-2}$
$5.00 \cdot 10^{-3}$	$1.28 \cdot 10^{-3}$	$3.163 \cdot 10^{-2}$	$3.136 \cdot 10^{-2}$
$1.00 \cdot 10^{-1}$	$1.28 \cdot 10^{-3}$	$3.163 \cdot 10^{-2}$	$3.136 \cdot 10^{-2}$
$1.00 \cdot 10^0$	$1.29 \cdot 10^{-3}$	$3.163 \cdot 10^{-2}$	$3.137 \cdot 10^{-2}$
$5.00 \cdot 10^1$	$2.32 \cdot 10^{-3}$	$3.171 \cdot 10^{-2}$	$3.173 \cdot 10^{-2}$
$1.00 \cdot 10^2$	$4.20 \cdot 10^{-3}$	$3.178 \cdot 10^{-2}$	$3.194 \cdot 10^{-2}$
$1.50 \cdot 10^2$	$7.58 \cdot 10^{-3}$	$3.185 \cdot 10^{-2}$	$3.205 \cdot 10^{-2}$
$2.00 \cdot 10^2$	$1.36 \cdot 10^{-2}$	$3.191 \cdot 10^{-2}$	$3.211 \cdot 10^{-2}$
$5.00 \cdot 10^2$	$4.42 \cdot 10^{-1}$	$3.219 \cdot 10^{-2}$	$3.219 \cdot 10^{-2}$

TABLE A.35.: Artificial MPTA data (n^{exp}), and Langmuir fit (n^L) for C₁₆ at 373 K.

P (bar)	f (bar)	n^{exp} ($\frac{mmol}{g}$)	n^L ($\frac{mmol}{g}$)
$1.00 \cdot 10^{-5}$	$1.00 \cdot 10^{-5}$	$1.363 \cdot 10^{-2}$	$1.412 \cdot 10^{-3}$
$2.00 \cdot 10^{-5}$	$2.00 \cdot 10^{-5}$	$1.477 \cdot 10^{-2}$	$2.704 \cdot 10^{-3}$
$3.00 \cdot 10^{-5}$	$3.00 \cdot 10^{-5}$	$1.548 \cdot 10^{-2}$	$3.891 \cdot 10^{-3}$
$4.00 \cdot 10^{-5}$	$4.00 \cdot 10^{-5}$	$1.604 \cdot 10^{-2}$	$4.986 \cdot 10^{-3}$
$5.00 \cdot 10^{-5}$	$5.00 \cdot 10^{-5}$	$1.647 \cdot 10^{-2}$	$5.998 \cdot 10^{-3}$
$1.00 \cdot 10^{-4}$	$1.00 \cdot 10^{-4}$	$1.775 \cdot 10^{-2}$	$1.010 \cdot 10^{-2}$
$2.00 \cdot 10^{-4}$	$2.00 \cdot 10^{-4}$	$1.917 \cdot 10^{-2}$	$1.534 \cdot 10^{-2}$
$3.00 \cdot 10^{-4}$	$3.00 \cdot 10^{-4}$	$2.016 \cdot 10^{-2}$	$1.855 \cdot 10^{-2}$
$4.00 \cdot 10^{-4}$	$4.00 \cdot 10^{-4}$	$2.073 \cdot 10^{-2}$	$2.072 \cdot 10^{-2}$
$5.00 \cdot 10^{-4}$	$5.00 \cdot 10^{-4}$	$2.130 \cdot 10^{-2}$	$2.229 \cdot 10^{-2}$
$7.50 \cdot 10^{-4}$	$7.50 \cdot 10^{-4}$	$2.229 \cdot 10^{-2}$	$2.478 \cdot 10^{-2}$
$1.00 \cdot 10^{-3}$	$1.00 \cdot 10^{-3}$	$2.300 \cdot 10^{-2}$	$2.625 \cdot 10^{-2}$
$5.00 \cdot 10^{-3}$	$5.00 \cdot 10^{-3}$	$2.755 \cdot 10^{-2}$	$3.060 \cdot 10^{-2}$
$1.00 \cdot 10^{-1}$	$1.60 \cdot 10^{-2}$	$3.118 \cdot 10^{-2}$	$3.150 \cdot 10^{-2}$
$1.00 \cdot 10^0$	$1.61 \cdot 10^{-2}$	$3.118 \cdot 10^{-2}$	$3.150 \cdot 10^{-2}$
$5.00 \cdot 10^1$	$2.75 \cdot 10^{-2}$	$3.129 \cdot 10^{-2}$	$3.167 \cdot 10^{-2}$
$1.00 \cdot 10^2$	$4.70 \cdot 10^{-2}$	$3.139 \cdot 10^{-2}$	$3.178 \cdot 10^{-2}$
$1.50 \cdot 10^2$	$8.02 \cdot 10^{-2}$	$3.148 \cdot 10^{-2}$	$3.184 \cdot 10^{-2}$
$2.00 \cdot 10^2$	$1.36 \cdot 10^{-1}$	$3.156 \cdot 10^{-2}$	$3.187 \cdot 10^{-2}$
$5.00 \cdot 10^2$	$3.08 \cdot 10^0$	$3.192 \cdot 10^{-2}$	$3.192 \cdot 10^{-2}$

TABLE A.36.: Artificial MPTA data (n^{exp}), and Langmuir fit (n^L) for C₁₆ at 423 K.

P (bar)	f (bar)	n^{exp} ($\frac{mmol}{g}$)	n^L ($\frac{mmol}{g}$)
$1.00 \cdot 10^{-5}$	$1.00 \cdot 10^{-5}$	$9.631 \cdot 10^{-3}$	$4.409 \cdot 10^{-4}$
$2.00 \cdot 10^{-5}$	$2.00 \cdot 10^{-5}$	$1.047 \cdot 10^{-2}$	$8.697 \cdot 10^{-4}$
$3.00 \cdot 10^{-5}$	$3.00 \cdot 10^{-5}$	$1.103 \cdot 10^{-2}$	$1.287 \cdot 10^{-3}$
$4.00 \cdot 10^{-5}$	$4.00 \cdot 10^{-5}$	$1.145 \cdot 10^{-2}$	$1.693 \cdot 10^{-3}$
$5.00 \cdot 10^{-5}$	$5.00 \cdot 10^{-5}$	$1.173 \cdot 10^{-2}$	$2.088 \cdot 10^{-3}$
$1.00 \cdot 10^{-4}$	$1.00 \cdot 10^{-4}$	$1.285 \cdot 10^{-2}$	$3.918 \cdot 10^{-3}$
$2.00 \cdot 10^{-4}$	$2.00 \cdot 10^{-4}$	$1.410 \cdot 10^{-2}$	$6.972 \cdot 10^{-3}$
$3.00 \cdot 10^{-4}$	$3.00 \cdot 10^{-4}$	$1.480 \cdot 10^{-2}$	$9.420 \cdot 10^{-3}$
$4.00 \cdot 10^{-4}$	$4.00 \cdot 10^{-4}$	$1.536 \cdot 10^{-2}$	$1.143 \cdot 10^{-2}$
$5.00 \cdot 10^{-4}$	$5.00 \cdot 10^{-4}$	$1.578 \cdot 10^{-2}$	$1.310 \cdot 10^{-2}$
$7.50 \cdot 10^{-4}$	$7.50 \cdot 10^{-4}$	$1.662 \cdot 10^{-2}$	$1.628 \cdot 10^{-2}$
$1.00 \cdot 10^{-3}$	$1.00 \cdot 10^{-3}$	$1.731 \cdot 10^{-2}$	$1.853 \cdot 10^{-2}$
$5.00 \cdot 10^{-3}$	$5.00 \cdot 10^{-3}$	$2.109 \cdot 10^{-2}$	$2.771 \cdot 10^{-2}$
$1.00 \cdot 10^{-1}$	$9.89 \cdot 10^{-2}$	$3.046 \cdot 10^{-2}$	$3.141 \cdot 10^{-2}$
$1.00 \cdot 10^0$	$1.04 \cdot 10^{-1}$	$3.067 \cdot 10^{-2}$	$3.143 \cdot 10^{-2}$
$5.00 \cdot 10^1$	$1.71 \cdot 10^{-1}$	$3.082 \cdot 10^{-2}$	$3.151 \cdot 10^{-2}$
$1.00 \cdot 10^2$	$2.81 \cdot 10^{-1}$	$3.096 \cdot 10^{-2}$	$3.156 \cdot 10^{-2}$
$1.50 \cdot 10^2$	$4.60 \cdot 10^{-1}$	$3.107 \cdot 10^{-2}$	$3.159 \cdot 10^{-2}$
$2.00 \cdot 10^2$	$7.47 \cdot 10^{-1}$	$3.118 \cdot 10^{-2}$	$3.161 \cdot 10^{-2}$
$5.00 \cdot 10^2$	$1.28 \cdot 10^1$	$3.164 \cdot 10^{-2}$	$3.164 \cdot 10^{-2}$

TABLE A.37.: Artificial MPTA data (n^{exp}), and Langmuir fit (n^L) for C₁₆ at 473 K.

P (bar)	f (bar)	n^{exp} ($\frac{mmol}{g}$)	n^L ($\frac{mmol}{g}$)
$1.00 \cdot 10^{-5}$	$1.00 \cdot 10^{-5}$	$4.832 \cdot 10^{-3}$	$9.211 \cdot 10^{-5}$
$2.00 \cdot 10^{-5}$	$2.00 \cdot 10^{-5}$	$5.372 \cdot 10^{-3}$	$1.837 \cdot 10^{-4}$
$3.00 \cdot 10^{-5}$	$3.00 \cdot 10^{-5}$	$5.766 \cdot 10^{-3}$	$2.747 \cdot 10^{-4}$
$4.00 \cdot 10^{-5}$	$4.00 \cdot 10^{-5}$	$6.033 \cdot 10^{-3}$	$3.652 \cdot 10^{-4}$
$5.00 \cdot 10^{-5}$	$5.00 \cdot 10^{-5}$	$6.291 \cdot 10^{-3}$	$4.552 \cdot 10^{-4}$
$1.00 \cdot 10^{-4}$	$1.00 \cdot 10^{-4}$	$6.970 \cdot 10^{-3}$	$8.971 \cdot 10^{-4}$
$2.00 \cdot 10^{-4}$	$2.00 \cdot 10^{-4}$	$7.772 \cdot 10^{-3}$	$1.744 \cdot 10^{-3}$
$3.00 \cdot 10^{-4}$	$3.00 \cdot 10^{-4}$	$8.303 \cdot 10^{-3}$	$2.544 \cdot 10^{-3}$
$4.00 \cdot 10^{-4}$	$4.00 \cdot 10^{-4}$	$8.590 \cdot 10^{-3}$	$3.302 \cdot 10^{-3}$
$5.00 \cdot 10^{-4}$	$5.00 \cdot 10^{-4}$	$8.975 \cdot 10^{-3}$	$4.020 \cdot 10^{-3}$
$7.50 \cdot 10^{-4}$	$7.50 \cdot 10^{-4}$	$9.520 \cdot 10^{-3}$	$5.663 \cdot 10^{-3}$
$1.00 \cdot 10^{-3}$	$1.00 \cdot 10^{-3}$	$9.928 \cdot 10^{-3}$	$7.118 \cdot 10^{-3}$
$5.00 \cdot 10^{-3}$	$5.00 \cdot 10^{-3}$	$1.274 \cdot 10^{-2}$	$1.855 \cdot 10^{-2}$
$1.00 \cdot 10^{-1}$	$9.94 \cdot 10^{-2}$	$2.024 \cdot 10^{-2}$	$3.000 \cdot 10^{-2}$
$1.00 \cdot 10^0$	$9.39 \cdot 10^{-1}$	$2.828 \cdot 10^{-2}$	$3.090 \cdot 10^{-2}$
$5.00 \cdot 10^1$	$1.97 \cdot 10^0$	$2.972 \cdot 10^{-2}$	$3.096 \cdot 10^{-2}$
$1.00 \cdot 10^2$	$3.08 \cdot 10^0$	$2.996 \cdot 10^{-2}$	$3.098 \cdot 10^{-2}$
$1.50 \cdot 10^2$	$4.76 \cdot 10^0$	$3.015 \cdot 10^{-2}$	$3.099 \cdot 10^{-2}$
$2.00 \cdot 10^2$	$7.30 \cdot 10^0$	$3.033 \cdot 10^{-2}$	$3.100 \cdot 10^{-2}$
$5.00 \cdot 10^2$	$8.49 \cdot 10^1$	$3.102 \cdot 10^{-2}$	$3.101 \cdot 10^{-2}$

TABLE A.38.: Artificial MPTA data (n^{exp}), and Langmuir fit (n^L) for C₁₆ at 573 K

Bibliography

1. Alexander, T. *et al.* Shale Gas Revolution. *Oilfield Review* **23**, 40–55. ISSN: 09231730 (2011).
2. Santos, V. E. S., Rego, E. E., dos Santos, E. M. & Ribeiro, C. O. Shale Gas and the Replacement of Coal-Fired Power Plants. *IEEE Latin America Transactions* **14**, 3721–3730. ISSN: 1548-0992 (2016).
3. *Technically Recoverable Shale Oil and Shale Gas Resources: An Assessment of 137 Shale Formations in 41 Countries Outside the United States* (U.S. Energy Information Administration, 2013).
4. Sakhaee-Pour, A. & Bryant, S. L. SPE 146944 Gas Permeability of Shale. *SPE Reservoir Evaluation & Engineering* (2012).
5. Luffel, D. L., Houston, R., Hopkins, C. W. & Holditch, S. A. *SPE 26633 Matrix Permeability Measurement of Gas Productive Shales in SPE 68th Annual Technical Conference and Exhibition* (Houston, Texas, USA, 1993).
6. Mallick, M. & Achalpurkar, M. *SPE-171823-MS Factors Controlling Shale Gas Production : Geological Perspective Factors Controlling Shale-gas Value in Abu Dhabi International Petroleum Exhibition and Conference* (Abu Dhabi, UAE, 2014), 10–13.
7. Dewhurst, D. *et al.* *ARMA 13-151 Mechanics , Physics , Chemistry and Shale Rock Properties in 47th US Rock Mechanics / Geomechanics Symposium* (San Francisco, CA, USA).
8. Fisher, L. & Israelachvili, J. Direct Experimental Verification of the Kelvin Equation for Capillary Condensation. *eng. Nature* **277**, 548–549. ISSN: 14764679, 14657392, 14764687, 00280836 (1979).
9. Fisher, L. & Israelachvili, J. Experimental studies on the applicability of the Kelvin equation to highly curved concave menisci. *Journal of Colloid and Interface Science* **80**, 528–541. ISSN: 00219797 (1981).
10. Fisher, L. & Israelachvili, J. Direct measurement of the effect of meniscus forces on adhesion: A study of the applicability of macroscopic thermodynamics to microscopic liquid interfaces. *Colloids and Surfaces* **3**, 303–319. ISSN: 0166-6622 (1981).
11. Christenson, H. Capillary condensation in systems of immiscible liquids. *Journal of Colloid and Interface Science* **104**, 234–249. ISSN: 00219797 (1985).
12. Luo, S., Lutkenhaus, J. L. & Nasrabadi, H. Use of differential scanning calorimetry to study phase behavior of hydrocarbon mixtures in nano-scale porous media. *Journal of Petroleum Science and Engineering*, 1–8. ISSN: 09204105 (2016).
13. Shapiro, A. & Stenby, E. Kelvin equation for a non-ideal multicomponent mixture. *Fluid Phase Equilibria* **134**, 87–101. ISSN: 03783812 (1997).

14. Shapiro, A. & Stenby, E. Thermodynamics of the multicomponent vapor – liquid equilibrium under capillary pressure difference. *Fluid Phase Equilibria* **178**, 17–32 (2001).
15. Sherafati, M. & Jessen, K. Stability analysis for multicomponent mixtures including capillary pressure. *Fluid Phase Equilibria* **433**, 56–66. ISSN: 03783812 (2017).
16. Michelsen, M. L. The isothermal flash problem. Part I. Stability. *Fluid Phase Equilibria* **9**, 1–19 (1982).
17. Wang, Y., Yan, B., Killough, J. & Texas, A. SPE 166267 Compositional Modeling of Tight Oil Using Dynamic Nanopore Properties (2013).
18. Firincioglu, T, Llc, N., Ozgen, C & Ozkan, E. *SPE 166459 An Excess-Bubble-Point-Suppression Correlation for Black Oil Simulation of Nano-Porous Unconventional Oil Reservoirs* in *SPE Annual Technical Conference and Exhibition* (New Orleans, Louisiana, USA, 2013).
19. Zhang, Y., Yu, W., Sepehrnoori, K. & Di, Y. Investigation of nanopore confinement on fluid flow in tight reservoirs. *Journal of Petroleum Science and Engineering*. ISSN: 09204105. doi:10.1016/j.petro1.2016.11.005 (2016).
20. Haider, B. A. & Aziz, K. *SPE-182603-MS Impact of Capillary Pressure and Critical Property Shift due to Confinement on Hydrocarbon Production in Shale Reservoirs* in *SPE Reservoir Simulation Conference* (Montgomery, TX, USA, 2017).
21. Shapiro, A. & Stenby, E. *Effects of Capillary Forces and Adsorption on Reserves Distribution* in *SPE European Petroleum Conference* (Milan, Italy, 1996), 441–448.
22. Ambrose, R. J. *et al.* Shale Gas-in-Place Calculations Part I : New Pore-Scale Considerations. *SPE Journal* **i**, 219–229 (2012).
23. Gasparik, M. *et al.* First international inter-laboratory comparison of high-pressure CH₄, CO₂ and C₂H₆ sorption isotherms on carbonaceous shales. *International Journal of Coal Geology* **132**, 131–146. ISSN: 01665162 (2014).
24. Collell, J. *et al.* Molecular simulation and modelisation of methane/ethane mixtures adsorption onto a microporous molecular model of kerogen under typical reservoir conditions. *Microporous and Mesoporous Materials* **197**, 194–203. ISSN: 13871811 (2014).
25. Collell, J. *et al.* Molecular Simulation of Bulk Organic Matter in Type II Shales in the Middle of the Oil Formation Window. eng. *Energy and Fuels* **28**, 7457–7466. ISSN: 15205029, 08870624 (2014).
26. Shapiro, A. a. & Stenby, E. H. Potential Theory of Multicomponent Adsorption. *Journal of Colloid and Interface Science* **157**, 146–157 (1998).
27. Polanyi, M. Potential Theory of Adsorption. *Verh. Disch. Phys. Ges.* **16**, 1012 (1914).
28. Li, Z., Jin, Z. & Firoozabadi, A. Phase Behavior and Adsorption of Pure Substances and Mixtures and Characterization in Nanopore Structures by Density Functional Theory. *SPE*. doi:10.2118/169819-PA (2014).
29. Travalloni, L., Castier, M., Tavares, F. W. & Sandler, S. I. Thermodynamic modeling of confined fluids using an extension of the generalized van der Waals theory. *Chemical Engineering Science* **65**, 3088–3099. ISSN: 00092509 (2010).
30. Travalloni, L., Castier, M., Tavares, F. W. & Sandler, S. I. Critical behavior of pure confined fluids from an extension of the van der Waals equation of state. *The Journal of Supercritical Fluids* **55**, 455–461 (2010).

31. Dong, X., Liu, H., Hou, J., Wu, K. & Chen, Z. Phase Equilibria of Confined Fluids in Nanopores of Tight and Shale Rocks Considering the Effect of Capillary Pressure and Adsorption Film. *Industrial & Engineering Chemistry Research* **55**, 798–811. ISSN: 0888-5885 (2016).
32. Nojabaei, B., Johns, R. T., Chu, L & Corporation, H. Effect of Capillary Pressure on Phase Behavior in Tight Rocks and Shales. *SPE August*, 281–289 (2013).
33. Pang, J., Zuo, J., Zhang, D., Du, L. & Corporation, H. *IPTC 16419 Effect of Porous Media on Saturation Pressures of Shale Gas and Shale Oil* in *IPTC* (Beijing, China, 2013), 26–28. ISBN: 1972952943.
34. Michelsen, L. Calculation of phase envelopes and critical points for multicomponent mixtures. *Fluid Phase Equilibria* **4**, 1–10 (1980).
35. Weinaug, C. F. & Katz, D. L. Surface Tensions of Methane-Propane Mixtures. *Industrial and Engineering Chemistry* **35**, 239–246. ISSN: 0019-7866 (1943).
36. Hugill, J. & Welsesens, A. V. Surface Tension: A simple correlation for natural gas + condensate systems. *Fluid Phase Equilibria* **29**, 383–390 (1986).
37. Lee, S.-T. & Chien, M. *A New Multicomponent Surface Tension Correlation Based on Scaling Theory* in *SPE/DOE Symposium on Enhanced Oil Recovery* (Tulsa, 1984), 147–145.
38. Danesh, A., Dandekar, A., Todd, A. & Sarkar, R. *A Modified Scaling Law and Parachor Method Approach for Improved Prediction of Interfacial Tension of Gas-Condensate Systems* in *SPE Annual Technical Conference and Exhibition* (Society of Petroleum Engineers, Dallas, 1991), 515–523. doi:10.2523/22710-MS.
39. Schechter, D. S. & Guo, B. Parachors Based on Modern Physics and Their Uses in IFT Prediction of Reservoir Fluids. *SPE June*, 207–217 (1998).
40. Brusilovsky, A. I. Mathematical Simulation of Phase Behavior of Natural Multicomponent Systems at High Pressures With an Equation of State. *SPE February*, 117–122 (1992).
41. Michelsen, M. & Mollerup, J. *Thermodynamic models; Fundamentals and Computational aspects* (1998).
42. Defay, R. & Prigogine, I. *Surface tension and adsorption* (Wiley, 1966).
43. Soave, G. Equilibrium constants from a modified Redlich-Kwong equation of state. *Chemical Engineering Science* **27**, 1197–1203. ISSN: 0009-2509 (1972).
44. Whitson, C. H. & Sunjerga, S. *SPE 155499 PVT in Liquid-Rich Shale Reservoirs* in *SPE Annual Technical Conference and Exhibition* (San Antonio, Texas, 2012), 8–10.
45. Hebden, M. D. An Algorithm for Minimization Using Exact Second Order Derivatives. *UKAEA Theoretical Physics Division Harwell* (1973).
46. Zhang, T., Ellis, G. S., Ruppel, S. C., Milliken, K. & Yang, R. Effect of organic-matter type and thermal maturity on methane adsorption in shale-gas systems. *Organic Geochemistry* **47**, 120–131. ISSN: 01466380 (2012).
47. Loucks, R. G., Reed, R. M., Ruppel, S. C. & Jarvie, D. M. Morphology, Genesis, and Distribution of Nanometer-Scale Pores in Siliceous Mudstones of the Mississippian Barnett Shale. *Journal of Sedimentary Research* **79**, 848–861. ISSN: 1527-1404 (2009).
48. Gasparik, M. *et al.* High-pressure methane sorption isotherms of black shales from the Netherlands. *Energy and Fuels* **26**, 4995–5004. ISSN: 08870624 (2012).

49. Rexer, T. F. T., Benham, M. J., Aplin, A. C. & Thomas, K. M. Methane adsorption on shale under simulated geological temperature and pressure conditions. *Energy and Fuels* **27**, 3099–3109. ISSN: 08870624 (2013).
50. Rexer, T. F., Mathia, E. J., Aplin, A. C. & Thomas, K. M. High-pressure methane adsorption and characterization of pores in posidonia shales and isolated kerogens. *Energy and Fuels* **28**, 2886–2901. ISSN: 15205029 (2014).
51. Bae, J. S. & Bhatia, S. K. High-pressure adsorption of methane and carbon dioxide on coal. *Energy and Fuels* **20**, 2599–2607. ISSN: 08870624 (2006).
52. Monsalvo, M. a. & Shapiro, A. a. Study of high-pressure adsorption from supercritical fluids by the potential theory. *Fluid Phase Equilibria* **283**, 56–64. ISSN: 03783812 (2009).
53. Chilev, C., Darkrim Lamari, F., Kirilova, E. & Pentchev, I. Comparison of gas excess adsorption models and high pressure experimental validation. *Chemical Engineering Research and Design* **90**, 2002–2012. ISSN: 02638762 (2012).
54. Langmuir, I. The Adsorption of Gases on Plane Surfaces of Glass, Mica and Platinum. *Journal of the American Chemical Society* **40**, 1361–1403 (1918).
55. Adamson, A. W. & Gast, A. P. *Physical Chemistry of surfaces* 6th Editio. ISBN: 0-471-14873-3 (Wiley & Sons, Inc, United States of America, 1997).
56. Myers, a. L. & Prausnitz, J. M. Thermodynamics of mixed-gas adsorption. *AIChE Journal* **11**, 121–127. ISSN: 0001-1541 (1965).
57. Monsalvo, M. a. & Shapiro, A. a. Modeling adsorption of binary and ternary mixtures on microporous media. *Fluid Phase Equilibria* **254**, 91–100. ISSN: 03783812 (2007).
58. Myers, A. L. Thermodynamics of adsorption in porous materials. *AIChE Journal* **48**, 145–160. ISSN: 1547-5905 (2002).
59. Mitchell, L. a. & Levan, M. D. Development of Adsorption Equilibrium Relations for Mixtures from Pure Component Isotherms and Henry ' s Law Behavior with Components in Excess. ISSN: 15205045. doi:10.1021/ie500765r (2014).
60. Peng, D.-Y. & Robinson, D. B. A New Two-Constant Equation of State. *Industrial & Engineering Chemistry Fundamentals* **15**, 59–64 (1976).
61. Dubinin, M. M. Microporous Structures and Absorption Properties of Carbonaceous Adsorbents. *Carbon* **21**, 359–366 (1983).
62. Bartholdy, S., Bjørner, M. G., Solbraa, E., Shapiro, A. & Kontogeorgis, G. M. Capabilities and Limitations of Predictive Engineering Theories for Multicomponent Adsorption. *Industrial & Engineering Chemistry Research* **52**, 11552–11563. ISSN: 0888-5885 (2013).
63. Monsalvo, M. a. & Shapiro, A. a. Modeling adsorption of liquid mixtures on porous materials. *Journal of colloid and interface science* **333**, 310–6. ISSN: 1095-7103 (2009).
64. Wang, Y., Tsotsis, T. T. & Jessen, K. Competitive Sorption of Methane/Ethane Mixtures on Shale: Measurements and Modeling. *Industrial and Engineering Chemistry Research* **54**, 12187–12195. ISSN: 15205045 (2015).
65. Luo, X. *et al.* Adsorption of methane, carbon dioxide and their binary mixtures on Jurassic shale from the Qaidam Basin in China. *International Journal of Coal Geology* **150-151**, 210–223. ISSN: 01665162 (2015).
66. Myers, A. & Monson, P. Adsorption in porous materials at high pressure: theory and experiment. *Langmuir* **18**, 10261–10273. ISSN: 0743-7463 (2002).

67. Costa, E., Sotelo, J. L., Calleja, G. & Marrón, C. Adsorption of binary and ternary hydrocarbon gas mixtures on activated carbon: Experimental determination and theoretical prediction of the ternary equilibrium data. *AIChE Journal* **27**, 5–12. ISSN: 1547-5905 (1981).
68. Payne, H. K., Sturdevant, G. A. & Leland, T. W. Improved Two-Dimensional Equation of State to Predict Adsorption of Pure and Mixed Hydrocarbons. *Industrial & Engineering Chemistry Fundamentals* **7**, 363–374 (1968).
69. Hyun, S. & Danner, R. Equilibrium Adsorption of Ethane, Ethylene, Isobutane, Carbon Dioxide, and their Binary-Mixtures on 13X Molecular-Sieves. eng. *Journal of Chemical and Engineering Data* **27**, 196–200. ISSN: 15205134, 00219568 (1982).
70. Nakahara, T, Hirata, M & Komatsu, S. Adsorption of a Gaseous Mixture of Ethane and Propane on a Molecular-Sieve. eng. *Journal of Chemical and Engineering Data* **26**, 161–163. ISSN: 15205134, 00219568 (1981).
71. Mason, J. A., Veenstra, M. & Long, J. R. Evaluating metal-organic frameworks for natural gas storage. *Chem. Sci.* **5**, 32–51 (1 2014).
72. Nojabaei, B., Siripatrachai, N., Johns, R. T. & Ertekin, T. Effect of large gas-oil capillary pressure on production: A compositionally-extended black oil formulation. *Journal of Petroleum Science and Engineering* **147**, 317–329. ISSN: 09204105 (2016).
73. Biswas, D. Shale Gas Predictive Model (SGPM)—An Alternate Approach To Model Shale Gas Production. *Proceedings of SPE Eastern Regional Meeting*. doi:10.2118/148491-MS (2011).
74. Orangi, A., Nagarajan, N., Honarpour, M. M. & Rosenzweig, J. Unconventional Shale Oil and Gas-Condensate Reservoir Production, Impact of Rock, Fluid, and Hydraulic Fractures. *Proceedings of SPE Hydraulic Fracturing Technology Conference*, 1–15 (2011).
75. Xiong, Y., Winterfeld, P. & Wu, Y.-S. Coupled Geomechanics and Pore Confinement Effects for Modeling Unconventional Shale Reservoirs. *Proceedings of the 2nd Unconventional Resources Technology Conference* (2014).
76. Yan, B., Wang, Y. & Killough, J. E. A Fully Compositional Model Considering the Effect of Nanopores in Tight Oil Reservoirs. *Journal of Petroleum Science and Engineering*. ISSN: 09204105. doi:10.1016/j.petrol.2017.01.005 (2017).
77. Acs, G., Doleschall, S. & Farkas, E. General Purpose Compositional Model. *Society of Petroleum Engineers Journal* **25**, 543–553. ISSN: 0197-7520 (1985).
78. Macneal, R. H. An asymmetrical finite difference network. *Quart. Appl. Math* **11**, 295–310 (1953).
79. Narasimhan, T. N. & Witherspoon, P. A. An integrated finite difference method for analyzing fluid flow in porous media. *Water Resour. Res.* **12**, 57–64 (1976).
80. Lohrenz, J., Bray, B. & Clark, C. Calculating Viscosities of Reservoir Fluids From Their Compositions. *Journal of Petroleum Technology* **16**, 1171–1176. ISSN: 0149-2136 (1964).
81. Peaceman, D. W. *Fundamentals of Numerical Reservoir Simulation* ISBN: 0444415785 (Elsevier Science Inc., New York, NY, USA, 1991).
82. Lei, G., Technologies, F. M. C., Cheng, N., Whitson, C. H. & Pera, N. SPE 167788 Liquid-Rich Shale Versus Conventional Depletion Performance, 25–27 (2014).
83. Yu, W., Lashgari, H. R., Wu, K. & Sepehrnoori, K. CO₂ injection for enhanced oil recovery in Bakken tight oil reservoirs. *Fuel* **159**, 354–363. ISSN: 00162361 (2015).

-
84. Yu, W., Lashgari, H. & Sepehrnoori, K. Simulation Study of CO₂ Huff-n-Puff Process in Bakken Tight Oil Reservoirs. *SPE Western North American and Rocky Mountain Joint Meeting* **2**, 16–18 (2014).
 85. Leverett, M., Lewis, W. & True, M. Dimensional-model Studies of Oil-field Behavior. *Society of Petroleum Engineers*. doi:10.2118/942175-G (1942).
 86. Brooks, R. & Corey, A. *Hydraulic Properties of Porous Media* (Colorado State University, 1964).